

Alma Mater Studiorum - Università di Bologna

DOTTORATO DI RICERCA IN
AUTOMOTIVE PER UNA MOBILITÀ INTELLIGENTE

Ciclo 35

Settore Concorsuale: 09/A2 - MECCANICA APPLICATA ALLE MACCHINE

Settore Scientifico Disciplinare: ING-IND/13 - MECCANICA APPLICATA ALLE MACCHINE

STABILITY ISSUES IN RACING MOTORCYCLES: AN IN-DEPTH ANALYSIS OF
THE CHATTER VIBRATION

Presentata da: Alexander Schramm

Coordinatore Dottorato

Nicolò Cavina

Supervisore

Silvio Sorrentino

Co-supervisore

Francesco Leali

Esame finale anno 2023

Summary

Racing motorcycles are prone to an unstable oscillatory motion of the swingarm and rear wheel, commonly known as 'chatter'. This vibration mode typically has a frequency of 17 Hz to 22 Hz and typically occurs during heavy braking manoeuvres. The appearance of chatter can cause reduced rider confidence, and therefore lead to longer lap times during races and the increased risk of crashing. This thesis looks to further the understanding of this mode. It includes the development of a simplified model to explore the effects roll angle and lateral dynamics have on the chatter mode using linear analysis. The mechanisms of instability and parameter sensitivities are also examined. The effects of the nonlinearities present in the minimal model equations of motion are examined, including the identification of limit cycles and their stability, inspecting individual nonlinear terms and their effects, and introducing tyre relaxation and determining the effect it has on the dynamics. Finally, an exploratory study of the mid-corner region of a typical racing manoeuvre is performed in hopes to better understand if any high frequency tyre induced instabilities like chatter can occur.

The minimal three degrees of freedom model developed models the rear section of a motorcycle and includes considerations for roll angle and later dynamics. Quasi-static linear root locus analysis is performed through a typical braking manoeuvre, finding an unstable driveline mode at 19 Hz. Energy flow analysis shows that the longitudinal forces are the main driver to instability, due to a 53.6° phase offset with slip velocity. Eigenvalue sensitivity analysis show that the most influential parameters are those that affect the natural frequencies of the rear hop and driveline modes, the tyre force gradients, and geometric parameters affecting the chain stiffness matrix. The mechanism of instability is analytically determined to be non-conservative restoring forces arising from an asymmetric system stiffness matrix, caused mainly by tyre force gradient terms. The roll and lateral dynamics do not play a direct role in instability, but an increased static roll angle causes instability which is attributed to the movement of the working point on the tyre characteristic function, which drives the tyre force gradients in destabilising directions.

The effects of relaxation length and the nonlinear characteristics of a two degrees of freedom minimal model are studied. Three versions of relaxation length are derived, and it is noted that the explicit dependence of vertical load vanishes from the nonlinear relaxation model. It is shown that the effects of relaxation in the linear stability analysis are minimal, and in fact the neglecting of relaxation behaviour would be a conservative assumption. The existence of a stable limit cycle in the unstable region of operation is shown and the driving nonlinear term in the equations of motion is found to be the tyre force function. Phase portraits are presented and the effects of pertinent parameters shown. The limit cycle is the result of a supercritical Hopf bifurcation in the forward velocity variable and, using Floquet theory, is found to be stable. The frequency response functions of the three relaxation models are found, separated from the other equations of motion by imposing first order limit cycle behaviour for the state variables. The Bode diagrams and numerical simulations show no discernable difference between the models in the frequency range of interest.

Finally, new operating regions that have not been widely studied in past literature are analysed. Both the three degrees of freedom minimal model and a full multi-body model are used to discern the modal behaviour of the rear suspension during high roll angle, high lateral acceleration manoeuvres in both traction and braking. The results show that the minimal model cannot adequately reproduce the dynamics of the multi-body model in the regions of interest, and is therefore insufficient for predicting stability behaviour for high roll angle manoeuvres. The multi-body is also unable to reproduce any unstable oscillations of interest. Further augmentations to the multi-body model are tested, including swingarm torsion and bending compliances of different stiffnesses and in different combinations. These have little effect on the rear stability of the motorcycle, though the bending flexibility of the swingarm is able to stabilise the driveline mode slightly in the braking region.

*To my wife, Jewli,
whose love and support has made this all possible.*

Acknowledgements

First and foremost, acknowledgement must be given to Dr. Silvio Sorrentino. Without his support, this endeavour would not have been possible. I would like to thank him for the opportunities he has provided me, and for the guidance and patience he has offered to me over the past three years.

I must give thanks to Dr. Luca Leonelli as well. His wealth of knowledge on the subject of motorcycle dynamics has been an inspiration, and I thank him for his support and guidance on this thesis, in our research, and in my career.

Without my colleagues support, this substantial undertaking would have been that much more difficult. I thank Dr. Alessandro De Felice for his assistance in learning and applying the necessary mathematical code, and for his collaboration with the efforts for developing Chapter 4. For his facilitation and camaraderie during my time as a visiting Ph.D. student, I also thank Dr. Francesco Passigato. Also, his collaboration and assistance in developing the multi-body model required for Chapter 5 is much appreciated.

Finally, I need to thank my family for their endless support and love over the years, without which I could not have pursued my ambitions.

Contents

List of Tables	xi
List of Figures	xiii
List of Acronyms	xv
List of Symbols	xvii
1 Introduction	1
1.1 Motivation	1
1.2 Problem Statement	1
1.3 Thesis Organisation	1
1.4 Contributions	2
2 Background	3
2.1 History of Single-Track Modelling and Stability	3
2.2 Motorcycle Tyre Modelling	7
2.3 Motorcycle Modelling and Stability	9
2.4 Frame Flexibility in Single-Track Vehicles	11
2.5 Nonlinear Analysis Concepts	11
2.6 Motorcycle Chatter	12
3 Motorcycle Chatter and Roll Angle	15
3.1 Introduction	15
3.2 Minimal Model	15
3.2.1 Chain Geometry	17
3.2.2 Tyre Model	21
3.2.3 Model Linearisation	24
3.2.4 Stationary Conditions	25
3.3 Analysis and Results	27
3.3.1 Comparison to a Multi-body Model	27
3.3.2 Eigenvalue Analysis of a Braking Manoeuvre	27
3.3.3 Energy Flow Analysis	28
3.3.4 Eigenvalue Sensitivity	31
3.3.5 Mechanism of Instability	34
3.3.6 Stabilisation via Natural Frequencies	34
3.3.7 Stabilisation via Chain Geometry	34

3.3.8	Effect of Swingarm Angle	34
3.3.9	Effect of Roll Angle	36
3.4	Conclusions	38
4	Nonlinear Effects on Motorcycle Chatter	41
4.1	Introduction	41
4.2	Model Description and Solution Methods	41
4.2.1	Minimal Model	42
4.2.2	Tyre Relaxation Model	44
4.2.3	Numerical Simulations	48
4.2.4	Limit Cycle Identification	49
4.2.5	Limit Cycle Stability	51
4.3	Results and Discussion	53
4.3.1	Effects of Tyre Relaxation on the Stability of the Linear Model	54
4.3.2	Numerical Results	55
4.3.3	Existence of Limit Cycles in the Nonlinear Model	58
4.3.4	Stability Analysis of the Nonlinear Model	61
4.3.5	Effects of Tyre Relaxation on the Stability of the Nonlinear Model	62
4.4	Conclusions	66
5	Chatter Stability in Mid-Corner and Acceleration	67
5.1	Introduction	67
5.2	Minimal Model Analysis	67
5.3	Multi-Body Model Analysis	71
5.4	Conclusions	75
6	Conclusions	77
6.1	Future Work	78
	References	79
	Appendix	89

List of Tables

Table 3.1:	Model reference parameter values not dependent on manoeuvre.	27
Table 3.2:	Summary of influential aspects on motorcycle chatter.	39
Table 4.1:	Magic Formula parameter values used in the nonlinear chapter.	43
Table 4.2:	Model parameters and equilibrium values.	44
Table 4.3:	Magic Formula relaxation length parameter values.	46
Table 4.4:	Asymptotic behaviours of different models of the nonlinear system.	57
Table 4.5:	Summary of nonlinear effects on motorcycle chatter.	66
Table 5.1:	Pertinent characteristic details of the multi-body model.	72
Table 5.2:	Variations of the multi-body model.	74

List of Figures

Figure 2.1:	Schematic of the bicycle as analytically modelled by Whipple [1899].	3
Figure 2.2:	Example Magic Formula tangential tyre ground forces.	8
Figure 3.1:	Rear suspension and driveline of a typical sport motorcycle.	16
Figure 3.2:	Model free body diagrams.	16
Figure 3.3:	Geometry of the drivetrain.	18
Figure 3.4:	Trigonometry of the drivetrain.	19
Figure 3.5:	Simplified chain geometry, change in sprocket centre angle.	19
Figure 3.6:	General chain geometry case, relation of ε_1 to α	20
Figure 3.7:	Simplified chain geometry, change in sprocket centre distance.	20
Figure 3.8:	Manoeuvre used to extract quasi-static equilibrium conditions.	26
Figure 3.9:	Comparison of the minimal model eigenvalues with those of a multi-body simulation.	28
Figure 3.10:	Quasi-static linear model eigenvalue analysis of the braking region.	29
Figure 3.11:	Tyre force and slip signals used for the energy flow analysis.	31
Figure 3.12:	Eigenvalue sensitivity to non-dimensional parameters of the driveline stability boundary.	32
Figure 3.13:	Eigenvalue sensitivity to model parameters of the driveline stability boundary.	33
Figure 3.14:	Routh-Hurwitz stability regions with respect to several non-dimensional parameters.	33
Figure 3.15:	Changes to eigenvalues with respect to natural frequency parameters.	35
Figure 3.16:	Stability with varying chain geometry σ	35
Figure 3.17:	Stability with varying static swingarm angle α_0	36
Figure 3.18:	Driveline stability boundary with respect to V_{fx} and ϕ_0	37
Figure 3.19:	Tyre tangential force gradient parameters as a function of roll angle.	37
Figure 4.1:	Schematic representation of the minimal two DOFs model.	42
Figure 4.2:	Longitudinal ground force transient model.	45
Figure 4.3:	Sample of numerical simulation, showing state variables.	49
Figure 4.4:	Stability regions of the relaxed linear system with non-relaxed shown with dashed lines.	54
Figure 4.5:	Effects of a constant relaxation length on system stability.	55
Figure 4.6:	Asymptotic behaviour of the nonlinear system as numerically simulated.	56
Figure 4.7:	Limit cycle phase space of the nonlinear system as numerically simulated.	56
Figure 4.8:	Tyre limit cycle phase spaces of the nonlinear system as numerically simulated.	57
Figure 4.9:	Effect of some relevant parameters on asymptotic behaviour.	58
Figure 4.10:	Phase portrait and limit cycle (shown in red) in the variables $\tilde{\alpha}(t)$ and $\tilde{\theta}(t)$	59
Figure 4.11:	Tyre forces and slip phase space of limit cycles refined up to the fourth harmonic.	59
Figure 4.12:	Tyre phase space of limit cycles for different values of moment of inertia J_α	60
Figure 4.13:	Tyre phase space of limit cycles for different values of suspension damping c_s	60
Figure 4.14:	Critical speed and bifurcation diagrams.	61
Figure 4.15:	Bode diagram of the LTI and nonlinear relaxation models.	63
Figure 4.16:	System response comparison of three different relaxation models.	64
Figure 4.17:	Maximum oscillation amplitudes of the semi-nonlinear model response.	64
Figure 4.18:	Tyre forces and slip phase space of limit cycles for different values of relaxation length.	65
Figure 4.19:	Tyre forces and slip phase space of limit cycles for different relaxation models.	65
Figure 5.1:	Manoeuvre used to extract quasi-static conditions.	68
Figure 5.2:	Quasi-static linear model eigenvalue analysis of the mid-corner regions.	69

Figure 5.3:	Quasi-static linear model eigenvalue analysis of the acceleration region.	70
Figure 5.4:	Tyre force and slip signals used for the energy analysis of the mid-corner region.	71
Figure 5.5:	Tyre force and slip signals used for the energy analysis of the acceleration region.	71
Figure 5.6:	Multi-body model schematic.	72
Figure 5.7:	Manoeuvre data and the simulation response of the multi-body model.	73
Figure 5.8:	Root locus comparison of the multi-body model and the minimal model eigenvalues.	74
Figure 5.9:	Root locus with structural flexibility variations to the multi-body model.	75
Figure 5.10:	Evolution of the real parts of the driveline and rear hop modes of the multi-body model.	75

List of Acronyms

CAD	Computer Aided Design
CAE	Computer Aided Engineering
COM	Centre Of Mass
DAE	Differential Algebraic Equation
DOF	Degree Of Freedom
EOM	Equation Of Motion
FEA	Finite Element Analysis
FRF	Frequency Response Function
LTI	Linear Time Invariant
MF	Magic Formula
PID	Proportional Integral Derivative
SWIFT	Short Wavelength Intermediate Frequency Tyre

List of Symbols

Symbol	Unit	Description
Γ_i		Linear combination of tyre force gradient damping terms
$\Delta \ell_c$	m	Equilibrium chain stretch
ΔE	J	Change in system energy over one period of oscillation
ΔE_{dis}	J	Change in system energy due to dissipative elements
ΔE_{kin}	J	Change in system kinetic energy over one period of oscillation
ΔE_{pot}	J	Change in system potential energy over one period of oscillation
Ψ_f		Normalised frame rotational damping
Φ_i		Normalised stiffness terms
Ω	rad s ⁻¹	Frequency
Ω_{fz}	rad s ⁻¹	Infinite inertia frame yaw rate
α	rad	Swingarm angle
α_{s0}	rad	Rear suspension spring preload
α_{slip}	rad	Tyre side-slip angle
β_p	rad	Front sprocket offset angle
γ_{ij}		Normalised tyre force gradient damping terms
δ		Sets the active portion of the chain (1 for braking and -1 for traction)
ε_1	rad	Chain wrap angle due to a change in sprocket centre angle
ε_2	rad	Chain wrap angle due to a change in sprocket centre distance
ζ		Normalised system damping ratio
η	rad	Real periodic functions approximating a limit cycle
η		Gradient of tyre rolling radius with respect to loaded radius
η_{fr}		Fractional location of reference frame centre of mass on line <i>FS</i>
η_{sa}		Fractional location of swingarm centre of mass on line <i>SA</i>
θ	rad	Wheel spin angle
θ_p	rad	Front sprocket spin angle
ϑ		Frequency response function phase angle
κ		Rear tyre longitudinal practical slip coefficient
κ_r		Transient rear tyre longitudinal practical slip coefficient
λ_j	rad s ⁻¹	System eigenvalue
λ'_j	rad s ⁻¹	System eigenvalue gradient with respect to a system parameter
λ_x		Time dependent nonlinear longitudinal relaxation length of the tyre
λ_{x0}		Static linearised longitudinal relaxation length of the tyre
λ_{x1}		Reduced tyre longitudinal force sensitivity to swingarm angle
λ_{x2}		Reduced tyre longitudinal force sensitivity to roll angle
λ_{y1}		Reduced tyre lateral force sensitivity to swingarm angle
λ_{y2}		Reduced tyre lateral force sensitivity to roll angle

Symbol	Unit	Description
μ_i		Normalised static tyre forces
ν_ψ	m^{-1}	Reduced frame yaw rate
ν_x		Reduced frame longitudinal velocity
ν_y		Reduced frame lateral velocity
ξ_R		Near-unity normalised system geometric term
ξ_z		Near-unity normalised system geometric term
ρ_r	m	Rear tyre toroidal radius
σ		Normalised chain geometry term
σ'		Normalised chain geometry term
σ_x		Rear tyre longitudinal theoretical slip coefficient
σ_y		Rear tyre lateral theoretical slip coefficient
ϕ	rad	Roll angle
ϕ_{f0}	rad	Roll angle spring preload (optional)
φ	$rad m^{-1}$	Rear tyre spin theoretical slip coefficient
χ_x	N	Reduced tyre longitudinal force sensitivity to wheelspeed
χ_y	N	Reduced tyre lateral force sensitivity to wheelspeed
ψ	rad	Chain-to-swingarm angle
ψ_1	rad	Angle between sprocket centres and chain
ψ_2	rad	Angle between swingarm and sprocket centres
A		Point of rear wheel axle on swingarm
\mathbf{A}		Time-varying system matrix
A_{ij}	rad	Harmonic balance constants
\mathbf{B}		Time-varying system matrix
B_{ij}	rad	Harmonic balance constants
B_x		Semi-empirical Magic Formula coefficient
C		Rear tyre ground contact point
\mathbf{C}		Normalised system damping matrix
$\mathbf{C}^*(t)$	s^{-1}	Nonlinear Jacobian damping matrix
$C_{\alpha_{slip,x}}$	N	Longitudinal tyre force gradient with respect to side-slip angle
$C_{\alpha_{slip,y}}$	N	Lateral tyre force gradient with respect to side-slip angle
$C_{\kappa,x}$	N	Longitudinal tyre force gradient with respect to practical longitudinal slip
$C_{\kappa,y}$	N	Lateral tyre force gradient with respect to practical longitudinal slip
$C_{\sigma_x,x}$	N	Longitudinal tyre force gradient with respect to theoretical longitudinal slip
$C_{\sigma_x,y}$	N	Lateral tyre force gradient with respect to theoretical longitudinal slip
$C_{\sigma_y,x}$	N	Longitudinal tyre force gradient with respect to theoretical lateral slip
$C_{\sigma_y,y}$	N	Lateral tyre force gradient with respect to theoretical lateral slip
C_ϕ		Normalised Coriolis stiffness term
$C_{\phi,x}$	$N rad^{-1}$	Longitudinal tyre force gradient with respect to roll angle
$C_{\phi,y}$	$N rad^{-1}$	Lateral tyre force gradient with respect to roll angle
$C_{F_z,x}$		Longitudinal tyre force gradient with respect to vertical load
$C_{F_z,y}$		Lateral tyre force gradient with respect to vertical load
\mathbf{C}_{gyro}		Normalised system gyroscopic damping matrix
C_i		Normalised centrifugal stiffness terms
\mathbf{C}_{tyre}		Normalised system tyre damping matrix
C_x		Semi-empirical Magic Formula coefficient

Symbol	Unit	Description
D_x		Semi-empirical Magic Formula coefficient
E_c	J	Potential energy store in the chain
E_x		Semi-empirical Magic Formula coefficient
F		Attachment point on infinite inertia frame
F_R	N	In-plane tyre force
F_c	N	Chain force
F_{damp}	N	Tyre transient model, damping element force
F_{stiff}	N	Tyre transient model, stiffness element force
F_x	N	Tyre longitudinal ground force
\tilde{F}_x	N	Perturbed, oscillating portion of tyre longitudinal force
F_{xf}	N	Front tyre longitudinal ground force
F_{xr}	N	Rear tyre longitudinal ground force
F_y	N	Tyre lateral ground force
\tilde{F}_y	N	Perturbed, oscillating portion of tyre lateral force
F_{yf}	N	Front tyre lateral ground force
F_{yr}	N	Rear tyre lateral ground force
F_z	N	Tyre vertical load
\tilde{F}_z	N	Perturbed, oscillating portion of tyre vertical load
F_{zf}	N	Front tyre vertical load
F_{zr}	N	Rear tyre vertical load
F_{z0P}	N	Magic Formula nominal tyre load
\overrightarrow{FO}	m	Vector position of point O with respect to point F
\mathbf{G}	N	Linearised system equations as a sum of forces and inertial terms
\mathcal{G}		Normalised gyroscopic damping term
H		Frequency response function
I_i^j	(various)	Numerical search algorithm interval
\mathbf{J}	(various)	Jacobian of the nonlinear homogeneous system
J_α	kg m ²	Reduced inertia about the swingarm pivot
J_ϕ	kg m ²	Reduced inertia about the roll angle pivot
\mathbf{J}_{fr}	kg m ²	Principal inertia tensor of the reference frame
J_{frx}	kg m ²	x component of the rotational inertia of the reference frame
J_{fry}	kg m ²	y component of the rotational inertia of the reference frame
J_{frz}	kg m ²	z component of the rotational inertia of the reference frame
\mathcal{J}_i		Normalised inertiae terms
\mathbf{J}_{sa}	kg m ²	Principal inertia tensor of the swingarm
J_{sax}	kg m ²	x component of the rotational inertia of the swingarm
J_{say}	kg m ²	y component of the rotational inertia of the swingarm
J_{saz}	kg m ²	z component of the rotational inertia of the swingarm
\mathbf{J}_{wh}	kg m ²	Principal inertia tensor of the rear wheel
J_{whxz}	kg m ²	x and z components of the rotational inertia of the rear wheel
J_{why}	kg m ²	y component of the rotational inertia of the rear wheel
K	N m ⁻¹	Tyre transient model, tyre contact point longitudinal stiffness
\mathbf{K}		Normalised system stiffness matrix
$\mathbf{K}^*(t)$	s ⁻²	Nonlinear Jacobian stiffness matrix
\mathbf{K}_{cent}		Normalised system centrifugal stiffness matrix

Symbol	Unit	Description
$\mathbf{K}_{\text{chain}}$		Normalised system chain stiffness matrix
\mathbf{K}_{Cori}		Normalised system Coriolis stiffness matrix
\mathbf{K}_{gyro}		Normalised system gyroscopic stiffness matrix
\mathbf{K}_{stat}		Normalised system static tyre force stiffness matrix
\mathbf{K}_{tyre}		Normalised system tyre gradient stiffness matrix
L_R	m	Characteristic model length, point F to tyre toroid centre
\mathbf{M}		Normalised system inertia matrix
M_{bf}	N m	Front braking moment
M_{br}	N m	Rear braking moment
M_c	N m	Moment on the engine crankshaft due to the chain force
$M_{c\alpha}$	N m	Moment on the swingarm due to the chain force
$M_{c\theta}$	N m	Moment on the rear wheel due to the chain force
$M_{\text{cent},\alpha}$	N m	Swingarm moment due to centrifugal forces
$M_{\text{cent},\phi}$	N m	Roll angle moment due to centrifugal forces
$M_{\text{cor},\alpha}$	N m	Swingarm moment due to Coriolis forces
$M_{\text{cor},\phi}$	N m	Roll angle moment due to Coriolis forces
M_e	N m	Engine torque
$M_{\text{gyro},\alpha}$	N m	Swingarm moment due to gyroscopic forces
$M_{\text{gyro},\phi}$	N m	Roll angle moment due to gyroscopic forces
$N_{1,2}$	$\text{m s}^{-1} \text{rad}^{-2}$	Nonlinear system coupling values
O		In-plane ground point
P		Rear tyre toroid centre point
P_i	N	Harmonic balance method terms
\mathbf{R}		In-plane (along ϕ) axis direction orthogonal to x
R_R	m	Rear tyre rolling radius
R_c	m	Rear tyre loaded radius
R_{c0}	m	Static rear tyre loaded radius
R_{c0}^i	m	Static rear tyre loaded radius partial derivative with respect to variable i
R_r	m	Rear tyre outer radius
S		Point of swingarm pivot on reference frame
T	s	System period of oscillation
V_{fx}	m s^{-1}	Infinite inertia frame velocity, x -direction
V_{fy}	m s^{-1}	Infinite inertia frame velocity, y -direction
\mathbf{V}_O	m s^{-1}	Velocity vector of point O
V_{Ox}	m s^{-1}	x velocity of point O
V_{Oy}	m s^{-1}	y velocity of point O
V_{sx}	m s^{-1}	Tyre longitudinal slip velocity
\tilde{V}_{sx}	m s^{-1}	Perturbed, oscillating portion of tyre longitudinal slip velocity
V_{sxr}	m s^{-1}	Transient tyre longitudinal slip velocity
\tilde{V}_{sy}	m s^{-1}	Perturbed, oscillating portion of tyre lateral slip velocity
V_x	m s^{-1}	Wheel centre velocity
\mathbf{a}		Congruence vector for the tyre longitudinal force
\mathbf{b}		Congruence vector for the tyre lateral force
c_f	N m s rad^{-1}	Roll angle equivalent damping coefficient (optional)
c_r	m	Vertical distance from point O to C

Symbol	Unit	Description
c_s	N m s rad^{-1}	Rear suspension equivalent damping coefficient
d	m	Centre distance between sprockets
g	m s^{-2}	Acceleration due to gravity
g_{ij}		Normalised gravitational terms
f		Normalised tyre static force stiffness term
f_x	N	Linearised longitudinal tyre force vector
f_y	N	Linearised lateral tyre force vector
h_f	m	Planar height from point F to S
k	N m rad^{-1}	Reduced total system stiffness
k_f	N m rad^{-1}	Roll angle equivalent spring stiffness (optional)
k_s	N m rad^{-1}	Rear suspension equivalent spring stiffness
k_z	N m^{-1}	Tyre vertical stiffness
l_α	m	Characteristic length for swingarm angle coordinate
l_{θ_c}	m	Chain length due to wrapping effects
$l_{\theta_{c1}}$	m	Chain wrapping effect due to sprocket centre angle variation
$l_{\theta_{c2}}$	m	Chain wrapping effect due to sprocket centre distance variation
l_α	m	Characteristic length for roll angle coordinate
l_{ω_c}	m	Chain length due to sprocket rotation
l_c	m	Dynamic total chain length
l_{fc}	m	Free chain length
l_p	m	Front sprocket offset distance
l_{sa}	m	Swingarm length
l_{tc}	m	Tangential chain length
m_α	kg	Reduced system mass
m_{fr}	kg	Mass of the reference frame
m_{sa}	kg	Mass of the swingarm
m_{wh}	kg	Mass of the rear wheel
P_{ijk}		Magic Formula parameters
\mathbf{q}		Vector of the generalised coordinates
$\tilde{\mathbf{q}}$	m	Vector of rectilinearised perturbations of the generalised coordinates
r_c	m	Rear sprocket radius
r_p	m	Front sprocket radius
u	m	Tyre transient model, contact displacement
u_{damp}	m	Tyre transient model, displacement of damping element
u_{damp}	m	Tyre transient model, displacement of stiffness element
\mathbf{w}^*	rad	First order perturbation from the limit cycle
x_f	m	Longitudinal distance from point F to S
\mathbf{y}^*	(various)	Vector of Floquet analysis system variables
\mathbf{y}_j	rad s^{-1}	System eigenvector
z	m	Rear tyre vertical deflection
z_f	m	Height of point F from the ground plane
z_{sa}	m	Height of point S from the ground plane

1 Introduction

1.1 Motivation

Single-track vehicles are prone to unique and complex oscillatory modes, particularly in motorcycles where travelling speeds can achieve much higher values [Koenen 1983]. The dynamics of these modes are also highly coupled since the ‘in-plane’ or vertical and ‘out-of-plane’ or lateral motions of the motorcycle become linked during cornering as the motorcycle encounters high roll angles. The understanding of the mechanisms which drive these oscillations is critical to the safe design of motorcycles.

Racing motorcycles, which tend to push the limits of the machine and the tyres, are especially prone to these unique and complex modes [Cossalter et al. 2008]. One such mode is the ‘chatter’ mode, a lightly damped oscillation of the rear suspension typically occurring during heavy braking with a frequency of 17 Hz to 22 Hz. The appearance of chatter can cause reduced rider confidence, and therefore lead to longer lap times during races and the increased risk of crashing [Catania et al. 2013].

1.2 Problem Statement

The objective of this thesis is to further the understanding of the unstable chatter mode experienced in racing motorcycles. This includes the development of a simplified model to explore the effects of roll angle and lateral dynamics on the chatter mode using linear analysis. The mechanisms of instability and parameter sensitivities are also examined. The effects of the nonlinearities present in the minimal model equations of motion (EOMs) are examined including the identification of limit cycles and their stability, inspecting individual nonlinear terms and their effects, and introducing tyre relaxation and determining its effects. Finally, an exploratory study of the mid-corner region of a typical racing manoeuvre is performed in hopes to better understand if any high frequency tyre induced instabilities like chatter can occur.

1.3 Thesis Organisation

This thesis is organised into six chapters. Chapter 2 introduces the background and history of modelling single-track vehicles, identification and analysis of their modes and instabilities, as well as an in-depth discussion of the existing analysis of chatter and similar modes in contemporary literature.

Chapter 3 contains the study of the effects of roll angle on the chatter instability using a minimal three degrees of freedom (DOFs) model. It outlines the construction of the minimal model, the methods used in analysis, and discussion and analysis of findings.

Chapter 4 concerns the nonlinear analysis of a simplified model with respect to the motorcycle chatter instability. It covers the simplifications made to the minimal model of Chapter 3, the nonlinear analysis methods employed, and the pertinent results and discussion.

Chapter 5 explores the possibility of other high frequency instabilities occurring in the mid-corner phase of a racing motorcycle manoeuvre. This chapter uses both the minimal model of Chapter 3 and a newly introduced multi-body model and reports the findings of both. Finally, Chapter 6 summarises and reports the major findings of this thesis and suggests further topics of study.

1.4 Contributions

The major contributions of this thesis are as follows:

- (i) Development of a minimal model to simulate the chatter instability in motorcycles which includes the effects of roll angle and lateral dynamics.
- (ii) Perform linear stability analysis on the minimal model, including root loci and Routh-Hurwitz methodologies.
- (iii) Determine eigenvalue sensitivities of the chatter mode with respect to modelling parameters.
- (iv) Outline the key aspects to the growth and stability of the chatter mode during a braking manoeuvre including roll angle.
- (v) Show the effects on the stability of the chatter mode due to the introduction of tyre transients, namely relaxation length.
- (vi) Determine the existence and stability of potential limit cycles in the minimal model through the use of nonlinear analysis methods.
- (vii) Investigate the effects of the use of different relaxation models on the nonlinear system and limit cycles.
- (viii) Explore the possible existence of modes similar to chatter in the mid-corner region of a racing manoeuvre using both the minimal model and a full multi-body motorcycle model.

2 Background

While there exists many types of two wheeled vehicles such as bicycles, motorcycles, and scooters of many varieties, they can all be categorised analytically as ‘single-track’ vehicles [Sharp 1976b]. Since the advent of these machines in the 19th century, there has been a continual effort to increase their speed and improve their stability [Limebeer and Massaro 2018]. This naturally leads to the need for analytical models to analyse the behaviour and stability of the vehicles [Sharp 1985]. This section outlines the history of major contributions and developments in the modelling of single-track vehicles, as well as the accompanying advances in the understanding of their stability characteristics. This is followed by a section dedicated to more specific topics relevant to this thesis, including advances in modelling and stability analysis, tyre modelling, and frame flexibility. Finally, the chapter ends with a review of the state of the art for the specific ‘chatter’ mode experienced mainly in racing motorcycles.

2.1 History of Single-Track Modelling and Stability

The first major contribution to the subject of modelling the behaviour of single-track vehicles was by Whipple [1899], who developed an analytic model to study the dynamics of a bicycle. The model consisted of two frames, front and rear, of a bicycle joined by the steering joint. The wheels and tyres were given non-holonomic constraints so that they experience no lateral or longitudinal slip at the contact points, enforcing a pure rolling state for each. The model was realised in straight running and only small perturbations from this condition were considered. This resulted in a two DOFs system, an example of which is shown in Figure 2.1. Though thorough numerical analysis was not convenient at the time, Whipple used the Routh-Hurwitz criterion to determine the stability of a bicycle operated without rider intervention on the handlebars. It was found that the bicycle has a stable region of velocity, in this case between 4.62 m s^{-1} and 5.45 m s^{-1} . Below this region there is an unstable oscillatory mode (two complex conjugate eigenvalues with positive real parts), while above that range there is a slightly unstable divergent mode (single real positive eigenvalue) and the bicycle is easily controlled by small motions of the rider’s body.

After the publication by Whipple, changes to the aspects of single-track modelling appeared to be few for many years, as outlined by Sharp [1985], Limebeer and Sharp [2006], Schwab and Meijaard [2013] and Limebeer and Massaro [2018]. Timoshenko and Young [1948] introduced in their book *Advanced Dynamics* a simplified dynam-

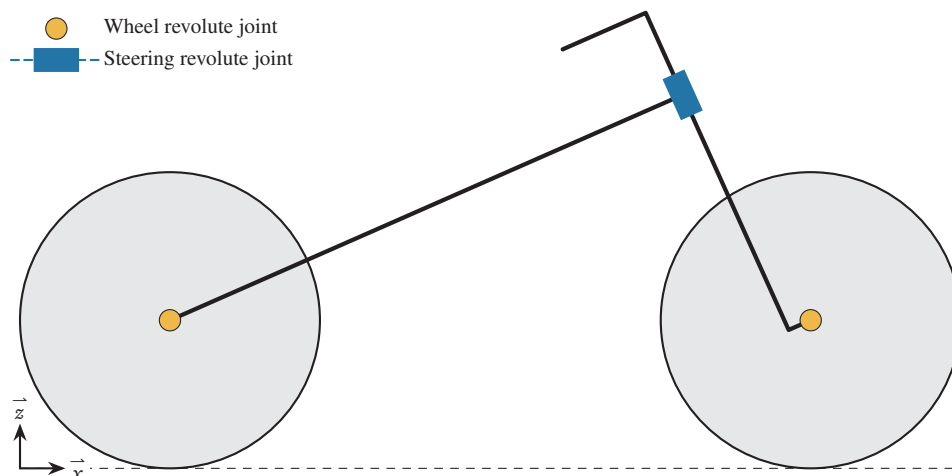


Figure 2.1: Schematic of the bicycle as analytically modelled by Whipple [1899].

ics model for a bicycle as an example of non-holonomic system modelling. This bicycle did not contain the mass or rotation of the wheels and was highly simplified with only small perturbations from straight running, but the resulting equations showed self-steering behaviour, and became unstable if the steering angle was fixed.

Several reproductions of the work by Whipple [1899] have been performed, with their model applied to differing machines. Herfkens [1949] reproduced the model for a Dutch bicycle with the goal of improving low speed stability through design parameters. The Routh-Hurwitz criterion were parameterised with respect to several modelling parameters, and the stability boundaries plotted. They concluded that the lower stability threshold can be reduced from 16 km h^{-1} to less than 11 km h^{-1} by means of a sufficiently heavy front wheel (in terms of moment of inertia), reducing trail (the distance between the steering axis and the tyre contact point), and straightening the rake angle closer to vertical (angle of the steering head with respect to vertical). Later, Döhning [1955] took the linearised equations and methods of Whipple and applied them to several contemporary motorcycles with an improved analytical consideration of the front wheel orientation. The results confirmed that the findings of Whipple are true also for motorcycles, that is: there is a stable region of velocity, and a lightly damped divergent instability at higher speeds. Later, Singh and Goel [1971] reproduced the basic bicycle model of previous studies with the addition of a viscous steering damper and compared a contemporary scooter to the scooter presented by Döhning [1955]. Design parameters were also tested to see the effects on oscillation frequency and stability of the unstable mode.

In a more practical study, Wilson-Jones [1951] presented the aspects of steering and geometric design, and their effects on the stability of motorcycles. In their study, they considered the lateral tyre forces to be products of lateral slip velocity of the contact point (side-slip) and the camber angle of the wheel, instead of as pure rolling constraints. They concluded that the self-steering capabilities of a motorcycle arose from three different effects: the steering system centre of mass (COM) offset with respect to the steering axis (most influential at low speeds), the reaction forces of the tyre contact point due to trail, and the gyroscopic moment of the front wheel (most influential at high speeds). They confirmed these conclusions via experimental testing, where they also found the tyre side-slip angles to be small relative to the camber angles for the purposes of producing the required lateral forces. Also during the experiments, they found that to initiate or terminate a cornering manoeuvre, the rider inputs steering torque in the opposite direction to the desired turn, an early appearance of the ‘counter-steer’ effect.

Collins [1963] formulated a model similar to that by Whipple [1899] and Figure 2.1 but used Newtonian methods in their derivations instead. Their model also included an external aerodynamic drag force term. The equations were linearised and linear eigenvalue analysis applied numerically, finding the stability properties for variations in different design parameters. The stability behaviour was consistent to that found in previous studies, and they found that trail and the location of the COM of the front frame to be the major design factors influencing stability.

Later, Fu [1966] introduced the concept of side-slip as well as toroidal wheels to the steady state solution for a cornering motorcycle. They concluded that motorcycles in cornering tend to roll further than the static centrifugal force requires due to factors such as the tyre toroidal radius, gyroscopic effects, and low COM. They also concluded that the side-slip angle experienced by motorcycles in steady cornering is smaller relative to those in four wheeled vehicles, due to the larger camber forces from the high roll angles experienced by motorcycles, as shown by Wilson-Jones [1951].

Neĭmark and Fufaev [1972] give a detailed derivation of the EOMs of a bicycle using Lagrangian methods in their book *Dynamics of Nonholonomic Systems*. They considered increasing complexity of the modelling of the tyres, beginning with the simple rigid thin disk form (as done by Whipple [1899]), and introducing toroidal wheels, and finally pneumatic deflection. In the simplest case, they arrive at the same governing equation as Timoshenko and Young [1948] for the relationship between steering and stability of a bicycle, and continue a thorough analysis of the stability of both uncontrolled and controlled bicycles.

In an attempt to produce an ‘unridable bicycle’, Jones [1970] performed several experimental tests to try to prove or refute the prevailing theories of bicycle stability. They produced a machine with the gyroscopic effect cancelled by a counter-rotating wheel, a machine with excessive trail, and one with negative trail (the front tyre contact point ahead of the steering axis). It was found that the machine without gyroscopic effects lost its ‘hands-off’ stability, though remained rideable. The machine with excessive trail became very stable, so much so that the rider found changing direction difficult. Finally, the bicycle with negative trail became unstable and nearly impossible to ride. The stability findings were supported with numerically determined kinematic maps of the steering geometry, and Jones suggests a critical stability gradient based on the findings.

In a fundamental study of motorcycle modelling, Sharp [1971] produced a model of a motorcycle extended from that by Whipple [1899]. Within, the force generation of the tyres were considered to be produced at the contact points and had linear behaviour with respect to lateral slip velocities and camber angles. The transient generation of these forces by means of relaxation length was introduced as well. The resulting model was a four DOFs system with an additional two first order equations for the tyre relaxation behaviour, giving a 10th order system. Sharp used linearised eigenvalue analysis to study steady straight-running manoeuvres of increasing speed with increasing complexity of the tyre model (pure rolling, side-slip, and relaxation length), the effect of design parameter changes, behaviour of steady cornering at low lateral acceleration values, as well as fixed rider control behaviour. Fundamentally, Sharp defines the three critical modes of the motorcycle model: ‘weave’, a low frequency oscillatory motion of the steering and roll angles whose frequency increases with forward velocity through the range 0.2 Hz to 3.4 Hz that is unstable at low speeds, stable at mid speeds, and can become unstable at high speeds; ‘wobble’, a high frequency steering oscillation with a speed independent frequency of about 9 Hz that can become unstable at high speeds; and ‘capsize’, a divergent mode that becomes unstable at mid to high speeds. The effect of tyre relaxation was shown to play a major role in the stability of the weave and wobble modes. The steering damper could increase the stability of the wobble mode to the detriment of the weave mode. Moving the rear frame COM forward and down would increase the stability of weave and capsize modes, at the expense of wobble mode damping. Moving the front frame COM rearward increased weave damping, and lowered wobble damping. A larger rake angle is advantageous for the damping of high speed weave, while more trail is advantageous for the capsize mode. A reduction in front wheel moment of inertia results in more wobble stability, while a higher rear wheel moment of inertia is beneficial to the weave and capsize modes.

Many developments would come from Cornell Aeronautical Laboratory, Inc. (later Calspan Corporation) in the form of reports produced for the Schwinn Bicycle Company. Rice and Roland [1970] introduced an eight DOFs bicycle model which includes tyre slide-slip and radial deflection, and a rider rotation DOF. The model was simulated and compared to experimental data. Roland and Massing [1971] furthered the validation of the model, and included a numerical parameter study testing the effects on stability of wheelbase, mass, COM height, steering moment of inertia, rake angle, fork offset (offset distance from steering axis to front axle), rolling radius, and wheel moment of inertia. Roland and Lynch [1972] continued by creating a rider path-following control model as well as tyre experimental testing to characterise tyre behaviour. Roland and Rice [1973] furthered the efforts of creating a rider model and introduced a rider model parameter study. Roland [1973] publicised the model that had been developed. Rice [1974] solved the EOMs for steady state and introduces several characteristic indices useful for bicycles and their control. Rice [1975] applied the developments to a motorcycle and simulates accident avoidance manoeuvres. Finally, Rice [1976] furthered the steady state characteristic and stability indices and applies them to a set of bicycles demonstrating their use.

Supplementing their 1971 work, Sharp [1974, 1976a] studied the effects of some additional dynamics on motorcycle stability. In 1974, they outlined the changes to the 1971 model required to add a rear frame torsional DOF. This resulted in a worsening in stability of the weave mode. In 1976, a simple four DOFs planar model was analysed using eigenvalue analysis to determine the in-plane vertical modes of the motorcycle, and Sharp compared these results to those of their previous work. They suggested that the similarity of the pitch mode frequency to the weave mode instability could play a role in destabilising the latter. It is apparent that at this time the suspension of a motorcycle was becoming more of interest with respect to its effects on the dynamics of the system. Jennings [1974] showed the bench tests results of several contemporary rear suspension dampers, which had very variable results. It was also suggested that the suspension and dampers could play a role in the cornering stability of the out-of-plane modes of a motorcycle.¹

The effects of frame flexibility on motorcycle stability also became a topic of interest. Taking from their experience with castor oscillations, Roe and Thorpe [1976] performed an extensive study on the effects of structural stiffness and mass loading on the stability of the wobble mode.² They showed that lateral deflection of the front contact point with respect to the steering axis due to structural flexibility played a critical role in the stability of the wobble mode. Interestingly, they also found that not only does moving the COM of the rear frame rearward reduce stability (as suggested by Sharp [1971]), but also the structural flexibility of the rear frame between the rear loading (rider or tail) and the steering played a crucial role in stability.

¹ In this paper, Jennings refers to a mode as ‘cornering wobble’. It is the belief of the author that they are referring to what would later more commonly be called ‘cornering weave’.

² Labelled ‘flutter’ in their study.

Returning to a simplified model without tyre slip, Kane [1975] outlines the kinematic relationships of a bicycle with toroidal wheels. Uniquely, they derive the equations without the assumption of small roll angles, instead relying only on a small steering angle assumption. This allows the model to be valid up to high roll angles, allowing solutions of cornering at lower radii, so long as steer angle remains small. These equations were applied by Kane [1977], where the dynamic equations of the motion of a bicycle are derived using Lagrangian methods and the previous constraint relationships. The steady state solutions to these equations were then plotted, showing the relationship between bicycle speed, roll angle, cornering radius, rider mass offset, steer angle, and steering torque.

Similar to the work of Sharp [1974], Kane [1978] introduces a simplified model to characterise the effect of frame flexibility on the weave mode. The model presented was a planar model without roll or rake angles, fixing the motorcycle to planar motion on a flat ground. The frame flexibility was introduced as a bending motion between the rear wheel and the steering joint, unlike the torsional rotation introduced by Sharp [1974]. Through eigenvalue analysis, the model successfully displayed an unstable weave oscillation, and parameter variations showed that a high frame stiffness was beneficial to stability, as well as moving COM forward, and that while trail did not change the critical speed of instability, lowering it did increase the damping of the mode.

An early attempt at characterising the motorcycle tyre, Sakai et al. [1979] presents the tyre lateral and rolling resistance forces as well as the overturning, rolling resistance, and self-aligning moments of several tyres produced from experimental testing. The paper mainly covers changes in camber and side-slip angles, vertical load, and inflation pressure, among other things. Simple empirical models were also proposed for the tyre forces and moments during relatively small camber and side-slip angles.

While Weir [1972] and Weir and Zellner [1978] mainly focused on the closed loop rider control of the motorcycle and its instabilities, in later work Zellner and Weir [1979] characterised a motorcycle and four mopeds of the time. They used the model and methods laid out by Sharp [1971], focusing on the potential implications for rider control. From real design parameters, the effects of each on the stability of the weave, wobble, and capsize modes were quantified. Aoki [1979] used experimentally obtained data to characterise the frequency response functions (FRFs) of four different contemporary motorcycles. The tests were conducted with several manoeuvres having differing input controls to the steering torque and rider lean, such as a step responses, motorcycle slalom, and so forth. The FRFs for each input, as well as a dual input FRF, were plotted for the different motorcycles and inputs. Other than characterising the input-output responses of motorcycles, the study also concluded that the input of rider lean is scarcely influential to large motorcycles.

Continuing the investigation of frame flexibility, Sharp and Alstead [1980] analysed four models of differing steering head flexibilities. The first was the rigid model by Sharp [1971], the rest introduced individually: a lateral compliance of the front wheel in the forks, a torsional compliance of the front wheel, and a torsional compliance in the rear frame at and perpendicular to the steering joint. Also introduced with this model was a state of the art tyre model, and the models were each parameterised using values from four real motorcycles, resulting in 16 sets of eigenvalue analyses. It was found that the capsize mode is insensitive to frame flexibilities and the fork torsional stiffness has little effect on any of the modes. The lateral fork flexibility added stability to the weave mode in the mid speed range, destabilising it at higher speeds, while slightly reducing the stability of the wobble mode. Frame torsional flexibility destabilised the weave mode at mid and high speeds, destabilised the wobble mode at low speeds, and stabilised it at high speeds. Sharp and Alstead also postulated that there may be an optimal value of frame stiffness to balance the effects on the stability of the weave and wobble modes. Analogous to this work, Splerings [1981] created a similar model with a bending flexibility in the front fork. The findings were similar in that the increasing flexibility would destabilize weave at high speeds, stabilize wobble at high speeds, and destabilize it at low speeds.

Cooper [1983] was interested in the effects of aerodynamics on the stability of a motorcycle, and presented a preliminary study on the topic. Experimental steady state wind tunnel drag measurements were performed on two common aerodynamic fittings for motorcycles (of the time), and the aerodynamic gradients with respect to motorcycle yaw angle, as well as damping coefficients, were presented. Cooper postulated that the positive damping coefficients found would have a stabilising effect on the motorcycle, but was unsure if their contributions would outweigh the additional mass on the front frame, and that the negative yaw moment gradient could be detrimental to stability.

In another fundamental study to the understanding of motorcycle stability, Koenen [1983] presented an 11 DOFs model for studying the stability of a motorcycle in straight running and, crucially, in steady cornering. The model,

which was provided both in a nonlinear form for the calculation of steady state operation and linearised form for stability analysis, included considerations for frame torsion, rider body lean, front and rear suspensions, and radial tyre deformations. After extensive numerical eigenvalue analysis, Koenen presented the common modes of a motorcycle in straight running as, from lowest frequency to highest (a review of these modes is also described in detail by Sharp [2001]):

- (i) Capsize: a slow divergent mode of the roll angle, becoming unstable at high speeds.
- (ii) Weave: an oscillating mode comprising of mainly the roll and yaw angles, as well lateral velocity, rider lean, and some steering angle. This mode is unstable at very low speed, and high speed.
- (iii) Bounce: in-phase oscillations of the sprung mass on the front and rear suspensions.
- (iv) Pitch: out-of-phase oscillations of the sprung mass on the front and rear suspensions.
- (v) Wobble: an oscillating mode of the steer angle that can become unstable at mid to high speeds (depending on motorcycle configuration).
- (vi) Front Hop: Unsprung mass oscillation of the front wheel on the tyre radial stiffness.
- (vii) Rear Hop: Unsprung mass oscillation of the rear wheel on the tyre radial stiffness.

During the cornering phase, Koenen demonstrated that there exists a merging of modes that are close in frequency changing their modal shape and behaviour, in part due to the interaction of in-plane and out-of-plane motions experienced at high roll angles. In particular, a mode deemed ‘cornering weave’ was seen to be unstable under most cornering conditions at high roll angle.

At this point, the research of single-track vehicles becomes widely diversified into many fields of interest such as dynamic modelling of bicycles or motorcycles, characterisation and modelling of tyres, rider modelling and control, stability, and modelling and effects of frame flexibility, among others. Hand [1988] gives a good overview of most of the models to date, checking, comparing, and validating the EOMs of each. Not every field is pertinent to this thesis, so the following three sections cover some details and major advancements of tyre modelling as it pertains to motorcycle modelling, the dynamic modelling and stability of motorcycles, and the study of structural flexibility and its effect on motorcycle stability. This is followed by a complete overview of the chatter mode.

2.2 Motorcycle Tyre Modelling

This section outlines the history of the key developments of tyre modelling as they pertain to motorcycle modelling and stability. The dynamics of vehicles, and therefore also the dynamics of motorcycles, depend highly on the mechanical behaviour of the wheels and tyres [Guiggiani 2018]. Consequently, it is often required to model the characteristic force generating functions of a tyre as it relates to the kinematics of the vehicle. These functions generally take as kinematic inputs:

- (i) The lateral slip: the out-of-plane velocity of the wheel.
- (ii) The longitudinal slip: briefly, the difference between the forward travelling velocity and rolling velocity at the contact point of the tyre.
- (iii) The wheel camber angle.
- (iv) The loaded radius: the radial distance between the wheel centre and the contact point, though this is more commonly replaced by the vertical load at the contact point.

Desired outputs of tyre characteristic functions are the longitudinal and lateral tangential ground forces, the vertical load (if not taken as an input), the rolling resistance moment, the self-aligning torque, and the overturning moment. Example forms of these functions are shown in Figure 2.2.

Earlier works tended to assume linear relationships between tyre slip and tangential force, for which small variations in slip are generally acceptable. More complex models can be categorised one of three ways: as an empirical model derived from experimental data (such as by Sakai et al. [1979]), as a physical model that is developed from theoretical models of a tyre, or as a semi-empirical model, something derived from theoretical baselines but with

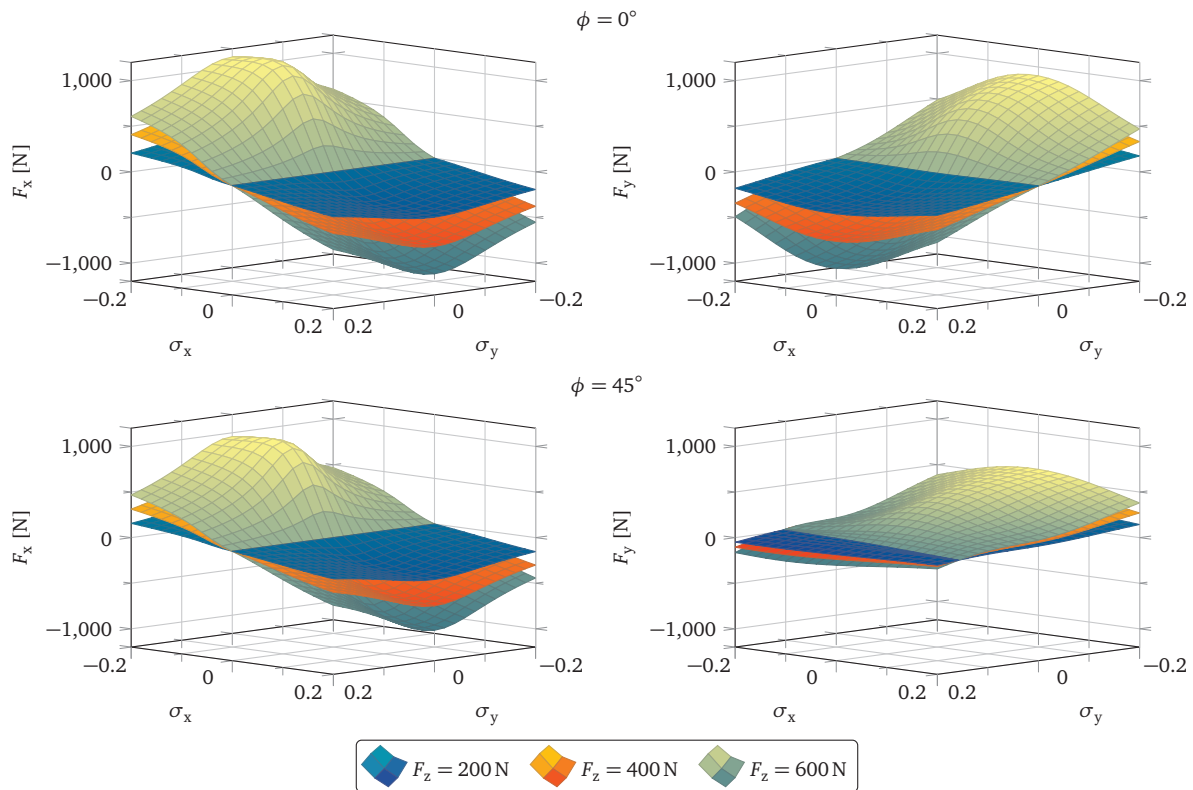


Figure 2.2: Example Magic Formula tangential tyre ground forces F_x and F_y generated based on tyre longitudinal slip σ_x , lateral slip σ_y , camber angle ϕ , and vertical load F_z .

allowances for fitting to experimental data. Pacejka and Sharp [1991] highlighted the differences, benefits, and drawbacks of several of such models of each type.

A widely used semi-empirical model is the Magic Formula (MF) as detailed by Pacejka [2012], which provides nonlinear tyre characteristic functions for steady state operation. Early iterations of the MF were presented by Bakker et al. [1987, 1989], where the basic form of the model was laid out and experimental fit was demonstrated. Pacejka and Bakker [1992] outline the third iteration of the model, and contained the first use of the moniker ‘Magic Formula’. Later, de Vries and Pacejka [1998] adapted the model using experimental testing for the use with motorcycles, due to the fact motorcycles experience much higher camber angles during operation. The study also introduced several transient modelling elements to adapt the steady state model for use in transient conditions. The concept of tyre relaxation was introduced, where a linear first order delay system is applied to either the slip input or the tyre force output to represent the transient build up of tyre force. A rigid ring model was also described, where the belt of the tyre is modelled as a rigid mass elastically suspended from the rim allowing carcass flexibility and out-of-plane motion with respect to the wheel. This setup allows the accurate modelling of the transient behaviour of the lateral tyre force in the range of 5 Hz to 60 Hz.

The use of the MF with motorcycles was tested by Tezuka et al. [2001], who compared a splined interpolation model to the MF model using a nine DOFs multi-body model, and tested their validity to experimental data. They found better matching with the MF model, as well as greater ease-of-use. Cossalter et al. [2003] detailed an experimental procedure for characterising motorcycle and scooter tyres using the MF model, as well as presented results of several contemporary tyres.

The considerations for motorcycle tyre carcass geometry and flexibility were discussed by Lot [2004]. In the case of geometry, the radial and lateral motions of the contact point due to tyre section profile was described as well as the effects they have on tyre forces and moments, particularly overturning moment. A model for tyre carcass radial and lateral deflection was proposed for steady state behaviour, and the interactions with a first order force relaxation model described. When tested against experimental data, a good fit was found for longitudinal and side-

slip, but the force response to camber variations was found to be nearly instantaneous, leading to an error in the modelled behaviour.

Schmeitz et al. [2010] adapted the short wavelength intermediate frequency tyre (SWIFT) model for use with motorcycles. This model is a more complex dynamic tyre model for better representing the transient response of the tyre up to 80 Hz. The model is represented by four elements: a steady state force characteristic model (the MF model), a carcass compliance model that determines the contact geometry, vertical loads, and slip velocities at the contact patch, a rigid ring model for adequately modelling higher frequency dynamics, and an obstacle enveloping model which determines an effective road surface in the presence of short wavelength obstacles. The model was compared with the standard MF motorcycle model and the automotive SWIFT model to experimentally measured data, and showed improvements over both.

Massaro et al. [2013] and Cossalter et al. [2014] characterised the effect tyre pressure has on the MF model for motorcycle and scooter tyres via an experimental campaign. Massaro et al. [2013] also studied the effects tyre pressure variations have on motorcycle stability using an 11 DOFs multi-body model and eigenvalue analysis in steady straight running. It was found that, in general, increasing tyre pressures led to more stability except in the case of front tyre pressure and high speed wobble. In more recent developments, Doria and Taraborrelli [2016a] found the out-of-plane vibration modes of the tyre belt via experimental testing for several tyres and varying tyre pressures. These results were then converted to modal stiffness approximations and used to create a lateral relaxation length model that took into account the modal properties. The model was then compared to experimental results.

2.3 Motorcycle Modelling and Stability

Beginning in 1990s, the advent of computer aided design (CAD) and computer aided engineering (CAE) software would facilitate the creation of ever more complex multi-body systems for the modelling of motorcycle dynamics. In the case of simulating dynamic systems, there are two common approaches: in the first approach, a software would offer a complete package of equations, solutions, and solvers for a particular system to the end user for simulation use, for example ADAMS.³ The second approach is a software that would automatically provide the governing equations themselves. For example, AUTOSIM⁴ is a Lisp based code for developing symbolic multi-body models that was developed by Sayers [1990, 1991, 1993]. The software automatically derives the governing equations for a desired system, which the end user can then apply with other computational methods. Sharp [1994] gave a review of contemporary software and discussed the benefits and shortcomings of each.

Demonstrating the use of AUTOSIM, Gani et al. [1996, 1997] reproduced the model by Sharp [1971] using the software. This allowed the reproduction of the previous results, but also the demonstration of other capabilities such as study of the frequency response of the system to steering input via the nonlinear time solution, confirming the existence of the counter-steer phenomenon, and linear eigenvalue analysis of the system undergoing linear acceleration. Sharp and Limebeer [2001] extended this model for more general use, allowing the study of stability during steady cornering, reproducing the work by Koenen [1983]. Limebeer et al. [2001] used this model to study the stability of a motorcycle undergoing tractive and braking accelerations, with considerations to the limitations of stability analysis in time-varying systems. It was found that the wobble mode is destabilised under deceleration, while the weave mode damping was insensitive to accelerations. In another use of the model by Sharp and Limebeer [2001], Limebeer et al. [2002] studied the effects of external excitation due to road unevenness. It was shown through FRFs and nonlinear simulations that the steer angle response to road excitation could be quite severe during cornering. They theorised that road unevenness may be of much more importance in motorcycle dynamics than it is in four wheeled dynamics. In another extension to the model by Sharp and Limebeer [2001], Evangelou [2003] and Sharp et al. [2003, 2004] detail the creation of a full multi-body model of a Suzuki GSX-R1000K1 motorcycle. This model advanced the previous with the inclusion of tyre section geometry, the MF tyre model, an updated load dependent tyre relaxation model, and a four bar linkage rear suspension layout. The full parameterisation was also made available to the reader. Using this model, Sharp and Limebeer [2004] studied the effect passive rider upper body motions have on the stability of the wobble mode. It was found that they play a role in the modal instability, and that neither loose nor tense rider behaviours were able to tame any wobble oscillations. Another application of

³<https://hexagon.com/products/adams-car>

⁴<https://www.carsim.com>

the model was by Evangelou et al. [2008], where the model was augmented to include the effects of road camber, and the stability of a motorcycle cornering on a cambered road was studied. It was found that during high speed cornering, the stability of the weave and wobble were both at their minimum when the tyre was orthogonal to the road. Evangelou et al. [2010, 2013] used the model to study steering oscillations of a racing motorcycle under acceleration. It was found that a motorcycle undergoing significant straight running acceleration has the potential to drive the weave and wobble mode frequencies closer together, causing modal interaction and resulting in an unstable weave mode.

In an independent development, FastBike⁵ was created by a similar symbolic multi-body systems approach. Preceding the full multi-body model, Cossalter et al. [1999] derived the steady state solution to a cornering motorcycle using the kinematic approach of Kane [1975], introducing tyre slip and the MF model. The numerical solutions of the nonlinear equations were presented as steady state handling maps and the effects different aspects of the model had on steering torque were investigated. The full 11 DOFs FastBike model was first presented by Cossalter and Lot [2002], which had considerations for the front and rear suspension, the MF tyre model with relaxation, and a kinematic chain drive. The model was derived using the natural coordinates approach resulting in a very efficient computation time, making real time simulation possible. The process by which the model was created was generalised and described by Lot and Lio [2004]. Cossalter et al. [2004] performed modal analysis of the model during steady turning using a moving frame of reference to transform the time-varying steady coordinates into stationary ones. Root loci for different speeds and cornering radii were displayed, and the pertinent modes successfully shown. The model of Cossalter and Lot [2002] received a major update by Cossalter et al. [2011], where the following aspects were introduced: the moving reference frame concept incorporated into the equations, the possibility of modelling flexible joints, alternative suspensions layouts, cambered and sloped road surface, a powertrain with viscoelastic elements, and a three DOFs passive rider. Use of the model was demonstrated with a steering torque decomposition analysis, an eigenvalue analysis showing the effects of structural flexibilities, an eigenvalue analysis showing the onset of chatter, and a time domain handling analysis. Massaro et al. [2012] used the newest model to test the effects of different passive rider properties had on weave stability. Both the model and experimental test data were compared, and it was found that smaller riders tend to destabilise the weave mode.

Other than the large modelling efforts of the previous two groups, several other advances in the understanding of motorcycle dynamics have occurred. The nonlinear characteristics of motorcycle dynamics were studied by Meijaard and Popov [2006, 2007], where the bifurcation behaviour of a six DOFs motorcycle model was studied. Importantly, they found the wobble mode to have supercritical Hopf bifurcation behaviour. Saccon and Hauser [2009] improved upon the kinematic solution of Cossalter et al. [1999] and produced a pitch angle constraint equation with the possible inclusion of frame twist. Katayama and Nishimi [1990] and Marumo and Katayama [2009a] introduced a novel approach to studying the sources of the wobble and weave mode instabilities. By taking the derivative of the kinetic energy of the mode of interest, the eigenmode was decomposed into its forcing components. The relative phase and amplitudes of these components could then be used to calculate the energy contribution over one period of oscillation. New methodology for the derivation of the motorcycle EOMs was presented by Nehaoua et al. [2013], where Jourdain's principle was used to develop an 11 DOFs model. This method was chosen for its simplicity and low computational load, as the goal was to synthesise a model for the purposes of control or state observation. Another multi-body motorcycle model was presented by Leonelli and Mancinelli [2015, 2016] which included the use of the SWIFT model for modelling the tyre forces. The highly complex and advanced model used the symbolic approach of Lot and Lio [2004] with the inclusion of the developments by Saccon and Hauser [2009] citing an improvement in model computational performance. An important development in the study of vehicle stability came from Salisbury et al. [2016], who applied the theories presented by Rosenbrook [1963] and Desoer [1969] to find the stability limits of the time-varying system of a braking racecar. It was shown that there was little difference between the time-varying and frozen-time analyses up to 20 m s^{-2} , validating the use of frozen time analysis in the case of vehicles under acceleration.

In some recent developments in the field of motorcycle dynamics, Leonelli and Limebeer [2020] described a method of determining optimal trajectories for a racing motorcycle with the use of optimal control strategies. An augmented simple bicycle model and three dimensional race circuit model were used, and the results were compared to an experimental racing trajectory. A systematic symbolic approach to modelling multi-body dynamic systems was presented by Pappalardo et al. [2021a,b], where the general model was described by a system of differential algebraic equations (DAEs) including the EOMs and the constraint equations for redundant coordin-

⁵<https://www.dynamotion.it>

ates. Methodologies for linear analysis and non-linear simulation were also provided, and a demonstration of the Whipple [1899] model produced. Later, Manrique-Escobar et al. [2021] offered another improvement in the kinematic model of a motorcycle, providing a formulation that used no linearisation assumptions. Finally, Passigato et al. [2021] proposed two steering torque control strategies to improve the damping of both weave and wobble modes simultaneously.

2.4 Frame Flexibility in Single-Track Vehicles

Past research has proven that the structural flexibility of motorcycle frames could play a crucial role in their stability [Sharp 1974, Roe and Thorpe 1976, Kane 1978, Sharp and Alstead 1980, Splerings 1981]. This section provides a brief review of some of the pertinent developments and findings with respect to structural flexibility and how they relate to motorcycle stability.

Roe and Thorpe [1989] attempts to create an optimised frame in terms of torsional and lateral stiffness for weave and wobble stability. Finite element analysis (FEA) was used in the design of two new frames, and experimental tests conducted to fine tune the stiffnesses to minimise instabilities. Later, Lot et al. [2005] and Cossalter et al. [2007] studied the effect on stability of fork and swingarm structural flexibilities by adding four lumped stiffness joints to the model of Cossalter and Lot [2002]. The studies found that lateral compliance of the front fork caused a major change to the wobble mode stability behaviour, causing mid speed instability, and stabilising the high speed range, while swingarm compliance had an effect on the damping of the weave mode, to a lesser extent. Applying the energy flow methods laid out by Katayama and Nishimi [1990], Marumo and Katayama [2009b] studied the key structural flexibilities affecting the stability of the weave and wobble modes. It was found that lateral fork and frame torsion compliances have the most effect on wobble, while lateral fork and swingarm torsion compliances have the most effect on weave.

Typically these compliances were modelled as single lumped stiffness joints, with location and orientation chosen quite arbitrarily. Raines and Thorpe [1986] spoke about the location of the twisting joint of the rear frame of a motorcycle, the effects of some design considerations, and the determination of its location using FEA. Later, Doria and Formentini [2011] examined the vibration modes of instrumented bicycles in laboratory experiments with the goal of determining the dominant structural modes, and discerning the possible locations and qualities of lumped stiffness joints. Ferretti et al. [2014] introduced a finite element flexible model of a swingarm to a multi-body motorcycle simulation, and compared the results of braking and uneven road simulations to its rigid counterpart, finding less stability with the flexible element. In laboratory tests, Cossalter et al. [2015] characterised two sets of motorcycle forks using static, dynamic, and modal testing methods, showing that the location, stiffness, and inertia of a potential lumped stiffness model change with respect to the excitation. Multi-body stability analysis was performed comparing the experimentally determined lumped stiffness models with a rigid model, demonstrating the inherent differences. Similar tests and formulations were performed for two motorcycle frames by Doria and Taraborrelli [2016b]. Finally, the procedure was applied to two motorcycle swingarms by Taraborrelli et al. [2017].

In some recent developments, Passigato et al. [2020] performed an in-depth investigation into the factors causing the fork lateral compliance to affect the weave and wobble modes of motorcycles. Passigato et al. [2022] deepened the understanding of structural flexibility on motorcycle stability by introducing flexible body models of the motorcycle frame, fork, and swingarm to a multi-body simulation and comparing the stability of the weave and wobble modes.

2.5 Nonlinear Analysis Concepts

While there have been some studies into the nonlinear characteristics of motorcycle behaviour by Meijaard and Popov [2006, 2007], it is still a subject oft overlooked in this field. Therefore, this thesis will dedicate a chapter to the study of the nonlinear characteristics of the unstable phenomenon at hand, and this section will introduce the works and methodologies used therein.

Perturbation methods, where the nonlinear behaviours of a system are assumed to act as ‘perturbations’ from the simpler linear system are described in great detail in the works of Nayfeh and Mook [2004] and Rand [2012]. The authors give the description and example usage of methods such as the Lyapunov direct method, the Lindstedt

method, the method of averaging, the method of multiple scales, and the harmonic balance method. Each of these methods increase in complexity and offer solutions to varying types of problems encountered in finding the solutions to nonlinear systems. The harmonic balance method, in particular, was used by Lee et al. [2005] and Hayes and Marques [2015] to study the nonlinear characteristics of the ‘flutter’ instability in aerofoils, a similar self-excited oscillation to chatter.

Another method of simplifying the behaviour of nonlinear systems is the describing function method, as found in the work by Gelb and Vander Velde [1968]. Here, the nonlinear characteristic of the system is transformed into an amplitude-dependent linear transfer function that adequately ‘describes’ the behaviour of the nonlinear system. Certain assumptions about the system must be made in order to use this method. These include that the nonlinear portions are excited by sinusoidal-like inputs, and that the dynamic system as a whole acts as a low-pass filter. Somieski [2001] used this method in conjunction with eigenvalue analysis of the quasi-linear systems to determine limit cycle stability.

Troger and Steindl [2012] outline a bifurcation method where a nonlinear system can be reduced to a lower-dimensional problem by use of the centre-manifold theorem. Troger and Zeman [1984] demonstrate the use of this method by analysing the nonlinear characteristics of a truck and trailer system, while Hagedorn et al. [2014] use the method to demonstrate the more general nonlinear characteristics of self-excited systems with circulatory terms.

For time-varying system analysis, the works by Yakubovich and Starzhinskiĭ [1975] are referred to. Within, the authors introduce the concepts required to analyse linear time-varying systems with methods such as the monodromy matrix and Floquet theory. By the combination of Floquet theory and the harmonic balance method, Lewis [2019, 2020] was able to investigate the stability of nonlinear limit cycles.

2.6 Motorcycle Chatter

As described so far, motorcycles and single-track vehicles are complex systems that can present difficult stability problems, the modelling and prediction of which is a subject of great interest [Manrique-Escobar et al. 2022]. Specifically in high performance and racing motorcycles, there exists lightly damped or unstable oscillatory motions of the front and rear wheels experienced during heavy braking manoeuvres which are typically denoted ‘patter’ and ‘chatter’, respectively. These motions are characterised by phased oscillations of the respective suspension and wheelspeed, and can cause reduced rider confidence, longer lap times during competitions, and increase the risk of crashing. Chatter typically has a frequency of 17 Hz to 22 Hz and though mitigation of the phenomenon might be achieved through improved damper technology [Martini et al. 2018], it is also important to understand the causes and mechanisms of the instability, including possible sources from both in-plane and out-of-plane dynamics. Presented here is the history and review of the studies on such unstable modes to date.

The first appearance of any such high frequency oscillation of wheels in vehicle dynamics was possibly by Sharp [1969]. Using an analogue computer to simulate an 11 DOFs powertrain and rear suspension of an automobile undergoing braking or driving acceleration, a self-excited oscillation called ‘axle tramp’ was reproduced. This was mainly oscillations of the vertical and longitudinal (or conversely, yaw and roll) DOFs of the rear suspension, and the torsional vibrations of the driving shafts. Two critical modes were identified, a symmetric motion and an antisymmetric motion, and it was found that decreasing the acceleration value or increasing the longitudinal axle mounting stiffness led to stabilisation. It was proposed that the phase lag between the force generating motions of the tyres (such as vertical displacement and forward velocity) were causing energy to be fed into the system, leading to a growth in oscillation amplitude.

Another early example of a self-excited oscillation driven by suspension and tyre forces was presented by Pacejka [1974]. A minimal model example was given by a two DOFs system consisting of a wheel and suspension with its travel angled with respect to vertical. The EOMs were derived and the Routh-Hurwitz method applied to plot stability regions. Two unstable regions were found, with oscillation frequencies close to that of the wheel torsional natural frequency and that of the sprung suspension natural frequency, respectively. The work demonstrated the use of minimal models and analytical methods in finding the cause and mechanisms of the instability, and that with instabilities of this nature, the governing geometry and force gradients are crucial factors.

A phenomena of similar nature was described by Sharp and Giles [1983] occurring at the front wheel and suspension of a motorcycle during heavy braking. Employing a similar simplified modelling approach, a four DOFs

model representing only the front forks and wheel of a motorcycle was derived. It included coordinates for the frame compliance at the steering head, the fork travel, wheel spin, and torsional wheel compliance (similar to a rigid ring model). Numerical integration of the EOMs indeed show an unstable oscillation near the front hop frequency. It was found that the torsional compliance of the tyre tread band played no role in the onset of instability. Similar to axle tramp, the onset of instability and self-excited vibration was surmised to be due to the phase relationship between the tyre vertical load and longitudinal slip. Higher speeds and higher braking torques led to more instability, while lowering tyre friction increased stability.

From experimentally obtained accelerometer data, Tezuka et al. [2004] discerned a 17.7 Hz vertical vibration of the front axle during a cornering manoeuvre near the limits of tyre grip. They found the instability to occur at the point of highest roll angle during initial throttle application. Modal analysis of a nine DOFs multi-body model was used to reproduce the unstable mode numerically. Increased roll angle and increased longitudinal tyre force decreased stability, and modal analysis characterised the instability as out-of-phase oscillations of the sprung mass on the suspension springs and the unsprung masses on the vertical stiffness of the tyres, driven by a coupling to the friction forces of the tyres.

Later, Catania and Mancinelli [2007, 2008] produced planar multi-body models to use in eigenvalue and time integration analyses. In the first study, the seven DOFs planar model with considerations for front and rear suspension, tyre radial deflections, and a kinematic representation of the chain drive was analysed through an acceleration and braking manoeuvre using quasi-static eigenvalue analysis. The model did not show any instability of the front or rear hop modes, though when the rear hop mode became lightly damped, it showed modal mixing tendencies with the front hop, evident in the mode shapes presented. In the second study, an 18 DOFs multi-body system was formulated with Newtonian methods for the purposes of time integration using commercial software. The model contained steering, front and rear suspensions, rigid ring tyres, tyre relaxation, crankshaft with kinematic chain drive, and aerodynamic forces. Results of the simulation showed an unstable self-excited oscillation of greater than 30 Hz mainly arising from the rigid ring tyre dynamics.

Although not directly pertaining to motorcycle dynamics, the study by Kröger et al. [2008] offers some useful results to the instability under study. In this work, Kröger et al. outlined several different mechanisms for the onset of self-excited oscillations in systems with contact friction, similar to tyre forces. The first type of mechanism is contact friction with a negative force gradient, which could easily occur in the case of a motorcycle if the peak tyre grip were to be exceeded. The second type is from fluctuating vertical loads, as could be experienced during chatter oscillations. Finally, the third type of onset mechanism is geometric factors and non-conservative restoring forces due to an asymmetric system stiffness matrix. This last type of mechanism could be pertinent to the case of the motorcycle when multiple DOFs systems are coupled through geometric factors or constraints (see Pacejka [1974]). Kröger et al. went on to give practical examples, and proposed particular solutions for mitigating each type of instability mechanism.

In two critical studies, Cossalter et al. [2008, 2012] were the first to introduce a viscoelastic transmission element to a multi-body model in an attempt to reproduce experimentally obtained data of the chattering phenomenon. Using a 12 DOFs multi-body model consisting of front and rear suspensions and a powertrain inertia connected to the rear wheel via a viscoelastic chain, linear eigenvalue analyses and time integration simulations were performed for braking manoeuvres. The newly introduced ‘driveline’ mode had an eigenfrequency nearly equal to that of the rear hop mode. This caused the modes to interact and drove the driveline mode to instability under certain conditions, such as decelerations with large engine braking. It was proposed that the mechanism to instability involves the phase relationship of rear tyre forces and slip velocities. An operational and model parameter study was also performed, the critical parameters effecting stability were found to be the deceleration value, braking ratio (between engine and rear brake), gear ratio, sprocket damping coefficient, and front sprocket location.

In contrast to the previous findings, Sharp and Watanabe [2013] used two independent multi-body models, one from a commercial software, to show that an instability of around 25 Hz occurs with sufficient torsional compliance in the steering head, affecting mainly the front wheel during high lateral acceleration operation. The oscillations comprised mainly of steer angle and frame twisting contributions approximately 90° out-of-phase with each other. This result suggests that there could be multiple mechanisms by which a high frequency instability can arise.

Catania et al. [2013] expanded their previous model into a 19 DOFs model by the addition of a full powertrain model including a viscoelastic chain. The model was analysed via quasi-static linear eigenvalue analysis, and by time simulation with comparisons to experimentally obtained MotoGP racing manoeuvre data. The eigenvalue

analysis confirmed the existence of an unstable rear hop mode during braking conditions with braking moments on the rear wheel, both from engine and brake. Numerical time simulation also showed good agreement with experimental data. Catania et al. showed that by removing the dependence of relaxation length on vertical load, the chatter instability could be mitigated. The reasoning behind this is the lessening of the dependence of, or removal of a critical link between, the tyre vertical load and longitudinal slip reducing the phase lag between the two. Catania et al. also postulated that the geometric link of the chain force between the wheel speed and swingarm angle was feeding the energy flow into the system.

Leonelli [2014] introduced a simplified planar model to study the chatter phenomenon analytically. The model, similar to that proposed by Pacejka [1974], included rear wheel spin, vertical rear suspension travel, and a chain drive component. The stability analysis by Pacejka [1974] was repeated with the addition of a novel coupling parameter brought on by the chain force term. The result was an additional two unstable regions, which could be unstable in the region of interest for motorcycle dynamics, though it was shown that a minute amount of damping could quell the instability. Furthering this simplification effort, Leonelli et al. [2016] examined three models of increasing complexity to discern the governing characteristics of the chatter mode. They were able to show that even for the simplest case, there were two possible mechanisms to instability. The first was a negative force gradient, as experienced at very high slip coefficients, and the other was excessive values of relaxation length, even under the assumption of a constant value.

Sorrentino and Leonelli [2017] returned to the two DOFs model presented by Leonelli [2014], but added in a slightly more complete chain drive geometry, as well as considering a null relaxation length. Within, the stability boundaries were studied analytically, with different aspects of the model individually introduced, and parameter variation effects shown. It was determined that instability exists despite the lack of relaxation length and is caused by an asymmetric stiffness matrix in the linearised EOMs giving rise to a critical phase lag between the tyre force and slip. This is driven by the tyre vertical and longitudinal slip force gradients, and the stability is sensitive also to chain geometry parameters which affect the coupling of the degrees of freedom through the chain stiffness matrix.

These findings were validated by Leonelli et al. [2018] using a planar 10 DOFs multi-body model. The model included considerations for suspension, drivetrain with chain, and rigid ring tyres. Importantly, relaxation length was neglected. First, the model was simulated in time and compared to experimental data, and showed agreement and the growth of the chatter instability during the straight braking manoeuvre. Particular interest was given to the working points on the MF function, and the force gradients at those points. Thorough linear eigenvalue analysis was performed by introducing fictitious forces to allow the model to operate in a steady state braking configuration, and a numerical method presented to calculate the stability boundary to compare to the two DOFs model of the previous study. Phase diagrams of the unstable oscillations for different variables were also shown, and the phase offsets of critical variables studied. The study confirmed previous findings, shared the agreement that the mechanism to stability is the phase lag between the tyre force and slip, and concluded that the parameters to which chatter is most sensitive are the tyre force gradients.

Recently, the similar phenomenon of front patter that oscillates at 7 Hz to 9 Hz was investigated by Cattabriga et al. [2021]. The minimal model presented by Sharp and Giles [1983] was modified by removing the rigid ring and relaxation behaviour but, crucially, moving the location of the frame flexure point. This reversed the effect of the fork damper, making it destabilising with increasing value. Again the tyre force gradients played a crucial role in the onset of instability, and it was suggested that factors such as high speed, high braking efforts, and the presence of Coulomb friction would lead to instability.

With that, the revision of the chatter phenomenon, motorcycle stability, and other general topics leading up to them is concluded. The current body of research contains some gaps and this thesis looks to continue and to expand the efforts of the works discussed above. To date, the effects of roll angle and lateral dynamics on the chattering phenomenon with a chain-drive transmission have not been widely studied. As well, the nonlinear characteristics of the phenomenon are as of yet unknown. Finally, other than a few studies that ignored the effects of the chain and powertrain, the mid-cornering region has been largely ignored. Herein, the simplified models of Leonelli et al. [2016] and Sorrentino and Leonelli [2017] are expanded upon to study the roles that roll angle and out-of-plane lateral dynamics have in the chatter phenomenon. The methodology set out by Kröger et al. [2008] is used to study the mechanisms by which instability arises. The nonlinear characteristics and behaviours of the system are investigated, with a focus on the existence of limit cycles and their stability. Finally, the possible existence of similar phenomena during a mid-cornering manoeuvre is explored in more detail.

3 Motorcycle Chatter and Roll Angle

3.1 Introduction

The objective of this chapter is to investigate the roles, if any, that motorcycle roll angle and tyre lateral force dynamics play in the stability of the chatter mode. Motorcycles, specifically racing machines, tend to experience large non-negligible roll angles [Romualdi et al. 2020], and therefore it is of practical interest to understand whether or not a static roll angle, or in fact a roll angle DOF, is required to fully predict the behaviour of this mode. This chapter extends the two DOFs model presented by Sorrentino and Leonelli [2017] to three DOFs with the addition of a roll angle, as well as a complete formulation of the chain drive mechanism. The study of driveline stability at increasing roll angles and the possible interactions of the lateral dynamics are the topics of interest, and to this end roll angle is introduced to a typical braking manoeuvre, beginning at small angles (with larger angles in mid-corner manoeuvres studied in Chapter 5). This chapter seeks to show the effects of both a varying static roll angle and the role lateral force oscillations play on the stability of the chatter mode. For this purpose, an adequate tyre model has been adopted, according to Besselink et al. [2010] and Pacejka [2012] (the MF tyre model). To date, the studies investigating the driveline mode have done so only in straight braking manoeuvres. It is anticipated that the addition of roll angle will also allow the minimal model to predict instabilities of the rear system in more than just braking manoeuvres, such as in cornering and traction manoeuvres, as is discussed in Chapter 5. This chapter presents the full equations of the new model in Section 3.2 and demonstrates its use analysing a braking manoeuvre. Section 3.3 compares the minimal model to a full multi-body simulation and provides the resulting stability analysis of the minimal system, as well as some root cause investigations and parameter sensitivity studies.

3.2 Minimal Model

The model in this chapter is developed as an extension to that of Sorrentino and Leonelli [2017]. The roll angle of a motorcycle in a curve is added as a third DOF in the model, and an exact derivation of the equations for the chain drive mechanism is added, accompanied by some nomenclature and methodology changes due to the increased complexity. The minimal model describes the dynamics of the rear suspension and driveline of a typical sport or racing motorcycle, for example that in Figure 3.1.

The geometry of the model is presented in Figure 3.2, which shows rear and planar (aligned with roll angle ϕ) views. The model represents the rear part of a motorcycle, which in this case is attached to an infinite inertia frame, translating, and rotating with stationary velocities V_{fx} , V_{fy} , and Ω_{fz} on a perfectly flat plane. In order to get the stationary operating points necessary for performing stability analysis, the model imposes stationary values for velocities even though a braking torque on the rear wheel is present. The reference frame is attached to the infinite inertia frame and given in x -forward, y -right, z -down SAE convention [Society of Automotive Engineers, Inc. 2022]. On this frame at point F , at a height of z_f from the ground plane, is a revolute joint aligned parallel with x -axis. To this joint connects the first part of the rear frame which serves to model the main mass of the motorcycle, onto which is attached the front sprocket of the drivetrain, whose radius is r_p . This member is defined by the joint angle ϕ and the line FS , whose geometry is defined by x_f and h_f . The mass of the reference frame m_{fr} is located a fraction η_{fr} of its length along line FS , and the reference system in which its inertia matrix J_{fr} is defined is aligned along the x -axis and rotated by ϕ to remain in-plane with the rest of the system. At point S there is a revolute joint orthogonal to the x -axis and the line FS defining the swingarm pivot. The swingarm is represented by the line SA , with a length of ℓ_{sa} and an angle α of the joint. The swingarm mass m_{sa} is located a fraction η_{sa} along line SA , and the reference system in which the inertia tensor J_{sa} is aligned has its x -axis along the line SA while its z -axis remains in-plane with the system. Connected at point A is the final revolute joint which is parallel to swingarm pivot. This joint connects the body representing the wheel, tyre, and rear sprocket. This body is characterised by

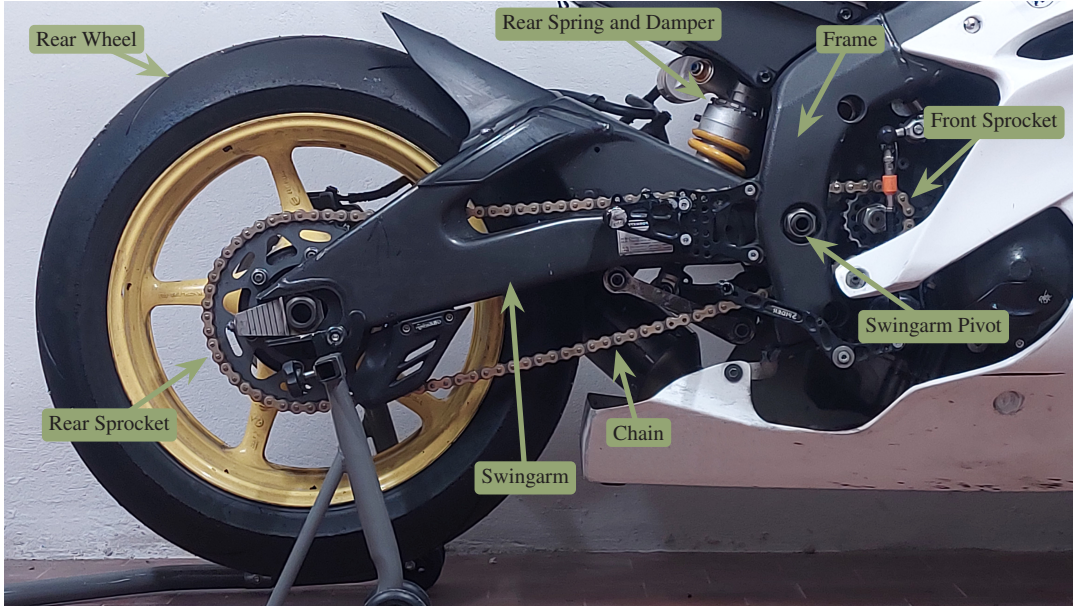


Figure 3.1: Rear suspension and driveline of a typical sport motorcycle.

the joint angle θ (which breaks convention and is aligned along the negative y -axis, so that wheel rotation is positive with motion in the forward x -direction), the outer radius of the tyre R_r , the toroid radius of the tyre ρ_r , and the rear sprocket radius r_c . The rear wheel mass m_{wh} is centred at point A , and the reference system in which the inertia tensor J_{wh} is aligned has its y -axis aligned with the revolute joint and is symmetric about that axis. All inertia matrices J_i are assumed to be in the principal axes, with no cross-terms.

The kinetics of the model are given corresponding to the three DOFs: α , θ , and ϕ . The non-constraint forces and moments in this model consist of the tyre forces F_x , F_y , F_z , chain force F_c , braking moment M_{br} , swingarm rotational spring k_s and damper c_s acting on joint S , and the optional frame rotational spring k_f and damper c_f

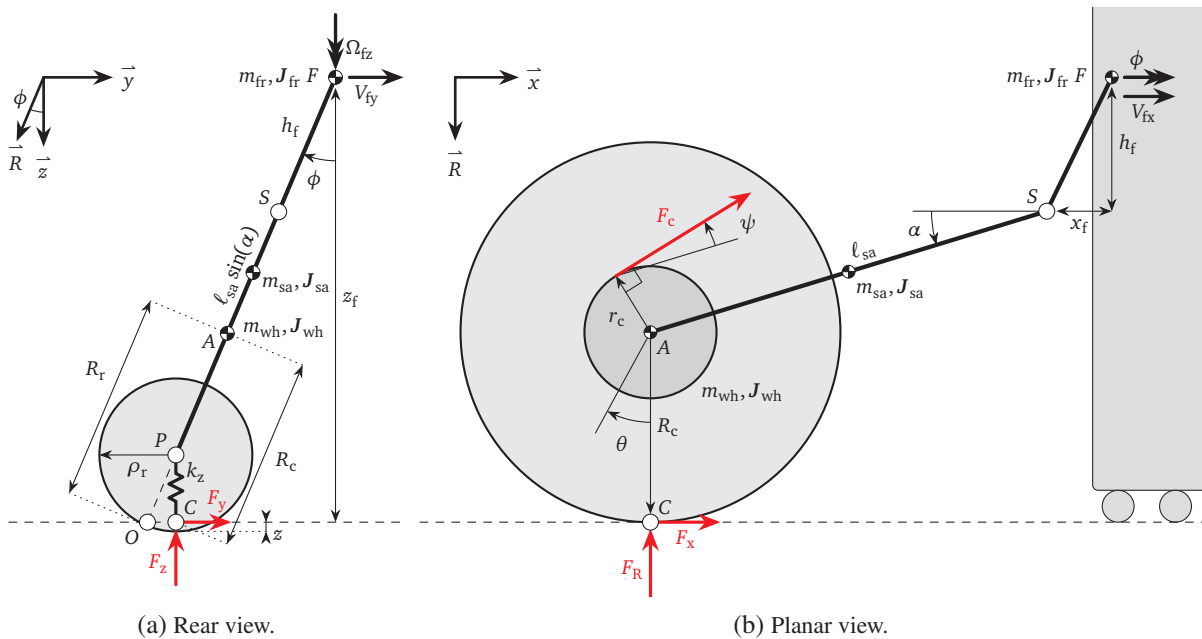


Figure 3.2: Model free body diagrams.

acting on joint F . The EOMs as formulated using the Lagrange equations are given by:

$$\mathbf{q} = \begin{Bmatrix} \alpha \\ \theta \\ \phi \end{Bmatrix} \quad (3.1)$$

$$J_\alpha \ddot{\alpha} = -k_s(\alpha - \alpha_{s0}) - c_s \dot{\alpha} + \sin(\alpha) \ell_{sa} F_x(\dot{\mathbf{q}}, \mathbf{q}) - \cos(\alpha) \ell_{sa} F_R(\dot{\mathbf{q}}, \mathbf{q}) - k_c(\ell_c(\alpha, \theta) - \ell_{fc}) \frac{\partial \ell_c(\alpha, \theta)}{\partial \alpha} \\ + \cos(\alpha) \ell_{sa} \cos(\phi) (m_{wh} + \eta_{sa} m_{sa}) g + M_{cent, \alpha} + M_{cor, \alpha} + M_{gyro, \alpha} - M_{br} \quad (3.2)$$

$$J_{why} \ddot{\theta} = -R_c(\alpha, \phi) F_x(\dot{\mathbf{q}}, \mathbf{q}) - k_c(\ell_c(\alpha, \theta) - \ell_{fc}) \frac{\partial \ell_c(\alpha, \theta)}{\partial \theta} - J_{why} \cos(\phi) \Omega_{fz} \dot{\phi} - M_{br} \quad (3.3)$$

$$J_\phi \ddot{\phi} = -k_f(\phi - \phi_{f0}) - c_f \dot{\phi} - z_f F_y(\dot{\mathbf{q}}, \mathbf{q}) - (h_f + \sin(\alpha) \ell_{sa} + R_r - \rho_r) \sin(\phi) F_z(\dot{\mathbf{q}}, \mathbf{q}) \\ - \sin(\phi) (h_f(\eta_{fr} m_{fr} + m_{sa} + m_{wh}) + \sin(\alpha) \ell_{sa} (m_{sa} \eta_{sa} + m_{wh})) g + M_{cent, \phi} + M_{cor, \phi} + M_{gyro, \phi} \quad (3.4)$$

where \mathbf{q} represents the vector of DOFs, g is acceleration due to gravity, ℓ_{fc} and ℓ_c represents the free and dynamic total length of the chain respectively, and α_{s0} and θ_{f0} give the spring preloads. The complete formulation can be found in the Appendix, Section A.1. The reduced inertiae J_α and J_ϕ , and the inertia elements $M_{cent, i}$, $M_{cor, i}$, $M_{gyro, i}$ can also be found in the Appendix, Section A.2.

Of Equation (3.2)–(3.4), F_R and R_c can be solved for geometrically using Figure 3.2:

$$F_R(\dot{\mathbf{q}}, \mathbf{q}) = \sin(\phi) F_y(\dot{\mathbf{q}}, \mathbf{q}) - \cos(\phi) F_z(\dot{\mathbf{q}}, \mathbf{q}) \quad (3.5)$$

$$R_c(\alpha, \phi) = R_r - \rho_r + \cos(\phi) (\rho_r - z(\alpha, \phi)) \quad (3.6)$$

$$z(\alpha, \phi) = \cos(\phi) (h_f + \sin(\alpha) \ell_{sa} + R_r - \rho_r) - z_f + \rho_r \quad (3.7)$$

while the other dependent terms need further derivation, as shown in the subsequent sections.

3.2.1 Chain Geometry

The derivation of the chain equations by Sorrentino and Leonelli [2017] uses linearised approximations of the chain length and small angle formulae. This section will develop the chain equations in their full symbolic form for their use in stability analysis and to confirm that the approximations made by Sorrentino and Leonelli [2017] are acceptable. The chain is modelled as a spring wrapped around two wheels (the front and rear sprockets) with no slip. Chain damping is neglected, as the term tends to be small in chain systems [De Rossi et al. 2022]. The length of the spring varies as the sprockets spin, and as the configuration geometry changes due to variations in the generalised coordinates. The force and potential energy of the spring are given as:

$$F_c(\alpha, \theta) = k_c(\ell_c(\alpha, \theta) - \ell_{fc}) \quad (3.8)$$

$$E_c(\alpha, \theta) = \frac{1}{2} k_c (\ell_c(\alpha, \theta) - \ell_{fc})^2 \quad (3.9)$$

where ℓ_{fc} represents the free length of the chain and $\ell_c(\alpha, \theta)$ represents the dynamic total length, for which an equation must be devised. From Figure 3.2b, the moments arising from the chain forces applied to the θ and α DOFs can be determined as:

$$M_{c\alpha}(\alpha, \theta) = -\ell_{sa} \sin(\psi(\alpha)) F_c(\alpha, \theta) \quad (3.10)$$

$$M_{c\theta}(\alpha, \theta) = -\delta r_c F_c(\alpha, \theta) \quad (3.11)$$

where the variable δ determines the active portion of the chain (1 for braking and -1 for traction). Since the chain force is conservative, the moments in Equation (3.10) and (3.11) can also be derived from the potential energy in Equation (3.8) and (3.9):

$$M_{c\alpha}(\alpha, \theta) = -k_c (\ell_c(\alpha, \theta) - \ell_{fc}) \frac{\partial \ell_c(\alpha, \theta)}{\partial \alpha} \quad (3.12)$$

$$M_{c\theta}(\alpha, \theta) = -k_c (\ell_c(\alpha, \theta) - \ell_{fc}) \frac{\partial \ell_c(\alpha, \theta)}{\partial \theta} \quad (3.13)$$

Finally, combining Equation (3.10)–(3.13) gives the partial derivatives that must be satisfied for the derived equation for $l_c(\alpha, \theta)$:

$$\frac{\partial l_c(\alpha, \theta)}{\partial \alpha} = l_{sa} \sin(\psi(\alpha)) \quad (3.14)$$

$$\frac{\partial l_c(\alpha, \theta)}{\partial \theta} = \delta r_c \quad (3.15)$$

To begin, the contributions to chain length are divided into three parts: the geometric tangential distance between the sprockets $l_{tc}(\alpha)$, the wrapping or unwrapping of the chain on the sprockets as the sprocket centre angle and distance changes $l_{\theta c}(\alpha)$, and the spin of the sprockets themselves $l_{\omega c}(\theta)$. Summing these values gives the dynamic total length of the chain:

$$l_c(\alpha, \theta) = l_{tc}(\alpha) + l_{\theta c}(\alpha) + l_{\omega c}(\theta) \quad (3.16)$$

$$l_c(\alpha, \theta) = l_{tc}(\alpha) + l_{\theta c}(\alpha) - \delta(r_p \theta_p - r_c \theta) \quad (3.17)$$

in which the effect of spin has already been included. This equation, and therefore the following derivations for $l_{tc}(\alpha)$ and $l_{\theta c}(\alpha)$, need to satisfy Equation (3.14) and (3.15).

Typical chain geometries are shown in Figure 3.3 for traction and braking configurations. The swingarm is shown with length l_{sa} and angle α , at the end of which is the rear sprocket with a radius of r_c . The front sprocket is held offset from the swingarm pivot by a distance l_p and an angle β_p from the horizontal, and has a radius of r_p . The centre distance between the sprockets is given as d , and shown is the chain tangential distance l_{tc} and chain angle ψ .

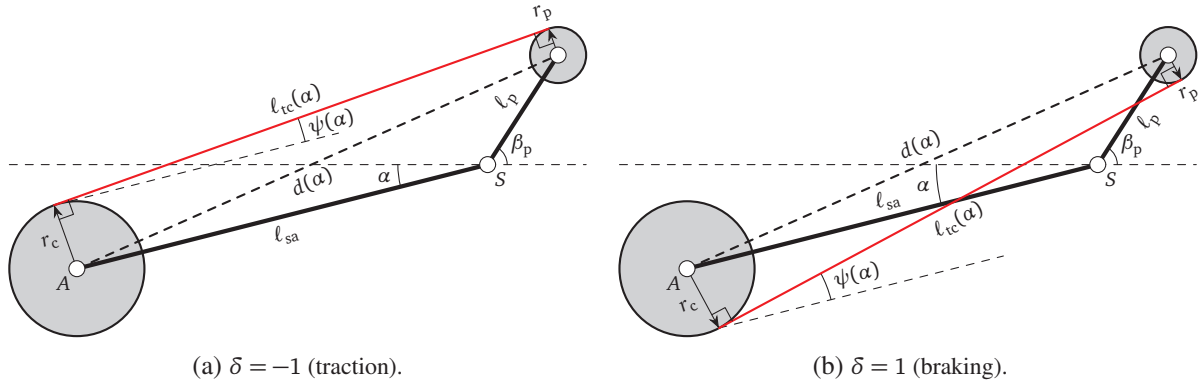


Figure 3.3: Geometry of the drivetrain.

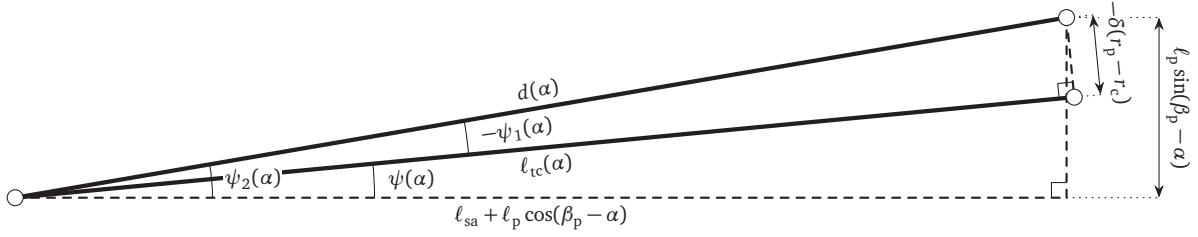
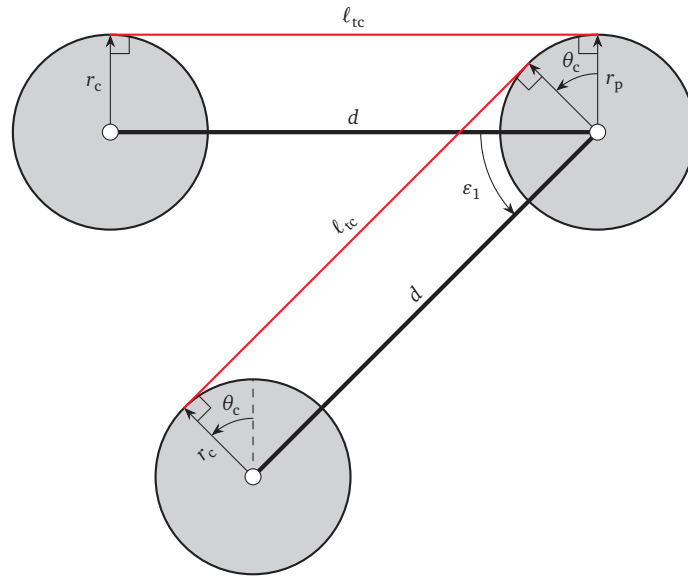
Using trigonometry, an equation for the tangential chain length l_{tc} can be found from Figure 3.3. Referencing off the common hypotenuse of the sprocket centre distance d , the relation between swingarm angle α and tangential length l_{tc} is evident, see Figure 3.4:

$$d(\alpha) = \sqrt{l_{sa}^2 + l_p^2 + 2l_{sa}l_p \cos(\beta_p - \alpha)} \quad (3.18)$$

$$l_{tc}(\alpha) = \sqrt{d(\alpha)^2 - (-\delta(r_p - r_c))^2} = \sqrt{l_{sa}^2 + l_p^2 + 2l_{sa}l_p \cos(\beta_p - \alpha) - (r_p - r_c)^2} \quad (3.19)$$

The change in chain length due to wrapping effects $l_{\theta c}(\alpha)$ is caused by both changes in sprocket centre angle and distance. During angular changes, the wrapping angle θ_c on both the front and rear sprockets is equal due to the chain line l_{tc} being tangent to both sprockets, and the change in arc length is given by Equation (3.20). In the simplified case of Figure 3.5 the portion of angular change θ_c due to a change in sprocket centre angle ε_1 is a direct correlation:

$$l_{\theta c1}(\alpha) = -\delta(r_p - r_c)\theta_c = -\delta(r_p - r_c)\varepsilon_1 \quad (3.20)$$


 Figure 3.4: Trigonometry of the drivetrain, shown for $\delta = -1$ (traction).

 Figure 3.5: Simplified chain geometry, change in sprocket centre angle. Shown with r_p and r_c equal for illustrative purposes.

Due to the swingarm pivot and front sprocket centre not being coincident (due to the offset l_p), the angle ε_1 is a function of swingarm angle α . Shown in Figure 3.6, the resulting equation can be derived using inner angle sums:

$$\varepsilon_1(\alpha) = (\pi - \psi_2(0) - (\pi - \beta_p)) - (\pi - \psi_2(\alpha) - (\pi - \beta_p + \alpha)) = \alpha + \psi_2(\alpha) - \psi_2(0) \quad (3.21)$$

Another effect of the distance l_p is the change in sprocket centre distance through the range of swingarm angles. This gives rise to another chain wrapping effect, as shown in the simplified Figure 3.7. In this case, the angular change is given as the change in angle of the chain referenced to the sprocket centres. In the general case (see Figure 3.3) this change is given as:

$$\begin{aligned} \ell_{\theta c 2}(\alpha) &= (r_p - r_c)\varepsilon_2(\alpha) = (r_p - r_c)(\delta\psi_1(0) - \delta\psi_1(\alpha)) \\ &= -\delta(r_p - r_c)(\psi_1(\alpha) - \psi_1(0)) \end{aligned} \quad (3.22)$$

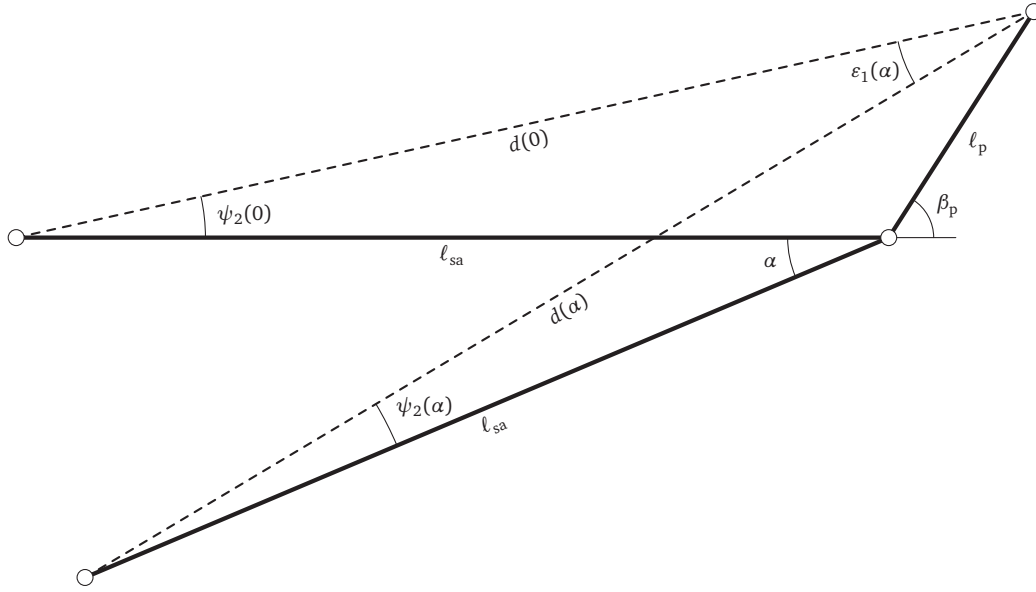
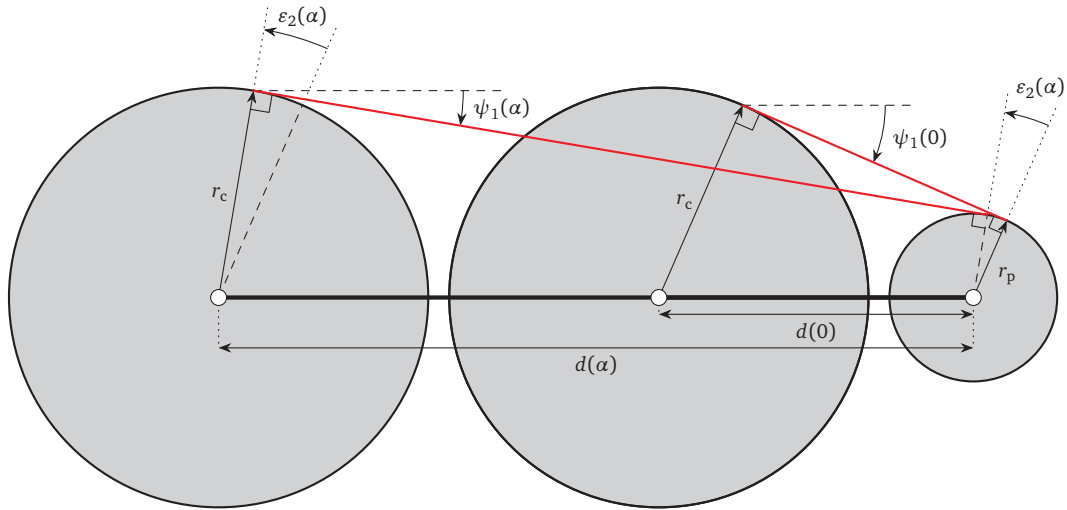

 Figure 3.6: General chain geometry case, relation of ε_1 to α .


Figure 3.7: Simplified chain geometry, change in sprocket centre distance. Dimensions are exaggerated for illustrative purposes.

Combining Equation (3.20)–(3.22), and simplifying using the geometry of Figure 3.4 gives the equation for the total wrapping effect:

$$\begin{aligned}
 \ell_{\theta c}(\alpha) &= \ell_{\theta c1}(\alpha) + \ell_{\theta c2}(\alpha) = -\delta(r_p - r_c)\varepsilon_1(\alpha) - \delta(r_p - r_c)(\psi_1(\alpha) - \psi_1(0)) \\
 &= -\delta(r_p - r_c)(\alpha + \psi_1(\alpha) + \psi_2(\alpha) - (\psi_1(0) + \psi_2(0))) \\
 &= -\delta(r_p - r_c)(\alpha + \psi(\alpha) - \psi(0))
 \end{aligned} \tag{3.23}$$

Combining the above passages gives the full equation for the dynamic chain length with respect to variables θ and α from Equation (3.17):

$$\ell_c(\alpha, \theta) = \ell_{tc}(\alpha) - \delta(r_p - r_c)(\alpha + \psi(\alpha) - \psi(0)) - \delta(r_p \theta_p - r_c \theta) \tag{3.24}$$

To determine the required angular values in Equation (3.24), trigonometric relations provided in Figure 3.4 are used. The cosine and sin definitions of $\psi_1(\alpha)$ and $\psi_2(\alpha)$ are:

$$\cos(\psi_1(\alpha)) = \frac{\ell_{tc}(\alpha)}{d(\alpha)} \quad (3.25)$$

$$\cos(\psi_2(\alpha)) = \frac{\ell_{sa} + \ell_p \cos(\beta_p - \alpha)}{d(\alpha)} \quad (3.26)$$

$$\sin(\psi_1(\alpha)) = \frac{-\delta(r_p - r_c)}{d(\alpha)} \quad (3.27)$$

$$\sin(\psi_2(\alpha)) = \frac{\ell_p \sin(\beta_p - \alpha)}{d(\alpha)} \quad (3.28)$$

The chain angle $\psi(\alpha)$ is the sum of these angles, which can be transformed into functions of their trigonometric forms via the angle sum identities:

$$\psi(\alpha) = \psi_1(\alpha) + \psi_2(\alpha) \quad (3.29)$$

$$\cos(\psi(\alpha)) = \cos(\psi_1(\alpha) + \psi_2(\alpha)) = \cos(\psi_1(\alpha)) \cos(\psi_2(\alpha)) - \sin(\psi_1(\alpha)) \sin(\psi_2(\alpha)) \quad (3.30)$$

$$\sin(\psi(\alpha)) = \sin(\psi_1(\alpha) + \psi_2(\alpha)) = \sin(\psi_1(\alpha)) \cos(\psi_2(\alpha)) + \cos(\psi_1(\alpha)) \sin(\psi_2(\alpha)) \quad (3.31)$$

Combining the above equations give the definition of chain angle in terms of the system variables:

$$\begin{aligned} \cos(\psi(\alpha)) &= \frac{\ell_{tc}(\alpha)}{d(\alpha)} \frac{\ell_{sa} + \ell_p \cos(\beta_p - \alpha)}{d(\alpha)} - \frac{-\delta(r_p - r_c)}{d(\alpha)} \frac{\ell_p \sin(\beta_p - \alpha)}{d(\alpha)} \\ &= \frac{\ell_{tc}(\alpha) (\ell_{sa} + \ell_p \cos(\beta_p - \alpha)) + \delta(r_p - r_c) \ell_p \sin(\beta_p - \alpha)}{d(\alpha)^2} \end{aligned} \quad (3.32)$$

$$\begin{aligned} \sin(\psi(\alpha)) &= \frac{\ell_{tc}(\alpha)}{d(\alpha)} \frac{\ell_p \sin(\beta_p - \alpha)}{d(\alpha)} + \frac{-\delta(r_p - r_c)}{d(\alpha)} \frac{\ell_{sa} + \ell_p \cos(\beta_p - \alpha)}{d(\alpha)} \\ &= \frac{\ell_{tc}(\alpha) \ell_p \sin(\beta_p - \alpha) - \delta(r_p - r_c) (\ell_{sa} + \ell_p \cos(\beta_p - \alpha))}{d(\alpha)^2} \end{aligned} \quad (3.33)$$

Finally, the validity of Equation (3.24) can be tested by checking its partial derivatives against those found in Equation (3.14) and (3.15). This is shown to be true, and the full proof is given in the Appendix, Section A.3.

3.2.2 Tyre Model

The tyre is geometrically modelled as a torus with minor radius ρ_r and major radius $R_r - \rho_r$. Tangential forces F_x , F_y , and vertical load F_z are produced at the tyre contact point C . In this chapter the tyre moments (overturning, self-aligning, and rolling resistance) are neglected. Lateral and longitudinal deflections of the tyre carcass and contact point are also neglected. Relaxation length is considered small enough in racing tyres as to be neglected, as demonstrated by Leonelli et al. [2016]. Rigid ring tyre models are not used as they have been demonstrated as unnecessary for the modes of interest [Sharp and Giles 1983].

Vertical load is produced by vertical deflection in the tyre carcass in the z -direction, similar to the MF-MCTire model presented by Schmeitz et al. [2010]:

$$F_z(\dot{\mathbf{q}}, \mathbf{q}) = F_z(\alpha, \phi) = -k_z z(\alpha, \phi) = -k_z \left(\cos(\phi) (h_f + \sin(\alpha) \ell_{sa} + R_r - \rho_r) + \rho_r - z_f \right) \quad (3.34)$$

In this chapter, theoretical tyre slips are used (σ_x , σ_y , φ as defined by Guiggiani [2018, Chapter 2]) due to their ease of use when deriving equations. Further, tyre camber reduction factor is assumed to be zero and spin slip is assumed to have negligible effect on the forces. Tyre tangential forces are produced based on the system kinematics given by generalised functions:

$$F_x(\dot{\mathbf{q}}, \mathbf{q}) = F_x(\sigma_x, \sigma_y, F_z, \phi) \quad (3.35)$$

$$F_y(\dot{\mathbf{q}}, \mathbf{q}) = F_y(\sigma_x, \sigma_y, F_z, \phi) \quad (3.36)$$

which are chosen to be the MF given by Besselink et al. [2010] and Pacejka [2012]. The full nonlinear forms of these equations are used in the calculation of equilibrium conditions.

For the linearised model, only the Taylor expansion terms are required and are presented here for clarity. The linear tyre force gradients about an equilibrium point are represented by $C_{\sigma_x, x}$, $C_{\sigma_y, x}$, $C_{F_z, x}$, $C_{\phi, x}$, $C_{\sigma_x, y}$, $C_{\sigma_y, y}$, $C_{F_z, y}$, and $C_{\phi, y}$, which can be found using the formulae from Pacejka [2012, Chapter 4]. The linearised force perturbations about a static equilibrium point can then be represented by:

$$\tilde{F}_x(\tilde{\sigma}_x, \tilde{\sigma}_y, \tilde{F}_z, \tilde{\phi}) = C_{\sigma_x, x} \tilde{\sigma}_x + C_{\sigma_y, x} \tilde{\sigma}_y + C_{F_z, x} \tilde{F}_z + C_{\phi, x} \tilde{\phi} \quad (3.37)$$

$$\tilde{F}_y(\tilde{\sigma}_x, \tilde{\sigma}_y, \tilde{F}_z, \tilde{\phi}) = C_{\sigma_x, y} \tilde{\sigma}_x + C_{\sigma_y, y} \tilde{\sigma}_y + C_{F_z, y} \tilde{F}_z + C_{\phi, y} \tilde{\phi} \quad (3.38)$$

The variation terms in Equation (3.37) and (3.38) need to be provided in terms of the system variables. Roll angle $\tilde{\phi}$ is already a system variable perturbation term, and vertical load \tilde{F}_z can be derived directly using Equation (3.34):

$$\begin{aligned} \tilde{F}_z &= \nabla [F_z(\alpha, \phi)]_{(\alpha, \phi) = (\alpha_0, \phi_0)} \cdot (\tilde{\alpha}, \tilde{\phi}) \\ &= (-\cos(\alpha_0) \ell_{sa} \cos(\phi_0) k_z) \tilde{\alpha} + (\sin(\phi_0) k_z (h_f + \sin(\alpha_0) \ell_{sa} + R_r - \rho_r)) \tilde{\phi} \end{aligned} \quad (3.39)$$

where the subscript 0 defines a stationary operating point while the diacritic \sim is used to define the perturbation portion of the first order Taylor expansion.

To find the slip coefficient variations, first the velocity of the tyre planar contact point O must be defined. Given the velocities of the frame V_{fx} , V_{fy} , and Ω_{fz} , the velocities at point O are defined as:

$$\mathbf{V}_O = \mathbf{V}_f + \frac{\delta}{\delta t} \overrightarrow{FO} + \Omega_{fz} \times \overrightarrow{FO} \quad (3.40)$$

$$\overrightarrow{FO} = -(x_f + \cos(\alpha) \ell_{sa}) \vec{x} - \tan(\phi) z_f \vec{y} - z_f \vec{z} \quad (3.41)$$

$$V_{Ox}(\dot{\alpha}, \alpha, \phi) = V_{fx} + \tan(\phi) z_f \Omega_{fz} + \sin(\alpha) \ell_{sa} \dot{\alpha} \quad (3.42)$$

$$V_{Oy}(\dot{\phi}, \alpha, \phi) = V_{fy} - (x_f + \cos(\alpha) \ell_{sa}) \Omega_{fz} - \frac{z_f}{\cos^2(\phi)} \dot{\phi} \quad (3.43)$$

Then, from Guiggiani [2018, Chapter 2], the slips at the tyre contact point C can be determined by:

$$\sigma_x(\dot{\theta}, \dot{\alpha}, \alpha, \phi) = \frac{V_{Ox}(\dot{\alpha}, \alpha, \phi) - \Omega_{fz} c_r(\alpha, \phi) - R_R(\alpha, \phi) \dot{\theta}}{R_R(\alpha, \phi) \dot{\theta}} \quad (3.44)$$

$$\sigma_y(\dot{\theta}, \dot{\alpha}, \dot{\phi}, \alpha, \phi) = \frac{V_{Oy}(\dot{\phi}, \alpha, \phi) + \dot{c}_r(\dot{\alpha}, \dot{\phi}, \alpha, \phi)}{R_R(\alpha, \phi) \dot{\theta}} \quad (3.45)$$

These expressions require the tyre geometry term c_r , which is the lateral offset of point C from the central plane FO . This and its derivative are given by:

$$c_r(\alpha, \phi) = \tan(\phi) (\rho_r - z(\alpha, \phi)) = \tan(\phi) (z_f - \cos(\phi) (h_f + \sin(\alpha) \ell_{sa} + R_r - \rho_r)) \quad (3.46)$$

$$\dot{c}_r(\dot{\alpha}, \dot{\phi}, \alpha, \phi) = -\cos(\alpha) \ell_{sa} \sin(\phi) \dot{\alpha} + \left(\frac{z_f}{\cos^2(\phi)} - \cos(\phi) (h_f + \sin(\alpha) \ell_{sa} + R_r - \rho_r) \right) \dot{\phi} \quad (3.47)$$

Finally, the rolling radius R_R is required. While it is assumed to be known and constant, its variation is based on the variation of the deflected radius \tilde{R}_c as formulated by Pacejka [2012]¹:

$$\begin{aligned} \tilde{R}_R(\tilde{\alpha}, \tilde{\phi}) &= \eta \tilde{R}_c(\tilde{\alpha}, \tilde{\phi}) = -(\eta \cos(\alpha_0) \ell_{sa} \cos^2(\phi_0)) \tilde{\alpha} \\ &\quad + \left(\eta \sin(\phi_0) (2 \cos(\phi_0) (h_f + \sin(\alpha_0) \ell_{sa} + R_r - \rho_r) - z_f) \right) \tilde{\phi} \end{aligned} \quad (3.48)$$

¹ Sorrentino and Leonelli [2017] use the factor $(1 - \eta)$ based on earlier work by Pacejka [1974], but this has been updated here to reflect his most recent work [2012].

Combining Equation (3.42)–(3.48), the variations of the tangential slips can be found:

$$\begin{aligned}\tilde{\sigma}_x = & \left(-\frac{1}{\omega_0} \left(v_x + \sin(\phi_0) L_R v_\psi \right) \right) \dot{\theta} + \left(\frac{\sin(\alpha_0) \ell_{sa}}{R_{R0} \omega_0} \right) \dot{\alpha} \\ & + \left(\cos(\alpha_0) \ell_{sa} \left(\cos^2(\phi_0) \frac{\eta}{R_{R0}} \left(v_x + \sin(\phi_0) L_R v_\psi \right) + \sin(\phi_0) v_\psi \right) \right) \tilde{\alpha} \\ & + \left(-\sin(\phi_0) L_R \frac{\eta \left(2 \cos(\phi_0) - \frac{z_f}{L_R} \right)}{R_{R0}} \left(v_x + \sin(\phi_0) L_R v_\psi \right) + \cos(\phi_0) L_R v_\psi \right) \tilde{\phi}\end{aligned}\quad (3.49)$$

$$\begin{aligned}\tilde{\sigma}_y = & \left(-\frac{1}{\omega_0} \left(v_y - (x_f + \cos(\alpha_0) \ell_{sa}) v_\psi \right) \right) \dot{\theta} + \left(-\frac{\cos(\alpha_0) \ell_{sa} \sin(\phi_0)}{R_{R0} \omega_0} \right) \dot{\alpha} + \left(-\frac{\cos(\phi_0) L_R}{R_{R0} \omega_0} \right) \dot{\phi} \\ & + \left(\cos(\alpha_0) \ell_{sa} \left(\cos^2(\phi_0) \frac{\eta}{R_{R0}} \left(v_y - (x_f + \cos(\alpha_0) \ell_{sa}) v_\psi \right) + \tan(\alpha_0) v_\psi \right) \right) \tilde{\alpha} \\ & + \left(-\sin(\phi_0) \frac{\eta \left(2 \cos(\phi_0) L_R - z_f \right)}{R_{R0}} \left(v_y - (x_f + \cos(\alpha_0) \ell_{sa}) v_\psi \right) \right) \tilde{\phi}\end{aligned}\quad (3.50)$$

where the following expressions have been used:

$$L_R = h_f + \sin(\alpha_0) \ell_{sa} + R_r - \rho_r \quad (3.51)$$

$$v_x = \frac{V_{fx}}{R_{R0} \omega_0} \quad (3.52)$$

$$v_y = \frac{V_{fy}}{R_{R0} \omega_0} \quad (3.53)$$

$$v_\psi = \frac{\Omega_{fz}}{R_{R0} \omega_0} \quad (3.54)$$

Substituting Equation (3.39), (3.49), and (3.50) into Equation (3.37) and (3.38) yields the tangential tyre force variations that are required during model linearisation:

$$\begin{aligned}\tilde{F}_x(\dot{\alpha}, \dot{\theta}, \dot{\phi}, \tilde{\alpha}, \tilde{\phi}) = & \left(-\frac{1}{\omega_0} \chi_x \right) \dot{\theta} + \left(\frac{\cos(\alpha_0) \ell_{sa}}{R_{R0} \omega_0} \left(\tan(\alpha_0) C_{\sigma_{x,x}} - \sin(\phi_0) C_{\sigma_{y,x}} \right) \right) \dot{\alpha} \\ & + \left(-\frac{\cos(\phi_0) L_R}{R_{R0} \omega_0} C_{\sigma_{y,x}} \right) \dot{\phi} + \left(-\cos(\alpha_0) \ell_{sa} k \lambda_{x1} \right) \tilde{\alpha} + \left(\cos(\phi_0) L_R k \lambda_{x2} \right) \tilde{\phi}\end{aligned}\quad (3.55)$$

$$\begin{aligned}\tilde{F}_y(\dot{\alpha}, \dot{\theta}, \dot{\phi}, \tilde{\alpha}, \tilde{\phi}) = & \left(-\frac{1}{\omega_0} \chi_y \right) \dot{\theta} + \left(\frac{\cos(\alpha_0) \ell_{sa}}{R_{R0} \omega_0} \left(\tan(\alpha_0) C_{\sigma_{x,y}} - \sin(\phi_0) C_{\sigma_{y,y}} \right) \right) \dot{\alpha} \\ & + \left(-\frac{\cos(\phi_0) L_R}{R_{R0} \omega_0} C_{\sigma_{y,y}} \right) \dot{\phi} + \left(-\cos(\alpha_0) \ell_{sa} k \lambda_{y1} \right) \tilde{\alpha} + \left(\cos(\phi_0) L_R k \lambda_{y2} \right) \tilde{\phi}\end{aligned}\quad (3.56)$$

where k is a total system stiffness to be defined in the subsequent section, and the following expressions have been used:

$$\chi_x = C_{\sigma_{x,x}} v_x + C_{\sigma_{y,x}} v_y + \left(C_{\sigma_{x,x}} \sin(\phi_0) L_R - C_{\sigma_{y,x}} (x_f + \cos(\alpha_0) \ell_{sa}) \right) v_\psi \quad (3.57)$$

$$\chi_y = C_{\sigma_{x,y}} v_x + C_{\sigma_{y,y}} v_y + \left(C_{\sigma_{x,y}} \sin(\phi_0) L_R - C_{\sigma_{y,y}} (x_f + \cos(\alpha_0) \ell_{sa}) \right) v_\psi \quad (3.58)$$

$$\lambda_{x1} = \cos(\phi_0) \frac{k_z}{k} C_{F_{z,x}} - \frac{\eta}{k R_{R0}} \cos^2(\phi_0) \chi_x - \frac{1}{k} \left(\sin(\phi_0) C_{\sigma_{x,x}} + \tan(\alpha_0) C_{\sigma_{y,x}} \right) v_\psi \quad (3.59)$$

$$\lambda_{y1} = \cos(\phi_0) \frac{k_z}{k} C_{F_{z,y}} - \frac{\eta}{k R_{R0}} \cos^2(\phi_0) \chi_y - \frac{1}{k} \left(\sin(\phi_0) C_{\sigma_{x,y}} + \tan(\alpha_0) C_{\sigma_{y,y}} \right) v_\psi \quad (3.60)$$

$$\lambda_{x2} = \tan(\phi_0) \frac{k_z}{k} C_{F_{z,x}} - \tan(\phi_0) \frac{\eta}{k R_{R0}} \left(2 \cos(\phi_0) - \frac{z_f}{L_R} \right) \chi_x + \frac{1}{k} C_{\sigma_{x,x}} v_\psi + \frac{C_{\phi,x}}{\cos(\phi_0) k L_R} \quad (3.61)$$

$$\lambda_{y2} = \tan(\phi_0) \left(\frac{k_z}{k} C_{F_z,y} - \frac{\eta}{k R_{R0}} \left(2 \cos(\phi_0) - \frac{z_f}{L_R} \right) \chi_y \right) + \frac{1}{k} C_{\sigma_{xy}} \nu_\psi + \frac{C_{\phi,y}}{\cos(\phi_0) k L_R} \quad (3.62)$$

With Equation (3.55) and (3.56) the linear expansions of the tyre tangential forces are fully defined in terms of the system variables and the tyre force gradients.

3.2.3 Model Linearisation

To assess the stability of the minimal model, the eigenvalues of the linearised system are used. The system is assumed to contain only small oscillations about a stationary operating point and therefore a first order Taylor series approximation is applied:

$$\tilde{f}(\tilde{\mathbf{x}}) = \nabla f(\mathbf{x}) \Big|_{\mathbf{x}=\mathbf{x}_0} \cdot \tilde{\mathbf{x}} \quad (3.63)$$

where $\tilde{f}(\tilde{\mathbf{x}})$ represents the Taylor expansion of $f(\mathbf{x})$ about a stationary point \mathbf{x}_0 with a state perturbation $\tilde{\mathbf{x}}$. Taking the Jacobian of Equation (3.2)–(3.4) and substituting for the formulae found in Equation (3.5)–(3.7), (3.14), (3.15), (3.24), (3.33), (3.55), and (3.56) gives the linearised EOMs about a stationary operating point, in this case an equilibrium point (denoted by the subscript 0). To simplify the expressions, the rotational coordinates are transformed into linear displacements using characteristic lengths. The EOMs are expressed with non-dimensional parameters normalised to the swingarm DOF, this eases the ensuing calculations and their readability. The new coordinates and their characteristic lengths are given by:

$$\tilde{\mathbf{q}} = \begin{pmatrix} l_\alpha \tilde{\alpha} \\ R_{R0} \tilde{\theta} \\ l_\phi \tilde{\phi} \end{pmatrix} \quad (3.64)$$

$$l_\alpha = \cos(\alpha_0) l_{sa} \quad (3.65)$$

$$l_\phi = \cos(\phi_0) L_R \quad (3.66)$$

where R_{R0} represents a static tyre rolling radius, and L_R is as defined in Equation (3.51). Trigonometric expressions are simplified as:

$$c_\alpha = \cos(\alpha_0), \quad s_\alpha = \sin(\alpha_0), \quad \tau_\alpha = \tan(\alpha_0)$$

$$c_\phi = \cos(\phi_0), \quad s_\phi = \sin(\phi_0), \quad \tau_\phi = \tan(\phi_0)$$

and the simplified EOMs are given as:

$$\mathbf{M} \ddot{\tilde{\mathbf{q}}} + 2\zeta \omega_n (\mathbf{C} + \mathbf{C}_{gyro} + \mathbf{C}_{tyre}) \dot{\tilde{\mathbf{q}}} + \omega_n^2 (\mathbf{K} + \mathbf{K}_{gyro} + \mathbf{K}_{cent} + \mathbf{K}_{Cori} + \mathbf{K}_{chain} + \mathbf{K}_{tyre} + \mathbf{K}_{stat}) \tilde{\mathbf{q}} = 0 \quad (3.67)$$

where ω_n is a resulting natural frequency of the normalisation, ζ the damping ratio. The remaining matrices are given by:

$$\mathbf{M} = \begin{bmatrix} 1 & 0 & 0 \\ 0 & \mathcal{I}_\theta & 0 \\ 0 & 0 & \mathcal{I}_\phi \end{bmatrix}, \quad \mathbf{C} = \begin{bmatrix} 1 & 0 & 0 \\ 0 & 0 & 0 \\ 0 & 0 & \Psi_f \end{bmatrix}, \quad \mathbf{C}_{gyro} = \begin{bmatrix} 0 & 0 & -\mathcal{G} \\ 0 & 0 & \xi_R \\ \mathcal{G} & -1 & 0 \end{bmatrix} \quad (3.68)$$

$$\mathbf{C}_{tyre} = \begin{bmatrix} -\tau_\alpha^2 \gamma_{xx} + \tau_\alpha s_\phi \gamma_{xy} + \tau_\alpha s_\phi \gamma_{yx} - s_\phi^2 \gamma_{yy} & \tau_\alpha \Gamma_x - s_\phi \Gamma_y & \xi_z (\tau_\alpha \gamma_{xy} - s_\phi \gamma_{yy}) \\ \tau_\alpha \gamma_{xx} - s_\phi \gamma_{xy} & -\Gamma_x & -\xi_z \gamma_{xy} \\ \xi_z (\tau_\alpha \gamma_{yx} - s_\phi \gamma_{yy}) & -\xi_z \Gamma_y & -\xi_z^2 \gamma_{yy} \end{bmatrix} \quad (3.69)$$

$$\mathbf{K} = \begin{bmatrix} 1 & 0 & -s_\phi (\Phi_z - g_{\alpha\phi}) \\ 0 & 0 & 0 \\ -s_\phi (\Phi_z - g_{\alpha\phi}) & 0 & \Phi_f + \tau_\phi^2 \Phi_z + g_\phi \end{bmatrix}, \quad \mathbf{K}_{gyro} = \Phi_{gyro} \begin{bmatrix} 0 & 0 & 0 \\ 0 & 0 & 0 \\ 0 & 0 & 1 \end{bmatrix} \quad (3.70)$$

$$\mathbf{K}_{\text{cent}} = \Phi_{\text{cent}} \begin{bmatrix} -\frac{\ell_\phi}{\ell_\alpha} \mathbb{C}_\alpha & 0 & 2c_\phi s_\phi \\ 0 & 0 & 0 \\ -2c_\phi s_\phi & 0 & -(c_\phi^2 - s_\phi^2) \frac{\ell_\alpha}{\ell_\phi} \mathbb{C}_\phi \end{bmatrix} \quad \mathbf{K}_{\text{Cori}} = \Phi_{\text{Cori}} \begin{bmatrix} \frac{\ell_\phi}{\ell_\alpha} (\tau_\alpha s_\phi - \zeta) & 0 & -c_\phi \\ 0 & 0 & 0 \\ -c_\phi & 0 & s_\phi \mathbb{C}_\phi \end{bmatrix} \quad (3.71)$$

$$\mathbf{K}_{\text{chain}} = \Phi_c \begin{bmatrix} \xi_R \sigma^2 (1 + \sigma') & \delta \sigma & 0 \\ \delta \xi_R \sigma & 1 & 0 \\ 0 & 0 & 0 \end{bmatrix} \quad \mathbf{K}_{\text{tyre}} = \begin{bmatrix} \tau_\alpha \lambda_{x1} - s_\phi \lambda_{y1} & 0 & -(\tau_\alpha \lambda_{x2} - s_\phi \lambda_{y2}) \\ -\lambda_{x1} & 0 & \lambda_{x2} \\ -\xi_z \lambda_{y1} & 0 & \xi_z \lambda_{y2} \end{bmatrix} \quad (3.72)$$

$$\mathbf{K}_{\text{stat}} = f \begin{bmatrix} \tau_\alpha c_\phi - \mu_{x0} - \tau_\alpha s_\phi \mu_{y0} & 0 & \frac{\ell_\alpha}{\ell_\phi} (s_\phi + c_\phi \mu_{y0}) \\ -\frac{R_{c0}'}{R_{c0}} \mu_{x0} & 0 & \tau_\phi \frac{\ell_\alpha}{\ell_\phi} \frac{R_{c0}'}{R_{c0}} \mu_{x0} \\ c_\phi \frac{\ell_\alpha}{\ell_\phi} & 0 & \frac{\ell_\alpha}{\ell_\phi} \end{bmatrix} \quad (3.73)$$

where the simplified compact notation terms are the normalised inertiae \mathcal{J}_i , a normalised frame rotational damping Ψ_f , a gyroscopic damping term \mathcal{G} , tyre force gradient damping terms γ_{ij} and Γ_i , normalised stiffnesses Φ_i , gravitational terms g_{ij} , centrifugal stiffness terms \mathbb{C}_i , a Coriolis stiffness term \mathbb{C}_ϕ , chain geometry terms σ and σ' , tyre force gradient stiffness terms λ_{ij} , a static force term f , the normalised static tyre forces μ_i , the static tyre loaded radius R_{c0} and its partial derivative with respect to roll angle $R_{c0}'^\phi$, and near unity geometric factors given by:

$$\xi_z = \frac{z_f}{\ell_\phi} \quad (3.74)$$

$$\xi_R = \frac{R_{c0}}{R_{R0}} \quad (3.75)$$

The definitions of all the compact notation terms are reported in the appendix. Note that the gyroscopic, centrifugal, Coriolis, and static tyre force matrices \mathbf{C}_{gyro} , \mathbf{K}_{gyro} , \mathbf{K}_{cent} , \mathbf{K}_{Cori} , and \mathbf{K}_{stat} are not numerically significant and are neglected in the sequel. This results in Equation (3.67) being simplified to the following:

$$\mathbf{M} \ddot{\mathbf{q}} + 2\zeta \omega_n (\mathbf{C} + \mathbf{C}_{\text{tyre}}) \dot{\mathbf{q}} + \omega_n^2 (\mathbf{K} + \mathbf{K}_{\text{chain}} + \mathbf{K}_{\text{tyre}}) \tilde{\mathbf{q}} = 0 \quad (3.76)$$

The role of the linearised tyre forces Equation (3.55) and (3.56) are shown in the \mathbf{C}_{tyre} and \mathbf{K}_{tyre} matrices. Effective damping terms from the tyre forces arise from the tyre force gradients, given by γ_{ij} which are the reduced gradients of tyre force gradients $C_{\sigma_{j,i}}$, and Γ_i which are linear combinations of the γ_{ij} based on operating conditions. Similarly, tyre force gradient terms arise from λ_{ij} , which depend on the tyre tangential force gradient due to vertical load $C_{F_{z,i}}$. The stiffness matrix $\mathbf{K}_{\text{chain}}$ represents the terms due to chain stiffness Φ_c and chain geometry σ (which depends on the chain to swingarm angle ψ).

3.2.4 Stationary Conditions

In order to study the stability of the linearised model it is required to extract quasi-static conditions from a time-varying manoeuvre performed by a motorcycle in simulation. According to Rosenbrook [1963] and Desoer [1969], in time-varying systems the real part of the eigenvalues is a necessary but not sufficient condition for stability and an additional bound exists on the size of the time derivative of the system matrix. In vehicle braking conditions, Salisbury et al. [2016] have shown this additional bound causes a miniscule change in the stability boundary from that found using frozen-time eigenvalue analysis. To reduce the likelihood of any discrepancy in stability boundaries, the quasi-static conditions are selected to be where the operating conditions are slowly varying, based on the tyre tangential forces. While this limitation means the definitive stability of the system requires an extra condition, the eigenvalue method remains a sufficient predictor of system instability.

For this chapter the stationary conditions are obtained from an optimal manoeuvre as calculated by the model developed by Leonelli and Limebeer [2020]. A simple 180° corner trajectory is obtained from the optimal control problem, considering the limitations of rider, motorcycle model, and circuit. The result is shown in Figure 3.8. The selected braking region is highlighted in red and occurs during the front rollover limit where tyre forces remain nearly constant. This area of operation has been shown experimentally to exhibit the instability in question, when tyre vertical load is near its minimum and a small longitudinal braking force is applied to the wheel through the

chain [Cossalter et al. 2012, Leonelli et al. 2018]. The region progresses through a forward speed of 260 km h^{-1} to 220 km h^{-1} , a roll angle of 8° to 26° , a swingarm angle of 14.3° to 10.6° , and has an average vertical load on the tyre of 134 N .

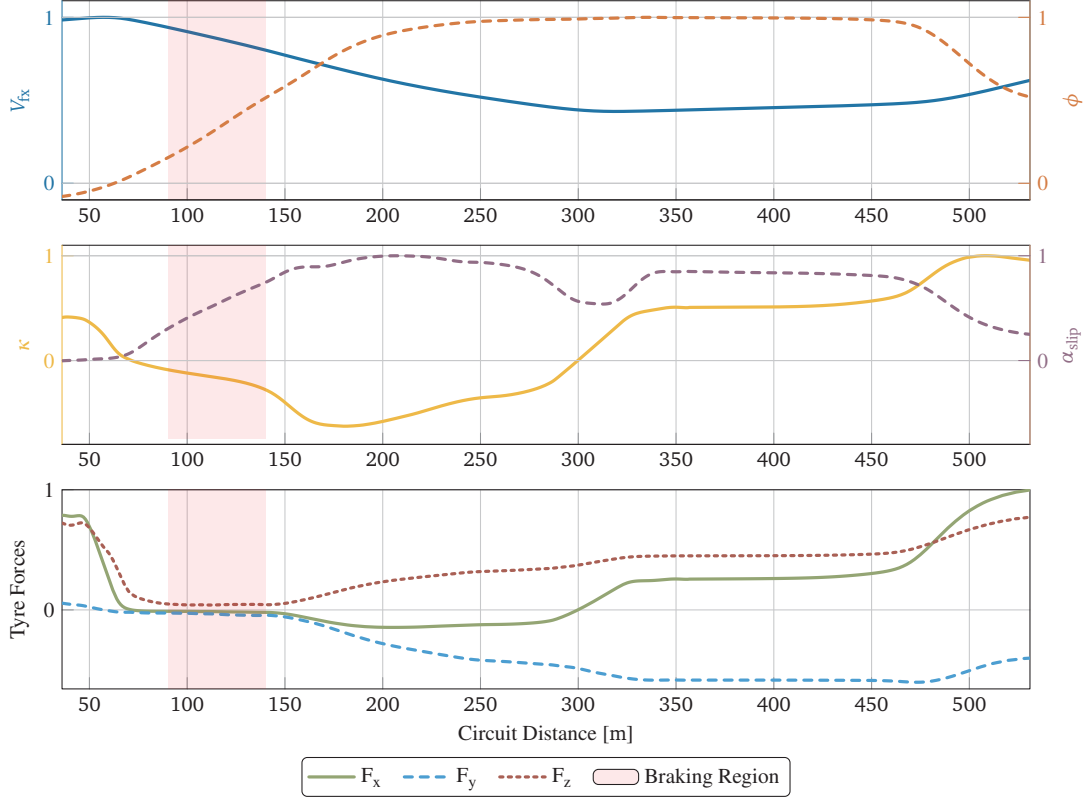


Figure 3.8: Manoeuvre used to extract quasi-static equilibrium conditions, as computed by Leonelli and Limebeer [2020]. y -axes have been normalised due to confidentiality agreements. The braking region is highlighted in red.

This optimal dataset gives the required tyre forces, slips, and parameters as well as the kinematics of the frame. The tyre force gradient parameters are given in the practical slip convention and need to be converted using:

$$C_{\sigma_{x,x}} = -(\kappa + 1)^2 C_{\kappa,x} \quad (3.77)$$

$$C_{\sigma_{y,x}} = -\cos^2(\alpha_{\text{slip}})(\kappa + 1)C_{\alpha_{\text{slip},x}} \quad (3.78)$$

$$C_{\sigma_{x,y}} = -(\kappa + 1)^2 C_{\kappa,y} \quad (3.79)$$

$$C_{\sigma_{y,y}} = -\cos^2(\alpha_{\text{slip}})(\kappa + 1)C_{\alpha_{\text{slip},y}} \quad (3.80)$$

The nonlinear EOMs (3.2)–(3.4) are used for calculating the remaining equilibrium values. The static swingarm angle α_0 is found geometrically using Equation (3.7) with z given by Equation (3.34) (F_{z0} is provided by the optimal dataset):

$$\sin(\alpha_0) = \frac{1}{\ell_{\text{sa}}} \left(\frac{-F_{z0} k_z^{-1} - \rho_r + z_f}{\cos(\phi_0)} - h_f + \rho_r - R_r \right) \quad (3.81)$$

The free chain length ℓ_{fc} is given by:

$$\ell_{\text{fc}} = \ell_{\text{tc}}(\alpha_0) + \ell_{\theta_c}(\alpha_0) \quad (3.82)$$

and the equilibrium chain stretch $\Delta\ell_c$ (a component of σ') is found from Equation (3.3), balancing the tyre force:

$$\Delta\ell_c = \ell_c(\alpha_0, \theta_0) - \ell_{fc} = \frac{R_{c0}}{k_c r_c} |F_{x0}| \quad (3.83)$$

The optimal manoeuvre data do not include the braking moment M_{br} and its effects on tyre loads, so it is set to zero.

With these data the model has all that is required to solve for quasi-static equilibrium conditions. Reference parameter values that are independent of the manoeuvre are given in Table 3.1.

Table 3.1: Model reference parameter values not dependent on manoeuvre.

Parameter	Unit	Value	Parameter	Unit	Value	Parameter	Unit	Value
β_p	rad	0.12	J_{say}	kg m ²	0.35	k_s	N rad ⁻¹	1.51×10^4
η	–	0.05	J_{saz}	kg m ²	0.30	k_z	N m ⁻¹	1.70×10^5
η_b	–	0.5	J_{whxz}	kg m ²	0.48	l_p	m	0.08
η_{fr}	–	0	J_{wh}	kg m ²	0.85	l_{sa}	m	0.65
η_{sa}	–	0.5	R_r	m	0.33	m_{fr}	kg	266
ρ_r	m	0.11	c_f	N s rad ⁻¹	0	m_{sa}	kg	8
J_{frx}	kg m ²	20	c_s	N s rad ⁻¹	353	m_{wh}	kg	15
J_{fry}	kg m ²	40	h_f	m	0.21	r_c	m	0.1036
J_{frz}	kg m ²	30	k_c	N m ⁻¹	1.15×10^6	r_p	m	0.043
J_{sax}	kg m ²	0.10	k_f	N rad ⁻¹	0	x_f	m	0.01

3.3 Analysis and Results

3.3.1 Comparison to a Multi-body Model

To validate the addition of the roll angle to the minimal model, data are extracted from a full multi-body simulation as provided by the commercial software VI-Motorcycle² and used to compare to the results of the minimal model. The multi-body simulation consists of a full rigid body model of a motorcycle as provided by VI-grade, includes 37 DOFs, and is operated in a braking manoeuvre similar to that provided in Subsection 3.2.4 (but not exactly the same due to model limitations). The frozen-time eigenvalues at multiple points are extracted and compared to those the minimal model produces using the same input data and model parameters. The results are compared in Figure 3.9.

It can be seen that Mode 1 of the minimal model is a pseudo-mode that captures the lower frequency modes of the multi-body model, such as bounce and pitch, while Mode 2 and Mode 3 show similar values and behaviour to the rear hop and driveline modes, respectively. The driveline mode from the minimal model does show less stability and a lower frequency than that of the multi-body simulation. This is attributed to two things: first, the multi-body simulation uses a small chain damping term, moving the eigenvalues slightly towards stability. This is assumed to be a negligible addition which only acts to add a small amount of stability to the system, while not affecting the overall behaviour. Second, the multi-body simulation also includes powertrain rotational dynamics, whereas the minimal model assumes an infinite inertia drivetrain. This results in a lower perceived driveline frequency in the minimal model. The most effective way of accommodating for this discrepancy is to raise the chain stiffness or lower the wheel inertia of the minimal model accordingly. These adjustments have shown to accurately represent the modal frequency of the driveline oscillations of the multi-body model, without affecting the behaviour of the other modes.

3.3.2 Eigenvalue Analysis of a Braking Manoeuvre

This section and all that follow focus on the analysis of the linearised model during the quasi-static manoeuvre provided in Subsection 3.2.4, using parameters from that dataset. The eigenvalue analysis of the quasi-static braking region is presented in Figure 3.10. The first mode is similar to that of ‘bounce’ and has been denoted such. The

²<https://www.vi-grade.com>

second mode is a rear hop mode with frequencies of 14 Hz to 17 Hz, and the third mode is the driveline mode with frequencies in the neighbourhood of 19 Hz that begins stable then crosses the stability boundary.

During the chosen manoeuvre, the inertial matrices (gyroscopic, centrifugal, and Coriolis) as well as the stationary force matrix prove to be numerically negligible due to the factors appearing in front of the matrices being nearly zero. Therefore stability of the system must depend on the tyre slip and chain matrices, as the remaining matrices (mass, damping, and stiffness) are all positive definite (or positive semi-definite in the case of the damping matrix). Also, the asymmetric factor ξ_R in the chain matrix remains close to unity, making the matrix effectively symmetric. Recall that in the presented model, the chain model is exact and Sorrentino and Leonelli [2017] used a simplified model that directly lead to a symmetric chain stiffness matrix as well.

Figure 3.10 also contains the eigenvectors and their evolution through the manoeuvre in the form of polar plots. The bounce mode (Figure 3.10b) mainly contains roll angle oscillations, with an increased presence of swingarm angle as the manoeuvre progresses. The rear hop mode (Figure 3.10c) is driven primarily by swingarm oscillations, though as the manoeuvre progresses and static roll angle increases, there is a larger presence of both wheelspeed and roll angle oscillations, suggesting interactions between the modes. Finally, the driveline mode (Figure 3.10d) has its main contribution come from the wheelspeed oscillations, the major factor in determining the chain and tyre forces, while also having a small contribution from the swingarm oscillations. Focus is now put on the stability of the driveline mode, which represents the ‘chattering’ experienced during heavy braking.

3.3.3 Energy Flow Analysis

To investigate the source of instability, an energy balance method is employed as used previously by Katayama and Nishimi [1990], Kröger et al. [2008] and Sorrentino and Leonelli [2017]. If there exists a switching mechanism whose energy flow into the system is greater than that dissipated over one oscillation cycle, vibration amplitude increases. First, recall the linearised EOMs (3.76) and recast them as a sum of forces and inertial components with the tyre force terms separated:

$$G = m_\alpha \mathbf{M} \ddot{\mathbf{q}} + 2m_\alpha \zeta \omega_n \mathbf{C} \dot{\mathbf{q}} + m_\alpha \omega_n^2 (\mathbf{K} + \mathbf{K}_{\text{chain}}) \tilde{\mathbf{q}} - (\mathbf{f}_x + \mathbf{f}_y) = 0 \quad (3.84)$$

where $\tilde{\mathbf{q}}$ is the vector of perturbed system coordinates, m_α is a system mass defined in the Appendix by Equation (A.31), \mathbf{M} is the mass matrix, \mathbf{C} is the damping matrix due to dissipative elements (in this case the damper), \mathbf{K} and $\mathbf{K}_{\text{chain}}$ are the matrices of conservative elastic elements (springs), while \mathbf{f}_x and \mathbf{f}_y are vectors arising from the

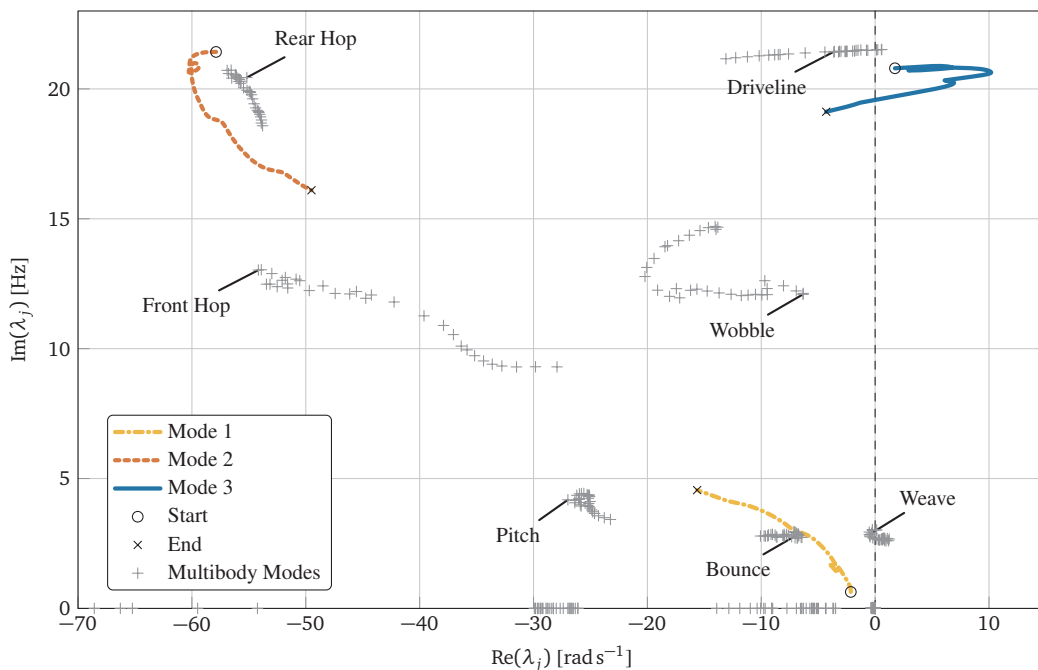


Figure 3.9: Comparison of the minimal model eigenvalues with those of a multi-body simulation.

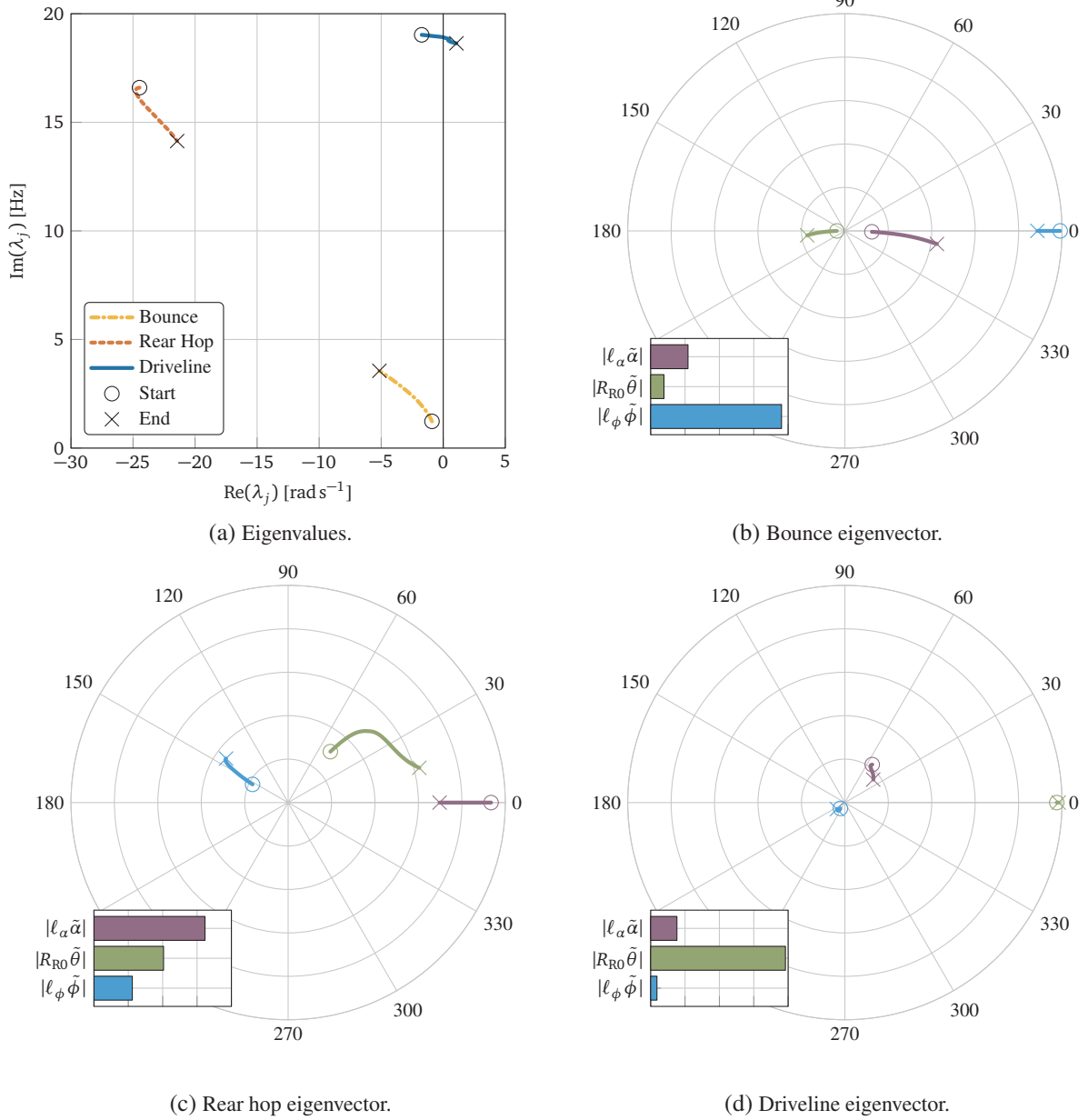


Figure 3.10: Quasi-static linear model eigenvalue analysis of the braking region. Evolution of the eigenvectors are shown normalised and phased to their largest component, while the bar chart legends show the average component magnitudes.

tyre tangential ground forces in the longitudinal and lateral directions, respectively. Note that \mathbf{f}_x and \mathbf{f}_y are linearised vectors containing state dependent non-stationary components, and therefore are not considered as external forces, but as dissipative elements in the linearised equations.

At the stability boundary, the free response of the system converges to harmonic oscillation with a period of T . The perturbation vector $\tilde{\mathbf{q}}$ is assumed to be modal solutions of the form found in Müller and Schiehlen [1985, p. 142]:

$$\begin{Bmatrix} \dot{\tilde{\mathbf{q}}} \\ \tilde{\mathbf{q}} \end{Bmatrix} = \frac{1}{2} e^{\text{Re}(\lambda_j)t} \left(e^{i\text{Im}(\lambda_j)t} \mathbf{y}_j + e^{-i\text{Im}(\lambda_j)t} \bar{\mathbf{y}}_j \right) \quad (3.85)$$

where λ_j is the mode eigenvalue, \mathbf{y}_j is the mode eigenvector, and $\bar{\mathbf{y}}_j$ is the complex conjugate of the eigenvector. The energy balance over one period can then be expressed as:

$$\Delta E = \Delta E_{\text{kin}} + \Delta E_{\text{pot}} + \Delta E_{\text{dis}} = \int_0^T \mathbf{G} \dot{\mathbf{q}} dt = 0 \quad (3.86)$$

where ΔE_{kin} and ΔE_{pot} are the change in kinetic and potential energies over one cycle. If the corresponding matrices are symmetric, then these terms will be zero. For this analysis, the asymmetry of the chain matrix is assumed to be negligible ($\xi_R \approx 1$). It follows that:

$$\Delta E_{\text{dis}} = \int_0^T \left[2m_\alpha \zeta \omega_n \dot{\mathbf{q}}^T \mathbf{C} \dot{\mathbf{q}} - \dot{\mathbf{q}}^T (\mathbf{f}_x + \mathbf{f}_y) \right] dt = 0 \quad (3.87)$$

which shows that over one period of oscillation, the energy dissipated by the damper is balanced by the energy introduced by the ground force terms. If \mathbf{f}_x and \mathbf{f}_y are cast as $\mathbf{a}\tilde{F}_x$ and $\mathbf{b}\tilde{F}_y$ where \tilde{F}_i are the oscillating portions of the ground forces, and \mathbf{a} and \mathbf{b} are congruence vectors arising from the EOMs, then Equation (3.87) can be reformed as:

$$\int_0^T \left[2m_\alpha \zeta \omega_n \dot{\mathbf{q}}^T \mathbf{C} \dot{\mathbf{q}} - \tilde{V}_{sx} \tilde{F}_x - \tilde{V}_{sy} \tilde{F}_y \right] dt = 0, \quad \begin{cases} \tilde{V}_{sx} = \mathbf{a} \cdot \dot{\mathbf{q}} \\ \tilde{V}_{sy} = \mathbf{b} \cdot \dot{\mathbf{q}} \end{cases} \quad (3.88)$$

where the oscillating slip velocities \tilde{V}_{sx} and \tilde{V}_{sy} have been introduced as a result.

Due to the harmonic motion, the two tyre force terms in Equation (3.88) are products of two cosine waves of equal frequencies and distinct phase offsets. It can be shown that for the product of two cosine waves with a relative phase offset, the result contains a constant term proportional to the cosine of that offset. For example, given two cosine waves with phases of ψ_1 and ψ_2 , their product can be simplified to:

$$R_1 \cos(\omega t + \psi_1) R_2 \cos(\omega t + \psi_2) = \frac{R_1 R_2}{2} \left(\cos(2\omega t + \psi_1 + \psi_2) + \underbrace{\cos(\psi_1 - \psi_2)}_{\text{constant term}} \right) \quad (3.89)$$

Clearly, a constant value appears based on the cosine of the relative phase. This allows for a non-zero result of the integration and therefore can cause positive energy flow into the system during phase offsets between -90° and 90° , and energy dissipation outside of this range.

Given this result, the source of an instability must come from the phase offset between tyre tangential forces and tyre slips. Even though the tyre is a dissipative element (being a friction element), under the combined effect of oscillating ground forces and vertical load acting with certain values of phase lag, it can become the means of energy flow feeding the system and sustaining a self-excited oscillation. In the specific case of the present analysis, the external source of energy able to sustain the self-excited oscillation is the kinetic energy of the frame travelling at an imposed constant speed.

The tyre force and slips for both tangential directions at the stability boundary are given in Figure 3.11. The longitudinal phase offset is found to be 53.6° resulting in energy flow into the system. The magnitude of this energy flow is close to but not surpassing the dissipation of the swingarm damper, as expected near the stability boundary. The lateral phase offset is 90.8° resulting in an insignificant energy dissipation.

The longitudinal phase offset arises from relative phase offset between the tyre vertical load \tilde{F}_z and the longitudinal slip velocity \tilde{V}_{sx} , as well as the fact that the longitudinal force is made up of a weighted linear combination of these terms (through the coefficients $C_{\sigma_x, x}$ and $C_{F_z, x}$). The phase relationship between vertical load and tyre slip is displayed in Figure 3.11c–3.11f. There it is shown that slip is largely dependent on the $\dot{\theta}$ term, while vertical load fluctuations are primarily driven by the $\tilde{\alpha}$ term. Figure 3.11c and 3.11d show the makeup and phase relationships of the tyre longitudinal force. The contribution from the tyre slip $\tilde{F}_x(\tilde{\sigma}_x)$ is 180° out of phase with the slip velocity \tilde{V}_{sx} which makes it dissipative, while the phase for the vertical load term is 32.1° and is the main contributor to instability (all other terms from Equation (3.55) are negligible). This shows that the tyre force gradient terms $C_{\sigma_x, x}$ and $C_{F_z, x}$ have major influences on stability, which is further supported in the following sections.

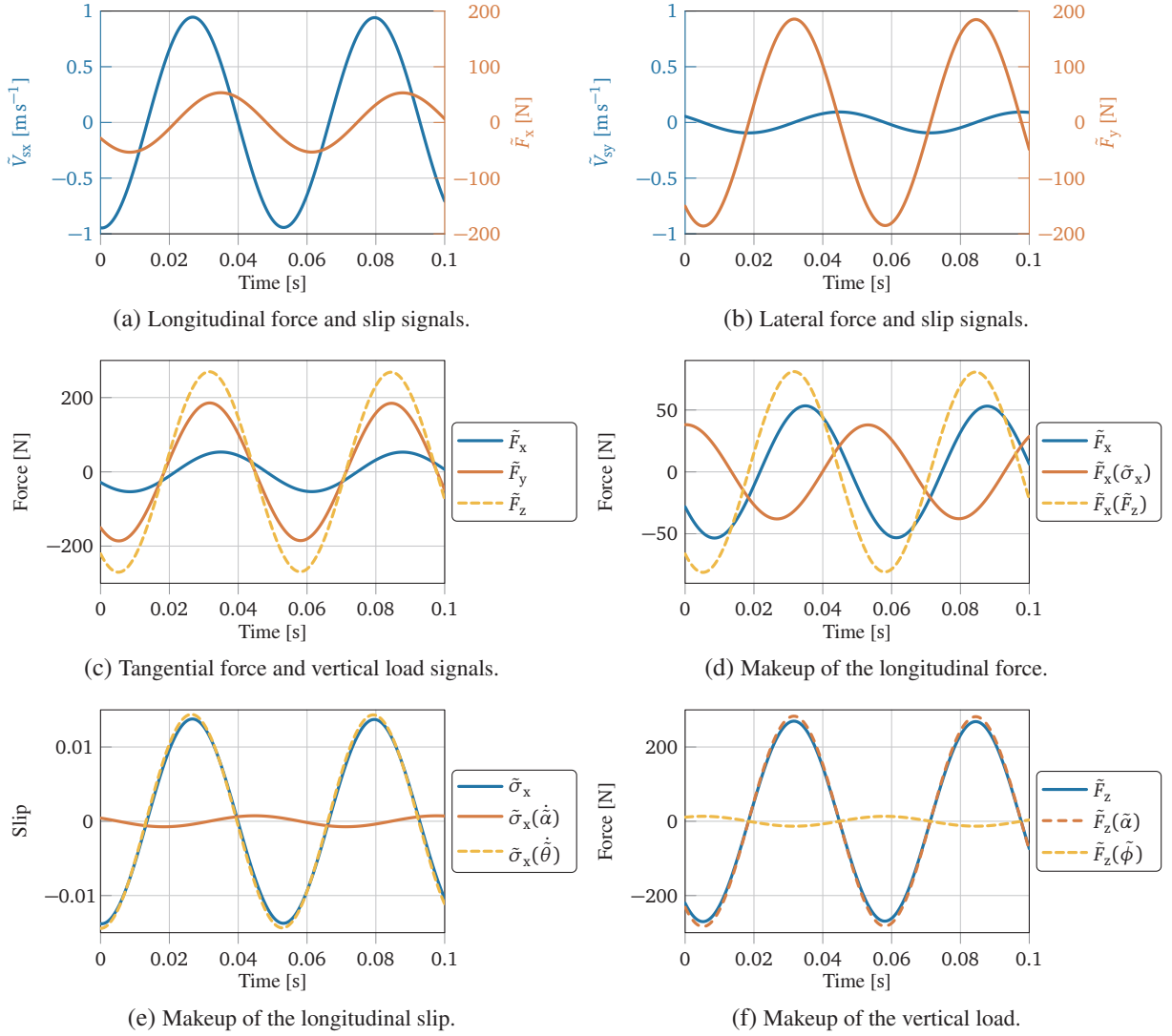


Figure 3.11: Tyre force and slip signals used for the energy flow analysis.

3.3.4 Eigenvalue Sensitivity

To understand the stability boundary of the driveline mode and its sensitivity to different model characteristics, eigenvalue sensitivities are calculated using the eigenvalue perturbation method [Greenbaum et al. 2020]. This gives the gradient of the eigenvalue of interest with respect to changes in model parameters, allowing the stability boundary sensitivity to be discerned. The sensitivity of an eigenvalue λ_j with respect to a parameter τ , on which the system matrix A depends, is defined as:

$$\frac{\partial \lambda_j}{\partial \tau} = \mathbf{y}'_j{}^T \frac{\partial A(\tau)}{\partial \tau} \mathbf{y}_j \quad (3.90)$$

where A is the linearised system matrix and \mathbf{y}_j and \mathbf{y}'_j are the right and left eigenvectors of λ_j , respectively, normalised such that $\mathbf{y}'_j{}^T \mathbf{y}_j = 1$. The gradient of interest is along the real axis, so the result of Equation (3.90) is decomposed into its real and imaginary parts:

$$\frac{\partial \lambda_j}{\partial \tau} = \text{Re}(\lambda'_j) + i \text{Im}(\lambda'_j) \quad (3.91)$$

where the shorthand λ'_j has been introduced for the eigenvalue gradient. The real part of Equation (3.91) is taken as the sensitivity of the stability boundary to parameter τ . These results are then scaled by the magnitude of the parameter (i.e., $|\tau| \text{Re}(\lambda'_j)$), to make the sensitivities proportional to a fractional change in any given parameter.

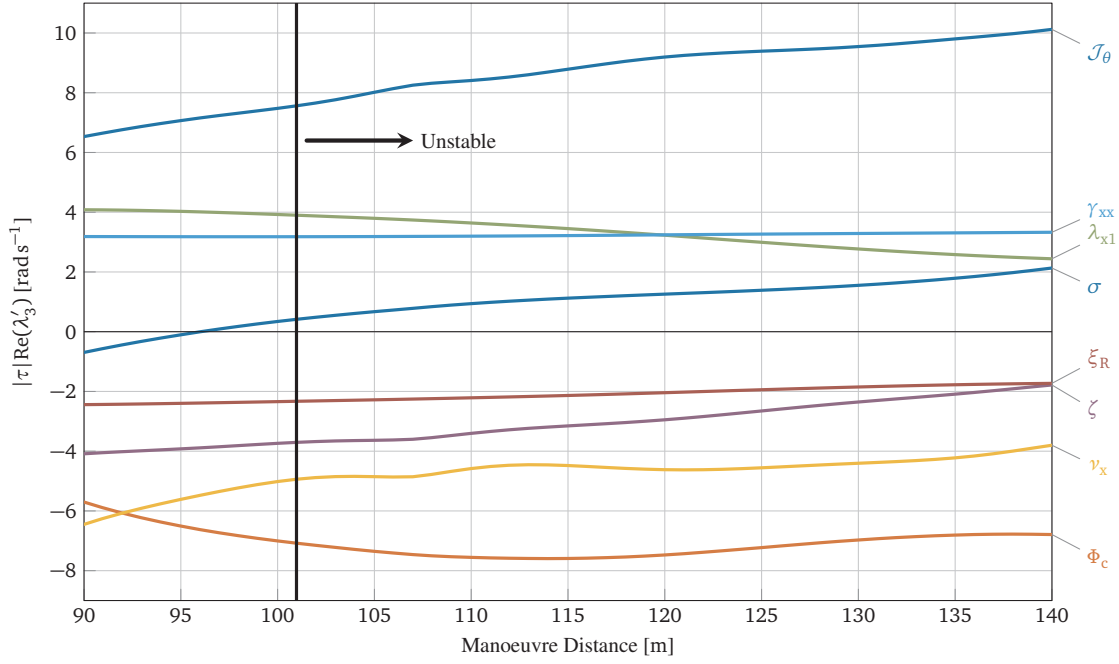


Figure 3.12: Eigenvalue sensitivity of the driveline stability boundary in the braking region with respect to several non-dimensional parameters. The vertical bar indicates the point of the manoeuvre where the stability boundary is crossed.

The eigenvalue sensitivities of the EOMs (3.76) are calculated to see which non-dimensional parameters have the most influence on the stability of the driveline mode eigenvalue λ_3 . The eigenvalue sensitivities and their evolution during the braking manoeuvre are presented in Figure 3.12. Here the sensitivity of each parameter is shown as they evolve through the quasi-static reference manoeuvre, which reaches instability where the vertical bar is shown on the graphs. A positive sensitivity to a parameter means the system stability decreases with an increase in that parameter, and vice versa.

To get a more practical understanding of the system stability boundary, the sensitivity procedure is performed again using dimensional model reference parameters. The results are shown in Figure 3.13a and 3.13b. The parameters with the biggest effect can be grouped into:

- (i) Frequency parameters: those that affect the natural frequencies of the driveline and rear hop modes, such as tyre vertical stiffness k_z , chain stiffness k_c , rear sprocket ratio r_c (which is prominent in the equivalent torsional chain stiffness about the wheel axis), wheel moment of inertia J_{wh} , wheel mass m_{wh} , and swingarm mass position η_{sa} .
- (ii) Tyre force gradient parameters: $C_{\sigma_{x,x}}$, $C_{F_z,x}$, and $C_{F_z,y}$.
- (iii) Geometric parameters: those that affect chain geometry and the chain matrix, such as front sprocket radius r_p , and tyre outer radius R_T .

As expected, increasing system damping c_s produces a small stabilising effect. Swingarm length ℓ_{sa} has a significant yet complicated effect, as it crosses the x -axis meaning the sensitivity gradient changes sign and any stabilising effects would be reversed after that point. This is assumed to be due to its appearance throughout many terms in the system.

To test the results of the sensitivity analysis presented in Figure 3.12, the stability regions of the non-dimensional EOMs (3.76) are plotted with varying parameter inputs. These regions are calculated using the Routh-Hurwitz criterion of the system characteristic polynomial and are shown in Figure 3.14. The regions are plotted with respect to the non-dimensional tyre force gradient parameters to facilitate comparisons to previous studies [Sorrentino and Leonelli 2017], and each sub-figure has a non-dimensional parameter selected from the groups above varied by $\pm 10\%$. The top row shows that varying the frequency parameters \mathcal{J}_θ and Φ_c have a large effect on the stability boundary, as does the manoeuvre dependent reduced velocity parameter ν_x . The second row confirms that geometric parameters ξ_R and σ have a smaller effect, similar to that of the system damping ζ . There is agreement

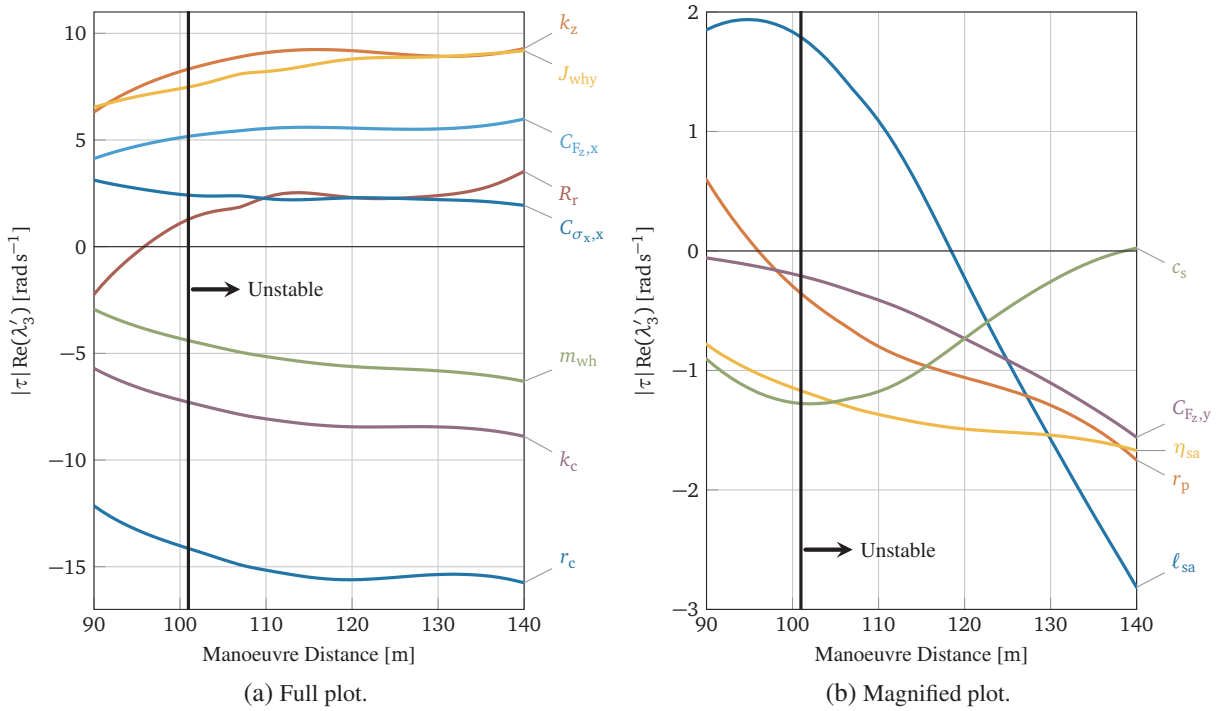


Figure 3.13: Eigenvalue sensitivity of the driveline stability boundary in the braking region with respect to several model reference parameters. The vertical bars indicate the point of the manoeuvre where the stability boundary is crossed.

both between the eigenvalue sensitivities and their respective changes in stability regions, and with previous work [Sorrentino and Leonelli 2017], where $\lambda_{x1} \cong \lambda$ and $\gamma_{xx} \cong -\gamma$ and Figure 3.14 can be compared to the general case presented there.

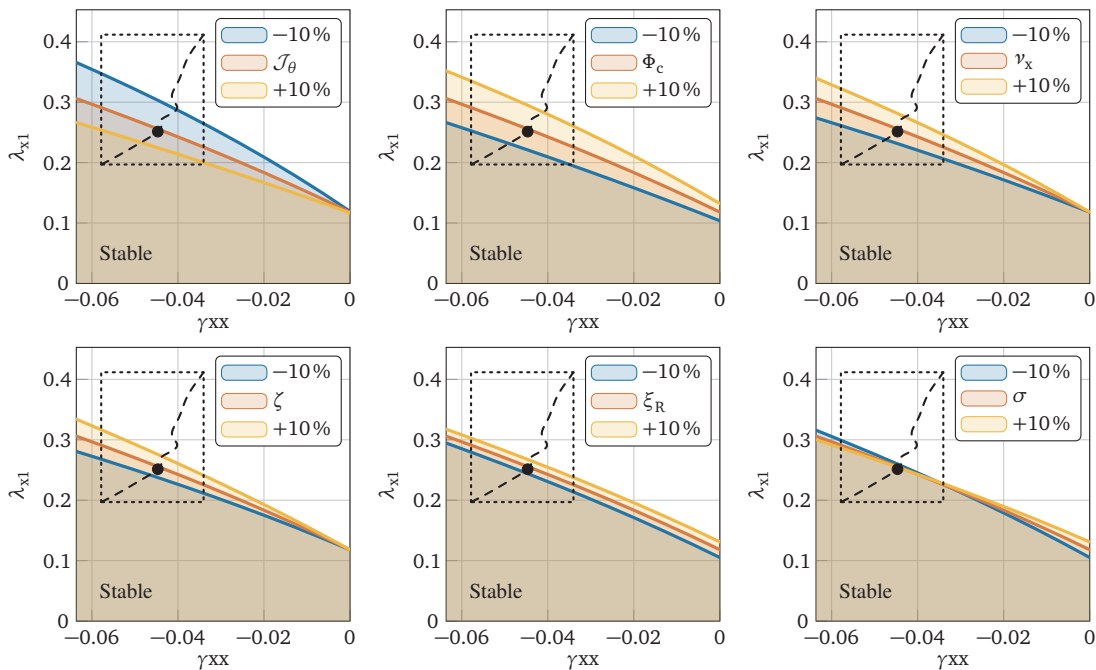


Figure 3.14: Routh-Hurwitz stability regions with respect to several non-dimensional parameters. The black point gives the linearisation point, the dotted box shows the region boundaries, and the dashed line traces the whole manoeuvre.

3.3.5 Mechanism of Instability

An attempt is made to determine the underpinnings of the eigenvalue sensitivities found in Figure 3.12 by analytically investigating the complete linearised EOMs (3.76). Negative terms in the diagonal of the damping matrix lead to decreased stability, as do asymmetric terms in both the damping and stiffness matrices [Hagedorn et al. 2014]. Reducing the total damping and total stiffness matrices by removing negligible and unimportant terms yields:

$$\mathbf{C} + \mathbf{C}_{\text{tyre}} = \nu_x \begin{bmatrix} \dots & \nu_x(\tau_\alpha \gamma_{xx} - s_\phi \gamma_{yx}) & \dots \\ \tau_\alpha \gamma_{xx} - s_\phi \gamma_{yx} & -\nu_x \gamma_{xx} & \dots \\ \dots & \dots & \dots \end{bmatrix} \quad (3.92)$$

$$\mathbf{K} + \mathbf{K}_{\text{chain}} + \mathbf{K}_{\text{tyre}} = \begin{bmatrix} \dots & \delta \sigma \Phi_c & \dots \\ \delta \xi_R \sigma \Phi_c - \lambda_{x1} & \Phi_c & \dots \\ \dots & \dots & \dots \end{bmatrix} \quad (3.93)$$

Here the role of some important parameters can be seen. The reduced velocity ν_x tends to increase damping in a scalar manner. The tyre slip term γ_{xx} , normally negative in regular operation of the tyre, provides positive damping in the main diagonal of the damping matrix. If this term changes sign, such as when peak tyre grip is exceeded, it would introduce negative damping, which can lead to instability. The tyre slip terms γ_{xy} , γ_{yx} , and λ_{x1} influence the asymmetry of both matrices respectively, and show increased stability when reduced. In the case of γ_{yx} , the asymmetry is multiplied by ν_x , but the scalar damping effect of ν_x is stronger than its asymmetric effect. The parameter ξ_R also brings about asymmetry in the total stiffness matrix (3.93), but its value tends to stay close to unity, largely affected by tyre toroidal geometry and rolling radius characteristics. Finally, the chain geometry term σ couples the α and θ equations through the total stiffness matrix (3.93), where asymmetry introduced by λ_{x1} can cause instability.

In general, when compared to the mechanisms of instability presented by Kröger et al. [2008], this instability can be categorised as ‘geometrical effects and non-conservative restoring forces’ caused by the asymmetric terms in the system stiffness matrix. The possibility of the ‘contacts with decreasing friction characteristic’ type of mechanism is present as well if the tyre force gradient term γ_{xx} (driven by $C_{\sigma_{x,x}}$) were to become positive, such as when the tyre exceeds peak grip. As possible solutions for the former type of instability, Kröger et al. [2008] suggest a reduction in friction coefficient, though this is not desirable for racing motorcycles. A change in contact geometry is also recommended, or possibly an increase in system damping, though damping coefficients could be fixed due to other design factors [Cossalter et al. 2000, Martini et al. 2018]. The subsequent sections explore several possible methods for stabilising the chatter mode.

3.3.6 Stabilisation via Natural Frequencies

Figure 3.15 shows the changes in the eigenvalues with respect to the parameters that affect the natural frequencies of the driveline and rear hop modes. It can be seen on the right of the figure that with stabilising changes in k_c , r_c , or J_{why} , the driveline mode natural frequency is raised and damping is increased. On the left of the figure, on the other hand, stabilising changes to k_z or m_{wh} causes the rear hop mode frequency to be lowered, and damping of the driveline mode is increased. This result suggests that a separation of the natural frequencies of the two modes reduces their interaction and leads to more stable behaviour.

3.3.7 Stabilisation via Chain Geometry

Another stabilising factor found is the chain geometry factor σ , although this parameter is highly based on the manoeuvre and dependent on the swingarm angle α . The stability with respect to varying σ is shown in Figure 3.16. First, there can be a stabilising effect by increasing σ (and therefore increasing the chain to swingarm relative angle ψ), but that effect quickly vanishes as the system approaches instability. A parallel swingarm and chain ($\sigma = 0$) remains stable throughout the whole manoeuvre. The change in sign of the eigenvalue sensitivity is due to the gradient of these curves.

3.3.8 Effect of Swingarm Angle

The effects of swingarm length are fairly complex, as it is a characteristic length of the system and appears throughout the EOMs. It is not an effective parameter for stabilising the system, due to its sensitivity gradient changing

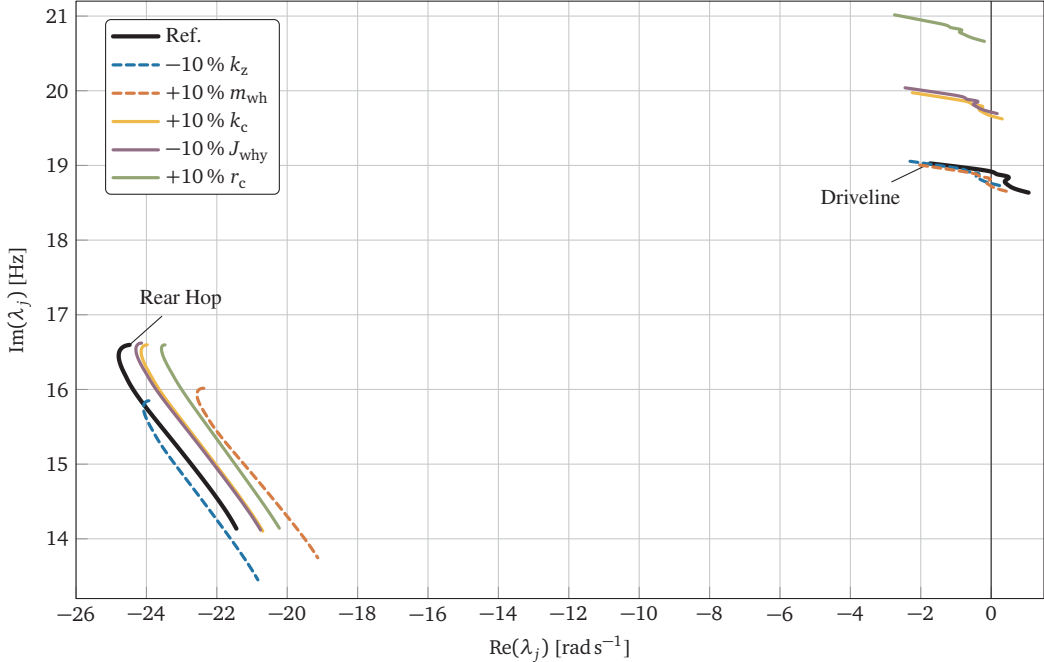


Figure 3.15: Changes to eigenvalues with respect to natural frequency parameters.

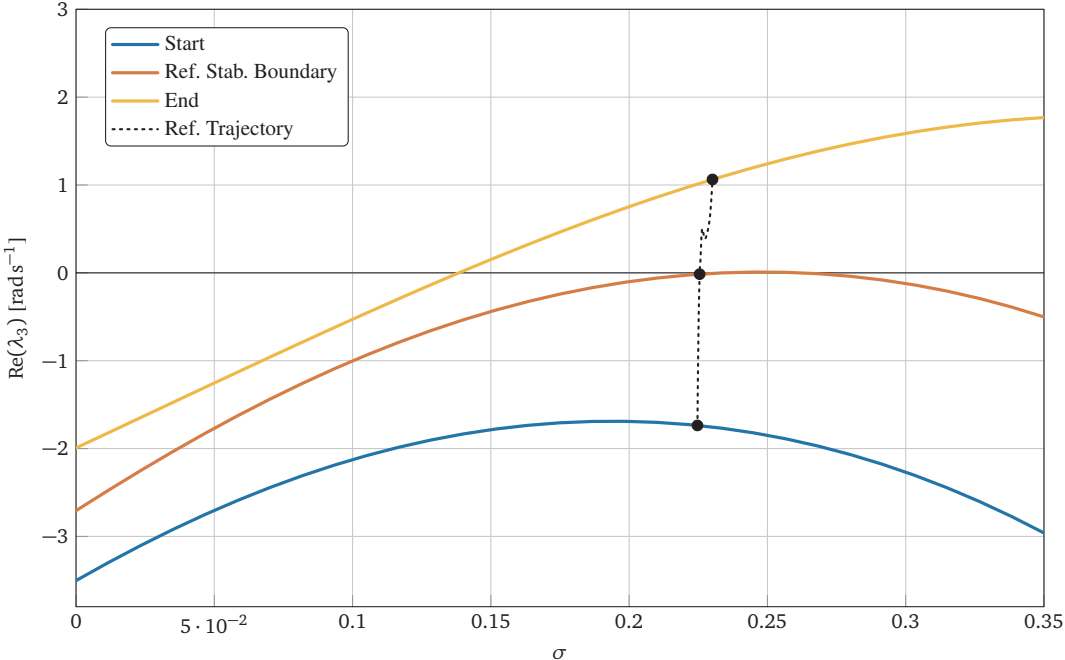


Figure 3.16: Stability with varying chain geometry σ . Coloured lines represent the beginning, end, and reference stability boundary of the region. The black dotted line shows the manoeuvre reference trajectory.

sign as seen in Figure 3.13b. In contrast, the static swingarm angle, which can effectively be set by the parameter h_f , does have a significant effect since it changes the chain geometry. This has an effect on stability as the previous section shows. To discern between the effects of chain geometry and a possible secondary effect of swingarm angle, analysis is performed with a chain geometry factor σ frozen at a value of 0.23, see Figure 3.17.

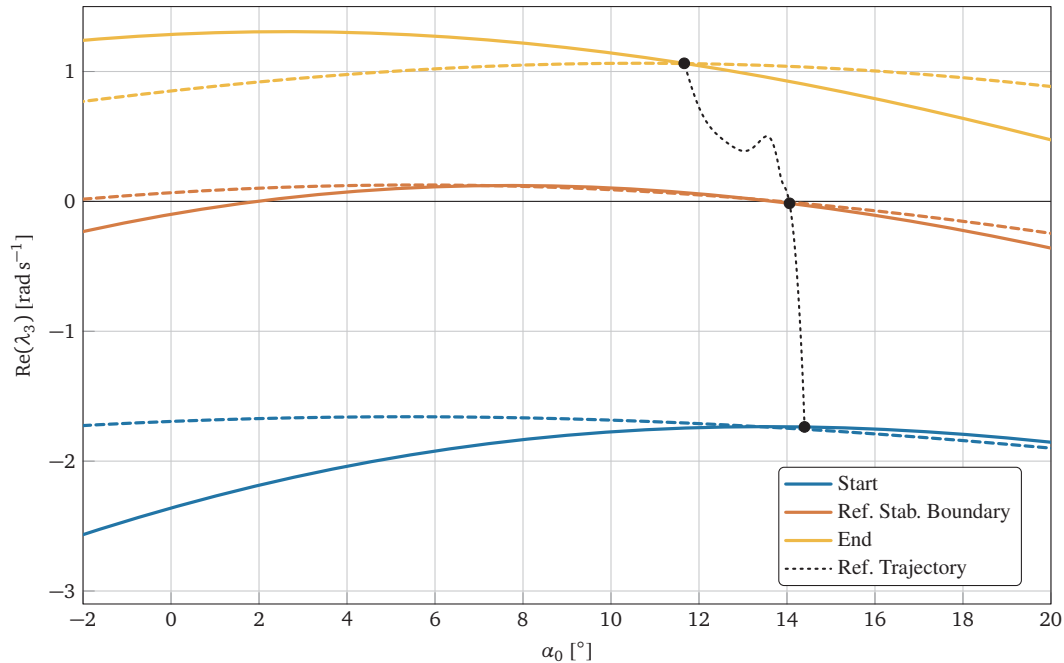


Figure 3.17: Stability with varying static swingarm angle α . Solid coloured lines represent the beginning, end, and the reference stability boundary of the region, while the coloured dashed lines represent the same analysis with a frozen chain geometry ($\sigma = 0.23$). The black dotted line shows the manoeuvre reference trajectory.

While the non-frozen analysis shows a negative gradient as static swingarm angle is increased (moving towards a parallel swingarm and chain), the frozen analysis loses this effect, and the dashed curves show flatter behaviour. There is a small secondary effect, with the manoeuvre operating close to the peak of instability on the α_0 curves. In the stable region, an increase in static swingarm angle leads to higher stability (with frozen chain geometry), while in the unstable region the effect is reversed with a more horizontal swingarm being more stable. Note that the main effect of braking moment M_{br} is the change in the stationary swingarm value α_0 , and thus σ , and therefore would affect system stability. Unfortunately, this cannot be properly captured in the linearised minimal model analysis.

3.3.9 Effect of Roll Angle

The effect of roll angle on stability is difficult to characterise with the simplified model due to so many externally determined equilibrium value dependencies. For example: the vertical height of point F , z_f , depends on ϕ , as do many of the tyre parameters. To view the effects of roll angle on system stability, the stability boundary with respect to the forward speed V_{fx} (critical speed) is determined during the manoeuvre as roll angle increases. This is shown in Figure 3.18, along with similar calculations with altered parameters to display some of the stabilising and destabilising effects they can have. The increase in rear sprocket radius (with corresponding increase in front sprocket radius to maintain final drive ratio) proves to be a useful adjustment in stabilising the system as described previously. The shortening of the swingarm length also initially shows increased stability, but at 21° of roll angle the effect is reversed. The conclusion from this figure is that with increased roll angle, the stability of the system decreases.

The decrease in system stability is not directly due to the presence of roll angle in the dynamics, as seen in the eigenvector plot in Figure 3.10, but due to some indirect effect on other equilibrium parameters. As shown in Figure 3.13a, the tyre force gradient parameters $C_{\sigma_{x,x}}$ and $C_{F_r,x}$ have a large effect on stability and are also highly dependent on roll angle (tyre camber). This effect is highlighted in Figure 3.19 where an increase in roll angle shows destabilising changes in tyre force gradient parameters, as proven in the energy and sensitivity analyses. This

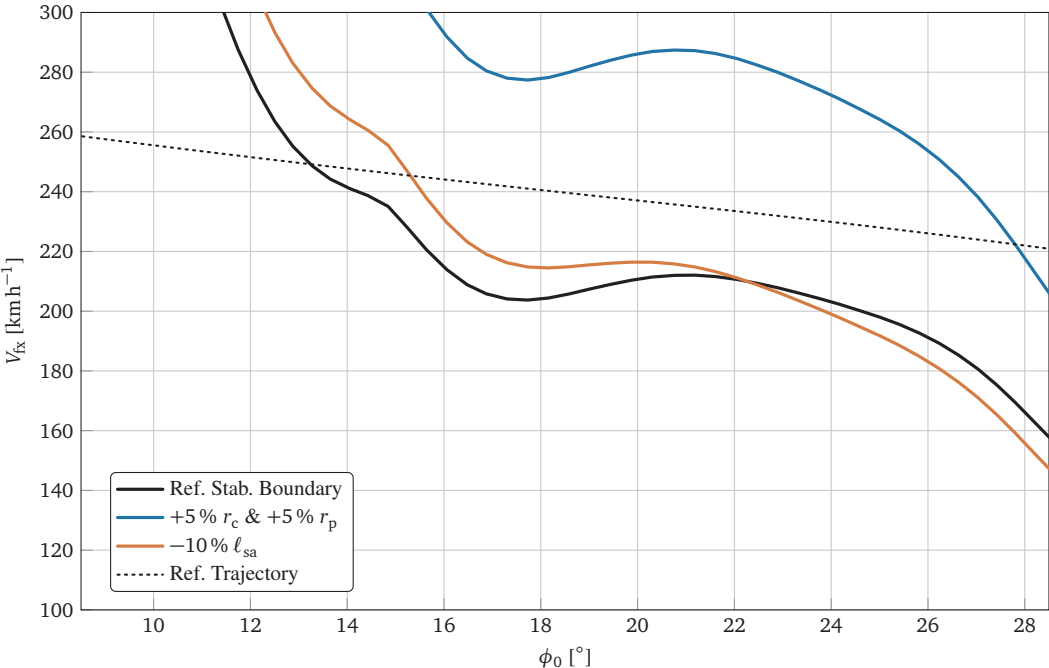


Figure 3.18: Driveline stability boundary with respect to forward speed V_{fx} and static roll angle ϕ_0 , along with some boundaries with altered parameter values to show effects on stability.

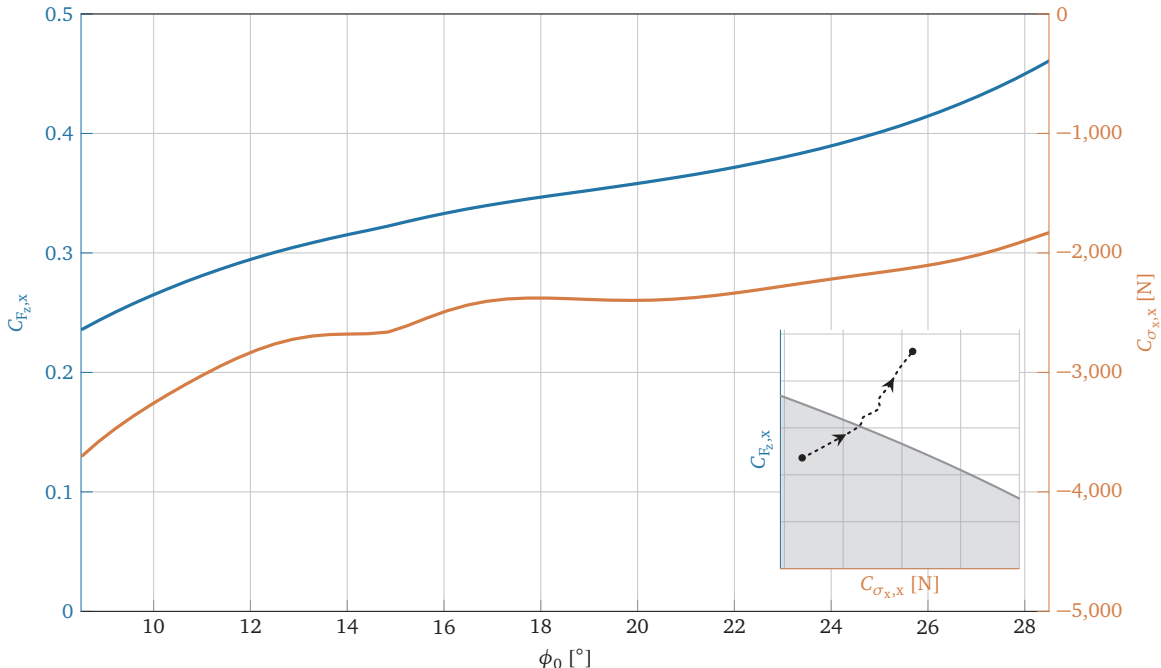


Figure 3.19: Tyre tangential force gradient parameters as a function of roll angle. Inset is the tyre gradient domain showing the stable region and the manoeuvre proceeding to unstable.

is the method by which increasing the roll angle ϕ indirectly destabilises the system. Further investigations into the effect of roll angle on system stability would require a more complete multi-body model, but the current results suggest that the two DOFs model presented by Sorrentino and Leonelli [2017] could be augmented to include a quasi-static roll angle parameter for increased accuracy during braking manoeuvres that include a motorcycle with roll angle.

3.4 Conclusions

In this chapter a new simplified model of the rear of a motorcycle was developed with a three DOFs framework that includes the lateral dynamics introduced by roll angle. This allows the expansion of previous works from straight braking investigation into more complex manoeuvres. The model is linearised about equilibrium values in a quasi-static braking region and linear methods such as eigensystem analysis, eigenvalue sensitivity, and Routh-Hurwitz stability criterion are used, as well as an energy flow analysis to detect sources of instability.

Results agree with those by Sorrentino and Leonelli [2017], showing an unstable driveline mode with a frequency of around 19 Hz. Instability arises from the longitudinal force affected by tyre force gradient parameters $C_{\sigma_x, x}$ and $C_{F_z, x}$ and the phase relationship between swingarm angle $\tilde{\alpha}$ and wheel speed $\dot{\theta}$ oscillations. Moreover, the novel findings with respect to the study by Sorrentino and Leonelli [2017] are:

- (i) The biggest factor to stability is the natural frequencies of the driveline and rear hop modes, parameters such as tyre vertical stiffness k_z , chain stiffness k_c , rear wheel mass m_{wh} , rear wheel inertia J_{why} , and rear sprocket radius r_c having the greatest effect.
- (ii) Stabilisation can also be achieved by reducing the chain to swingarm angle ψ , while the effect of the static value of swingarm angle α_0 is minimal when the chain to swingarm angle ψ is held constant.
- (iii) The out-of-plane dynamics do not play a role in the stability of the system, as supported by the eigenvectors and the energy flow analysis, but the static value of the roll angle ϕ_0 plays a significant role through its effect on the tyre force gradient parameters $C_{\sigma_x, x}$ and $C_{F_z, x}$, both of which move in a destabilising direction as roll angle is increased.

A summary of the findings of this chapter are highlighted in Table 3.2. The table lists different characteristics of the model and reviews their impacts on the chatter mode.

In the adopted model the effects of tyre relaxation have been considered negligible, as in other similar studies [Sorrentino and Leonelli 2017, Leonelli et al. 2018]. It should be recalled, however, that increasing the relaxation length to sufficiently high values would produce destabilising effects on the model, reducing the range of stability with respect to travelling speed [Catania et al. 2013]. An effect that can be explained considering that tyre relaxation influences the phase lag between the force and slip terms exchanged at the ground contact point and thus the energy flow, which is able to bring the system to critical condition. This effect is expanded on further in Chapter 4.

Also, for assessing the validity of the presented linear analysis in predicting stability, the post-bifurcation behaviour of the related nonlinear system should be investigated, focusing on bifurcation diagrams and existence of limit cycles. Results on the effects of nonlinear terms on this kind of self-excited oscillation is presented in Chapter 4. They show that the nonlinear system (at zero roll angle) has supercritical behaviour with a single stable limit cycle in the parameter domain of technological interest which grows with linearised instability, reinforcing that the linearised model is valid in predicting stability.

Chapter 5 investigates other quasi-static regions of the cornering manoeuvre, such as mid-corner and acceleration at high roll angle, using the minimal model and a multi-body model to analyse the stability of the rear swingarm system. These operating regions and the stability of the rear swingarm system within them are not yet studied in literature. The results here only explore a part of the potential of the developed model. Further, an augmentation could be made to the minimal model parameters to simulate a torsional DOF of the swingarm pivot and be used to investigate the swingarm torsional rigidity and its effects on stability.

Table 3.2: Summary of influential aspects on motorcycle chatter.

Model Characteristic	Impact on the Chatter Mode
Minimal model validity	When compared to a higher fidelity multi-body model, the minimal model was able to reproduce the behaviours of the driveline and rear hop modes in the operational domain of interest.
Energy analysis	The switching mechanism to instability is attributed to the phase lag between the tyre longitudinal slip velocity and longitudinal ground force. This arises from the eigenmode, but is exemplified by the tyre force gradients.
Parameter sensitivity	The three most influential groups of parameters are those that affect the system natural frequencies, the tyre force gradients, and chain geometry terms.
Tyre forces	The static tyre forces do not directly affect the system in a large way. Instead, the tyre force gradients, driven by the operating point on the tyre characteristic function, play a major role. In particular, the longitudinal force gradient with respect to longitudinal slip appears in the diagonal of the system damping matrix, and can drive the system to instability if it becomes negative.
Roll angle	Roll angle does not have a direct effect on system stability, though as more static roll angle is introduced, the operating point of the tyre characteristic function is driven to regions where the tyre force gradients cause instability.

4 Nonlinear Effects on Motorcycle Chatter

4.1 Introduction

To the best of the author's knowledge, an in-depth nonlinear analysis of the chatter phenomenon is missing in contemporary literature. It would be of great practical use to assess the criticality of the post-bifurcation behaviour. In the subcritical case, the motion could become unstable even in the linearly stable domain if a perturbation were to be large enough [Troger and Zeman 1984, Troger and Steindl 2012]. In this case, linear analysis would not be sufficient for assessing the stability of the motorcycle. In the supercritical case, the existence of a stable limit cycle in the linearly unstable domain might help in keeping the self-excited oscillation under control, if its amplitude were to be small enough.

This chapter looks to deepen the understanding of the nonlinear effects of tyre forces and chain geometry on motorcycle chatter. This also includes the contribution of tyre relaxation since this aspect has not been investigated in-depth in previous studies. A two DOFs minimal model is considered, according to those described by Sorrentino and Leonelli [2017] and Chapter 3 (considering a frozen roll angle in the latter). The model includes nonlinear terms due to geometry, the tyre characteristic function, and tyre relaxation. The linearised system stability analysis of Chapter 3 provides information about the onset of self-excited vibrations, and can be used to mitigate them in the design process, but nonlinear analysis can reveal more information about the system dynamics [Hagedorn et al. 2014].

Numerical time domain simulation is possible with the nonlinear forms of the EOMs, though it is limited in scope with respect to the nonlinear behaviour and the discovery of possible limit cycles [Lewis 2020]. Several techniques have therefore been proposed to investigate nonlinear systems, in particular their limit cycles and domains of attraction. These include classical averaging methods such as the Krylov-Bogoliubov method [Nayfeh and Mook 2004], the describing function method (a quasi-linearisation in the frequency domain) [Gelb and Vander Velde 1968, Somieski 2001], perturbation methods such as the centre-manifold theory [Troger and Steindl 2012] and the method of multiple scales [Nayfeh and Mook 2004], and the harmonic balance method [Nayfeh and Mook 2004, Lee et al. 2005, Lewis 2020].

In this chapter post-bifurcation behaviour is investigated in comparison to the linearised response first by means of numerical integration of the nonlinear EOMs, performed at stable, neutral, and unstable linear equilibria with different initial conditions. Attention is focused on the existence and stability of limit cycles. Next, a method is specifically developed to study the post-bifurcation behaviour and the existence of limit cycles by combining the harmonic balance method with Floquet theory. The aim is to understand under which conditions the results of the linear analysis are still valid and to identify the most influential parameters in limit cycle generation, their amplitude, and their stability. Section 4.2 contains a description of the adopted minimal model and methods of analysis, while in Section 4.3 the results of the stability analysis are presented and discussed.

4.2 Model Description and Solution Methods

A two DOFs minimal model representing the rear swingarm and wheel of a motorcycle is described, also including the nonlinear terms due to geometry, the tyre characteristic function and tyre relaxation. The methods adopted for the identification and approximation of limit cycles (a specific application of the harmonic balance method), and for studying their stability (Floquet theory applied to limit cycle perturbation) are also briefly described.

4.2.1 Minimal Model

The model adopted for the analysis is a minimal two DOFs planar model representing the rear swingarm and wheel of a motorcycle, derived from that presented in Chapter 3 and reduced by fixing the roll angle to zero. The model consists of an infinite inertia translating frame attached to which is a swingarm and wheel, including suspension and chain drive mechanisms. A representation of the model is shown in Figure 4.1.

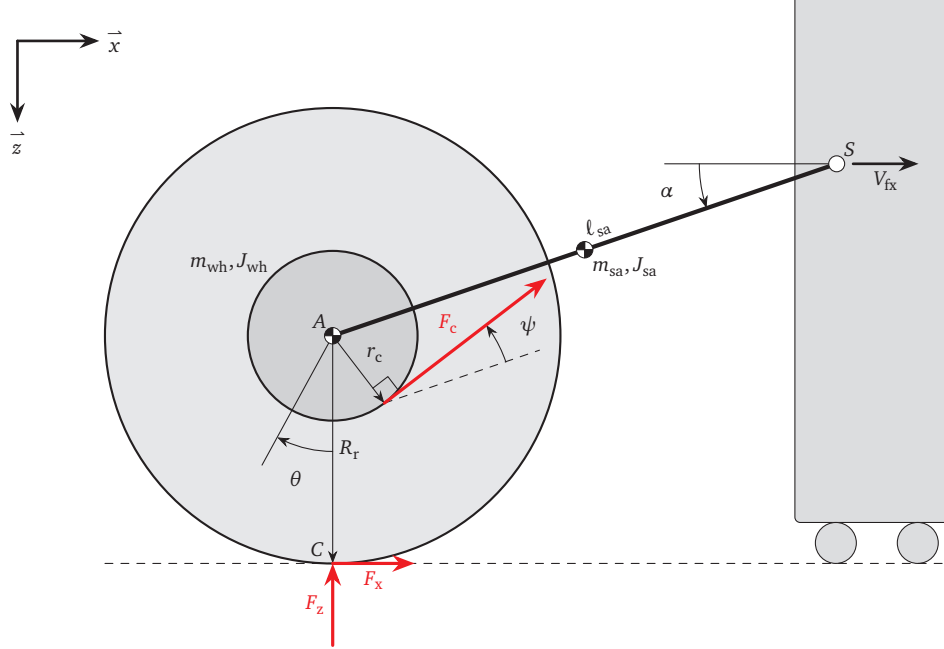


Figure 4.1: Schematic representation of the minimal two DOFs model.

The frame is translated at a constant speed V_{fx} across a flat surface and a braking force is applied to the wheel through the chain drive. The swingarm is represented by the line SA , with length ℓ_{sa} and an angle α of the revolute joint S . The distance from the swingarm pivot S to the ground is z_{sa} . The equivalent moment of inertia of the swingarm and wheel assembly about the axis of pivot S is J_a . At point A there is another revolute joint to which the wheel is connected, including the rim, tyre, and rear sprocket, with moment of inertia J_{why} about the joint axis. The outer radius of the unloaded wheel is R_r , which in the adopted model also approximates its free rolling radius. The motion of the rim is described by the revolute joint angle θ , which breaks sign convention and is aligned along the negative y -axis, so that wheel rotation is positive with motion in the forward x -direction. The model states are swingarm angle α , wheel rotation θ , and their time derivatives.

The tyre vertical load F_z is modelled by a vertical spring, while the longitudinal force F_x is modelled by a characteristic function of the tyre given by the pure longitudinal MF [Pacejka 2012], as defined by Besselink et al. [2010]. Using the longitudinal slip coefficient κ and semi-empirical coefficients B_x , C_x , D_x , E_x depending on the vertical load F_z , the function is given as:

$$F_z(\alpha) = k_z(z_{sa} - \ell_{sa} \sin(\alpha) - R_r) \quad (4.1)$$

$$\kappa(\dot{\alpha}, \dot{\theta}, \alpha) = - \left(1 - \frac{R_r \dot{\theta}}{V_{fx} + \ell_{sa} \dot{\alpha} \sin(\alpha)} \right) \quad (4.2)$$

$$F_x(\dot{\alpha}, \dot{\theta}, \alpha) = D_x \sin \left(C_x \arctan \left(B_x \kappa - E_x (B_x \kappa - \arctan(B_x \kappa)) \right) \right) \quad (4.3)$$

with

$$B_x = \frac{F_z(\alpha)}{C_x D_x} (p_{kx1} + p_{kx2} \Delta_{F_z}) e^{p_{kx3} \Delta_{F_z}} \quad (4.4)$$

$$C_x = p_{cx1} \quad (4.5)$$

$$D_x = F_z(\alpha) (p_{dx1} + p_{dx2} \Delta_{F_z}) \quad (4.6)$$

$$E_x = p_{ex1} + p_{ex2} \Delta_{F_z} + p_{ex3} \Delta_{F_z}^2 \quad (4.7)$$

$$\Delta_{F_z} = \frac{F_z(\alpha) - F_{z0P}}{F_{z0P}} \quad (4.8)$$

where p_{ijk} and F_{z0P} are MF parameters given in Table 4.1. The developed model does not account for wheel detachment during oscillation, which requires the monitoring of the sign of F_z during simulations. The relaxation behaviour of the tyre is not introduced at this stage, as it is addressed separately in Subsection 4.2.2.

Table 4.1: Magic Formula parameter values used in the nonlinear chapter.

Parameter	Unit	Value
F_{z0P}	N	600
p_{cx1}	–	1.32
p_{dx1}	–	1.90
p_{dx2}	–	-0.186
p_{ex1}	–	1.03×10^{-3}
p_{ex2}	–	-9.00×10^{-4}
p_{ex3}	–	5.37×10^{-4}
p_{kx1}	–	22.0
p_{kx2}	–	2.18×10^{-4}
p_{kx3}	–	-0.149

Using Equation (4.1)–(4.3) and the chain equations given in Subsection 3.2.1, the two nonlinear EOMs can be written in the following form:

$$J_\alpha \ddot{\alpha} + c_s \dot{\alpha} + k_s (\alpha - \alpha_{s0}) = (\ell_{sa} \cos(\alpha)) F_z(\alpha) + (\ell_{sa} \sin(\alpha)) F_x(\dot{\alpha}, \dot{\theta}, \alpha) + M_{c\alpha}(\alpha, \theta) \quad (4.9)$$

$$J_\theta \ddot{\theta} = - (z_{sa} - \ell_{sa} \sin(\alpha)) F_x(\dot{\alpha}, \dot{\theta}, \alpha) + M_{c\theta}(\alpha, \theta) \quad (4.10)$$

where k_s and c_s are the equivalent rotational stiffness (with preload angle α_{s0}) and damping coefficients of the suspension, acting on the joint S . In Equation (4.9) and (4.10) the contribution of the weight of swingarm and wheel is omitted since it is found to be negligible. The three sources of nonlinearities that are represented in Equation (4.9) and (4.10) are:

- (i) The tyre forces, due to F_x terms.
- (ii) Geometry, due to F_z terms (not present in the second equation).
- (iii) The chain, due to $M_{c\alpha}$ and $M_{c\theta}$ terms.

Due to very small oscillation amplitudes of the swingarm (see limit cycles in Subsection 4.3.3 and 4.3.5), the suspension spring is assumed to be linear as well as the suspension damper (see the characteristic function reported by Cattabriga et al. [2021], for a similar problem).

The steady state equilibrium of the nonlinear system is determined by taking as inputs the tyre longitudinal slip κ_0 and vertical load F_{z0} , in fact the stationary working point on the characteristic function of the tyre, as well as the constant travelling speed V_{fx} and the equilibrium swingarm angle α_0 . Then all the other parameters are sequentially computed as follows:

$$\omega_0 = \dot{\theta}_0 = \frac{V_{fx}}{R_r} (\kappa_0 + 1) \quad (4.11)$$

$$\omega_p = \omega_0 \frac{r_c}{r_p} \quad (4.12)$$

$$z_{sa} = (\ell_{sa} \sin(\alpha_0) + R_r) + \frac{F_{z0}}{k_z} \quad (4.13)$$

$$\theta_0 = (\ell_{sa} \sin(\alpha_0) - z_{sa}) \frac{F_{x0}}{r_c^2 k_c} \quad \text{with} \quad F_{x0} = F_x(\kappa_0, F_{z0}) = F_x(0, \omega_0, \alpha_0) \quad (4.14)$$

$$\alpha_{s0} = \alpha_0 - \frac{1}{k_s} \left((\ell_{sa} \cos(\alpha_0)) F_{z0} + (\ell_{sa} \sin(\alpha_0)) F_{x0} - k_c r_c \theta_0 \ell_{sa} \sin(\psi(\alpha)) \right) \quad (4.15)$$

where $\psi(\alpha)$ is given by Equation (3.33). The EOMs (4.9) and (4.10) are then expanded in a Taylor series up to the third order about the equilibrium point $(0, \omega_0, \alpha_0, \theta_0)$, considering the following perturbations of the steady state equilibrium:

$$\alpha(t) = \alpha_0 + \tilde{\alpha}(t) \quad (4.16)$$

$$\dot{\alpha}(t) = \dot{\tilde{\alpha}}(t) \quad (4.17)$$

$$\ddot{\alpha}(t) = \ddot{\tilde{\alpha}}(t) \quad (4.18)$$

$$\theta(t) = \theta_0 + \omega_0 t + \tilde{\theta}(t) \quad (4.19)$$

$$\dot{\theta}(t) = \omega_0 + \dot{\tilde{\theta}}(t) \quad (4.20)$$

$$\ddot{\theta}(t) = \ddot{\tilde{\theta}}(t) \quad (4.21)$$

resulting in a nonlinear system with polynomial nonlinearities in the variables $\tilde{\alpha}(t)$, $\tilde{\theta}(t)$, and their time derivatives. The explicit time term in the $\theta(t)$ equation is there to remove the cyclic variable from the expanded equations, and this explicit time is cancelled in the EOMs when considering Equation (3.24) and (4.12). Two sets of differential equations are therefore created from the minimal model: the first is a linearised system about equilibrium conditions, while the second uses the nonlinear equations expanded in a Taylor series. The states are referenced to the equilibrium conditions, so that the output gives oscillations about zero.

Values for the model reference parameters are taken to be the same as those presented in Section 3.2, while the equilibrium conditions are chosen to be sufficiently close to the stability boundary so that the stability of the system is easily modified by slight changes in reference speed V_{fx} . The equilibrium value of F_{z0} is also chosen to be sufficiently large in an attempt to avoid wheel lift, which is not accounted for in the present model. The adopted values are reported in Table 4.2.

Table 4.2: Model parameters and equilibrium values.

(a) Model parameters.			(b) Equilibrium values.		
Parameter	Unit	Value	Parameter	Unit	Value
β_p	rad	0.12	α_0	rad	0.237
J_α	kg m ²	7.54	α_{s0}	rad	0.260
J_{why}	kg m ²	0.85	θ_0	rad	8.11×10^{-3}
R_r	m	0.33	κ_0	–	–0.035
c_s	N m s rad ⁻¹	353	ω_0	rad s ⁻¹	129
k_c	N m ⁻¹	1.15×10^6	ω_p	rad s ⁻¹	310
k_s	N m rad ⁻¹	1.51×10^4	F_{x0}	N	–305
k_z	N m ⁻¹	1.70×10^5	F_{z0}	N	–400
ℓ_p	m	0.08	V_{fx}	m s ⁻¹	44.0
ℓ_{sa}	m	0.65	z_{sa}	m	0.480
r_c	m	0.1036			
r_p	m	0.043			

4.2.2 Tyre Relaxation Model

To properly account for the evolution of the ground force F_x during transients, a relaxation model must be added to the EOMs (4.9) and (4.10). In the specific case of this chapter, the focus is on the system transient following a perturbation from a stationary equilibrium point at $F_x = F_{x0}$. More generally, deriving reliable models for describing the evolution of tyre forces during transients is considered an extremely difficult problem [Guiggiani 2018], and the results of any new model should be assessed through appropriate experimental campaigns. Here, however, a simplified and well established approach is adopted, consisting of a single contact point model describing the transient behaviour of the longitudinal slip velocity (say V_{sx} , and consequently the longitudinal slip coefficient κ), developed relying on the viscoelastic Maxwell model [Pacejka 2012].

As with the previous literature, the formulation starts by considering the evolution of the system under a constant vertical load, in this case obtained by considering a frozen value at the stationary equilibrium point ($F_z = F_{z0}$). Without relaxation, as in Subsection 4.2.1, the model can be analogously represented by a single Newton element (viscous damper). See Figure 4.2a for an outline of the steady state description. The model with relaxation is then

obtained by adding a spring in series with the damper, yielding the Maxwell model as represented in Figure 4.2b. Referring to the schematic and to the nomenclature reported in Figure 4.2b, the Maxwell model is defined according to two sets of equations. The first are congruence equations for displacement:

$$u = u_{\text{damp}} + u_{\text{stiff}} \quad (4.22)$$

$$\dot{u} = -V_{\text{sx}} = \dot{u}_{\text{damp}} + \dot{u}_{\text{stiff}} \quad (4.23)$$

$$\dot{u}_{\text{stiff}} = V_{\text{sxr}} - V_{\text{sx}} \quad (4.24)$$

where $V_{\text{sxr}} = -\dot{u}_{\text{damp}}$. The second of equations are the dynamic equilibrium equations:

$$F_x = F_{\text{damp}} = F_{\text{stiff}} \quad (4.25)$$

$$F_x(V_{\text{sxr}}, F_{z0}) = Ku_{\text{stiff}} \quad (4.26)$$

where K represents the tyre contact point longitudinal stiffness and V_{sxr} is the longitudinal slip velocity of the massless contact point C in Figure 4.2b, affected by relaxation denoted with subscript r .

Introducing the longitudinal slip coefficients and their derivatives (including time dependent travelling speed V_x at the wheel centre):

$$\kappa = -\frac{V_{\text{sx}}}{V_x} \quad (4.27)$$

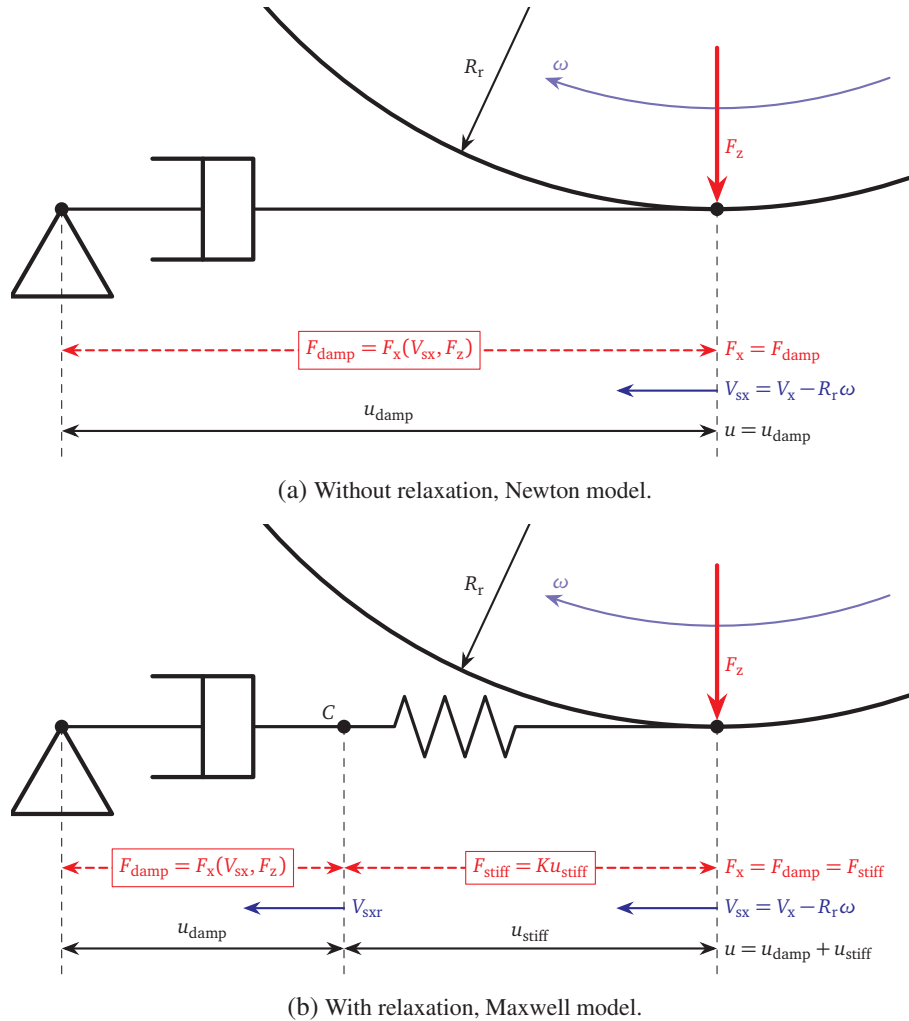


Figure 4.2: Longitudinal ground force transient model.

$$\kappa_r = -\frac{V_{sxr}}{V_x} \quad (4.28)$$

$$\dot{\kappa}_r = -\frac{\dot{V}_{sxr}}{V_x} + \frac{V_{sxr}\dot{V}_x}{V_x^2} \quad \text{with } V_x > 0 \quad (4.29)$$

as well as the definition of the gradient of the tyre characteristic function with respect to slip (in non-stationary and stationary conditions):

$$C_{\kappa,x} = \left. \frac{\partial F_x}{\partial \kappa} \right|_{(\kappa, F_z)} \quad (4.30)$$

$$C_{\kappa 0,x} = \left. \frac{\partial F_x}{\partial \kappa} \right|_{(\kappa_0, F_{z0})} \quad (4.31)$$

$$C_{\kappa_r,x} = \left. \frac{\partial F_x}{\partial \kappa_r} \right|_{(\kappa_r, F_z)} \quad (4.32)$$

and combining these with Equation (4.24) and (4.26), yields the well known relaxation equation for the transient longitudinal slip κ_r , which in its linearised form can be written as:

$$\frac{\lambda_{x0}}{V_{x0}} \dot{\kappa}_r + \kappa_r = \kappa \quad \text{with } \lambda_{x0} = \frac{C_{\kappa 0,x}}{K(F_{z0})}, \quad V_{x0} > 0 \quad (4.33)$$

where the parameter λ_{x0} is known as longitudinal relaxation length of the tyre, and V_{x0} is the stationary value of V_x . Equation (4.33) approaches steady state as either V_{x0} approaches infinity or λ_{x0} approaches zero, which occurs when the stiffness of the relaxation spring $K(F_{z0})$ approaches infinity (as shown in Figure 4.2a), but also when the tyre partial derivative with respect to κ_0 approaches zero (as when peak force is achieved).

The inclusion of a non-stationary term $F_z(t)$ in the model is a more delicate matter. In this case, it is no longer sufficient to determine unequivocally $F_x(t)$, being that $F_z(t)$ is a second input to the model. Consequently, the Maxwell model alone (which has one DOF) is no longer able to represent the full dynamics of $F_x(t)$. It can only produce a partial representation by describing the evolution of the slip velocity (in terms of V_{sxr} or κ_r) during transients. Referring again to Figure 4.2b, this means that u_{damp} is independent with respect to F_z , as well as u , which represents the actual input of the system in terms of slip velocity. Hence also u_{stiff} must be independent from the vertical load. Then, by respecting the equilibrium of forces in Equation (4.26), F_{stiff} must depend on the vertical load, which in turn, implies that the stiffness coefficient K must be a function of $F_z(t)$. According to recent MF developments [Delft-Tyre 2013], the dependency of K on vertical load is defined as:

$$K = K_0(1 + p_{cfx1}\Delta_{F_z} + p_{cfx2}\Delta_{F_z}^2) \quad (4.34)$$

where the constant terms are given in Table 4.3, and Δ_{F_z} is defined by Equation (4.8). Therefore in the Maxwell model F_{damp} is a damping force now assumed to be generated by a nonlinear, parametric damper (with respect to time dependent vertical load) given by the characteristic function of the tyre Equation (4.26), while F_{stiff} is an elastic force represented by separation of variables in terms of u_{stiff} and of a parametric spring with stiffness $K(F_z)$.

Table 4.3: Magic Formula relaxation length parameter values.

Parameter	Unit	Value
K_0	N m^{-1}	1.48×10^5
p_{cfx1}	–	0.152
p_{cfx2}	–	0.378
λ_{x0}	m	0.053

Based on this premise, a novel and more general formulation than that given in Equation (4.33) can now be derived, valid for both small slip values (linear conditions) and large slip values (nonlinear conditions). Recalling

Equation (4.24) and (4.26) yields:

$$\begin{cases} \dot{u}_{\text{stiff}} = V_{\text{sxr}} - V_{\text{sx}} \\ F_x(V_{\text{sxr}}, F_{z0}) = K(F_z)u_{\text{stiff}} \end{cases} \implies \frac{\dot{F}_x}{K} - \frac{F_x \dot{K}}{K^2} = V_{\text{sxr}} - V_{\text{sx}} \quad (4.35)$$

where the visual dependency on states is dropped for brevity, but are still implied. Then, using the chain rule the derivatives can be expanded to their partials and state derivatives without loss of generality:

$$\dot{F}_x = C_{V_{\text{sxr}},x} \dot{V}_{\text{sxr}} + C_{F_z,x} \dot{F}_z \quad (4.36)$$

$$\dot{K} = C_K \dot{F}_z \quad (4.37)$$

with

$$C_{V_{\text{sxr}},x} = \left. \frac{\partial F_x}{\partial V_{\text{sxr}}} \right|_{(\kappa_r, F_z)} = -\frac{C_{\kappa_r,x}}{V_x} \quad (4.38)$$

$$C_{F_z,x} = \left. \frac{\partial F_x}{\partial F_z} \right|_{(\kappa_r, F_z)} \quad (4.39)$$

$$C_K = \frac{\partial K}{\partial F_z} \quad (4.40)$$

Introducing Equation (4.36)–(4.40) into Equation (4.35) and rearranging for V_{sxr} and F_z gives:

$$\frac{C_{V_{\text{sxr}},x}}{K} \dot{V}_{\text{sxr}} - V_{\text{sxr}} + \left(\frac{C_{F_z,x}}{K} - \frac{C_K}{K^2} F_x \right) \dot{F}_z = -V_{\text{sx}} \quad (4.41)$$

From here, focus is drawn to the \dot{F}_z term and the difference within the brackets. Starting from Equation (4.26) and its partial derivative with respect to F_z , the following equality is found:

$$C_{F_z,x} = C_K u_{\text{stiff}} = \frac{C_K}{K} F_x \quad (4.42)$$

From this, the bracketed term in Equation (4.41) is determined to be zero, and the explicit dependency on vertical load vanishes from the relaxation equation, which leaves:

$$\frac{C_{V_{\text{sxr}},x}}{K} \dot{V}_{\text{sxr}} - V_{\text{sxr}} = -V_{\text{sx}} \quad (4.43)$$

Recalling now the definitions given in Equation (4.27)–(4.29) and (4.38), a novel relaxation equation valid for general nonlinear transients can be finally written in terms of the transient slip variable κ_r as:

$$\frac{\lambda_x}{V_x} \dot{\kappa}_r + \left(1 + \frac{\lambda_x \dot{V}_x}{V_x^2} \right) \kappa_r = \kappa \quad \text{with} \quad \lambda_x = \frac{C_{\kappa_r,x}}{K}, \quad V_x > 0 \quad (4.44)$$

where λ_x is a generalised state dependent representation of the relaxation length.

The limit cases for Equation (4.44) are the same as described for Equation (4.33), and the effects of system speed variations can be seen in the latter term of the equation. The model is sensitive to instantaneous variations of tyre vertical load through parametric dependency of λ_x , even though F_z has explicitly vanished from the relaxation equation. This is logical, since Equation (4.44) descends from the Maxwell model where the dependency on F_z is parametric only, as discussed previously. However, it should be mentioned here that in some studies, explicit dependency on F_z appears even in the linear model in terms of first derivative with respect to time [Pacejka 2012]. The vertical load comes into play explicitly when considering the transient longitudinal force due to κ_r , say F_{xr} , which can be evaluated by using the characteristic function of the tyre again:

$$F_{\text{xr}} = F_x(\kappa_r, F_z) \quad (4.45)$$

which represents a widely adopted solution both in practice and in the scientific literature [Pacejka 2012].

Introducing into Equation (4.45) the transient slip coming from the linear time invariant (LTI) relaxation model, Equation (4.33), and linearising F_x yields a linear transient model for F_{xr} . Introducing the same transient slip into the nonlinear characteristic function of the tyre yields the ‘semi-nonlinear’ model [Pacejka 2012]. While a ‘fully nonlinear’ model is obtained introducing into Equation (4.45) the transient slip coming from the relaxation model, Equation (4.44).

In the fully linearised problem, Equation (4.44) reduces exactly to the form of Equation (4.33), since the term related to system speed variations vanishes. It should also be noted that the model in Equation (4.33) is not sensitive to non-stationary values of F_z since the relaxation length λ_{x0} only depends on the stationary equilibrium point.

Regarding the LTI model, if κ is described by a FRF, then Equation (4.33) can be represented in the frequency domain according to:

$$\hat{\kappa}_r(\Omega) = H(\Omega)\hat{\kappa}(\Omega) \quad (4.46)$$

$$|H| = \frac{1}{\sqrt{1 + \left(\frac{\lambda_{x0}}{V_{x0}}\Omega\right)^2}} \quad (4.47)$$

$$\tan(\vartheta) = -\frac{\lambda_{x0}}{V_{x0}}\Omega \quad (4.48)$$

with the following asymptotic values:

$$\Omega \rightarrow 0 \quad \text{or} \quad V_{x0} \rightarrow \infty \quad \text{or} \quad \lambda_{x0} \rightarrow 0 \quad \implies \quad \begin{cases} |H| \rightarrow 1 \\ \vartheta \rightarrow 0 \end{cases} \quad (\text{no relaxation}) \quad (4.49)$$

$$\Omega \rightarrow \infty \quad \implies \quad \begin{cases} |H| \rightarrow 0 \\ \vartheta \rightarrow -\frac{\pi}{2} \end{cases} \quad (4.50)$$

where both attenuation and phase lag increase with the angular frequency Ω .

4.2.3 Numerical Simulations

The full nonlinear form of the EOMs (4.9) and (4.10) are first solved using typical ordinary differential equation numerical methods, in this case an explicit Runge-Kutta method. The equilibrium conditions presented in Table 4.2b represent a braking manoeuvre and are near the stability boundary for the driveline mode. This allows the stability of the system to be easily modified by slight changes in reference speed V_{fx} . Different sets of numerical simulations are run at slightly stable, equilibrium, and slightly unstable points, and these are run for enough time to determine the presumed asymptotic behaviour of the nonlinear model. Additionally, different state disturbances are used at these points to look for any sensitivities to varying initial conditions. A sample of an unstable numerical simulation with a disturbance in wheel speed is shown in Figure 4.3. It is found that the nonlinear system is not sensitive to which state is disturbed, and that a supercritical limit cycle exists during unstable behaviour. Therefore, in the sequel, only the unstable simulations with a wheel speed initial disturbance are used.

Figure 4.3 shows a time span late in the simulation since during the initial response both models respond in a very similar manner. Only after the oscillations begin to grow large do the behaviours of the two split, with the linear system growing exponentially and the response of the nonlinear system flattening out. The behaviour of the nonlinear system looks to be asymptotic towards a limit cycle. Although this cannot be proven numerically, in this chapter the behaviour is assumed to be a limit cycle when simulated to a sufficiently long time period.

To test the significance of the individual nonlinear terms, the nonlinear equation of each term is systematically introduced into the linearised system. This is achieved by a first order linearisation of the other nonlinear terms about the equilibrium conditions, while keeping the terms of interest in the nonlinear form. This allows for a relatively similar system to the proven linear method, with the nonlinearities introduced one at a time, giving insight into which terms are important to the asymptotic behaviour.

Finally, a study of the sensitivities to modelling parameters is achieved by selecting certain important parameters, identified as described above and from the linear analysis of Chapter 3, and modifying their values. This results in a change in asymptotic behaviour, notably limit cycle amplitude, but also a change in stability in the linear sense. Therefore, both the linear and nonlinear systems are modified and simulated, the former providing the real part of

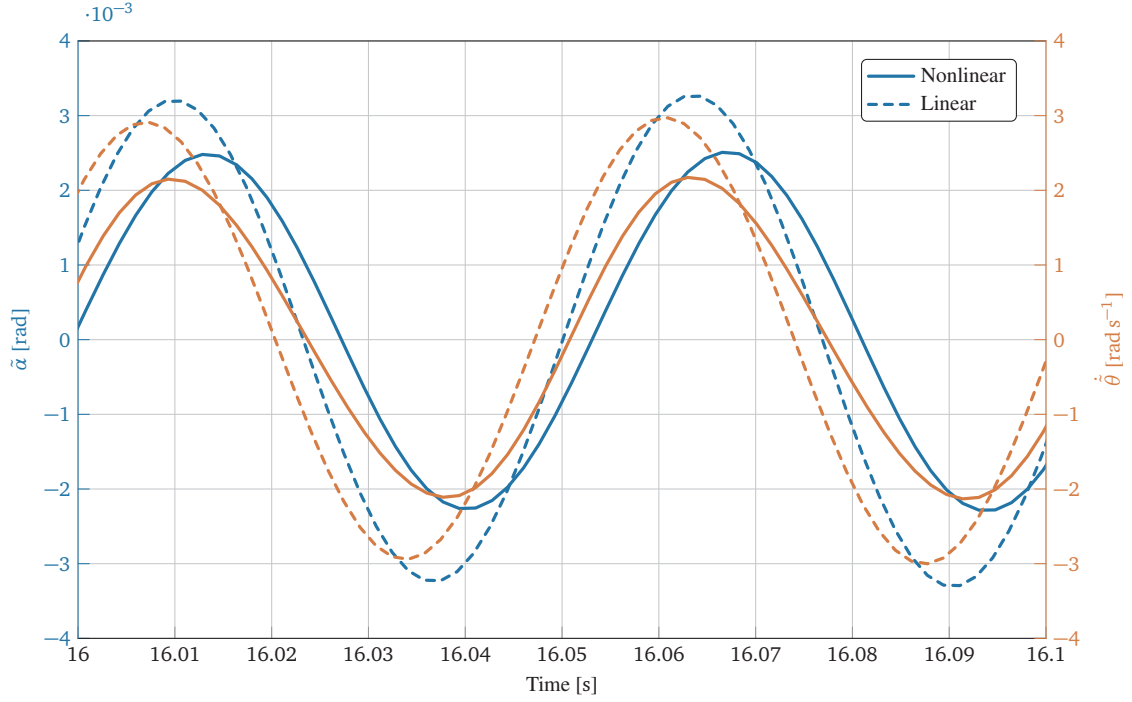


Figure 4.3: Sample of numerical simulation, showing state variables.

the driveline mode eigenvalue to detect changes in outright stability, and the latter providing insights into changes in the asymptotic behaviour.

4.2.4 Limit Cycle Identification

To identify limit cycles and find their analytic solutions, several methods are attempted. A good overview of the available methods are presented by Nayfeh and Mook [2004]. For each of these methods, typically, fairly simple nonlinearities are required such as polynomials, single trigonometric functions, and so forth. For this reason, the nonlinear EOMs (4.9) and (4.10) are expanded in a Taylor series approximation to the third order containing both even and odd nonlinear polynomial terms.

At first, the method of multiple scales is used on the Taylor expanded system. Being a two DOFs system makes the problem a fourth order problem, leading to quite large unwieldy time scale equations to which suitable solutions could not be found. Based on numerical results (described later in Subsection 4.3.2), the system is further simplified by removing all but the single biggest contributor to nonlinearities, giving the following simplified second order nonlinear coupled system:

$$M\ddot{q} + C\dot{q} + Kq = \begin{bmatrix} N_1 \\ -N_2 \end{bmatrix} \alpha \dot{\theta} \quad (4.51)$$

where M , C , and K are the linearised matrices of the EOMs (4.9) and (4.10), and $N_{1,2}$ are positive coupling parameters arising from the nonlinear model. Unfortunately, expanding these equations using the method of multiple scales led only to trivial solutions, in part due to the existence of only even terms.

Next, the ‘describing function’ method is applied to the Taylor expanded system. It is found to be difficult to apply such a method to a system of many coincident nonlinearities, in this case many different even and odd polynomial terms, since a different integral function is required for each term. Moreover, the method becomes fairly complicated when investigating higher order harmonics, even if only odd terms are considered. The method is better suited to systems with a single harmonic and in which the linear part acts as a low pass filter. In the case under study, the method produces many non-physical or spurious solutions, with no simple strategy for detecting and removing them.

Finally, successful approximations of the limit cycle solutions are found using the harmonic balance method [Nayfeh and Mook 2004, Hayes and Marques 2015, Lewis 2020]. The adopted numerical procedure is divided into two steps: the first part of the computational algorithm yields a set of first-approximation solutions. Then a refinement procedure is adopted for discarding redundant and spurious solutions, and for improving the accuracy of the solutions of interest. Differently to the techniques proposed for instance by Nayfeh and Mook [2004] and Lewis [2019] (perturbations and integro-differential equations), here the harmonic balance method is adopted also for the refinement procedure. Given the following autonomous homogeneous system of n second order ordinary differential equations with constant coefficients and nonlinear terms in polynomial form:

$$\begin{cases} m\ddot{x}_1 + p_1(x_1, x_2, \dots, x_n, \dot{x}_1, \dot{x}_2, \dots, \dot{x}_n) = 0 \\ m\ddot{x}_2 + p_2(x_1, x_2, \dots, x_n, \dot{x}_1, \dot{x}_2, \dots, \dot{x}_n) = 0 \\ \vdots \\ m\ddot{x}_n + p_n(x_1, x_2, \dots, x_n, \dot{x}_1, \dot{x}_2, \dots, \dot{x}_n) = 0 \end{cases} \quad (4.52)$$

the existence of periodic solutions, that is:

$$\mathbf{x}(t) = \mathbf{x}(t + kT) \quad \text{where} \quad \mathbf{x}(t) = \{x_1, x_2, \dots, x_n\}^T, \quad k \in \mathbb{Z}, \quad T \in \mathbb{R} \quad (4.53)$$

where T is the period of the limit cycle, are sought by expanding each component in a Fourier series up to N harmonics:

$$x_i = \sum_{h=0}^N (A_{ih} \sin(h\Omega t) + B_{ih} \cos(h\Omega t)), \quad i = 1, \dots, n \quad (4.54)$$

where $\Omega = 2\pi/T$ is the angular frequency of the (approximated) limit cycle. The periodic approximated solutions given by Equation (4.54) are substituted into Equation (4.52), where applying the sum and difference formulae to the products of trigonometric functions, and collecting and equating to zero the terms with the same simple trigonometric functions, yields an algebraic nonlinear system. This system is in general non-homogeneous, and consists of $n(2N + 1) + 1$ equations in $n(2N + 1) + 1$ unknowns represented by the $n(2N + 1)$ coefficients in the truncated Fourier series, and the angular frequency Ω :

$$\begin{cases} P_1(A_{1h}, \dots, A_{nh}, B_{10}, \dots, B_{n0}, B_{1h}, \dots, B_{nh}, \Omega) = 0 \\ P_2(A_{1h}, \dots, A_{nh}, B_{10}, \dots, B_{n0}, B_{1h}, \dots, B_{nh}, \Omega) = 0 \\ \vdots \\ P_{n(2N+1)}(A_{1h}, \dots, A_{nh}, B_{10}, \dots, B_{n0}, B_{1h}, \dots, B_{nh}, \Omega) = 0 \\ P_{n(2N+1)+1}(A_{1h}, \dots, A_{nh}, B_{10}, \dots, B_{n0}, B_{1h}, \dots, B_{nh}, \Omega) = 0 \end{cases}, \quad h = 1, \dots, N \quad (4.55)$$

It should be noted that in Equation (4.55) the terms with angular frequency higher than $N\Omega$ are discarded, and that the last equation is not a result of the harmonic balance, which in fact only yields $n(2N + 1)$ equations. This final equation can be written as linear combination of any of the EOMs (4.9) and (4.10), expanded including Equation (4.54) and evaluated at a given instant of time $t = t_0$. In this case the simplest possibility is given by considering a single equation at $t = 0$, provided it does not reduce to an identity.

The system in Equation (4.55) may be solved directly, yielding the total number of real solutions (limit cycles) for a given number of harmonic terms in the Fourier expansion. However, systems with several nonlinear terms or high order Taylor expansions can easily lead to prohibitively large computational loads. Consequently, a different approach is adopted here. Roots are computed in succession by means of an iterative algorithm considering Fourier expansions limited to the first harmonic term. In this case a single state variable is approximated by:

$$x_i^{(1)} = B_{i0} + A_{i1} \sin(\Omega t) + B_{i1} \cos(\Omega t) \quad (4.56)$$

This part of the computational algorithm yields a set of first harmonic approximate solutions, including bias and first harmonic components. Then a refinement procedure is adopted for discarding redundant and spurious solutions, and for improving the accuracy of the actual solutions of interest for the analysis.

The selected iterative procedure is initialised by assuming intervals of maximum variation for the A_{i1} coefficients as well as for the angular frequency $\Omega = \omega_i$, while the B_{i0} coefficients are initialised with arbitrarily small values, and the B_{i1} coefficients can be initialised to zero without loss of generality:

$$\begin{cases} I_{i1}^A = [-a_{i1}, a_{i1}] \\ I_1^\Omega = (0, \omega_1] \\ B_{i0} = \epsilon_{i1} \\ B_{i1} = 0 \end{cases}, \quad a_{i1} > 0, \quad \omega_1 > 0, \quad 0 < \epsilon_{i1} \ll a_{i1}, \quad i = 1, \dots, n \quad (4.57)$$

The initialisation intervals are then partitioned to determine sets of initial values for the iterative procedure. For each set of initial values, a single solution is sought by iterative solving of a system of $3n + 1$ equations with $3n + 1$ unknowns (ω_1, B_{i0}, A_{i1} , and $B_{i1}, i = 1, \dots, n$). The total number of solutions is not known in advance, therefore some of them may be multiples while others may be immediately recognised as spurious and discarded.

At this stage, a second step in the iterative procedure yields the desired refinement in a selected solution. This refinement procedure consists of a perturbation of the previously obtained solution (approximated to the first harmonic term) by an arbitrary number of higher harmonic terms. For example, a perturbation including the second harmonic term requires the following initialisation step:

$$\begin{cases} A_{i1} = A_{i1}^*, \quad B_{i0} = B_{i0}^*, \quad B_{i1} = B_{i1}^*, \quad \Omega = \Omega^* \\ I_{i2}^A = [-a_{i2}, a_{i2}] \\ B_{i2} = 0 \end{cases}, \quad a_{i2} > 0, \quad i = 1, \dots, n \quad (4.58)$$

where $A_{i1}^*, B_{i0}^*, B_{i1}^*$, and Ω^* are the $3n + 1$ values computed in the first step of the iterative procedure. The computation can follow sequentially, by adding a further harmonic terms with each step. However, if the first harmonic term is dominant, the refinement of the solution can be obtained in a single step by adding together a given number of harmonic terms.

The described refinement procedure can identify both redundant and spurious solutions. Redundant solutions are identified when two different first approximation solutions converge to the same refined solution. Spurious solutions are identified when either:

- (i) A first approximation solution converges to a degenerate solution (limit cycle with either null amplitude or zero frequency).
- (ii) The refinement procedure yields a non-convergent series, which therefore cannot represent a limit cycle.
- (iii) A third method for the identification of spurious solutions, based on an application of Floquet theory, is suggested at the end of the following Subsection 4.2.5.

According to the procedure described above, the existence of limit cycles can be assessed and eventually confirmed by phase portraits. Then the limit cycles of interest can be studied in terms of their amplitude, frequency, and shape.

4.2.5 Limit Cycle Stability

Stability of limit cycles is studied by applying Floquet analysis, which has been proven to be effective in both supercritical and subcritical post-bifurcation behaviour, for both stable and unstable limit cycles [Lewis 2019]. Once a limit cycle has been identified and approximated, its stability can be assessed by considering again the nonlinear homogeneous system given in Equation (4.9) and (4.10), which can be rewritten in the following compact form:

$$I\ddot{\mathbf{q}} + \mathbf{f}(\dot{\mathbf{q}}, \mathbf{q}) = \mathbf{0} \quad (4.59)$$

where \mathbf{q} is the vector of the two system variables α and θ , and \mathbf{f} is a vector of the nonlinear polynomial functions of system variables. Note that nonlinear terms due to inertial effects, such as those due to the time derivative of V_x in Equation (4.44), are neglected in Equation (4.59) for simplicity. However, they could be included in the adopted procedure and formulation considering the nonlinear relaxation model by augmenting the equations with a nonlinear inertial term.

Any approximated limit cycle must respect the following equation:

$$I\dot{\boldsymbol{\eta}} + \mathbf{f}(\dot{\boldsymbol{\eta}}, \boldsymbol{\eta}) = \boldsymbol{\varepsilon} \quad (4.60)$$

where $\boldsymbol{\eta}$ is a vector of real periodic functions of time t representing an approximation of the exact limit cycle:

$$\boldsymbol{\eta} = \begin{Bmatrix} \eta_\alpha(t) \\ \eta_\theta(t) \end{Bmatrix}, \quad \boldsymbol{\eta}(t) = \boldsymbol{\eta}(t + kT), \quad k \in \mathbb{Z} \quad (4.61)$$

The period $T = 2\pi/\Omega$ is determined by adopting the refinement procedure described above. The time-varying non-homogeneous term $\boldsymbol{\varepsilon}$ in Equation (4.60) is a consequence of introducing an approximated expression for the limit cycle, given by a truncated Fourier series. It tends to zero as the number of harmonics in the Fourier expansion tends to infinity and it would be zero in case of exact expression of the limit cycle.

A first order perturbation is now introduced in the expression of the limit cycle, and substituted into the nonlinear dynamic equilibrium equations, yielding:

$$\boldsymbol{\eta}^* = \boldsymbol{\eta} + \mathbf{w}^* \quad \text{with} \quad \mathbf{w}^* = \begin{Bmatrix} \alpha^*(t) \\ \theta^*(t) \end{Bmatrix} \quad (4.62)$$

$$I\dot{\boldsymbol{\eta}}^* + \mathbf{f}(\dot{\boldsymbol{\eta}}^*, \boldsymbol{\eta}^*) = \boldsymbol{\varepsilon} \implies I\dot{\boldsymbol{\eta}} + I\dot{\mathbf{w}}^* + \mathbf{f}(\dot{\boldsymbol{\eta}}^*, \boldsymbol{\eta}^*) = \boldsymbol{\varepsilon} \quad (4.63)$$

where $\alpha^*(t)$, $\theta^*(t)$ are unknown functions representing the first order perturbation obtained by expanding \mathbf{f} in Taylor series up to the first order:

$$I\dot{\boldsymbol{\eta}} + I\dot{\mathbf{w}}^* + \mathbf{f}(\dot{\boldsymbol{\eta}}, \boldsymbol{\eta}) + \mathbf{J}\mathbf{y}^* = \boldsymbol{\varepsilon} \implies I\dot{\mathbf{w}}^* + \mathbf{J}\mathbf{y}^* = 0 \quad (4.64)$$

with

$$\mathbf{y}^* = \begin{Bmatrix} \dot{\mathbf{w}} \\ \mathbf{w} \end{Bmatrix} \quad \text{and} \quad J_{ij} = \left. \frac{\partial f_i}{\partial y_j^*} \right|_{\mathbf{y}^*=0} \implies \mathbf{J} = \begin{bmatrix} \frac{\partial f_1}{\partial \dot{\alpha}^*} & \frac{\partial f_1}{\partial \dot{\theta}^*} & \frac{\partial f_1}{\partial \alpha^*} & \frac{\partial f_1}{\partial \theta^*} \\ \frac{\partial f_2}{\partial \dot{\alpha}^*} & \frac{\partial f_2}{\partial \dot{\theta}^*} & \frac{\partial f_2}{\partial \alpha^*} & \frac{\partial f_2}{\partial \theta^*} \end{bmatrix}_{\mathbf{y}^*=0} \quad (4.65)$$

The Jacobian matrix \mathbf{J} (whose calculation is not necessary when the nonlinearities are given by polynomial expansions, as in the case under analysis) can also be represented in terms of two blocks:

$$\mathbf{J} = \begin{bmatrix} \mathbf{C}^*(t) & \mathbf{K}^*(t) \end{bmatrix} \quad (4.66)$$

where $\mathbf{C}^*(t)$ and $\mathbf{K}^*(t)$ are the equivalent damping and stiffness matrices of the system, respectively. Note how the spurious term $\boldsymbol{\varepsilon}$ vanishes in Equation (4.64), due to the linearisation procedure. Then the linearised system describing the dynamics over the limit cycle is represented by:

$$I\dot{\mathbf{w}}^* + \mathbf{C}^*(t)\dot{\mathbf{w}}^* + \mathbf{K}^*(t)\mathbf{w}^* = 0 \quad (4.67)$$

The functions in \mathbf{f} are polynomials, therefore all the elements of $\mathbf{C}^*(t)$ and $\mathbf{K}^*(t)$ are given by sums and products of the sine and cosine functions, and the angular frequency of each of these sine and cosine functions is equal to, or a multiple of, the limit cycle angular frequency. As a result, the period of all the elements in $\mathbf{C}^*(t)$ and $\mathbf{K}^*(t)$ are the same, and equal to that of the (approximated) limit cycle. This is simply because the polynomials retain linear terms, while the products of sines and cosines lead to terms with whole number multiples of the base frequency. Hence the dynamics over the limit cycle is described by a linear time-varying system, whose time dependent coefficients have the same period of the approximated limit cycle.

Stability is studied by applying Floquet theory to Equation (4.67), in the form of the monodromy matrix method [Yakubovich and Starzhinskiĭ 1975]. As a first step of the procedure, Equation (4.67) is rewritten in the state space format:

$$I\dot{\mathbf{w}}^* + \mathbf{C}^*(t)\dot{\mathbf{w}}^* + \mathbf{K}^*(t)\mathbf{w}^* = 0 \implies \mathbf{A}\dot{\mathbf{y}}^* + \mathbf{B}\mathbf{y}^* = 0 \implies \dot{\mathbf{y}}^* = -\mathbf{A}^{-1}\mathbf{B}\mathbf{y}^* \quad (4.68)$$

where

$$A = \begin{bmatrix} I & 0 \\ 0 & I \end{bmatrix} \quad (4.69)$$

$$B = \begin{bmatrix} C^*(t) & K^*(t) \\ -I & 0 \end{bmatrix} \quad (4.70)$$

The choice of the state space representation in Equation (4.68) is made in order to obtain a time invariant and non-symbolic A matrix, holding the property $A^{-1} = A^T = A$. The 4×4 matrix $A^{-1}B$ is real, therefore the associated monodromy matrix is a real 4×4 matrix as well, with four multipliers characterising the system in Equation (4.68). Since the monodromy matrix is real, the time invariant Floquet multipliers occur in complex conjugate pairs or in pairs of distinct or coincident real parts. Thus, determining their position with respect to the unit circle in the Argand-Gauss plane gives a complete picture of the system stability properties, regardless initial conditions [Yakubovich and Starzhinskiĭ 1975]. The monodromy matrix in the case under analysis can be computed carrying very low computational costs, making Floquet direct analysis very convenient. It can be noted that:

- (i) One Floquet multiplier is always in position $(1, 0)$ on the complex plane (trivial multiplier, representing the exact solution given by the limit cycle itself), and this result is consistent with the analysis presented by Lewis [2019].
- (ii) If all the remaining multipliers have modulus smaller than one, then the limit cycle is stable.
- (iii) If at least one multiplier has modulus larger than 1, then the limit cycle is unstable.
- (iv) In case of coincident multipliers on the unit circle, this procedure is not sufficient for assessing stability of the system, and further steps are necessary for concluding its stability analysis.

The adopted method works also in presence of unstable limit cycles, as also noted by Lewis [2019], yielding the same trivial multiplier at $(1, 0)$. Note how the approximation in the expression of the limit cycle affects this kind of stability analysis: the trivial multiplier, which in case of exact expression of the limit cycle would be exactly $(1, 0)$, actually takes a slightly different real part (which in the case under analysis, with an approximation up to the fourth harmonic, is slightly less than unity, with an error of magnitude 10^{-8}). This error (difference with respect to unity of the trivial multiplier, with sign) can be taken as a measure of the accuracy in the approximation of the limit cycle.

Floquet analysis can also help in the identification of spurious solutions in the refinement procedure described above (see Subsection 4.2.4), which may require more attention in the case of high amplitude limit cycles, when their first order approximations are very different from their actual shapes. This is due to the fact that the refinement procedure is sensitive to initial values, and therefore to perturbations in lower order harmonics. In the case of high amplitude limit cycles, the root search routines may fail, leading to singular Jacobians or non-convergent results. As a novel and efficient method for identifying spurious solutions due to the refinement algorithm, it is here proposed to adopt Floquet analysis for the calculation of the multipliers which describe the dynamics on the limit cycle (i.e., the perturbation of the first-order approximation of the limit cycle). In presence of an actual limit cycle, and independently from its stability, the analysis gives a pair of real multipliers, one of which is equal to unity (trivial multiplier) unless there are numerical errors due to truncation in the harmonic series. Instead, the presence of only complex conjugate multipliers is not consistent with the definition of a limit cycle as a periodic solution (with period equal to that of the fundamental component of the harmonic series), which leads to the identification of spurious solutions, and a restart of the initialisation procedure.

4.3 Results and Discussion

Stability analysis of the linear model is briefly revisited with the simplified two DOFs model, with an emphasis on the effects of linear tyre relaxation, since this aspect was not investigated in-depth in the previous chapter. Next, the results of the preliminary numerical simulations are presented and discussed. Stability analysis of the nonlinear model is then performed, focusing on the existence and stability of limit cycles, studying the case without tyre relaxation first. Finally the effects of tyre relaxation on the generation and stability of limit cycles is presented.

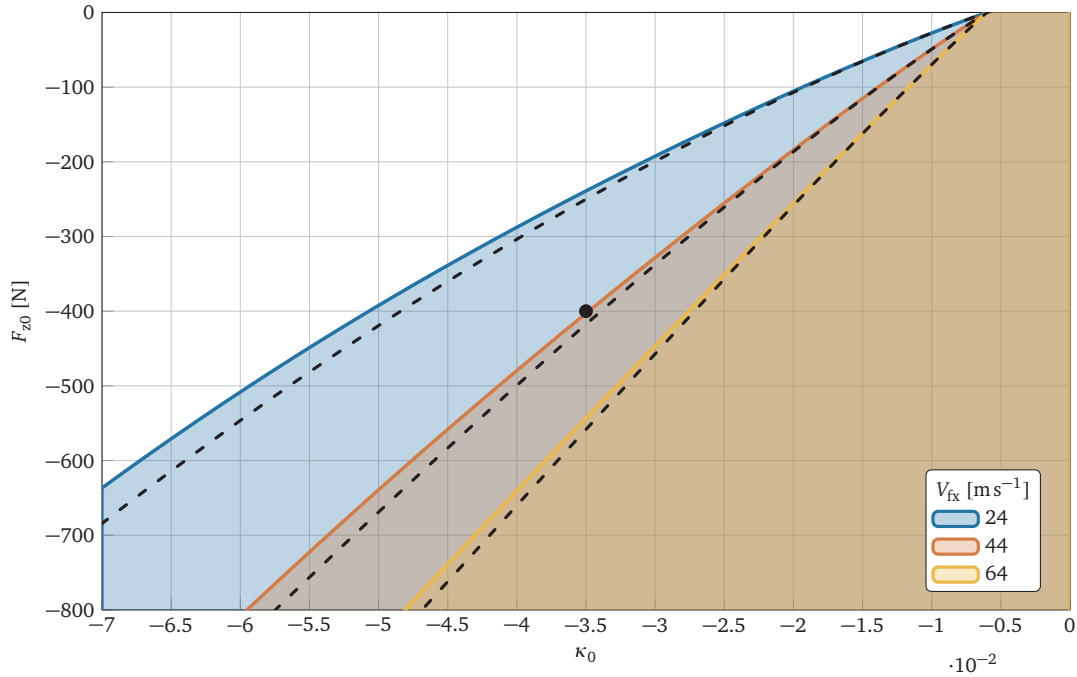


Figure 4.4: Stability regions of the relaxed linear system with non-relaxed shown with dashed lines, the reference condition is signified by the black dot.

4.3.1 Effects of Tyre Relaxation on the Stability of the Linear Model

Tyre relaxation, namely relaxation length, can play a role in linear system stability, even though in some studies its effect has been neglected [Sorrentino and Leonelli 2017, Leonelli et al. 2018]. Here the effects of tyre relaxation on the stability of the simplified model are investigated by including the LTI model, Equation (4.33), into the EOMs (4.9) and (4.10) in their linearised form, replacing the longitudinal slip coefficient κ with its relaxed counterpart κ_r .

The first of the results are presented in Figure 4.4, where the linear stability regions for differing system configurations are plotted using the Routh-Hurwitz criterion. There the solid lines and shaded areas present the stability regions with relaxation behaviour, while the dashed lines show the original unrelaxed stability boundaries. From these data, the introduction of relaxation behaviour shows to have a very small stabilising effect on the results of the linear system stability in the case under study. The adopted relaxation model parameters can be found in Table 4.3.

Given that tyre relaxation behaviour can change from tyre to tyre, the system is augmented to treat the tyre relaxation length λ_{x0} as a constant input parameter. The results of varying this parameter on linear system stability is presented in Figure 4.5. It is shown that around the reference condition of relaxation length (approximately 53 mm), the stability boundary is relatively stationary with respect to any change in relaxation length. Not until much larger values of relaxation length does the parameter start to play a greater role in the linear system stability. Also, as the relaxation length approaches zero, the system loses some stability, showing that in the absence of relaxation, linear analysis tends to overestimate instability, a conservative and practical finding. This supports the actions of Sorrentino and Leonelli [2017] and Leonelli et al. [2018], wherein the relaxation length was considered to be small enough to not have a major effect on linear stability and was therefore neglected. In this regard, it should also be mentioned that in the specific case of chatter, working points of the tyre at high slip and low vertical load (due to longitudinal load transfer in braking conditions) contribute significantly to lowering the relaxation length [Pacejka 2012], especially for racing tyres. Further increasing the slip κ_0 , the gradient $C_{\kappa_0,x}$ would become negative and according to the adopted relaxation model so would λ_{x0} , bringing Equation (4.33) to intrinsic instability (see the map in Figure 4.5, where the cut of stable regions a λ_{x0} is due to the sign change in the relaxation length, which may be infeasible, as discussed by Pacejka [2012]). Recalling Chapter 3 however, it should be noted that negative values of $C_{\kappa_0,x}$ would lead to instability of the dynamic system in Equation (4.9) and (4.10) independently from tyre relaxation.

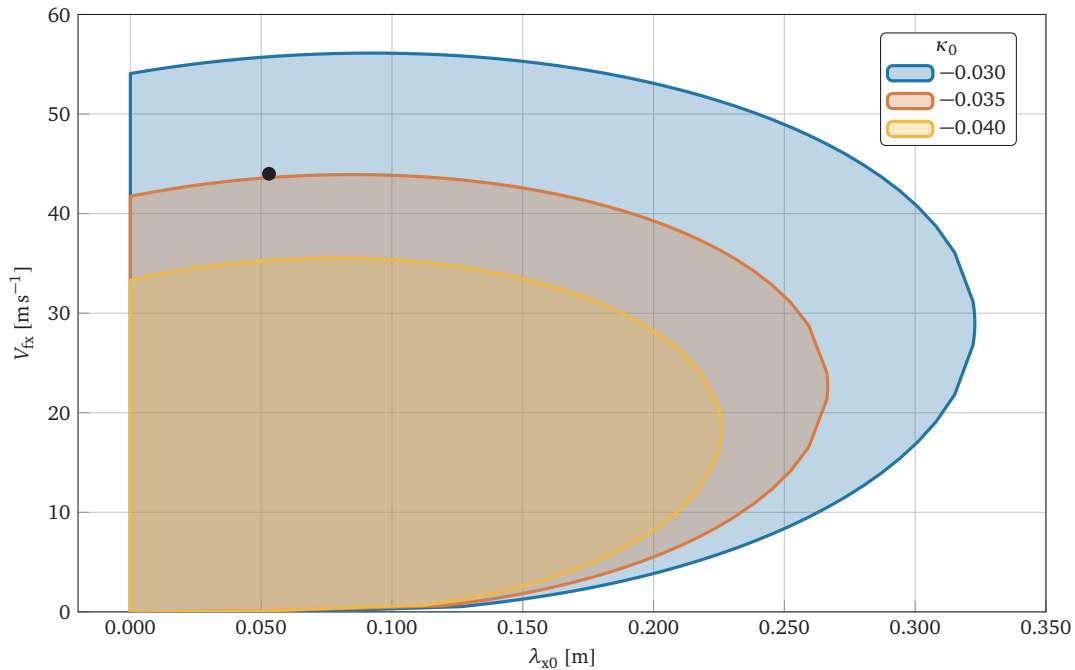


Figure 4.5: Effects of a constant relaxation length on system stability, the reference condition is signified by the black dot.

In any case, looking at the regions displayed in Figure 4.5, it is clear that large positive values of relaxation length produce destabilising effects on the linear model, reducing the interval of stability with respect to travelling speed, until the model becomes indefinitely unstable (critical relaxation length at a given operating condition). This effect can be in part explained recalling the FRF given by Equation (4.46) – (4.48). In that case, the stabilising effect due to attenuation (reduction of FRF modulus by increasing frequency) is counteracted by a concurrent increase in phase lag. The latter evidently becomes dominant and contributes indirectly to destabilise the system, influencing the phase lag between the factors of the power flow at the ground contact point, which is able to bring the system to critical conditions, as described in Chapter 3. For an in-depth analysis of the frequency response behaviour of the relaxation models of Equation (4.33) and (4.44), the reader is referred to the following Subsection 4.3.5.

4.3.2 Numerical Results

Returning to the system without relaxation, the results of the numerical analysis of Subsection 4.2.3 is discussed. The asymptotic behaviours of the two systems are shown in Figure 4.6. During the earlier stages after the initial disturbance both systems respond in a similar manner, which suggests that the linearised approximation is accurate in low amplitude oscillations. Initially as the oscillations begin to grow, both systems grow equally fast, but at approximately 13 s, the nonlinear system begins its decay to a presumed asymptotic limit cycle while the linearised system continues its exponential growth. This result suggests a supercritical bifurcation in the nonlinear system, resulting in stable limit cycles when the linear system predicts unstable behaviour. Note that during simulations, very large initial disturbances still compatible to a motorcycle are tested in the stable region, and no notable difference in stability between linear and nonlinear systems is found. The existence of any presumable unstable limit cycle (divergent amplitude responses in the linearly stable domain) is not found. Clearly, in that case the amplitude of presumed limit cycles cannot be evaluated by numerical simulation.

A look at the phase space of the limit cycle is shown in Figure 4.7. This figure shows the asymptotic behaviour of swingarm angle and wheel speed oscillations, while also showing a portion of the linear trace near similar values undergoing exponential growth for comparison. This allows the asymmetric behaviour of the nonlinear system to be seen clearly, with less amplitude in the left half plane, and more in the right, suggesting the existence of some higher harmonics.

The limit cycle in terms of the tyre forces and slip are shown in Figure 4.8. Even though the amplitude of swingarm angle oscillations is small, the amplitude of oscillations of the limit cycles in terms of forces is quite large. There-

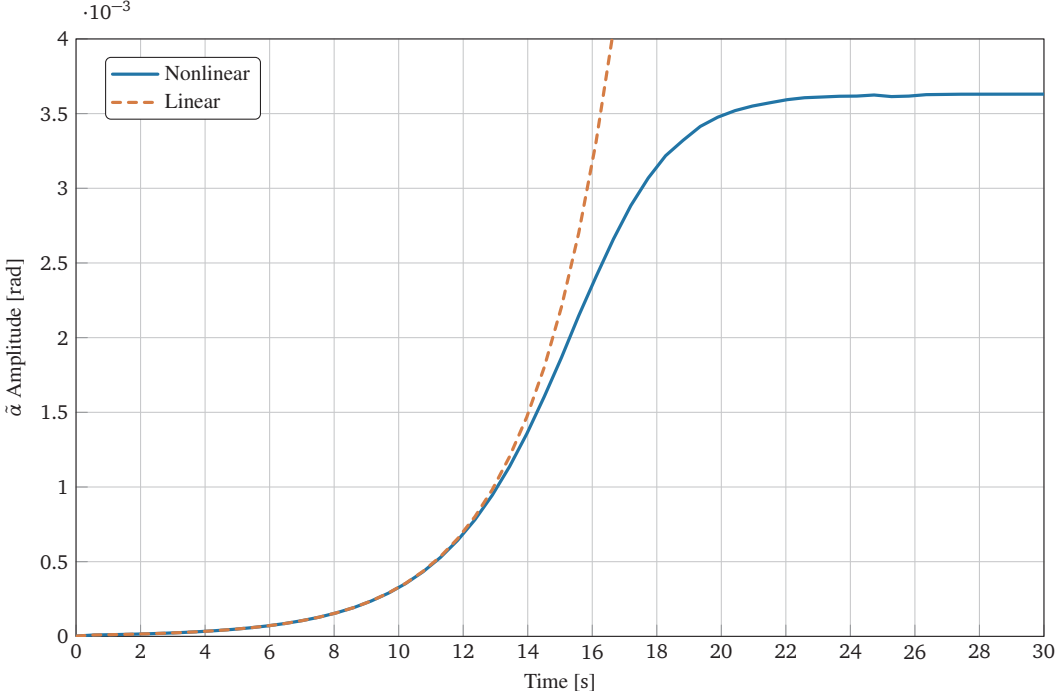


Figure 4.6: Asymptotic behaviour of the nonlinear system as numerically simulated.

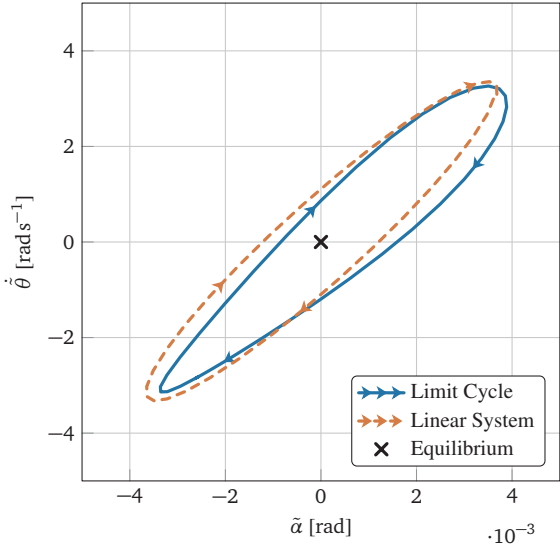


Figure 4.7: Limit cycle phase space of the nonlinear system as numerically simulated.

fore, the amplitudes of the limit cycles are not acceptable in terms of motorcycle stability even if the equilibrium point is close to the stability threshold.

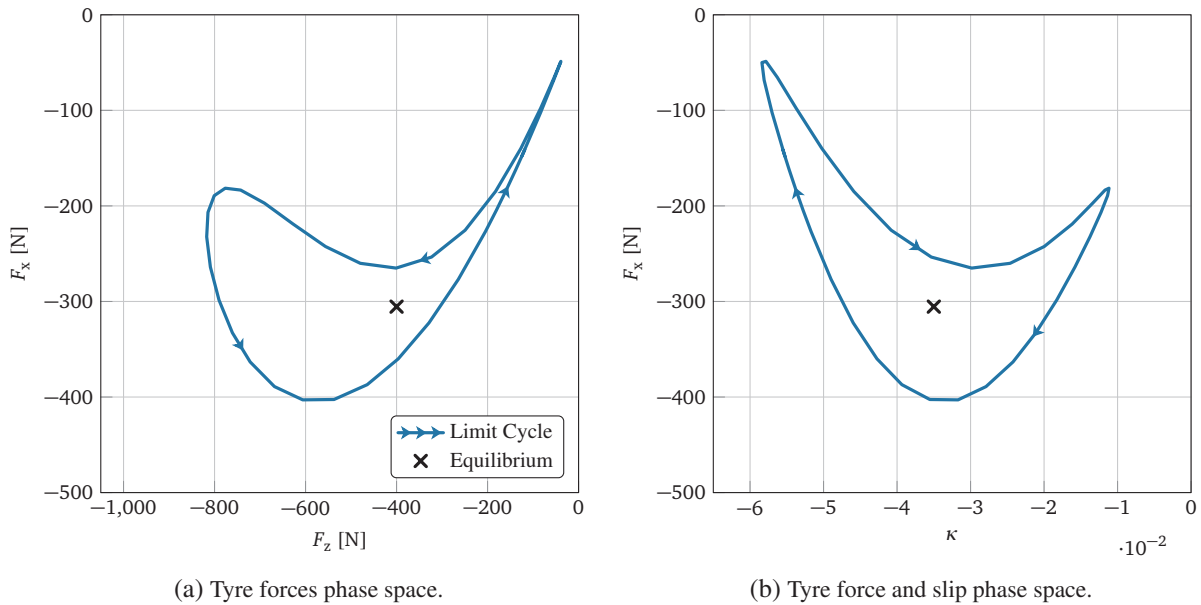


Figure 4.8: Tyre forces and slip limit cycle phase spaces representations of the nonlinear system as numerically simulated.

When nonlinearities are introduced individually, as described in Subsection 4.2.3, it is possible to compare the stability and asymptotic behaviour to those of the linearised and fully nonlinear systems. Table 4.4 shows how the limit cycle swingarm angle amplitudes vary with the introduction of the separate nonlinear terms described in Subsection 4.2.1.

Table 4.4: Asymptotic behaviours of different models of the nonlinear system as numerically simulated.

Model	Limit Cycle Amplitude [rad]
Linear	∞
Geometry nonlinearities only	0.9160
Chain nonlinearities only	1.2010
Tyre nonlinearities only	0.0073
Full nonlinear	0.0072

The geometry and chain nonlinearities lead to very large limit cycles, indicating very small nonlinear effects on the system. The tyre nonlinearities are the only terms to introduce a significant limit cycle to the asymptotic behaviour. This suggests that the nonlinear tyre characteristic function from Equation (4.1)–(4.8) is the primary nonlinear driver to the limit cycle, with very slight influences of the geometry and chain nonlinearities.

A selection of model parameters are tested to see their effects on the asymptotic behaviour of the nonlinear system. Each parameter is swept from 90 % to 110 % of its reference value in steps of 2 %. The real eigenvalue from the driveline mode is taken from the linearised system, and the swingarm angle amplitude of the limit cycle is obtained from the nonlinear system. The results are displayed in Figure 4.9, where the black point represents the reference position. The limit cycle amplitude shows the most sensitivity to variations of parameter p_{kx1} (MF nominal tyre slip stiffness). Again, the tyre force gradient confirms to be one of the most important parameters in governing this instability problem.

It is also shown in Figure 4.9 that, while some parameters tend to not affect amplitude, the effects of most parameters on limit cycle amplitude follow a square root function similar to that described by the analytical solution of the limit cycle amplitude of the generalised van der Pol's equation presented by Rand [2012]. This result suggests that a similar solution may be possible with this nonlinear system, or could be approximated by a similar, previously

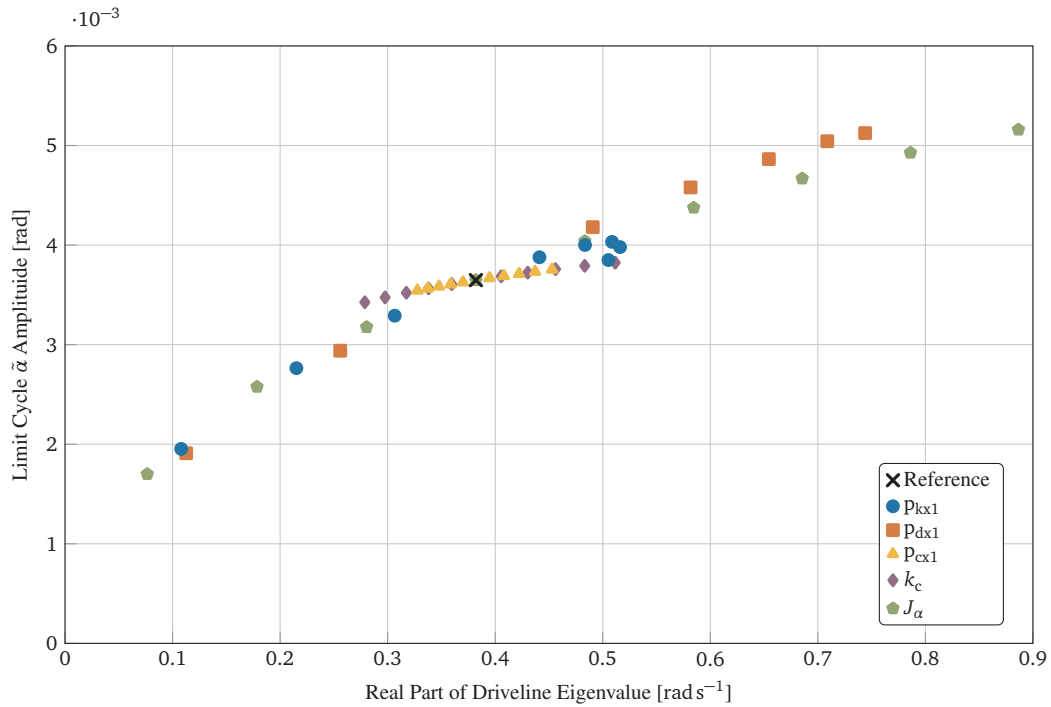


Figure 4.9: Effect of some relevant parameters on asymptotic behaviour: limit cycle amplitude versus real part of driveline eigenvalue.

solved, analytical equation. There are some parameters which deviate slightly from the general trend, such as p_{cx1} or k_c , but to better understand the effects of parameters on asymptotic behaviour and limit cycle amplitude, an analytical approach is required.

4.3.3 Existence of Limit Cycles in the Nonlinear Model

The numerical results suggest the existence of a stable limit cycle. An application of the method described in Subsection 4.2.4 then confirms the existence of this limit cycle, which is unique in the parameter domain of technological interest. The effects of tyre relaxation are not considered in this section, assuming $\lambda_x = 0$ in all cases.

In Figure 4.10, the limit cycle determined by the harmonic balance method (red cycle) is superimposed onto a numerical phase portrait. In this case (and in all the following in this chapter) the approximations of the limit cycles are refined using the first four harmonics, which gives an accurate representation (assessed after several tests involving computations up to the 20th harmonic, finding errors less than 0.01 % when using fourth order harmonics). The method is also employed in the linearly stable regions (by slowing the reference speed V_{fx}), but no non-trivial limit cycles are found. Note that the bias terms due to the Fourier expansion in Equation (4.56), given by non-symmetric nonlinear terms, are not negligible [Gelb and Vander Velde 1968].

Limit cycles in terms of the tyre forces and slip as found by the harmonic balance method are shown in Figure 4.11. The large amplitudes support the findings of the numerical simulations and Figure 4.8a and 4.8b. Again, the findings are that these amplitudes are too large to be considered acceptable in terms of motorcycle stability. The contour plots in Figure 4.11, drawn by varying the travelling speed V_{fx} , show a great sensitivity of limit cycle amplitude with respect to this equilibrium value. Note that the higher speed contours contain portions with positive F_z and F_x , indicating wheel lift. The current model does not have contingencies for the nonlinear effects of wheel lift, and are therefore not captured in the given limit cycles.

A study of limit cycle sensitivities to modelling parameters is achieved by selecting certain important parameters, identified in Subsection 4.3.2, and modifying their values. This results in a change in asymptotic behaviour, notably limit cycle amplitude, but also a change in stability in the linear sense (which in turn also contributes to modify limit cycle amplitude). The inertial parameter J_α , whose effects are displayed in Figure 4.12, shows that with decreasing values, the limit cycle grows in amplitude and shows more high order harmonics. The suspension damping c_s , effects shown in Figure 4.13, shows similar behaviour, with more of an effect on limit cycle amplitude. All the

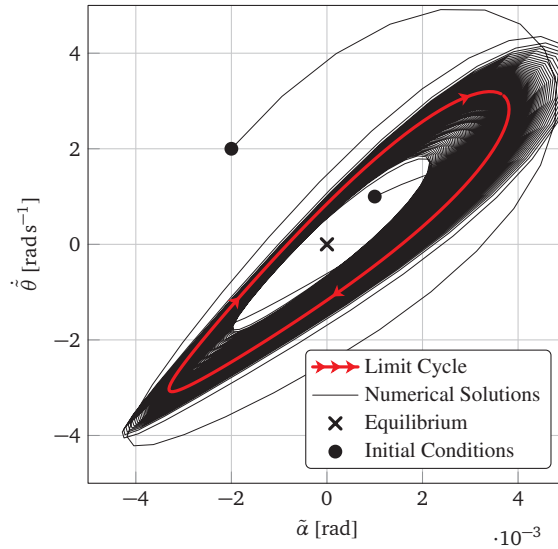
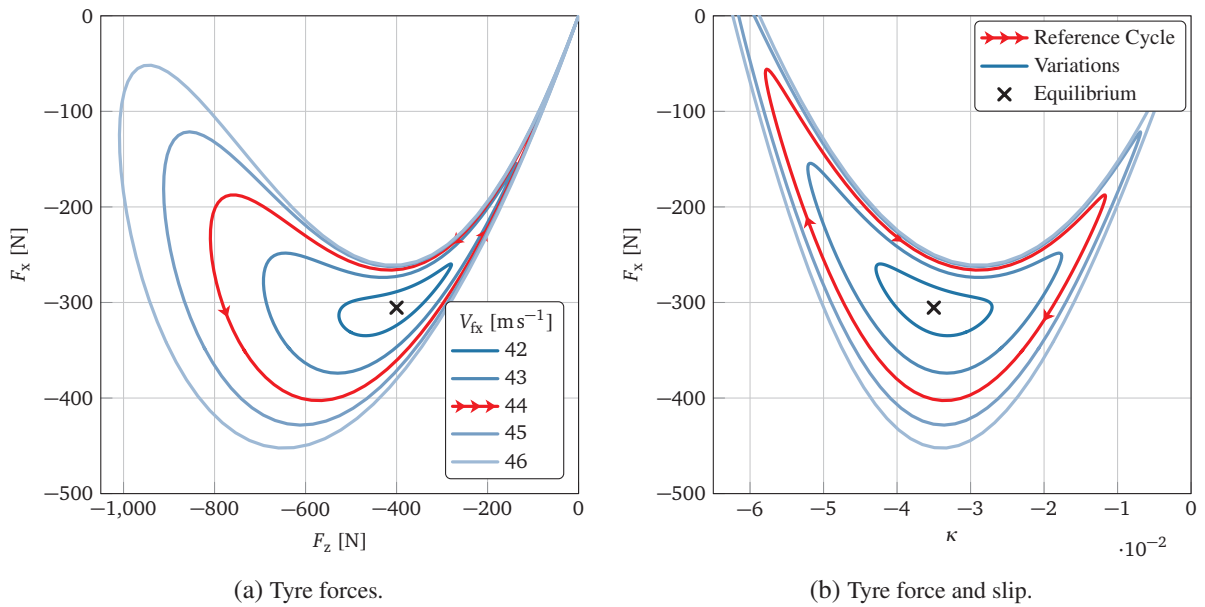


Figure 4.10: Phase portrait and limit cycle (shown in red) in the variables $\tilde{\alpha}(t)$ and $\dot{\tilde{\theta}}(t)$.



(a) Tyre forces.

(b) Tyre force and slip.

Figure 4.11: Tyre forces and slip phase space of limit cycles refined up to the fourth harmonic.

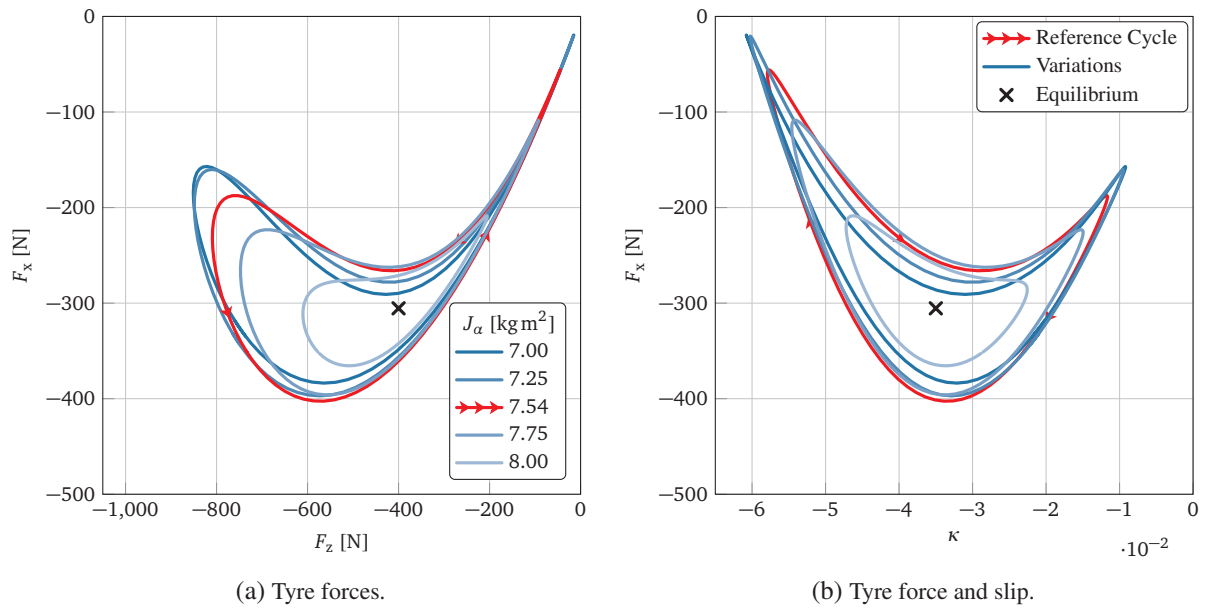


Figure 4.12: Tyre forces and slip phase space of limit cycles for different values of moment of inertia J_α refined up to the fourth harmonic ($V_{fx} = 44 \text{ m s}^{-1}$).

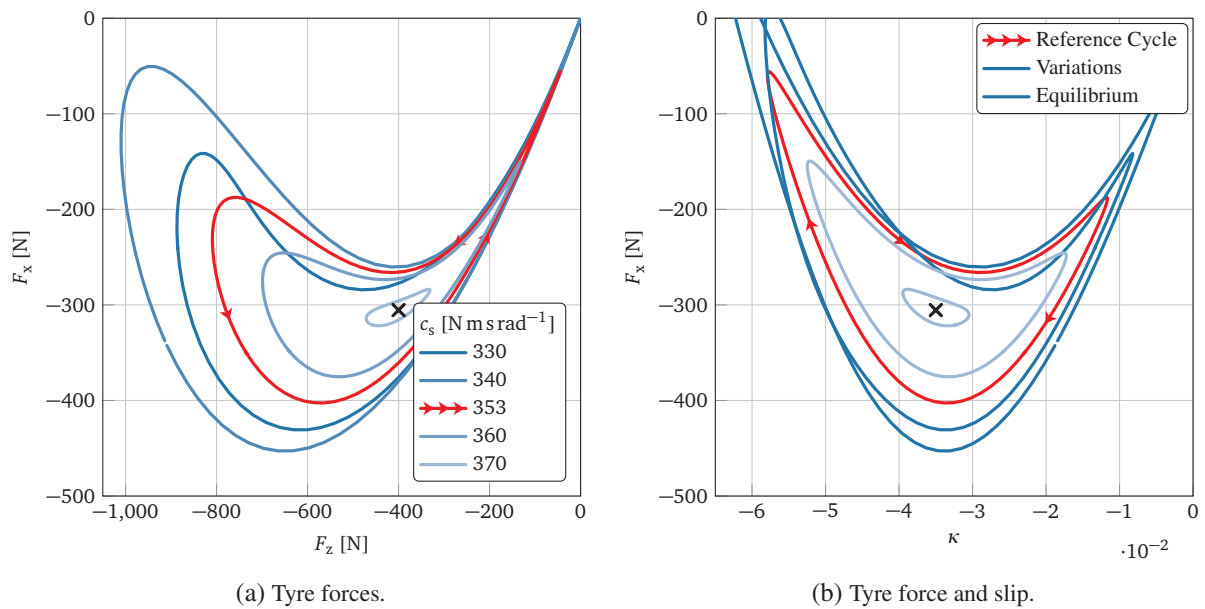


Figure 4.13: Tyre forces and slip phase space of limit cycles for different values of suspension damping c_s refined up to the fourth harmonic ($V_{fx} = 44 \text{ m s}^{-1}$).

limit cycles displayed in Figure 4.11–4.13 occur in a very narrow frequency range about the reference value of 18.56 Hz (18.61 Hz to 18.51 Hz for increasing V_{fx} , 18.78 Hz to 18.43 Hz for increasing J_α , and 18.54 Hz to 18.65 Hz for increasing c_s). The F_z - F_x limit cycles are counter-clockwise, while the cycles κ - F_x are clockwise.

4.3.4 Stability Analysis of the Nonlinear Model

The application of the methods described in Subsection 4.2.4 and 4.2.5 show that in the case under analysis there is always one trivial multiplier at the position (1, 0), two complex-conjugate multipliers with modulus smaller than unity (inside the unit circle), and a fourth real positive multiplier with modulus smaller than one. This makes it possible to demonstrate that within the parameter domain of technological interest and with no relaxation, the nonlinear system has a supercritical post-bifurcation behaviour with a single stable limit cycle growing with linearised instability. This in turn means that the linearised system can be used as a stability predictor.

The bifurcation diagram displayed in Figure 4.14 shows the critical speeds and the limit cycle amplitude of vertical load F_z as a function of travelling speed V_{fx} for different working points on the characteristic tyre function (the MF model). These confirm that even if the equilibrium point is close to the stability threshold, the growth of limit cycle amplitude is not acceptable in terms of motorcycle stability.

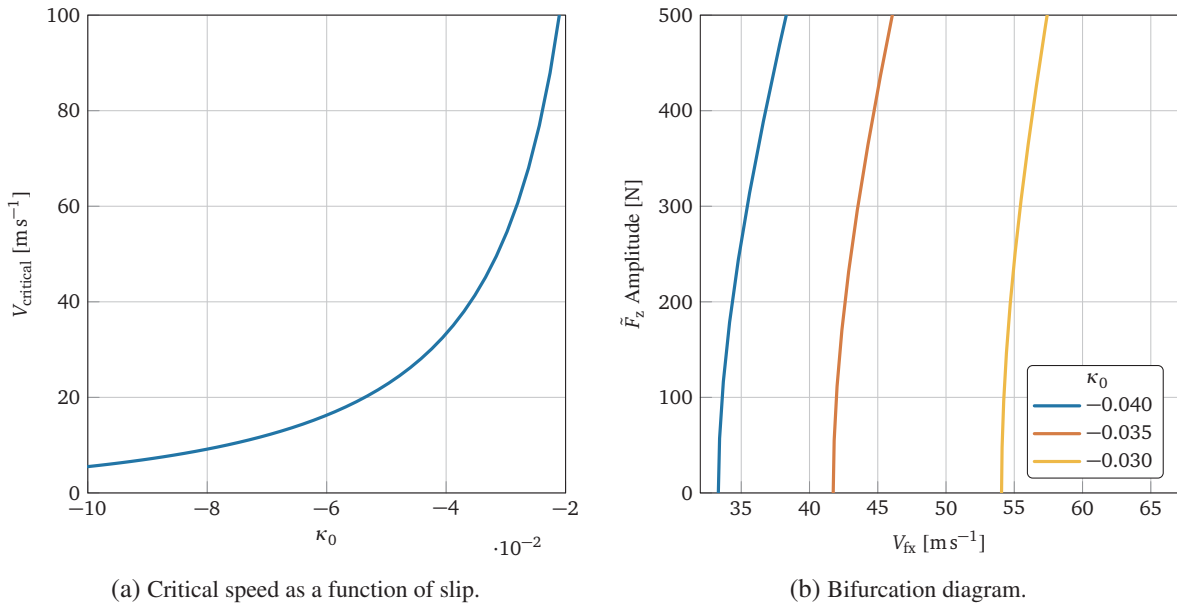


Figure 4.14: Critical speed and bifurcation diagrams. Limit cycle amplitude of vertical load F_z as a function of travelling speed V_{fx} for different working points on the characteristic tyre function.

Further, the existence and stability of this limit cycle is investigated by varying the stationary equilibrium point on the characteristic function of the tyre for different values of κ_0 and F_{z0} while leaving all the other parameters unchanged. Assuming a value of κ_{limit} for which instability occurs in the linear sense for which $C_{\kappa_{\text{limit}},x} > 0$, then increasing κ_0 until $C_{\kappa_0,x} = 0$ (at a given value of F_{z0}) brings the system well inside the linear instability region (while the linear stability threshold does not change). Hence, a faster growth in oscillation amplitude is expected following a perturbation due to the larger positive real part of the critical eigenvalue and consequently, in the case of its existence, also an increase in the limit cycle amplitude. The analysis of the nonlinear system at $C_{\kappa_0,x} = 0$ for different values of F_{z0} in this case confirmed the existence of a stable limit cycle, however with such a high amplitude that realistically it could not be reached. This confirms that the limit cycle remains a stable one even when the oscillations of κ pass through the region of the MF where $C_{\kappa,x} < 0$, normally a very unstable region. It should be noted that at the amplitudes seen in this chapter, additional effects would need to be considered, such as wheel detachment (not considered in the present model), or rider intervention, both of which would affect the stability results of this analysis.

A more in-depth analysis is then performed, aimed at understanding the relative influence of the three sources of nonlinear terms as identified in Subsection 4.2.1, that is: tyre forces due to F_x terms, geometry due to F_z terms,

and chain due to $M_{c\alpha}$ and $M_{c\theta}$ terms. The effects of geometric nonlinearities in the F_z terms are found to be totally negligible, while those due to the chain, if considered as the only nonlinear terms in Equation (4.9) and (4.10), are able to produce a post-bifurcation stable limit cycle, however with an amplitude at least two orders of magnitude higher than that of the fully nonlinear system (see the similar numerical results in Table 4.4). Therefore, it can be stated that, from a practical point of view, the nonlinear behaviour of the system is given totally by the tyre force F_x . In fact, the nonlinear terms descending from the characteristic function of the tyre, if considered as the only nonlinear terms in Equation (4.9) and (4.10), are able to produce a post-bifurcation stable limit cycle which is almost totally superimposed on that due to the fully nonlinear system. The limit cycles displayed in Figure 4.11–4.13 would remain practically unchanged, if computed considering the tyre nonlinear terms only. Which confirms what was found in Subsection 4.3.2, that is, that the nonlinear tyre characteristic function (the MF model) is the primary nonlinear driver to the limit cycle, with a negligible influence of the chain geometry nonlinearities. As already pointed out in Subsection 4.2.1, very small limit cycle amplitudes for the swingarm angle are required to make the assumption of linear suspension spring and damper acceptable.

4.3.5 Effects of Tyre Relaxation on the Stability of the Nonlinear Model

As noted in Subsection 4.3.1, linear tyre relaxation has an indirect effect on system stability since it influences the phase lag between ground force and slip velocity, which in turn controls the switching mechanism to instability. Therefore as a first step into the analysis of Equation (4.44), its frequency response is compared to the one given by Equation (4.46)–(4.48), the FRF of the LTI relaxation model of Equation (4.33). For this purpose, it is convenient to observe that in the problem under investigation, except for very low values of travelling speed, the term dependent on the time derivative of V_x in Equation (4.44) can be neglected, as well as the non-stationary component of V_x , that is:

$$\left(1 + \frac{\lambda_x \dot{V}_x}{V_x^2}\right) \cong 1 \implies V_x \cong V_{x0} \quad (4.71)$$

Then, assuming two coupled harmonic inputs:

$$\kappa = \kappa_0 + A \cos(\Omega t) \quad (4.72)$$

$$F_z = F_{z0} + B \cos(\Omega t + \varphi) \quad (4.73)$$

makes Equation (4.44) independent from the states of the system of Equation (4.9) and (4.10). In this way, Equation (4.44) is reduced to a nonlinear first order differential equation (with respect to κ_r) with a harmonic non-homogeneous forcing term given by $\kappa(\Omega t)$. The frequency response of Equation (4.44) with the simplifying assumptions of Equation (4.71) and harmonic inputs from Equation (4.72) and (4.73) can be represented in modulus and phase then compared to Equation (4.46)–(4.48).

Figure 4.15 compares the Bode diagram of the FRF of Equation (4.46)–(4.48) for the LTI system to the one given by the FRF of Equation (4.44) (adopting values reported in Table 4.2 and taking from the reference limit cycle the values for simulating the periodic system). It can be seen from Figure 4.15 that in the frequency range of interest (the limit cycle occurring at 116.6 rad s^{-1}) the curves are almost perfectly superimposed, and that while the attenuation effect is negligible, the phase delay follows closely to what happens in the linear system. Differences become relevant at higher frequencies, beyond 500 rad s^{-1} .

Note that introducing a further simplifying assumption, Equation (4.44) may be reduced to a linear (with respect to κ_r) equation with a periodic time-varying coefficient. This assumption regards the definition of λ_x in Equation (4.44), descending from Equation (4.38):

$$C_{V_{sx},x} = \frac{\partial F_x}{\partial V_{sx}} \Big|_{(\kappa_r, F_z)} \cong C_{V_{sx},x} = \frac{\partial F_x}{\partial V_{sx}} \Big|_{(\kappa, F_z)} = -\frac{C_{\kappa,x}}{V_x} \implies \lambda_x \cong \frac{C_{\kappa,x}}{K} \quad (4.74)$$

Introducing into Equation (4.44) the simplifying assumption given in Equation (4.74) yields a third possible relaxation model (here referred to as ‘time-varying’). However, in the case under study the differences between the results obtained with the time-varying and the fully nonlinear relaxation models are found to be very small. In fact, the FRF computed adopting the time-varying model would be totally superimposed on that shown in Figure 4.15

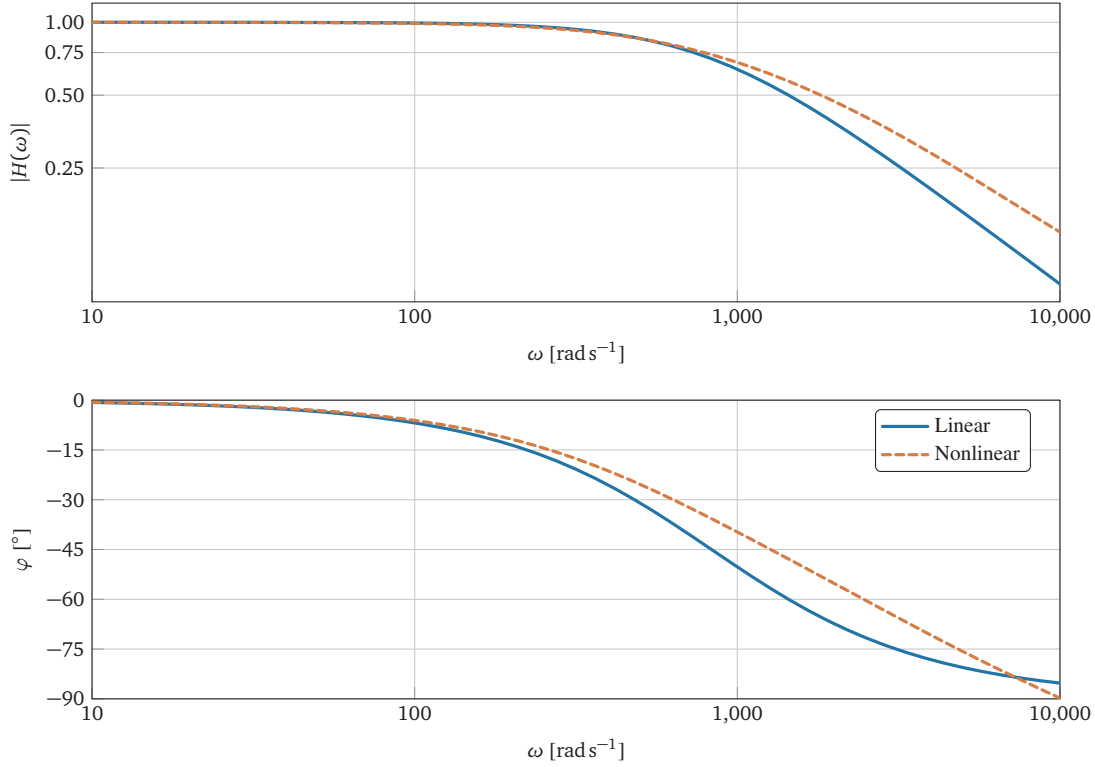


Figure 4.15: Bode diagram of the FRF given by the LTI relaxation model, solid line, compared to the one given by the nonlinear model, dashed line. Parameter values as in Table 4.2.

for the fully nonlinear model. Further evidence of the validity of the approximation in Equation (4.74) is provided in the sequel.

Either Equation (4.33) or Equation (4.44) are now coupled to the equilibrium equations (4.9) and (4.10) to investigate the effects of relaxation in the semi-nonlinear and in the nonlinear models (the latter studied by considering either the time-varying or the fully nonlinear relaxation models). Some preliminary numerical results are displayed in Figure 4.16 and 4.17. Figure 4.16 shows a comparison in terms of numerically computed responses of the nonlinear system at the linear stability boundary, given for three different approximations of the relaxation equation: the LTI model given in Equation (4.33), yielding the semi-nonlinear model; the time-varying model obtained through Equation (4.74); and the fully nonlinear model in Equation (4.44). Simulations are performed at the reference condition, but with speed slowed down to the stability boundary ($V_{fx} = 43.6 \text{ m s}^{-1}$) and with an initial disturbance on wheel angular speed (0.01 rad s^{-1}). No appreciable differences can be observed among the three responses, which suggests that at the linear stability threshold the nonlinearities do not modify system stability. On the other hand, Figure 4.17 shows four different transient responses (maximum oscillation amplitudes) of the semi-nonlinear model. Solutions are numerically computed at the reference condition with an initial disturbance on wheel angular speed (0.01 rad s^{-1}) for increasing values of relaxation length λ_{x0} (from 30 mm to 150 mm). Noticeably, both very small and very large values of relaxation length produce shorter transients and larger limit cycles, as suggested by Figure 4.5. On the contrary, values close to the peak of the stability region produce slow transients and lower limit cycle amplitudes. These effects are attributed mainly to the smaller positive real eigenvalues in these areas.

The effects on limit cycles of tyre relaxation are also investigated, highlighting the differences between relaxation models. The simplifying assumptions in Equation (4.71) are adopted in the analysis, and stability is studied following the method described in Subsection 4.2.5, but in this case representing the system with the additional first order relaxation equation in a state space of dimension five, including κ_r among the five state variables.

Some limit cycles generated by the semi-nonlinear model are shown in Figure 4.18 for different values of relaxation length λ_{x0} ranging from 30 mm to 150 mm (including the reference case, 53 mm). Very small values of relaxation length produce limit cycles similar to those of no relaxation length, only smaller, indicating more stability. The values closer to peak stability produce smaller limit cycles with less high order harmonics. As the relaxation length

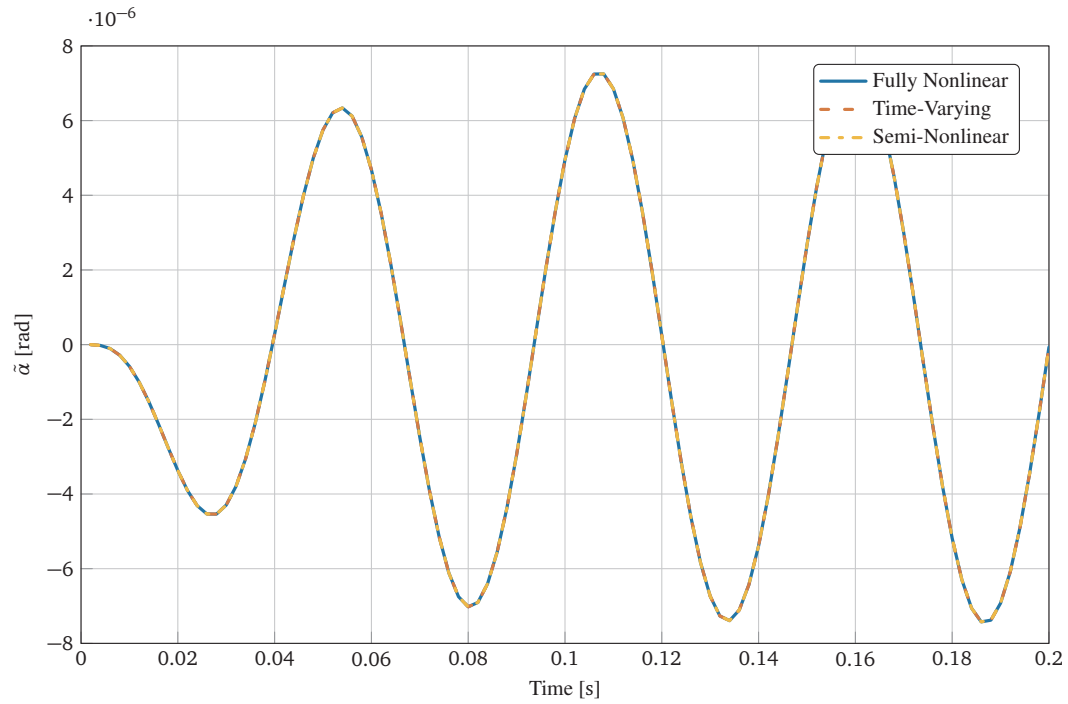


Figure 4.16: System responses at the stability threshold, with comparison of three different relaxation models.

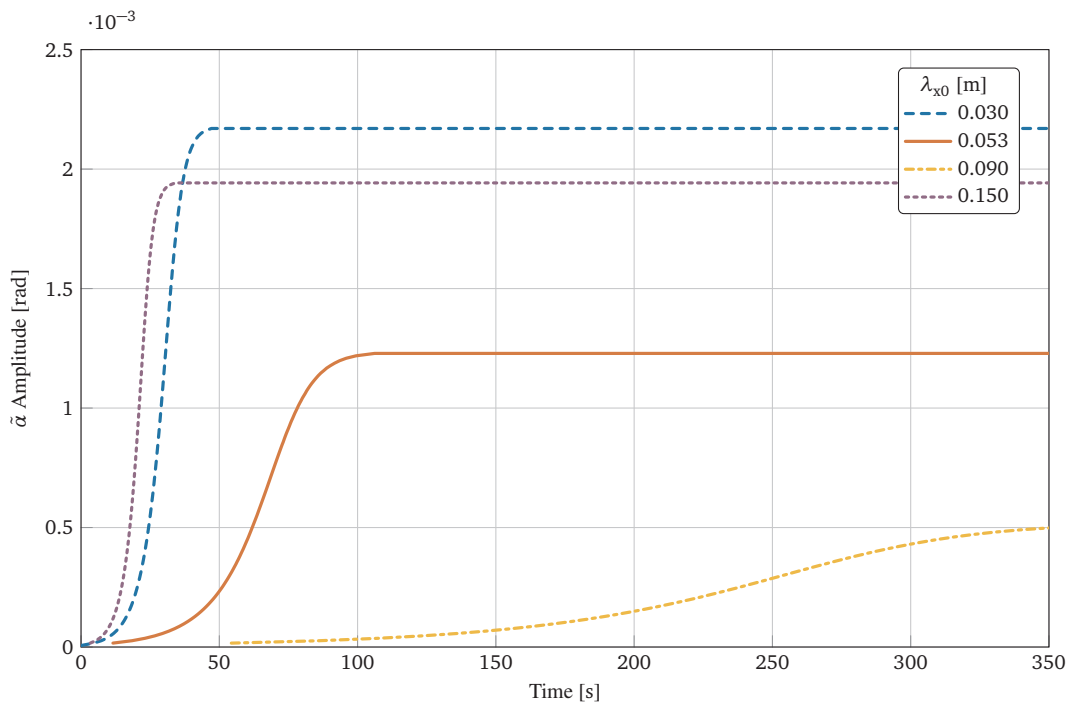


Figure 4.17: Maximum oscillation amplitudes of the semi-nonlinear model response at the reference condition during the transient for different values of relaxation length.

grows to larger values, the limit cycle grows larger and stretched, indicating a larger role of higher order harmonics.

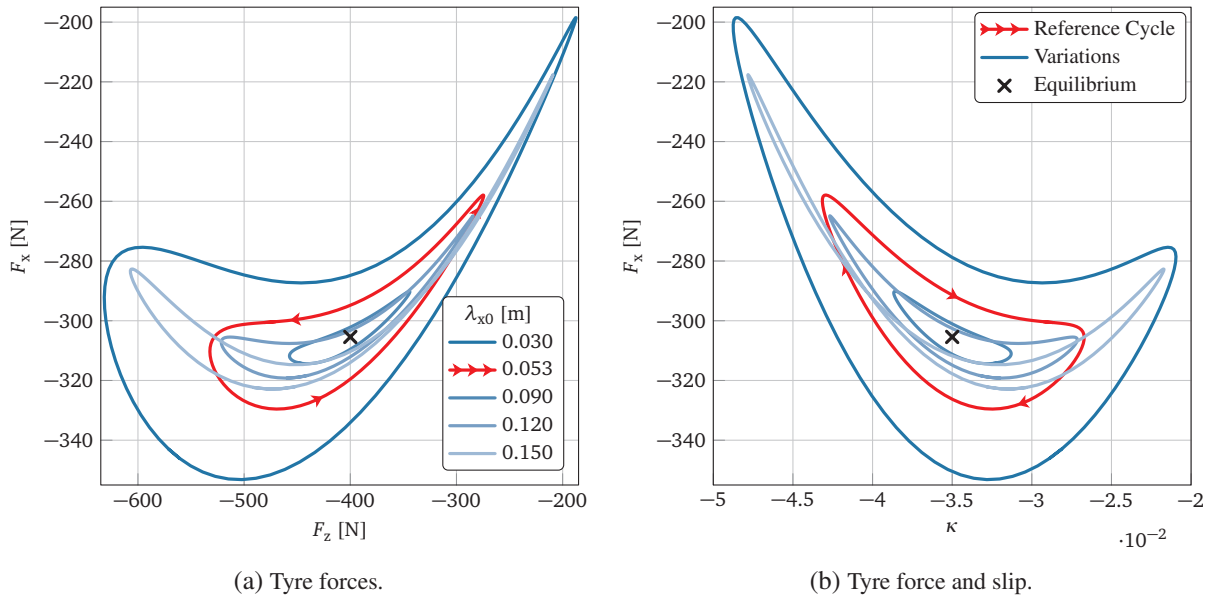


Figure 4.18: Tyre forces and slip phase space of limit cycles for the semi-nonlinear model and different values of relaxation length λ_{x0} refined up to the fourth harmonic ($V_{fx} = 44 \text{ m s}^{-1}$).

Limit cycles generated in the reference case adopting different relaxation models are compared in Figure 4.19, showing the differences due to the semi-nonlinear and nonlinear models (the latter with either time-varying or fully nonlinear relaxation equations) with respect to the case with no relaxation. Note that the phase spaces in this section are zoomed in with respect to those without relaxation, to better show the smaller limit cycles. Some

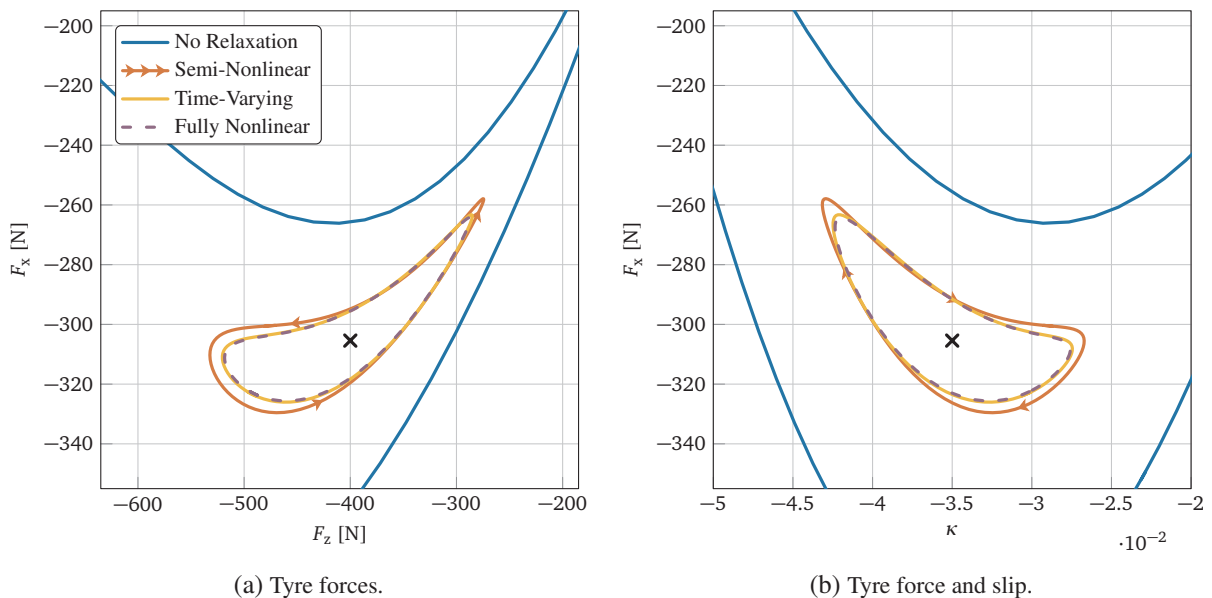


Figure 4.19: Tyre forces and slip phase space of limit cycles for different relaxation models (no relaxation, semi-nonlinear, time-varying and fully nonlinear) refined up to the fourth harmonic ($V_{fx} = 44 \text{ m s}^{-1}$).

important comments descend from the analysis of Figure 4.19. The limit cycles displayed suggest that:

- (i) the semi-nonlinear model is slightly less stable than the nonlinear ones.

- (ii) The fully nonlinear model and the time-varying one are nearly identical.

Furthermore, it has also been observed that the larger the limit cycle amplitude is, the smaller (in modulus) the Floquet multipliers governing its stability will be, as in the case with no relaxation. This means that larger limit cycles are more effective in attracting the solutions. The fifth multiplier, generated by the addition of the relaxation equation in a state space representation of dimension five, is therefore real and is found to be extremely small in modulus. A further difference with respect to the case with no relaxation is found in the relationship between frequency and amplitudes of the limit cycles: with no relaxation the frequency decreases with increasing amplitude, while the opposite is true with relaxation.

As a final remark, it can also be observed that, since the effects of relaxation on motorcycle chatter in most cases are small, the use of simplified models as those discussed here are conservative with respect to stability, and well justified. In any case, it can be concluded that reducing relaxation to reasonably small values (<100 mm) has beneficial effects with respect to chatter stability, while relaxation lengths near zero tend to be slightly destabilising.

4.4 Conclusions

In this chapter, a contribution to the nonlinear investigation of the unstable driveline ‘chatter’ mode of a motorcycle is given. A minimal two DOFs model including tyre relaxation is analysed both in a linearised form and with full nonlinear equations to study its post-bifurcation behaviour. The nonlinear system without tyre relaxation is found to have a supercritical behaviour with a single stable limit cycle in the parameter domain of technological interest growing with linearised instability. This confirms that linear analysis is valid in predicting system stability. The growth of the limit cycle soon after the linear stability boundary in any case is strong enough to overcome the limits of what could be acceptable for motorcycle stability. Further, a sensitivity analysis is performed to identify the influence of each of the model parameters on the limit cycle amplitude, identifying the most influential ones with the aid of bifurcation diagrams and confirming that the main driver of nonlinear asymptotic behaviour comes from the tyre characteristic function. Tyre relaxation can produce destabilising effects both in the linear and nonlinear models, reducing the interval of stability with respect to travelling speed, until the model becomes indefinitely unstable. However, adopting realistic values of relaxation length, those effects are found to play a minor role. A summary of the findings of this chapter is presented in Table 4.5.

Table 4.5: Summary of nonlinear effects on motorcycle chatter.

Model Characteristic	Summary of Effects
Limit cycle solutions	Of the methods described by Nayfeh and Mook [2004], it is found that the harmonic balance method is best suited for the problem at hand. It is able to provide a high order harmonic solution to the Taylor expanded nonlinear system quickly and accurately.
Relaxation on the linear system	With sufficiently small relaxation lengths (<100 mm), the stability of system tends to be insensitive to changes in relaxation length. Very large values introduce instability via the LTI FRF by the introduction of de-stabilising phase lag. The system without relaxation tends to be less stable than one with small relaxation, leading to the conclusion that linear analysis without the use of relaxation length is practically conservative in terms of estimating stability.
Prominent nonlinear terms	The leading cause of the system nonlinear behaviour is found to be the tyre longitudinal force characteristic function (the MF model).
Limit cycles	In the parameter domain of interest, a single stable supercritical limit cycle is found, though its amplitudes are larger than can be considered acceptable for motorcycle stability. This confirms that the use of linear analysis is capable of predicting system stability.
Nonlinear relaxation	It is found that a LTI relaxation model is able to reproduce the nonlinear behaviour of the fully nonlinear with sufficient accuracy.

5 Chatter Stability in Mid-Corner and Acceleration

5.1 Introduction

Motorcycles which approach tyre limits, such as those found in racing, tend to experience high frequency oscillations caused by tyre characteristics [Tezuka et al. 2004, Cossalter et al. 2008]. Some of these modes have come to be known as ‘chatter’ or ‘patter’, among other things, as discussed in the previous chapters. Recently, a similar high frequency mode with tyre interaction has been encountered during cornering manoeuvres of a racing motorcycle indicating that there possibly exists a similar mode to chatter that can occur mid-corner which could also include lateral elements.¹ Typically single-track vehicles in cornering manoeuvres tend to experience a merging of their in-plane and out-of-plane modes, resulting in new ‘mixed modes’ that could introduce instability [Koenen 1983]. It is possible that the chatter mode experiences a similar merging with another out-of-plane mode, leading to instability.

Past research into these phenomena in the mid-corner region has been sparse and diverse, and the possible root causes identified for these vibrations have varied. For example, Tezuka et al. [2004] studied the oscillation of a multi-body motorcycle during cornering and concluded the phase relationship of the pitch, bounce, and hop modes were causing instability, driven by a coupling to the friction forces of the tyres. Whereas Sharp and Watanabe [2013] studied constant speed cornering manoeuvres at varying lateral accelerations with the effects of the structural flexibility of the steering head considered. The study demonstrated that a sufficiently flexible steering head could cause instability during high lateral acceleration manoeuvres.

This chapter explores the possible existence of a mixed chatter or tyre influenced mode of the rear suspension of a motorcycle in the range of 8 Hz to 25 Hz during high roll angle, high lateral acceleration mid-corner manoeuvres. Beginning from the minimal model presented in Chapter 3, the stability of the driveline mode is investigated, and the switching mechanisms determined. The same is done for a similar mid-corner manoeuvre, but with tractive acceleration, changing the sign of the chain torque and resulting geometry. Finally, a more complete multi-body model is presented and tested in a similar manoeuvre in an attempt to validate the existence of possible modes that can become unstable in the frequencies of interest.

5.2 Minimal Model Analysis

The three DOFs minimal model presented in Chapter 3 is employed to simulate mid-corner manoeuvres. The stationary operating points used to linearise the model are taken from the same dataset presented in Subsection 3.2.4, but later in the manoeuvre during high roll angle and high lateral acceleration. The figure is reproduced here with the new regions highlighted in Figure 5.1.

Two quasi-static regions are identified where tyre forces are generally steady or close to zero. The mid-corner region represent high roll angle, high lateral acceleration operation with differing chain configurations and tyre use limits. The region is split into three subregions: the first has a chain in braking configuration with both tyres on the slip limit, the second has a slack chain with the front tyre on the slip limit, and the third has the chain in the traction condition and is again on the slip limit of both tyres. The transients between these subregions are removed for the linear analysis. Finally an acceleration region is chosen which represents the transition out of the corner with higher longitudinal acceleration values and lower roll angles, again with the chain in the traction condition.

Figure 5.2a shows the eigenvalues for the combined mid-corner region. It shows an unstable rear hop mode, though at a lower eigenfrequency range of 6 Hz to 9 Hz. Figure 5.2b–5.2d show the respective eigenvectors for these

¹Personal communications with a MotoGP engineer, 2021.

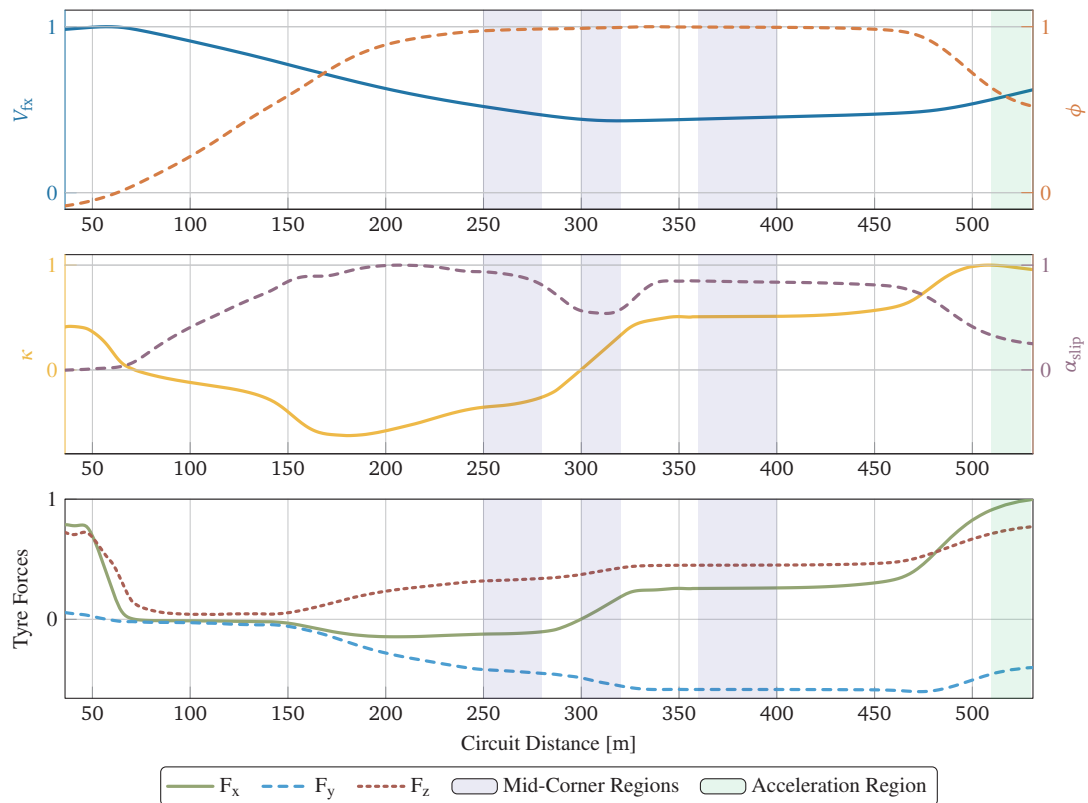


Figure 5.1: Manoeuvre used to extract quasi-static conditions, as computed by Leonelli and Limebeer [2020]. y -axes have been normalised due to confidentiality agreements. The mid-corner region used in this chapter is highlighted in blue, while the acceleration region is highlighted in green.

modes. The rear hop eigenvector contains a larger contribution of the roll angle DOF which explains the lower experienced frequencies of the mode, given the high inertia values about the roll axis. The reversal of the chain force shows little effect on the modes, other than to flip the phase of the wheel speed oscillations which themselves do not play a large role in the unstable mode.

The eigenvalues for the acceleration region are shown in Figure 5.3a. This region also shows an unstable rear hop mode with a lower eigenfrequency, though the mode moves towards stability as the manoeuvre progresses. The eigenmodes are displayed in Figure 5.3b–5.3d, and the unstable rear hop eigenvector has its main contribution from the roll angle DOF. The mode also shows a reduced presence of swingarm oscillations and an increased role of wheelspeed oscillations.

Energy flow analysis is performed by inspecting the energy dissipated by the non-conservative forces in the model over one cycle as outlined in Subsection 3.3.3. Instability arises when the contribution from the tyre forces overcome the dissipation provided by the system damper. Therefore, a key factor in the switching mechanism to instability is the phase offsets between the ground forces and the state velocity vector. For example, the oscillating components of the tyre forces and corresponding slip velocities from Equation (3.88) are shown in Figure 5.4 for the most stable point in the mid-corner region. Note that in this figure, the exponential growth term due to the instability of the mode at this operating point has been removed to more clearly focus on the phase offsets. The figure shows a phase offset of the longitudinal components of 35.7° , while the lateral components are closer to quadrature at 83.0° . Despite this, the size of the lateral component amplitudes cause their contribution to energy accumulation to be 65% of the total energy accumulation. This metric during different mid-corner subregions remains large, growing to nearly 100% while the chain is slack, and remaining approximately 75% when the chain is active in the traction condition.

Figure 5.5 shows the tyre force and slip velocity relationships for the acceleration region at a point near the stability boundary. Here, the phase offsets are found to be 83.4° and 89.2° for the longitudinal and lateral components, respectively. In this region, unlike the mid-corner ones, the primary driver to the growth of unstable oscillations is

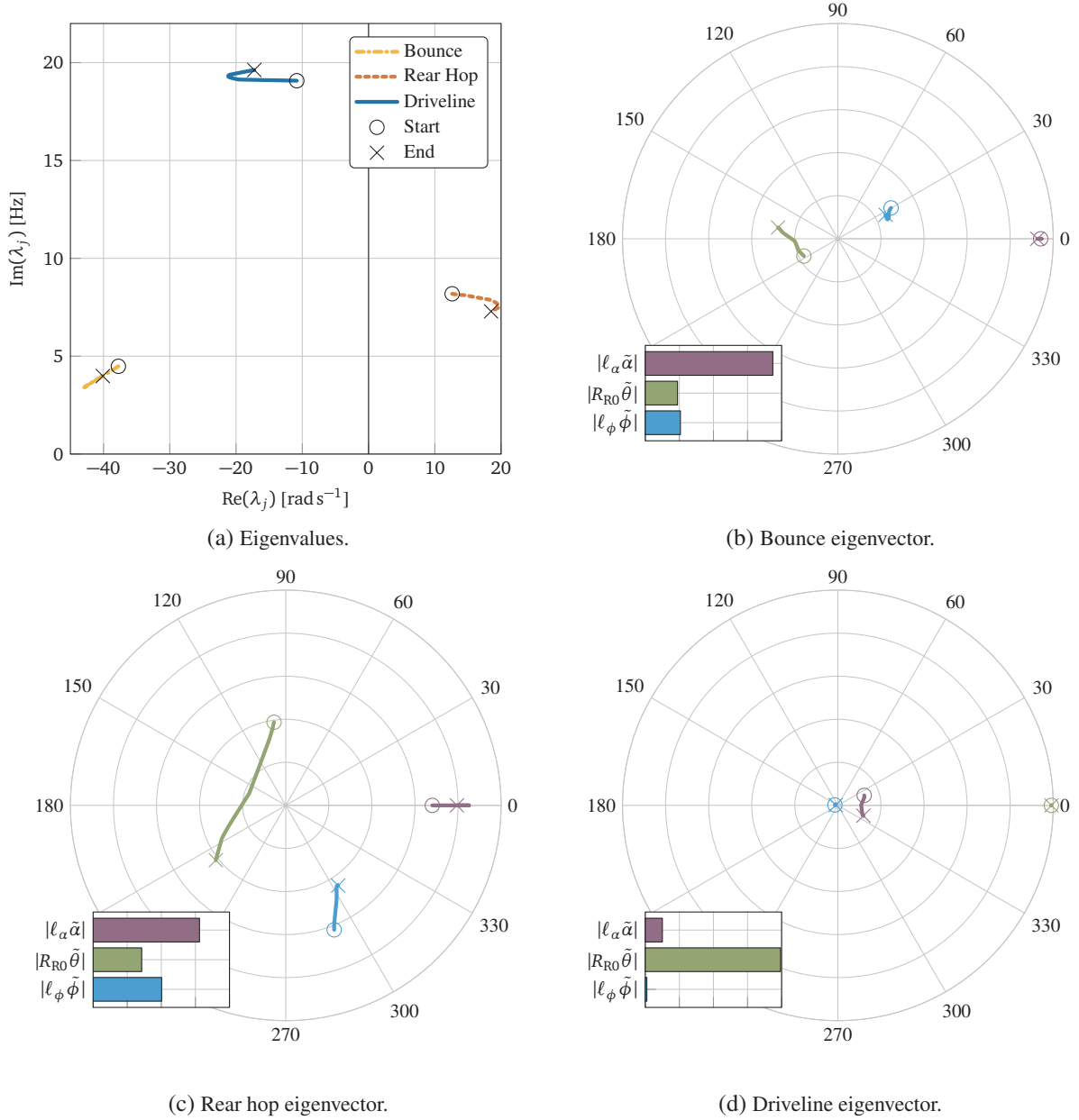


Figure 5.2: Quasi-static linear model eigenvalue analysis of the mid-corner regions. Evolution of the eigenvectors are shown normalised and phased to their largest component, while the bar chart legends show the average component magnitudes.

the longitudinal components, contributing 86 % of the total energy accumulation over one cycle, while the lateral components remain close to quadrature.

In general, through the use of the minimal model presented in Chapter 3, an unstable rear hop mode is found in both the mid-corner and acceleration regions of a racing manoeuvre. In both cases, due to the high roll angles experienced, the mode shows a lower oscillation frequency and a larger contribution of the roll angle DOF, signifying the vertical oscillation of the tyre is facilitated more by this DOF. In the mid-corner region the lateral force is the major contributor to instability, irrespective of the loading condition of the chain. This is expected due to the region encompassing high roll angle operation when longitudinal forces are at their minimum. In the acceleration region these contributions are closer to those of the braking region, with longitudinal remaining the largest contributor to energy accumulation over one cycle. This preliminary study of the minimal three DOFs model gives insight into what types of instabilities could be occurring during the high roll angle mid-corner and acceleration regions of a racing manoeuvre and the mechanisms which drive them, but ultimately a high fidelity multi-body model will need to be tested in a similar manner to validate the findings here.

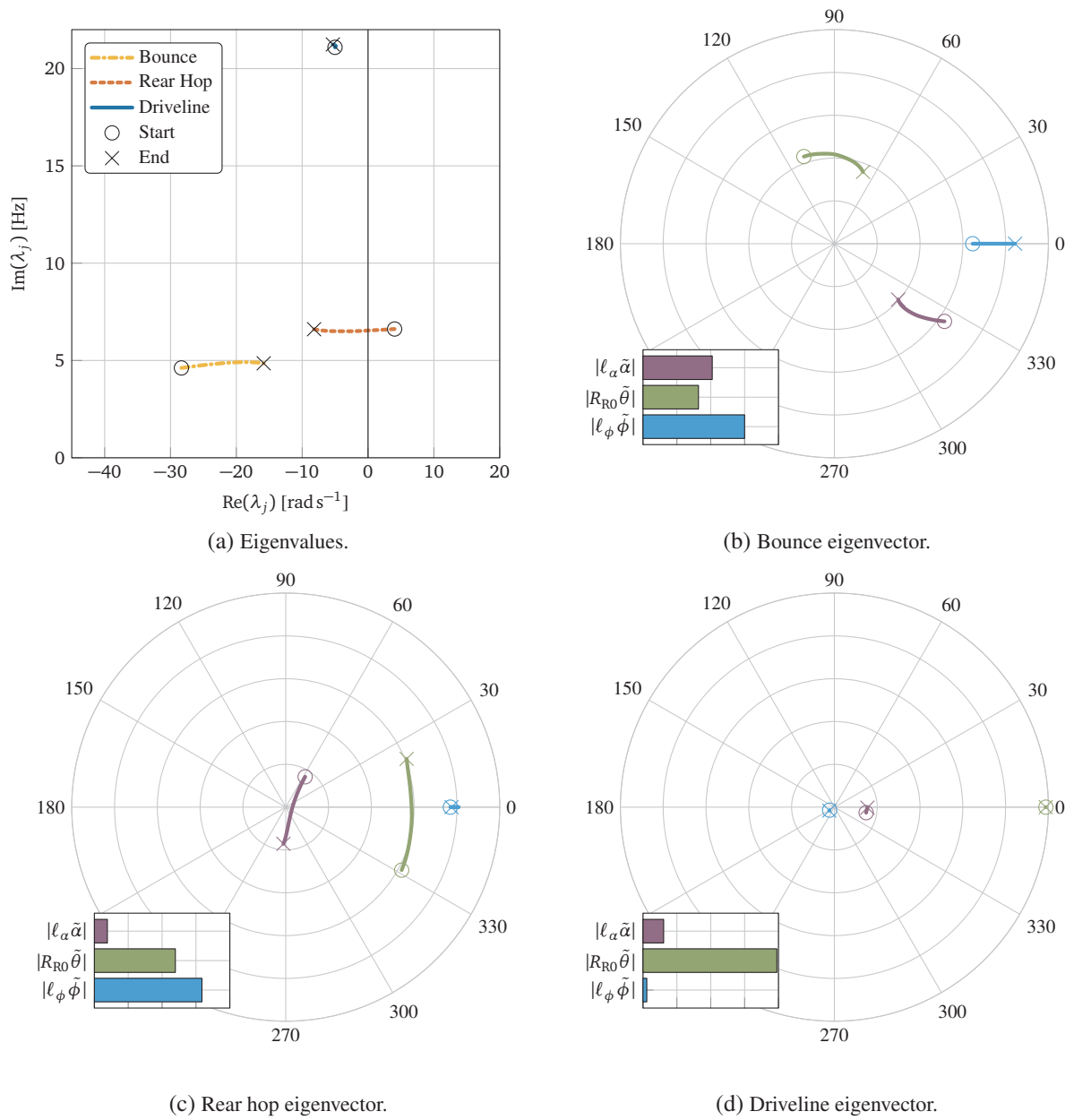


Figure 5.3: Quasi-static linear model eigenvalue analysis of the acceleration region. Evolution of the eigenvectors are shown normalised and phased to their largest component, while the bar chart legends show the average component magnitudes.

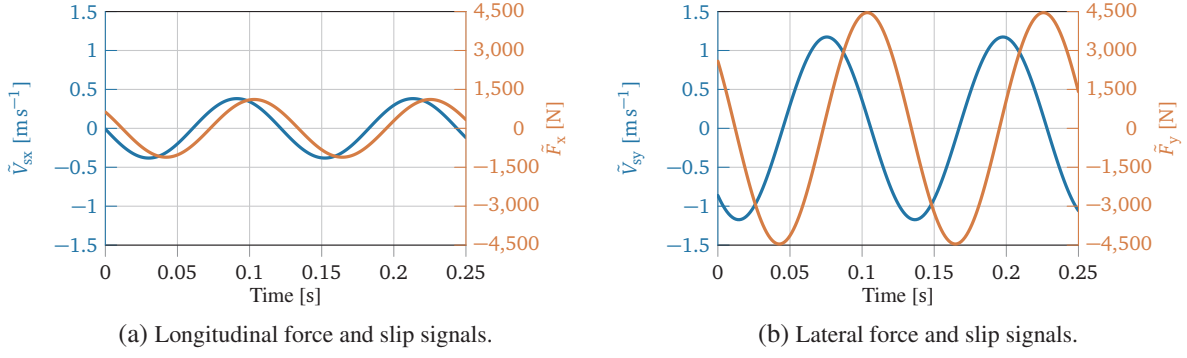


Figure 5.4: Tyre force and slip signals used for the energy analysis of the mid-corner region.

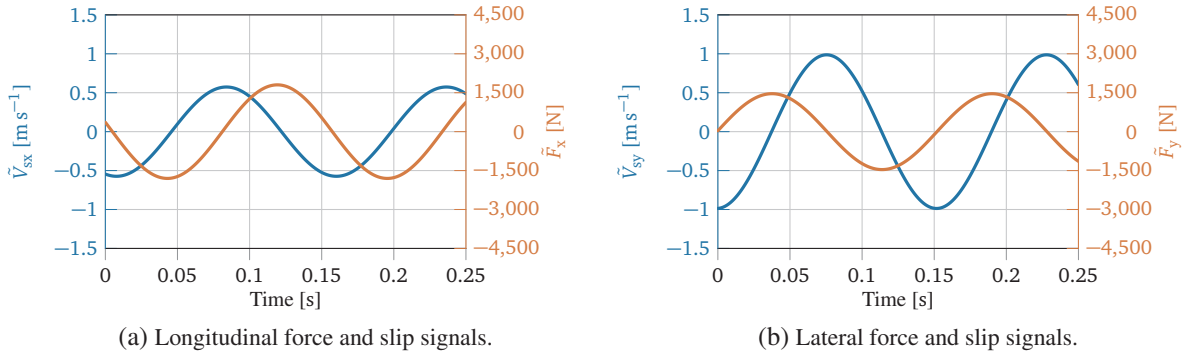


Figure 5.5: Tyre force and slip signals used for the energy analysis of the acceleration region.

5.3 Multi-Body Model Analysis

An attempt to validate the findings of the minimal model analysis of the previous section is performed using a multi-body model. The model is simulated through a similar manoeuvre to investigate the behaviour of the motorcycle and search for the instabilities in question. Multi-body models are, in general, more complex and difficult to analyse but offer a closer approximation to the real motorcycle [Sharp et al. 2004, Cossalter et al. 2011]. Consequently, a multi-body representation of a motorcycle is adapted from a model produced by Passigato et al. [2020] using open-source multi-body simulation software.² The choice to use open-sourced software is made due to its increased accessibility and adaptability. The multi-body model developed consists of seven bodies with 13 DOFs and is presented in a simplified form in Figure 5.6.

The first body is the main frame, translating and rotating (in the yaw–roll–pitch convention) in a Cartesian plane, considering a flat ground. Attached to the main body are the swingarm with an in-plane revolute joint (the swingarm joint), the crankshaft with an in-plane revolute joint (the crank shaft axle), and the upper fork assembly with an out-of-plane revolute joint (the steering joint). In turn, the rear wheel is attached to the swingarm by means of another in-plane revolute joint (the rear axle). Attached to the upper fork assembly is the lower fork assembly by means of a two DOFs joint representing the in-plane prismatic linear travel of the front fork, and the out-of-plane bending flexibility of the front assembly. The prismatic joint represents the traditional telescoping fork suspension of a motorcycle, while the lateral bending flexibility is added as it is a critical feature in the stability of the wobble mode [Passigato et al. 2020]. Finally, attached to the lower fork assembly by an in-plane revolute joint (the front axle) is the front wheel. The main frame contains the total sprung mass of the motorcycle, including rider, with the exception of the rotating components of the drivetrain, which are represented by the mass and inertia of the crankshaft body.

The forces shown in red are: the tyre forces F_{xf} , F_{yf} , F_{zf} , F_{xr} , F_{yr} , F_{zr} , the braking moments M_{bf} , M_{br} (which are internal and applied to both their respective wheel and suspension component), the engine torque M_e , the chain force F_c , which is determined using the model developed in Subsection 3.2.1 (there is also a reaction component

²MBSim (www.mbsim-env.de).

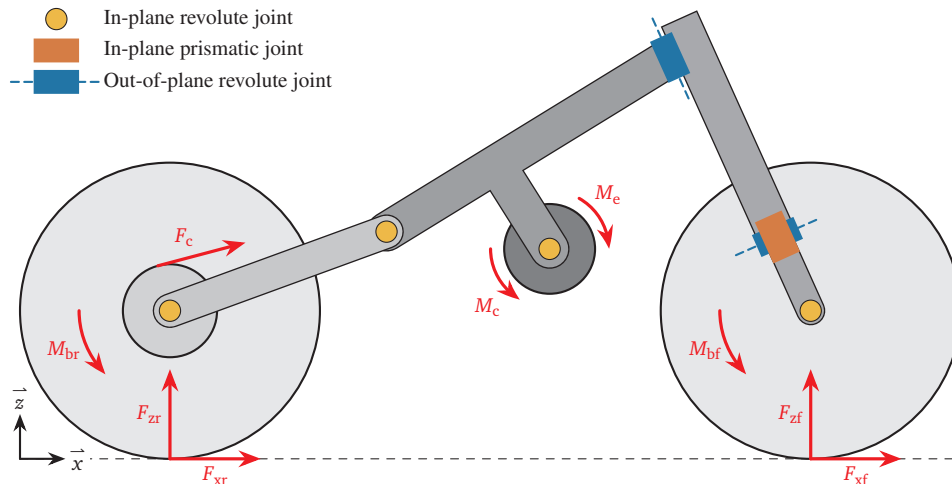


Figure 5.6: Multi-body model schematic. External forces shown in red, out-of-plane forces and the y -axis (into the page) are not shown.

of this force applied to the frame at the pinion, but is not shown in Figure 5.6), and the chain moment on the engine M_c , which is the resultant of the chain force applied through the powertrain gear ratios. Internal forces include the steering control and steering damper torques applied across the steering joint, the front suspension spring and damper forces applied across the prismatic joint, the rear suspension spring and damper torques applied across the swingarm joint (which themselves are calculated via a four bar linkage mechanism common to most modern motorcycles), and the front assembly structural flexibility applied across the front fork rotation joint. The tyre vertical loads are modelled using the MF-MCTire method as presented by Schmeitz et al. [2010], and the tangential forces are calculated using the MF as presented by Pacejka [2012].

The model is characterised using the parameter set outlined by Leonelli et al. [2018], with the rear suspension parameters updated to better match those of Chapter 3 and Section 5.2. A similar validation procedure to Subsection 3.3.1 is performed to ensure the models appropriately match. The pertinent characteristics of the motorcycles are outlined in Table 5.1, but the complete list of parameters is left out for brevity.³

The model is controlled via two proportional integral derivative (PID) controllers. The first controls the forward speed of the vehicle, this PID controller uses the engine torque M_e to match a target velocity. This controller also contains a feed-forward term based on the target velocity. The lateral PID controller uses the steering torque to control roll angle ϕ , with feed-forward terms from the roll angle target, its time derivative, and the steering torque introduced by the front brakes. The manoeuvre chosen to be simulated is the same as the one presented in Subsection 3.2.4, though for the multi-body model to complete this tyre limited racing manoeuvre with such simple rider controls, the input targets need to be adjusted. The roll angle target is lowered by 10%, and the time is scaled longer by a factor of 10%. These reduce the lateral and longitudinal acceleration demands of the motorcycle and tyres, allowing the multi-body model to complete a simulation without tyre lift or exceeding the tyre limits.

The time domain results of the simulation are presented in Figure 5.7, where the manoeuvre data are shown with dashed lines, and the multi-body simulation data are shown with solid lines. The velocity, roll angle, and rear tyre

Table 5.1: Pertinent characteristic details of the multi-body model.

Characteristic	Unit	Value
Caster angle	$^\circ$	24.0
Front tyre radius	m	0.298
Rear tyre radius	m	0.330
Total drivetrain ratio (excluding sprockets)	–	3.45
Total mass	kg	261
Weight distribution	% front	47.6
Wheelbase	m	1.41

³Full model and parameters are available upon reasonable request to the author (alexander.schramm@studio.unibo.it).

forces are well matched between the two datasets, with the tangential rear tyre forces being slightly less due to the reduced acceleration demands from the roll angle and time scaling. The side-slip angle of the rear tyre begins the manoeuvre with a good match, but diverges after the braking region. This could be due to several factors: an inadequate rider model not able to keep the motorcycle on the rear tyre limit causing the front tyre to slide more than necessary, an inadequate front tyre model not able to reproduce the desired grip levels, or lack of rear brake usage by the rider controller. The multi-body model shows an unstable chatter vibration in the braking region, as expected from the analysis in Chapter 3, as well as an unstable cornering weave mode, similar to the combined mode found by Koenen [1983]. The region of interest to this chapter begins after the chatter instability stabilises and the mid-corner region begins, from 5 s onwards.

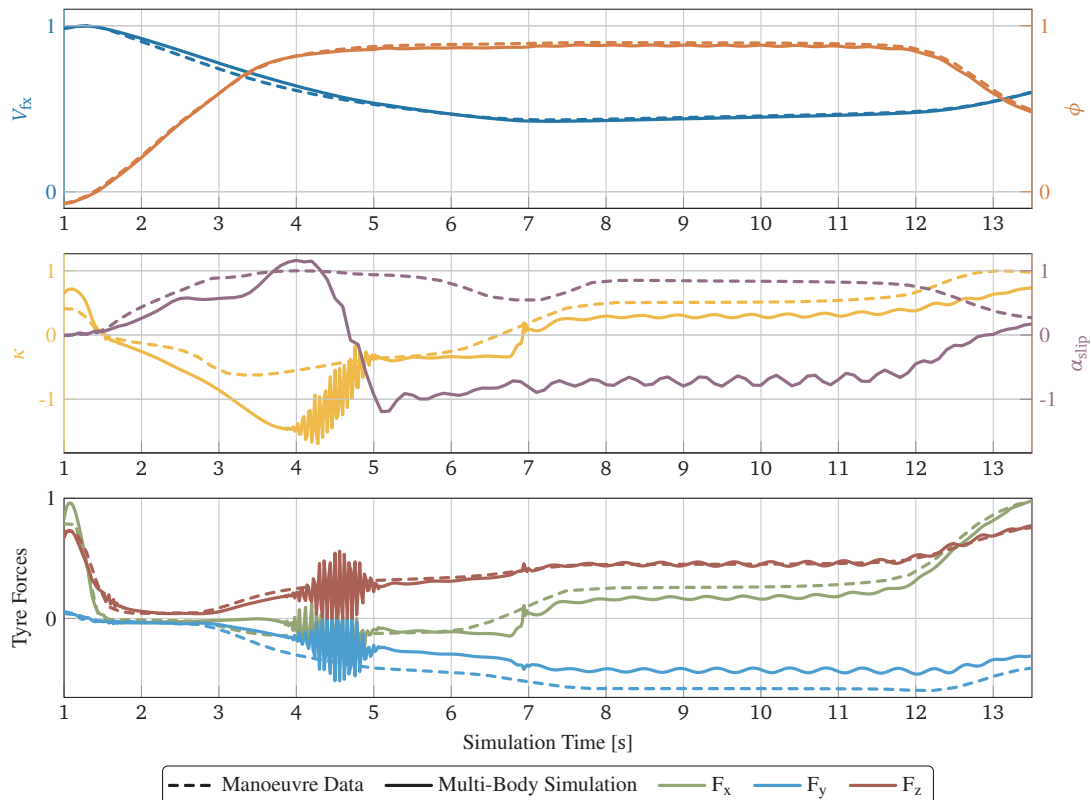


Figure 5.7: Manoeuvre data and the simulation response of the multi-body model. Values shown for the rear tyre.

An unstable rear suspension mode in the range of 8 Hz to 25 Hz, though, is not immediately apparent in this time-series data. The chatter mode during braking is present, and the unstable cornering weave mode seen in the latter portion of the manoeuvre has too low of a frequency to be considered pertinent in this investigation. Consequently, quasi-static linear analyses are performed at time intervals across the manoeuvre using the multi-body model to discern the eigenvalue behaviours of the system. The resulting root locus plot is presented in Figure 5.8 with the minimal model modes overlaid. Note that this chapter is interested only in modes pertaining to the rear of the motorcycle, those are the driveline and rear hop modes, and to some extent the pitch, bounce, and weave modes, if their frequencies were to become high enough. The figure shows the oscillatory modes of the multi-body model as points, grouped by colour and labelled with the generally accepted modal names of a motorcycle. As seen in the time histories of the manoeuvre, the driveline mode becomes unstable during the braking portion of the manoeuvre but returns to stability during the mid-corner region (this can be better seen in the time histories of the real part of the eigenvalues in Figure 5.10, shown later). Overlaid in black are the modes from the minimal model which, as described in Section 5.2, show a high frequency stable driveline mode, a lower frequency unstable rear hop mode, and a well damped low frequency bounce mode. The figure refutes the existence of the unstable mode which the minimal model exhibits becoming unstable. While the driveline modes of both models tend to have similar behaviours, neither the rear hop mode nor the other in-plane modes involving the rear suspension (pitch or bounce) show any instability, or indeed any similarity in behaviour to what the minimal model is predicting. This suggests

Table 5.2: Variations of the multi-body model.

Model	Swingarm Torsional Stiffness	Swingarm Bending Stiffness
Reference Model	—	—
Variation 1	62 700 N m rad ⁻¹	—
Variation 2	31 400 N m rad ⁻¹	—
Variation 3	—	406 000 N m rad ⁻¹
Variation 4	—	203 000 N m rad ⁻¹
Variation 5	62 700 N m rad ⁻¹	406 000 N m rad ⁻¹
Variation 6	31 400 N m rad ⁻¹	203 000 N m rad ⁻¹

that in the case of very large roll angles, the minimal model is insufficient for modelling the full behaviour of the rear suspension of the motorcycle.

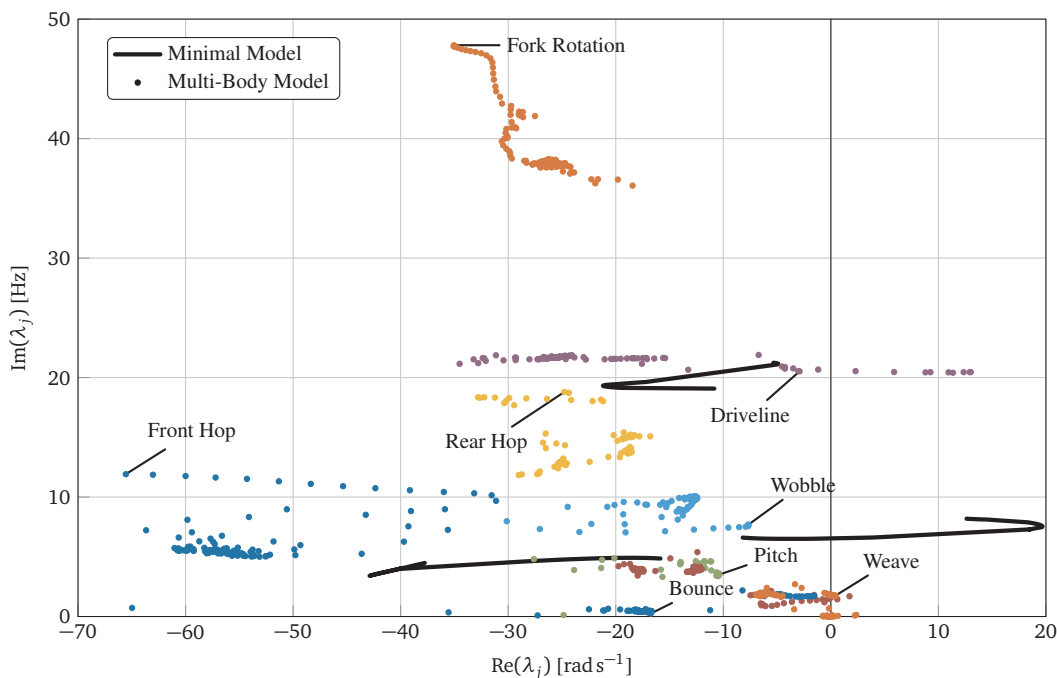


Figure 5.8: Root locus comparison of the multi-body model and the minimal model eigenvalues. Multi-body eigenvalues are shown as coloured points, the minimal model modes are overlaid as black lines. The minimal model modes shown are the high frequency driveline mode, the unstable rear hop mode, and the damped low frequency bounce mode.

As a final step, several different structural flexibilities in the swingarm are introduced into the multi-body model to see if they play a role in the development of any instabilities, as they do at the front of the motorcycle in the case of wobble [Passigato et al. 2020]. Introduced at the swingarm axis, two additional degrees of freedom are added to the multi-body model: a swingarm torsional rotation aligned along the swingarm line and a swingarm bending rotation aligned orthogonal to the torsional and in-plane axis rotations. These work to represent the two major structural flexibility modes in the swingarm. Table 5.2 outlines the variations of the reference multi-body model tested. The first two include only the swingarm torsional flexibility at nominal and halved stiffness values. The next two include only the swingarm bending flexibility again at nominal and halved stiffness values. The final two variations introduce both flexibilities at nominal and halved values of stiffness.

The quasi-static linear analyses of Figure 5.8 is again performed for each model variation, the results are shown in Figure 5.9. The region of interest for this investigation is also highlighted in yellow and the new structural flexibility modes can be seen in the upper quadrant of the figure. In general, the swingarm bending mode is less damped than the torsional mode, and has a lower natural frequency, similar to that of the fork rotation mode. In the region of interest, there is no appreciable difference in the modes between the variations, the rear hop mode remains relatively constant for all variations, while the driveline mode only has an appreciable change during the unstable braking region of the manoeuvre.

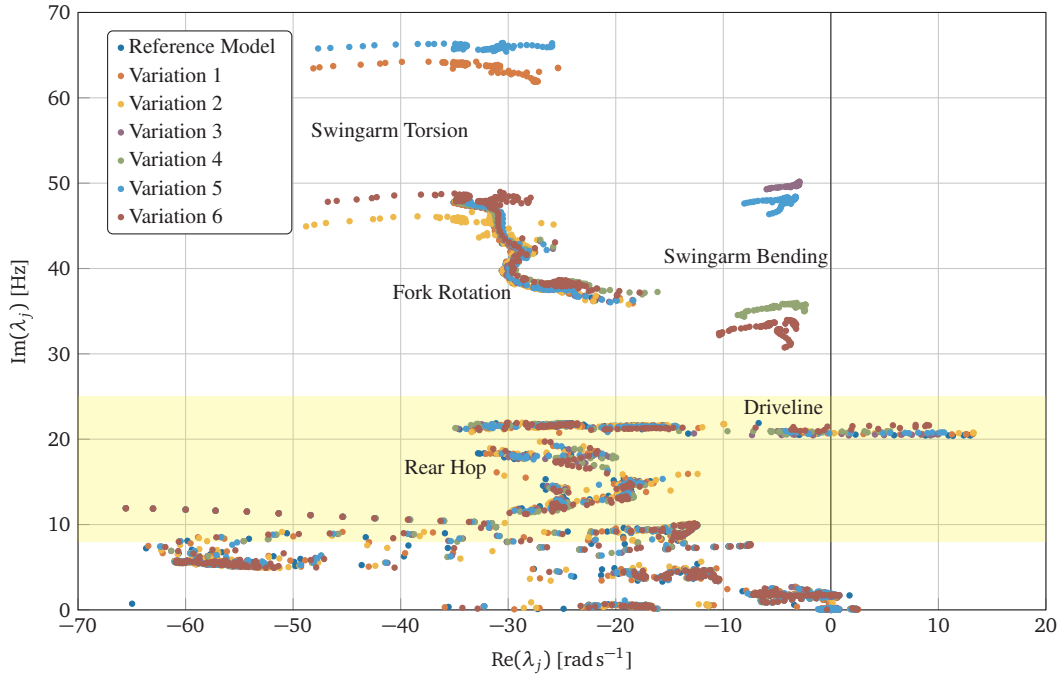


Figure 5.9: Root locus with structural flexibility variations to the multi-body model. Region of interest to the current investigation is highlighted in yellow.

This is better represented in Figure 5.10, where the time domain evolution of the driveline and rear hop eigenvalue real parts are shown for each model variation. The region of interest, after braking and during the mid-cornering and acceleration portions of the manoeuvre, tend to show no differences to the real parts of the modes with the model variations. Although, it can be seen that Variation 4, the model with only swingarm bending flexibility at half of the nominal value, shows a much lower real part in the driveline mode during the braking instability. This could indicate that the structural bending mode of the swingarm plays a role in the stability of the chatter mode of a motorcycle, and warrants further investigation.

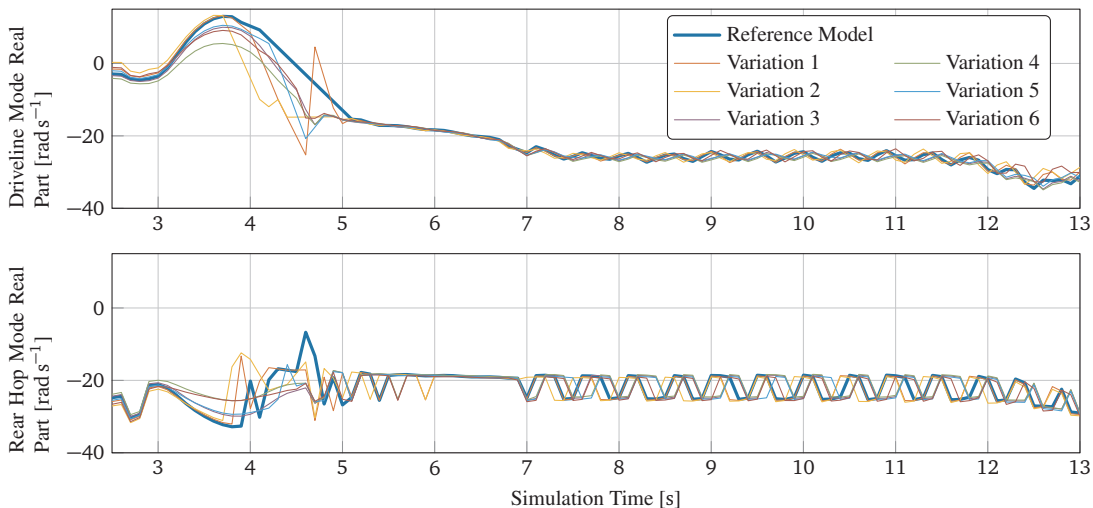


Figure 5.10: Evolution of the real parts of the driveline and rear hop modes of the multi-body model.

5.4 Conclusions

This chapter set out to investigate the possible existence of unstable high frequency modes of the rear suspension of the motorcycle during mid-corner manoeuvres. Of interest is the possible interaction of the rear suspension and

driveline with the lateral and vertical dynamics of the rear tyre. A racing cornering manoeuvre is considered, and the post-braking mid-corner region and the initial acceleration region are of particular interest, where the driveline undergoes different chain loading conditions.

At first the minimal model from Chapter 3 is used to investigate the stability of the rear suspension while in high roll angle operation. The model predicted an unstable rear hop mode in both the mid-corner and acceleration regions of the manoeuvre, but with much lower frequencies due to the higher interaction of the roll angle DOF. Energy flow analysis also revealed that in the mid-corner region the main driver to instability was the lateral tyre force and its phase relationship with the lateral slip velocity.

Next, a full multi-body model of a motorcycle is considered to validate the results of the minimal model. The 13 DOFs model is operated through the same manoeuvre as the minimal model, and the time history and quasi-static linear analyses plotted. The results of the multi-body analysis show that the minimal model is insufficient in predicting instability at very large roll angles such as those encountered in the given manoeuvre. Since the minimal model is not able to correctly reproduce the dynamics of the multi-body model for the given manoeuvre, it can not be considered as a minimal model for the study of the phenomena in question. It may be possible to add additional dynamics to the minimal model to better reproduce the behaviours witnessed in the multi-body model, however this would introduce more complexity to the analysis, and the current three DOFs system is analytically cumbersome as is. Moreover, since the multi-body model was unable to reproduce the unstable behaviour that was experimentally reported, seeking an appropriate minimal model would be meaningless at the moment. Further developments into the multi-body model would first need to be performed, in an attempt to reproduce the phenomena in question.

Additionally, several different variations of the model where different structural flexibilities of the swingarm are introduced are tested. The resulting linear analyses showed no effect on the rear hop mode, though the bending flexibility of the swingarm was able to stabilise the driveline mode slightly in the braking region, which warrants further investigation. In conclusion, the models presented here are not able to properly capture any possible unstable high frequency modes in the mid-corner, if they exist.

6 Conclusions

This thesis sets out to deepen the understanding of an unstable oscillatory motion in racing motorcycles known as chatter. In Chapter 3, a minimal three DOFs model is developed to model the rear suspension, wheel, and driveline of a racing motorcycle that includes considerations for motorcycle roll angle and lateral dynamics. The minimal model is validated through comparison with a multi-body code, and shows a good fit for the manoeuvre and modes of interest.

Quasi-static linear root locus analysis is performed through a typical braking manoeuvre, finding an unstable driveline mode causing chatter. Energy flow analysis shows that the longitudinal forces are the main driver to instability, given its phase offset with the slip velocity is such that it causes an energy accumulation over one oscillation cycle. The lateral force is found to have insignificant energy contributions. Eigenvalue sensitivity analysis gives insight into the most influential factors affecting the stability of chatter. These are parameters that affect the frequencies of the rear hop and driveline modes, tyre force gradients, and geometric parameters affecting the chain stiffness matrix. The mechanism of instability is analytically determined to be non-conservative restoring forces arising from an asymmetric system matrices, caused mainly by tyre force gradient terms. The possibility of another mechanism arises if the tyre force exceeds peak values, and a negative tyre force gradient with respect to slip occurs.

Several methods of stabilising a system with unstable chatter oscillations are demonstrated. Splitting the driveline and rear hop mode frequencies by varying tyre or chain stiffness, wheel mass and inertia, or rear sprocket radius shows stabilising effects. Chain geometry shows stabilising behaviour as it becomes more parallel with the swingarm. Swingarm angle itself, if the chain to swingarm angle is held fixed, does not have much effect on stability. Finally, the roll and lateral dynamics do not play a direct role in instability, but increased static roll angle moves the system to instability which is attributed to the movement of the working point of the tyre characteristic function (the MF model), which drives the tyre force gradients in destabilising directions.

Chapter 4 studies the effects of relaxation length and the nonlinear characteristics of the minimal model. The model is reduced to two DOFs by removal of the roll angle, and the option for relaxation behaviour is introduced. Three versions of relaxation length are derived, the first being the classic LTI relaxation model. The second and third models are nonlinear and derived from the general definition of the Maxwell model with the inclusion of variable vertical load. It is noted that the explicit dependence of vertical load vanishes from the resulting nonlinear relaxation model. The second model applies the assumption that relaxation length depends on the instantaneous state variables, while the third model remains the fully nonlinear version of the equations, wherein the relaxation length depends on the relaxed slip itself. It is shown that the effects of relaxation in the linear stability analysis are minimal, and in fact the neglecting of relaxation behaviour would be a somewhat conservative assumption in terms of stability analysis.

The existence and properties of nonlinear limit cycles are studied through numerical simulation and the harmonic balance method. Other analytical methods are attempted without success due to complexities in the model. Numerical analysis shows the existence of a stable limit cycle in the unstable region of operation, and the harmonic balance method confirms the finding. The driving nonlinear term in the EOMs is found to be the tyre force function (the MF model). The effects of parameter variations on limit cycle amplitude are tested and compared to the effects on linear stability. Phase portraits are presented and the effects of pertinent parameters shown. Using Floquet theory, the limit cycle is found to be stable, and the result of a supercritical Hopf bifurcation in the forward velocity variable. The FRFs of the three relaxation models are found, separated from the other EOMs by imposing first order limit cycle behaviour for the state variables. The Bode diagrams and numerical simulations show no discernable difference between the models in the frequency range of interest.

Finally, Chapter 5 explores new operating regions that have not been widely studied in past literature. Both the three DOFs minimal and a full multi-body model are used to discern the modal behaviour of the rear suspension

during high roll angle, high lateral acceleration manoeuvres in both traction and braking. The results show that the minimal model cannot adequately reproduce the dynamics of the multi-body model in the regions of interest, and therefore is insufficient for predicting stability behaviour for high roll angle manoeuvres. The multi-body was also unable to reproduce any unstable oscillations of interest. Further augmentations to the multi-body model are tested, including swingarm torsion and bending compliances of different stiffnesses and in different combinations. These have little effect on the rear stability of the motorcycle, though the bending flexibility of the swingarm was able to stabilise the driveline mode slightly in the braking region.

6.1 Future Work

There are several lines of open research that arise from either the unanswered questions of this thesis or from newly introduced ones. This section will reflect on the work performed, the shortfalls herein, and contemplate the possible future lines of research this thesis lays the foundation for.

Chapter 3 does a thorough investigation of not only the role that motorcycle roll angle has in the chatter instability, but also confirms past assumptions made around the use of simplified models. It would be beneficial to better understand the relationship between the minimal model and the more complex multi-body simulations, especially in terms of the powertrain dynamics. It also lacks, perhaps as a concluding section, the simplification of the minimal model to small, static roll angles, as suggested in the concluding remarks.

In regards to Chapter 4, an analytical solution to the limit cycle of the two DOFs minimal model, even if in simplified form, is still missing. A suitable analytical solution would be greatly beneficial in the study of the nonlinear characteristics of these systems, especially in determining the driving parameters to limit cycle generation and stability. The methodologies presented here could also be applied to related problems such as the front padder instability.

Finally, Chapter 5, as an exploratory chapter, leaves a lot of research questions unanswered. It was not successful in identifying the mid-corner instability it had set out to find, and further investigation is required in that aspect. This includes further improvements in the multi-body model and perhaps a derivation of a more appropriate minimal model for use in studying the mid-corner manoeuvres. On a positive note, the multi-body simulations were able to detect an effect of swingarm bending stiffness on chatter stability during the braking region of a racing manoeuvre. In this case, the three DOFs minimal model could be modified to introduce a bending compliance DOF for the swingarm to study the effect swingarm structural flexibility has on chatter.

References

- Aoki, A. (1979). 'Experimental Study on Motorcycle Steering Performance'. In: *1979 Automotive Engineering Congress and Exposition* (01/02/1979). No. 790265. Society of Automotive Engineers, Inc. DOI: 10.4271/790265. Available: <https://www.sae.org/publications/technical-papers/content/790265>.
- Bakker, E., Nyborg, L. and Pacejka, H. B. (1987). 'Tyre Modelling for Use in Vehicle Dynamics Studies'. In: *SAE International Congress and Exposition* (23–27/02/1987). No. 870421. Detroit, USA: Society of Automotive Engineers, Inc. DOI: 10.4271/870421. Available: <https://www.sae.org/publications/technical-papers/content/870421>.
- Bakker, E., Pacejka, H. B. and Lidner, L. (1989). 'A New Tire Model with an Application in Vehicle Dynamics Studies'. In: *Autotechnologies Conference and Exposition* (01/04/1989). No. 890087. Society of Automotive Engineers, Inc. DOI: 10.4271/890087. Available: <https://www.sae.org/publications/technical-papers/content/890087>.
- Besselink, I. J. M., Schmeitz, A. J. C. and Pacejka, H. B. (2010). 'An Improved Magic Formula/SWIFT Tyre Model That Can Handle Inflation Pressure Changes'. In: *Vehicle System Dynamics* 48.S1, pp. 337–352. DOI: 10.1080/00423111003748088. Available: <https://www.tandfonline.com/doi/10.1080/004231119808969565>.
- Catania, G. and Mancinelli, N. (2007). 'Motorcycle Local Stability Analysis Under Acceleration and Braking by Model Linearization and Eigenproblem Solution'. In: *Proceedings of the ASME 2007 International Design Engineering Technical Conferences and Computers and Information in Engineering Conference. Volume 1: 21st Biennial Conference on Mechanical Vibration and Noise, Parts A, B, and C* (04–07/09/2007). Las Vegas, USA: ASME, pp. 393–403. DOI: 10.1115/DETC2007-34824. Available: <https://asmedigitalcollection.asme.org/IDETC-CIE/proceedings/IDETC-CIE2007/393/325134>.
- Catania, G. and Mancinelli, N. (2008). 'Modeling Nonlinear Motorcycle Dynamical Behavior During Severe Acceleration and Braking'. In: *Proceedings of the ASME 2008 International Mechanical Engineering Congress and Exposition. Volume 17: Transportation Systems* (31/10–06/11/2008). Boston, USA: ASME, pp. 315–319. DOI: 10.1115/IMECE2008-67441. Available: <https://asmedigitalcollection.asme.org/IMECE/proceedings/IMECE2008/315/337137>.
- Catania, G., Leonelli, L. and Mancinelli, N. (2013). 'A Multibody Motorcycle Model for the Analysis and Prediction of Chatter Vibrations'. In: *Proceedings of the ASME 2013 International Mechanical Engineering Congress and Exposition. Volume 13: Transportation Systems* (15–21/11/2013). V013T14A006. San Diego, USA: ASME. DOI: 10.1115/IMECE2013-62903. Available: <https://asmedigitalcollection.asme.org/IMECE/proceedings/IMECE2013/V013T14A006/256433>.
- Cattabriga, S., De Felice, A. and Sorrentino, S. (2021). 'Patter Instability of Racing Motorcycles in Straight Braking Manoeuvre'. In: *Vehicle System Dynamics* 59.1, pp. 33–55. DOI: 10.1080/00423114.2019.1663389. Available: <https://www.tandfonline.com/doi/10.1080/00423114.2019.1663389>.
- Collins, R. N. (1963). 'A Mathematical Analysis of the Stability of Two Wheeled Vehicles' [Ph.D. Thesis]. Madison, USA: University of Wisconsin. Available: <http://digital.library.wisc.edu/1793/394>.
- Cooper, K. R. (1983). 'The Effect of Handlebar Fairings on Motorcycle Aerodynamics'. In: *SAE International Congress and Exposition* (28/02–04/03/1983). No. 830156. Detroit, USA: Society of Automotive Engineers, Inc. DOI: 10.4271/830156. Available: <https://www.sae.org/publications/technical-papers/content/830156>.
- Cossalter, V., Doria, A. and Lot, R. (1999). 'Steady Turning of Two-Wheeled Vehicles'. In: *Vehicle System Dynamics* 31.3, pp. 157–181. DOI: 10.1076/vesd.31.3.157.2013. Available: <https://www.tandfonline.com/doi/10.1076/vesd.31.3.157.2013>.
- Cossalter, V., Doria, A. and Lot, R. (2000). 'Optimum Suspension Design for Motorcycle Braking'. In: *Vehicle System Dynamics* 34.3, pp. 175–198. DOI: 10.1076/vesd.34.3.175.2034. Available: <https://www.tandfonline.com/doi/10.1076/vesd.34.3.175.2034>.

- Cossalter, V. and Lot, R. (2002). 'A Motorcycle Multi-Body Model for Real Time Simulations Based on the Natural Coordinates Approach'. In: *Vehicle System Dynamics* 37.6, pp. 423–447. DOI: 10.1076/vesd.37.6.423.3523. Available: <https://www.tandfonline.com/doi/10.1076/vesd.37.6.423.3523>.
- Cossalter, V., Doria, A., Lot, R., Ruffo, N. and Salvador, M. (2003). 'Dynamic Properties of Motorcycle and Scooter Tyres: Measurement and Comparison'. In: *Vehicle System Dynamics* 39.5, pp. 329–352. DOI: 10.1076/vesd.39.5.329.14145. Available: <https://www.tandfonline.com/doi/abs/10.1076/vesd.39.5.329.14145>.
- Cossalter, V., Lot, R. and Maggio, F. (2004). 'The Modal Analysis of a Motorcycle in Straight Running and on a Curve'. In: *Meccanica* 39.1, pp. 1–16. DOI: 10.1023/A:1026269926222. Available: <https://link.springer.com/article/10.1023/a:1026269926222#citeas>.
- Cossalter, V., Lot, R. and Massaro, M. (2007). 'The Influence of Frame Compliance and Rider Mobility on the Scooter Stability'. In: *Vehicle System Dynamics* 45.4, pp. 313–326. DOI: 10.1080/00423110600976100. Available: <https://www.tandfonline.com/doi/10.1080/00423110600976100>.
- Cossalter, V., Lot, R. and Massaro, M. (2008). 'The Chatter of Racing Motorcycles'. In: *Vehicle System Dynamics* 46.4, pp. 339–353. DOI: 10.1080/00423110701416501. Available: <https://www.tandfonline.com/doi/10.1080/00423110701416501>.
- Cossalter, V., Lot, R. and Massaro, M. (2011). 'An Advanced Multibody Code for Handling and Stability Analysis of Motorcycles'. In: *Meccanica* 46.5, pp. 943–958. DOI: 10.1007/s11012-010-9351-7. Available: <https://link.springer.com/article/10.1007/s11012-010-9351-7>.
- Cossalter, V., Lot, R. and Massaro, M. (2012). 'The Significance of Powertrain Characteristics on the Chatter of Racing Motorcycles'. In: *Proceedings of the ASME 2012 11th Biennial Conference on Engineering Systems Design and Analysis. Volume 3: Advanced Composite Materials and Processing; Robotics; Information Management and PLM; Design Engineering* (02–04/07/2012). Nantes, France: ASME, pp. 607–613. DOI: 10.1115/ESDA2012-82274. Available: <https://asmedigitalcollection.asme.org/ESDA/proceedings/ESDA2012/607/231458>.
- Cossalter, V., Doria, A., Giolo, E., Taraborrelli, L. and Massaro, M. (2014). 'Identification of the Characteristics of Motorcycle and Scooter Tyres in the Presence of Large Variations in Inflation Pressure'. In: *Vehicle System Dynamics* 52.10, pp. 1333–1354. DOI: 10.1080/00423114.2014.940981. Available: <https://www.tandfonline.com/doi/10.1080/00423114.2014.940981>.
- Cossalter, V., Doria, A., Massaro, M. and Taraborrelli, L. (2015). 'Experimental and Numerical Investigation on the Motorcycle Front Frame Flexibility and Its Effect on Stability'. In: *Mechanical Systems and Signal Processing* 60, pp. 452–471. DOI: 10.1016/j.ymsp.2015.02.011. Available: <https://www.sciencedirect.com/science/article/pii/S0888327015000849>.
- De Rossi, L., Schramm, A. E. and De Felice, A. (2022). 'Multibody Efficiency Analysis of Chain Drives in Racing Motorcycles'. In: *Journal of Applied and Computational Mechanics* 8.3, pp. 1091–1102. DOI: 10.22055/jacm.2022.39795.3467. Available: https://jacm.scu.ac.ir/article_17379.html.
- de Vries, E. J. H. and Pacejka, H. B. (1998). 'Motorcycle Tyre Measurements and Models'. In: *Vehicle System Dynamics* 29.S1, pp. 280–298. DOI: 10.1080/00423119808969565. Available: <https://www.tandfonline.com/doi/10.1080/00423119808969565>.
- Delft-Tyre (2013). *MF-Tyre/MF-Swift 6.2 Equation Manual* [Tech. Report]. Document revision: 20130706. Delft, The Netherlands: TNO.
- Desoer, C. (1969). 'Slowly Varying System $\dot{x} = A(t)x$ '. In: *IEEE Transactions on Automatic Control* 14.6, pp. 780–781. DOI: 10.1109/TAC.1969.1099336. Available: <https://ieeexplore.ieee.org/document/1099336>.
- Döhring, E. (1955). 'Die Stabilität von Einspurfahrzeugen'. In: *Forschung Ing.-Wes.* 21.2, pp. 50–62. Translated by J. Lotsof. DOI: 10.1007/BF02592590. Available: <https://link.springer.com/article/10.1007/BF02592590>.
- Doria, A. and Formentini, M. (2011). 'Identification of the Structural Modes of High Performance Bicycles in the Perspective of Wobble Control'. In: *Proceedings of the ASME 2011 International Design Engineering Technical Conferences and Computers and Information in Engineering Conference. Volume 4: 8th International Conference on Multibody Systems, Nonlinear Dynamics, and Control, Parts A and B* (28–31/08/2011). Washington, DC, USA: ASME, pp. 551–560. DOI: 10.1115/DETC2011-47030. Available: <https://asmedigitalcollection.asme.org/IDETC-CIE/proceedings/IDETC-CIE2011/551/353739>.
- Doria, A. and Taraborrelli, L. (2016a). 'Out-of-Plane Vibrations and Relaxation Length of the Tyres for Single-Track Vehicles'. In: *Proceedings of the Institution of Mechanical Engineers, Part D: Journal of Automobile Engineering* 230.5, pp. 609–622. DOI: 10.1177/0954407015590703. Available: <https://journals.sagepub.com/doi/10.1177/0954407015590703>.

- Doria, A. and Taraborrelli, L. (2016b). 'The Twist Axis of Frames With Particular Application to Motorcycles'. In: *Proceedings of the Institution of Mechanical Engineers, Part C: Journal of Mechanical Engineering Science* 230.17, pp. 3026–3039. DOI: 10.1177/0954406215604862. Available: <https://journals.sagepub.com/doi/10.1177/0954406215604862>.
- Evangelou, S. (2003). 'The Control and Stability Analysis of Two-Wheeled Road Vehicles' [Ph.D. Thesis]. London, UK: Imperial College. Available: https://library-search.imperial.ac.uk/permalink/44IMP_INST/mek6kh/alma995251274401591.
- Evangelou, S., Limebeer, D. J. N. and Tomas-Rodriguez, M. (2008). 'Influence of Road Camber on Motorcycle Stability'. In: *Journal of Applied Mechanics* 75.6. DOI: 10.1115/1.2937140. Available: <https://asmedigitalcollection.asme.org/appliedmechanics/article/75/6/061020/476306>.
- Evangelou, S., Limebeer, D. J. N. and Tomas-Rodriguez, M. (2010). 'Suppression of Burst Oscillations in Racing Motorcycles'. In: *49th IEEE Conference on Decision and Control (CDC)* (15–17/12/2010). Atlanta, USA: IEEE, pp. 5578–5585. DOI: 10.1109/CDC.2010.5717690. Available: <https://ieeexplore.ieee.org/document/5717690>.
- Evangelou, S., Limebeer, D. J. N. and Tomas-Rodriguez, M. (2013). 'Suppression of Burst Oscillations in Racing Motorcycles'. In: *Journal of Applied Mechanics* 80.1. DOI: 10.1115/1.4006491. Available: <https://asmedigitalcollection.asme.org/appliedmechanics/article/80/1/011003/367729>.
- Ferretti, G., Scaglioni, B. and Rossi, A. (2014). 'Multibody Model of a Motorbike With a Flexible Swingarm'. In: *Proceedings of the 10th International Modelica Conference* (10–12/03/2014). Ed. by Tummescheit, H. and Årzén, K. E. No. 096. Lund, Sweden: Modelica Association and Linköping University Electronic Press, pp. 273–282. DOI: 10.3384/ECP14096273.
- Fu, H. (1966). 'Fundamental Characteristics of Single-Track Vehicles in Steady Turning'. In: *Bulletin of JSME* 9.34, pp. 284–293. DOI: 10.1299/jsme1958.9.284. Available: https://www.jstage.jst.go.jp/article/jsme1958/9/34/9_34_284/_article.
- Gani, M., Sharp, R. S. and Limebeer, D. J. N. (1996). 'Multi-Body Simulation Software in the Study of Two-Wheeled Road Vehicles'. In: *Proceedings of 35th IEEE Conference on Decision and Control* (13/12/1996). Vol. 3. Kobe, Japan, pp. 2804–2805. DOI: 10.1109/CDC.1996.573540. Available: <https://ieeexplore.ieee.org/document/573540>.
- Gani, M., Sharp, R. S. and Limebeer, D. J. N. (1997). 'Multi-Body Simulation Software in the Analysis of Motorcycle Dynamics'. In: *8th IFAC/IFIP/IFORS Symposium on Transportation Systems* (16–18/06/1997). Vol. 30. No. 8. Chania, Greece, pp. 227–232. DOI: [https://doi.org/10.1016/S1474-6670\(17\)43828-6](https://doi.org/10.1016/S1474-6670(17)43828-6). Available: <https://www.sciencedirect.com/science/article/pii/S1474667017438286>.
- Gelb, A. and Vander Velde, W. E. (1968). *Multiple-Input Describing Functions and Nonlinear System Design*. McGraw-Hill. ISBN: 978-0-07-023124-5.
- Greenbaum, A., Li, R. C. and Overton, M. L. (2020). 'First-Order Perturbation Theory for Eigenvalues and Eigenvectors'. In: *SIAM Review* 62.2, pp. 463–482. Available: <https://epubs.siam.org/doi/10.1137/19M124784X>.
- Guiggiani, M. (2018). *The Science of Vehicle Dynamics: Handling, Braking, and Ride of Road and Race Cars*. Cham, Switzerland: Springer. ISBN: 978-3-031-06461-6. DOI: 10.1007/978-3-031-06461-6. Available: <https://link.springer.com/book/10.1007/978-3-031-06461-6>.
- Hagedorn, P., Eckstein, M., Heffel, E. and Wagner, A. (2014). 'Self-Excited Vibrations and Damping in Circulatory Systems'. In: *Journal of Applied Mechanics* 81.10. 101009. DOI: 10.1115/1.4028240. Available: <https://asmedigitalcollection.asme.org/appliedmechanics/article/81/10/101009/370171>.
- Hand, R. S. (1988). 'Comparisons and Stability Analysis of Linearized Equations of Motion for a Basic Bicycle Model' [M.Sc. Thesis]. Ithaca, USA: Cornell University. Available: <https://newcatalog.library.cornell.edu/catalog/1524580>.
- Hayes, R. and Marques, S. P. (2015). 'Prediction of Limit Cycle Oscillations Under Uncertainty Using a Harmonic Balance Method'. In: *Computers & Structures* 148, pp. 1–13. DOI: 10.1016/j.compstruc.2014.10.010. Available: <https://www.sciencedirect.com/science/article/pii/S0045794914002399>.
- Herfkens, B. D. (1949). *De Stabiliteit van het Rijwiel* (Report No. IRO-3). Translated by J. D. G. Kooijman. The Hague, The Netherlands: Instituut voor Rijwielontwikkeling.
- Jennings, G. (1974). 'A Study of Motorcycle Suspension Damping Characteristics'. In: *National West Coast Meeting* (12–16/08/1974). No. 740628. Anaheim, USA: Society of Automotive Engineers, Inc. DOI: 10.4271/740628. Available: <https://www.sae.org/publications/technical-papers/content/740628>.
- Jones, D. E. H. (1970). 'The Stability of the Bicycle'. In: *Physics Today* 23.4, pp. 34–40. DOI: 10.1063/1.3022064. Available: <https://physicstoday.scitation.org/doi/10.1063/1.3022064>.

- Kane, T. R. (1975). 'Fundamental Kinematical Relationships for Single-Track Vehicles'. In: *International Journal of Mechanical Sciences* 17.8, pp. 499–504. DOI: 10.1016/0020-7403(75)90014-4. Available: <https://www.sciencedirect.com/science/article/pii/0020740375900144>.
- Kane, T. R. (1977). 'Steady Turning of Single-Track Vehicles'. In: *1977 International Automotive Engineering Congress and Exposition (28/02–04/03/1977)*. No. 770057. Detroit, USA: Society of Automotive Engineers, Inc. DOI: 10.4271/770057. Available: <https://www.sae.org/publications/technical-papers/content/770057>.
- Kane, T. R. (1978). 'The Effect of Frame Flexibility on High Speed Weave of Motorcycles'. In: *1978 Automotive Engineering Congress and Exposition (01/02/1978)*. No. 780306. Society of Automotive Engineers, Inc. DOI: 10.4271/780306. Available: <https://www.sae.org/publications/technical-papers/content/780306>.
- Katayama, T. and Nishimi, T. (1990). 'Energy Flow Method for the Study of Motorcycle Wobble Mode'. In: *Vehicle System Dynamics* 19.3, pp. 151–175. DOI: 10.1080/00423119008968940. Available: <https://www.tandfonline.com/doi/10.1080/00423119008968940>.
- Koenen, C. (1983). 'The Dynamic Behaviour of a Motorcycle when Running Straight Ahead and when Cornering' [Ph.D. Thesis]. Delft, The Netherlands: TU Delft. Available: <http://resolver.tudelft.nl/uuid:dd93034a-e750-49c2-8abb-f9b57d00c3d2>.
- Kröger, M., Neubauer, M. and Popp, K. (2008). 'Experimental Investigation on the Avoidance of Self-Excited Vibrations'. In: *Philosophical Transactions of the Royal Society A: Mathematical, Physical and Engineering Sciences* 366.1866, pp. 785–810. Available: <https://royalsocietypublishing.org/doi/10.1098/rsta.2007.2127>.
- Lee, B. H. K., Liu, L. and Chung, K. W. (2005). 'Airfoil Motion in Subsonic Flow With Strong Cubic Nonlinear Restoring Forces'. In: *Journal of Sound and Vibration* 281.3, pp. 699–717. DOI: 10.1016/j.jsv.2004.01.034. Available: <https://www.sciencedirect.com/science/article/pii/S0022460X04001981>.
- Leonelli, L. (2014). 'Dynamic Analysis of the Motorcycle Chattering Behaviour by Means of Symbolic Multibody Modelling' [Ph.D. Thesis]. Bologna, Italy: Alma Mater Studiorum Università di Bologna. DOI: 10.6092/unibo/amsdottorato/6587. Available: <http://amsdottorato.unibo.it/6587>.
- Leonelli, L. and Mancinelli, N. (2015). 'A Multibody Motorcycle Model With Rigid-Ring Tyres: Formulation and Validation'. In: *Vehicle System Dynamics* 53.6, pp. 775–797. DOI: 10.1080/00423114.2015.1014820. Available: <https://www.tandfonline.com/doi/10.1080/00423114.2015.1014820>.
- Leonelli, L. and Mancinelli, N. (2016). 'Correction To: A Multibody Motorcycle Model With Rigid-Ring Tyres: Formulation and Validation'. In: *Vehicle System Dynamics* 54.12, p. 1808. DOI: 10.1080/00423114.2016.1203506. Available: <https://www.tandfonline.com/doi/10.1080/00423114.2016.1203506>.
- Leonelli, L., Mancinelli, N. and Sorrentino, S. (2016). 'A Study of Motorcycle Chatter Vibration with Multibody Models of Increasing Complexity'. In: *The Dynamics of Vehicles on Roads and Tracks: Proceedings of the 24th Symposium of the International Association for Vehicle System Dynamics (IAVSD 2015) (17–21/08/2015)*. Ed. by Rosenberger, M., Plöchl, M., Six, K. and Edelmann, J. Graz, Austria: CRC Press, pp. 209–218. DOI: 10.1201/b21185. Available: <https://www.taylorfrancis.com/chapters/edit/10.1201/b21185-23>.
- Leonelli, L., Cattabriga, S. and Sorrentino, S. (2018). 'Driveline Instability of Racing Motorcycles in Straight Braking Manoeuvre'. In: *Proceedings of the Institution of Mechanical Engineers, Part C: Journal of Mechanical Engineering Science* 232.17, pp. 3045–3061. DOI: 10.1177/0954406217730093. Available: <https://journals.sagepub.com/doi/10.1177/0954406217730093>.
- Leonelli, L. and Limebeer, D. J. N. (2020). 'Optimal Control of a Road Racing Motorcycle on a Three-Dimensional Closed Track'. In: *Vehicle System Dynamics* 58.8, pp. 1285–1309. DOI: 10.1080/00423114.2019.1617886. Available: <https://www.tandfonline.com/doi/10.1080/00423114.2019.1617886>.
- Lewis, A. P. (2019). 'Refined Analytical Approximations to Limit Cycles for Non-Linear Multi-Degree-of-Freedom Systems'. In: *International Journal of Non-Linear Mechanics* 110, pp. 58–68. DOI: 10.1016/j.ijnonlinmec.2018.12.009. Available: <https://www.sciencedirect.com/science/article/pii/S0020746218306905>.
- Lewis, A. P. (2020). 'Approximations to Limit Cycles for a Nonlinear Multi-Degree-of-Freedom System With a Cubic Nonlinearity Through Combining the Harmonic Balance Method With Perturbation Techniques'. In: *International Journal of Non-Linear Mechanics* 126, p. 103590. DOI: 10.1016/j.ijnonlinmec.2020.103590. Available: <https://www.sciencedirect.com/science/article/pii/S0020746220302523>.
- Limebeer, D. J. N., Sharp, R. S. and Evangelou, S. (2001). 'The Stability of Motorcycles Under Acceleration and Braking'. In: *Proceedings of the Institution of Mechanical Engineers, Part C: Journal of Mechanical Engineering Science* 215.9, pp. 1095–1109. DOI: 10.1177/095440620121500910. Available: <https://journals.sagepub.com/doi/10.1177/095440620121500910>.

- Limebeer, D. J. N., Sharp, R. S. and Evangelou, S. (2002). 'Motorcycle Steering Oscillations Due to Road Profiling'. In: *Journal of Applied Mechanics* 69.6, pp. 724–739. DOI: 10.1115/1.1507768. Available: <https://asmedigitalcollection.asme.org/appliedmechanics/article/69/6/724/471995>.
- Limebeer, D. J. N. and Sharp, R. S. (2006). 'Bicycles, Motorcycles, and Models'. In: *IEEE Control Systems Magazine* 26.5, pp. 34–61. DOI: 10.1109/MCS.2006.1700044. Available: <https://ieeexplore.ieee.org/document/1700044>.
- Limebeer, D. J. N. and Massaro, M. (2018). *Dynamics and Optimal Control of Road Vehicles*. Oxford, UK: Oxford University Press. ISBN: 9780198825715. DOI: 10.1093/oso/9780198825715.001.0001. Available: <https://academic.oup.com/book/43936>.
- Lot, R. and Lio, M. D. (2004). 'A Symbolic Approach for Automatic Generation of the Equations of Motion of Multibody Systems'. In: *Multibody System Dynamics* 12.2, pp. 147–172. DOI: 10.1023/B:MUBO.0000044319.63215.22. Available: <https://link.springer.com/article/10.1023/B:MUBO.0000044319.63215.22>.
- Lot, R. (2004). 'A Motorcycle Tire Model for Dynamic Simulations: Theoretical and Experimental Aspects'. In: *Meccanica* 39.3, pp. 207–220. DOI: 10.1023/B:MECC.0000022842.12077.5c. Available: <https://link.springer.com/article/10.1023/B:MECC.0000022842.12077.5c>.
- Lot, R., Cossalter, V. and Massaro, M. (2005). 'The Significance of Frame Compliance and Rider Mobility on the Motorcycle Stability'. In: *ECOMAS Thematic Conference (21–24/06/2005)*. Ed. by Goicolea, J. M., Cuadrado, J. and García Orden, J. C. Madrid, Spain: Multibody Dynamics.
- Manrique-Escobar, C. A., Pappalardo, C. M. and Guida, D. (2021). 'A Multibody System Approach for the Systematic Development of a Closed-Chain Kinematic Model for Two-Wheeled Vehicles'. In: *Machines* 9.11. DOI: 10.3390/machines9110245. Available: <https://www.mdpi.com/2075-1702/9/11/245>.
- Manrique-Escobar, C. A., Pappalardo, C. M. and Guida, D. (2022). 'On the Analytical and Computational Methodologies for Modelling Two-wheeled Vehicles within the Multibody Dynamics Framework: A Systematic Literature Review'. In: *Journal of Applied and Computational Mechanics* 8.1, pp. 153–181. DOI: 10.22055/jacm.2021.37935.3118. Available: https://jacm.scu.ac.ir/article_16970.html.
- Martini, A., Bellani, G. and Fragassa, C. (2018). 'Numerical Assessment of a New Hydro-Pneumatic Suspension System for Motorcycles'. In: *International Journal of Automotive and Mechanical Engineering* 15.2. Available: <https://journal.ump.edu.my/ijame/article/view/19>.
- Marumo, Y. and Katayama, T. (2009a). 'Analysis of Motorcycle Weave Mode by Using Energy Flow Method'. In: *Journal of Mechanical Systems for Transportation and Logistics* 2.2, pp. 157–169. DOI: 10.1299/jmtl.2.157. Available: https://www.jstage.jst.go.jp/article/jmtl/2/2/2_2_157/_article.
- Marumo, Y. and Katayama, T. (2009b). 'Effects of Structural Flexibility on Motorcycle Straight Running Stability by using Energy Flow Method'. In: *Journal of Mechanical Systems for Transportation and Logistics* 2.2, pp. 170–181. DOI: 10.1299/jmtl.2.170. Available: https://www.jstage.jst.go.jp/article/jmtl/2/2/2_2_170/_article.
- Massaro, M., Lot, R., Cossalter, V., Brendelson, J. and Sadauckas, J. (2012). 'Numerical and Experimental Investigation of Passive Rider Effects on Motorcycle Weave'. In: *Vehicle System Dynamics* 50.S1, pp. 215–227. DOI: 10.1080/00423114.2012.679284. Available: <https://www.tandfonline.com/doi/abs/10.1080/00423114.2012.679284>.
- Massaro, M., Cossalter, V. and Cusimano, G. (2013). 'The Effect of the Inflation Pressure on the Tyre Properties and the Motorcycle Stability'. In: *Proceedings of the Institution of Mechanical Engineers, Part D: Journal of Automobile Engineering* 227.10, pp. 1480–1488. DOI: 10.1177/0954407013496231. Available: <https://journals.sagepub.com/doi/10.1177/0954407013496231>.
- Meijaard, J. P. and Popov, A. A. (2006). 'Numerical Continuation of Solutions and Bifurcation Analysis in Multibody Systems Applied to Motorcycle Dynamics'. In: *Nonlinear Dynamics* 43.1, pp. 97–116. DOI: 10.1007/s11071-006-0753-y. Available: <https://link.springer.com/article/10.1007/s11071-006-0753-y>.
- Meijaard, J. P. and Popov, A. A. (2007). 'Multi-Body Modelling and Analysis Into the Non-Linear Behaviour of Modern Motorcycles'. In: *Proceedings of the Institution of Mechanical Engineers, Part K: Journal of Multibody Dynamics* 221.1, pp. 63–76. DOI: 10.1243/1464419JMBD49. Available: <https://journals.sagepub.com/doi/10.1243/1464419jmbd49>.
- Müller, P. C. and Schiehlen, W. O. (1985). *Linear Vibrations: A Theoretical Treatment of Multi-Degree-of-Freedom Vibrating Systems*. Translated by S. Swierczkowski. Dordrecht, The Netherlands: Springer. ISBN: 978-90-247-2983-8. DOI: 10.1007/978-94-009-5047-4. Available: <https://link.springer.com/book/10.1007/978-94-009-5047-4>.

- Nayfeh, A. H. and Mook, D. T. (2004). *Nonlinear Oscillations*. Weinheim, Germany: Wiley-VCH. ISBN: 978-0-47-112142-8. DOI: 10.1002/9783527617586. Available: <https://onlinelibrary.wiley.com/doi/book/10.1002/9783527617586>.
- Nehaoua, L., Arioui, H., Seguy, N. and Mammari, S. (2013). ‘Dynamic Modelling of a Two-Wheeled Vehicle: Jourdain Formalism’. In: *Vehicle System Dynamics* 51.5, pp. 648–670. DOI: 10.1080/00423114.2012.762536. Available: <https://www.tandfonline.com/doi/10.1080/00423114.2012.762536>.
- Neĭmark, Y. I. and Fufaev, N. A. (1972). *Dynamics of Nonholonomic Systems*. Translated from Russian by J. R. Barbour. Providence, USA: American Mathematical Society. ISBN: 0-8218-1583-0.
- Pacejka, H. B. (1974). ‘Some Recent Investigations into Dynamics and Frictional Behavior of Pneumatic Tires’. In: *The Physics of Tire Traction: Theory and Experiment*. Ed. by Hays, D. F. and Browne, A. L. Boston, USA: Springer, pp. 257–279. ISBN: 978-1-4757-1370-1. DOI: 10.1007/978-1-4757-1370-1_15. Available: https://link.springer.com/chapter/10.1007/978-1-4757-1370-1_15.
- Pacejka, H. B. and Sharp, R. S. (1991). ‘Shear Force Development by Pneumatic Tyres in Steady State Conditions: A Review of Modelling Aspects’. In: *Vehicle System Dynamics* 20.3-4, pp. 121–175. DOI: 10.1080/00423119108968983. Available: <https://www.tandfonline.com/doi/10.1080/00423119108968983>.
- Pacejka, H. B. and Bakker, E. (1992). ‘The Magic Formula Tyre Model’. In: *Vehicle System Dynamics* 21.S1, pp. 1–18. DOI: 10.1080/00423119208969994. Available: <https://www.tandfonline.com/doi/10.1080/00423119208969994>.
- Pacejka, H. B. (2012). *Tire and Vehicle Dynamics*. Oxford, UK: Elsevier. ISBN: 978-0-08-097016-5. DOI: 10.1016/B978-0-08-097016-5.00008-5. Available: <https://www.elsevier.com/books/tire-and-vehicle-dynamics/pacejka/978-0-08-097016-5>.
- Pappalardo, C. M., Lettieri, A. and Guida, D. (2021a). ‘A General Multibody Approach for the Linear and Nonlinear Stability Analysis of Bicycle Systems. Part I: Methods of Constrained Dynamics’. In: *Journal of Applied and Computational Mechanics* 7.2, pp. 655–670. DOI: 10.22055/jacm.2020.35438.2653. Available: https://jacm.scu.ac.ir/article_16125.html.
- Pappalardo, C. M., Lettieri, A. and Guida, D. (2021b). ‘A General Multibody Approach for the Linear and Nonlinear Stability Analysis of Bicycle Systems. Part II: Application to the Whipple-Carvallo Bicycle Model’. In: *Journal of Applied and Computational Mechanics* 7.2, pp. 671–700. DOI: 10.22055/jacm.2020.35439.2654. Available: https://jacm.scu.ac.ir/article_16126.html.
- Passigato, F., Eisele, A., Wisselmann, D., Gordner, A. and Diermeyer, F. (2020). ‘Analysis of the Phenomena Causing Weave and Wobble in Two-Wheelers’. In: *Applied Sciences* 10.19, p. 6826. DOI: 10.3390/app10196826. Available: <https://www.mdpi.com/2076-3417/10/19/6826>.
- Passigato, F., Wischniewski, A., Gordner, A. and Diermeyer, F. (2021). ‘Two Approaches for the Synthesis of a Weave-Wobble-Stabilizing Controller in Motorcycles’. In: *2021 IEEE International Intelligent Transportation Systems Conference (ITSC) (19–22/09/2021)*. Indianapolis, USA: IEEE, pp. 3496–3501. DOI: 10.1109/ITSC48978.2021.9565019. Available: <https://ieeexplore.ieee.org/document/9565019>.
- Passigato, F., Gordner, A. and Diermeyer, F. (2022). ‘Modeling of the Weave and Wobble Eigenmodes of Motorcycles Using Flexible Multibody Simulation’. In: *Proceedings of the ASME 2022 International Design Engineering Technical Conferences and Computers and Information in Engineering Conference (IDETC-CIE2022). Volume 9: 18th International Conference on Multibody Systems, Nonlinear Dynamics, and Control (MSNDC) (14–17/08/2022)*. St. Louis, USA: ASME. DOI: 10.1115/DETC2022-89945. Available: <https://asmedigitalcollection.asme.org/IDETC-CIE/proceedings/IDETC-CIE2022/V009T09A010/1150637>.
- Raines, M. and Thorpe, T. E. (1986). ‘The Relationship Between Twist Axis and Effective Torsional Stiffness of a Motorcycle Frame’. In: *Proceedings of the Institution of Mechanical Engineers, Part D: Transport Engineering* 200.1, pp. 69–73. DOI: 10.1243/PIME_PROC_1986_200_165_02. Available: https://journals.sagepub.com/doi/10.1243/PIME_PROC_1986_200_165_02.
- Rand, R. H. (2012). *Lecture Notes on Nonlinear Vibrations* [Lecture Notes]. Ithaca, USA: Cornell University. Available: <https://ecommons.cornell.edu/handle/1813/28989>.
- Rice, R. S. and Roland Jr., R. D. (1970). *An Evaluation of the Performance and Handling Qualities of Bicycles* (CAL Report No. VJ-2888-K). Buffalo, USA: Cornell Aeronautical Laboratory, Inc.
- Rice, R. S. (1974). *Bicycle Dynamics: Simplified Steady State Response Characteristics and Stability Indices* (CAL Report No. ZN-5431-V-1). Buffalo, USA: Calspan Corporation.
- Rice, R. S. (1975). *Accident Avoidance Capabilities of Motorcycles* [Tech. Report]. NHTSA Contract No. DOT-HS-4-00976. Buffalo, USA: Calspan Corporation.

- Rice, R. S. (1976). *Bicycle Dynamics: Simplified Dynamic Stability Analyses* (CAL Report No. ZN-5921-V-2). Buffalo, USA: Calspan Corporation.
- Roe, G. E. and Thorpe, T. E. (1976). 'A Solution of the Low-Speed Wheel Flutter Instability in Motorcycles'. In: *Journal of Mechanical Engineering Science* 18.2, pp. 57–65. DOI: 10.1243/JMES_JOUR_1976_018_012_02. Available: https://journals.sagepub.com/doi/10.1243/JMES_JOUR_1976_018_012_02.
- Roe, G. E. and Thorpe, T. E. (1989). 'The Influence of Frame Structure on the Dynamics of Motorcycle Stability'. In: *Small Engine Technology Conference & Exposition* (11–13/09/1989). No. 891772. Society of Automotive Engineers, Inc. DOI: 10.4271/891772. Available: <https://www.sae.org/publications/technical-papers/content/891772>.
- Roland Jr., R. D. and Massing, D. E. (1971). *A Digital Computer Simulation of Bicycle Dynamics* (CAL Report No. YA-3063-K-1). Buffalo, USA: Cornell Aeronautical Laboratory, Inc.
- Roland Jr., R. D. and Lynch, J. P. (1972). *Bicycle Dynamics: Tire Characteristics and Rider Modeling* (CAL Report No. YA-3063-K-2). Buffalo, USA: Cornell Aeronautical Laboratory, Inc.
- Roland Jr., R. D. (1973). 'Simulation Study of Motorcycle Stability at High Speed'. In: *Second International Congress on Automotive Safety: Motorcycle and Recreational Vehicle Safety* (16–18/07/1973). San Francisco, USA.
- Roland Jr., R. D. and Rice, R. S. (1973). *Bicycle Dynamics: Rider Guidance Modeling and Disturbance Response* (CAL Report No. ZS-5157-K-1). Buffalo, USA: Calspan Corporation.
- Romualdi, L., Mancinelli, N., De Felice, A. and Sorrentino, S. (2020). 'A New Application of the Extended Kalman Filter to the Estimation of Roll Angles of a Motorcycle With Inertial Measurement Unit'. In: *FME Transactions* 48.2, pp. 255–265. DOI: 10.5937/fme2002255R. Available: <https://scindeks.ceon.rs/article.aspx?artid=1451-20922002255R>.
- Rosenbrook, H. H. (1963). 'The Stability of Linear Time-Dependent Control Systems'. In: *International Journal of Electronics* 15.1, pp. 73–80. DOI: 10.1080/00207216308937556. Available: <https://www.tandfonline.com/doi/10.1080/00207216308937556>.
- Sacon, A. and Hauser, J. (2009). 'An Efficient Newton Method for General Motorcycle Kinematics'. In: *Vehicle System Dynamics* 47.2, pp. 221–241. DOI: 10.1080/00423110801966108. Available: <https://www.tandfonline.com/doi/10.1080/00423110801966108>.
- Sakai, H., Kanaya, O. and Iijima, H. (1979). 'Effect of Main Factors on Dynamic Properties of Motorcycle Tires'. In: *1979 Automotive Engineering Congress and Exposition* (01/02/1979). No. 790259. Society of Automotive Engineers, Inc. DOI: 10.4271/790259. Available: <https://www.sae.org/publications/technical-papers/content/790259>.
- Salisbury, I. G., Limebeer, D. J. N., Tremlett, A. and Massaro, M. (2016). 'The Unification of Acceleration Envelope and Driveability Concepts'. In: *The Dynamics of Vehicles on Roads and Tracks: Proceedings of the 24th Symposium of the International Association for Vehicle System Dynamics (IAVSD 2015)*. Ed. by Rosenberger, M., Plöchl, M., Six, K. and Edelmann, J. Graz, Austria: CRC Press, pp. 571–580. DOI: 10.1201/b21185. Available: <https://www.taylorfrancis.com/chapters/edit/10.1201/b21185-60>.
- Sayers, M. W. (1990). 'Symbolic Computer Methods to Automatically Formulate Vehicle Simulation Codes' [Ph.D. Thesis]. Ann Arbor, USA: University of Michigan. Available: <https://deepblue.lib.umich.edu/handle/2027.42/105578>.
- Sayers, M. W. (1991). 'Symbolic computer language for multibody systems'. In: *Journal of Guidance, Control, and Dynamics* 14.6, pp. 1153–1163. DOI: 10.2514/3.20770. Available: <https://arc.aiaa.org/doi/10.2514/3.20770>.
- Sayers, M. W. (1993). 'AUTOSIM'. In: *Vehicle System Dynamics* 22.S1, pp. 53–56. DOI: 10.1080/00423119308969467. Available: <https://www.tandfonline.com/doi/10.1080/00423119308969467>.
- Schmeitz, A. J. C., Jansen, S. T. H., Tezuka, Y., Hasegawa, M. and Miyagishi, S. (2010). 'Application of the Rigid Ring Model for Simulating the Dynamics of Motorcycle Tyres on Uneven Roads'. In: *Proceedings, Bicycle and Motorcycle Dynamics 2010 Symposium on the Dynamics and Control of Single Track Vehicles*, pp. 20–22. Available: <http://www.bicycle.tudelft.nl/ProceedingsBMD2010/papers/schmeitz2010application.pdf>.
- Schwab, A. L. and Meijaard, J. P. (2013). 'A Review on Bicycle Dynamics and Rider Control'. In: *Vehicle System Dynamics* 51.7, pp. 1059–1090. DOI: 10.1080/00423114.2013.793365. Available: <https://www.tandfonline.com/doi/10.1080/00423114.2013.793365>.
- Sharp, R. S. (1969). 'The Nature and Prevention of Axle Tramp'. In: *Proceedings of the Institution of Mechanical Engineers: Automobile Division* 184.1, pp. 41–54. DOI: 10.1243/PIME_AUTO_1969_184_011_02. Available: https://journals.sagepub.com/doi/10.1243/pime_auto_1969_184_011_02.

- Sharp, R. S. (1971). 'The Stability and Control of Motorcycles'. In: *Journal of Mechanical Engineering Science* 13.5, pp. 316–329. DOI: 10.1243/JMES_JOUR_1971_013_051_02. Available: https://journals.sagepub.com/doi/10.1243/jmes_jour_1971_013_051_02.
- Sharp, R. S. (1974). 'The Influence of Frame Flexibility on the Lateral Stability of Motorcycles'. In: *Journal of Mechanical Engineering Science* 16.2, pp. 117–120. DOI: 10.1243/JMES_JOUR_1974_016_021_02. Available: https://journals.sagepub.com/doi/10.1243/jmes_jour_1974_016_021_02.
- Sharp, R. S. (1976a). 'The Influence of the Suspension System on Motorcycle Weave-Mode Oscillations'. In: *Vehicle System Dynamics* 5.3, pp. 147–154. DOI: 10.1080/00423117608968410. Available: <https://www.tandfonline.com/doi/10.1080/00423117608968410>.
- Sharp, R. S. (1976b). 'The Dynamics of Single Track Vehicles'. In: *Vehicle System Dynamics* 5.1-2, pp. 67–77. DOI: 10.1080/00423117508968406. Available: <https://www.tandfonline.com/doi/10.1080/00423117508968406>.
- Sharp, R. S. and Alstead, C. J. (1980). 'The Influence of Structural Flexibilities on the Straight-Running Stability of Motorcycles'. In: *Vehicle System Dynamics* 9.6, pp. 327–357. DOI: 10.1080/00423118008968629. Available: <https://www.tandfonline.com/doi/10.1080/00423118008968629>.
- Sharp, R. S. and Giles, C. G. (1983). 'Motorcycle Front Wheel Patter in Heavy Braking'. In: *Vehicle System Dynamics* 12.1-3, pp. 159–160. DOI: 10.1080/00423118308968746. Available: <https://www.tandfonline.com/doi/10.1080/00423118308968746>.
- Sharp, R. S. (1985). 'The Lateral Dynamics of Motorcycles and Bicycles'. In: *Vehicle System Dynamics* 14.4-6, pp. 265–283. DOI: 10.1080/00423118508968834. Available: <https://www.tandfonline.com/doi/10.1080/00423118508968834>.
- Sharp, R. S. (1994). 'The Application of Multi-Body Computer Codes to Road Vehicle Dynamics Modelling Problems'. In: *Proceedings of the Institution of Mechanical Engineers, Part D: Journal of Automobile Engineering* 208.1, pp. 55–61. DOI: 10.1243/PIME_PROC_1994_208_158_02. Available: https://journals.sagepub.com/doi/10.1243/PIME_PROC_1994_208_158_02.
- Sharp, R. S. and Limebeer, D. J. N. (2001). 'A Motorcycle Model for Stability and Control Analysis'. In: *Multibody System Dynamics* 6.2, pp. 123–142. DOI: 10.1023/A:1017508214101. Available: <https://link.springer.com/article/10.1023/A:1017508214101>.
- Sharp, R. S. (2001). 'Stability, Control and Steering Responses of Motorcycles'. In: *Vehicle System Dynamics* 35.4-5, pp. 291–318. DOI: 10.1076/vesd.35.4.291.2042. Available: <https://www.tandfonline.com/doi/10.1076/vesd.35.4.291.2042>.
- Sharp, R. S., Evangelou, S. and Limebeer, D. J. N. (2003). 'Improved Modelling of Motorcycle Dynamics'. In: *ECCOMAS Thematic Conference on Advances in Computational Multibody Dynamics (01–04/07/2003)*. Ed. by Ambrósio, J. A. C. Lisbon, Portugal: Multibody Dynamics.
- Sharp, R. S., Evangelou, S. and Limebeer, D. J. N. (2004). 'Advances in the Modelling of Motorcycle Dynamics'. In: *Multibody System Dynamics* 12.3, pp. 251–283. DOI: 10.1023/B:MUBO.0000049195.60868.a2. Available: <https://link.springer.com/article/10.1023/B:MUBO.0000049195.60868.a2>.
- Sharp, R. S. and Limebeer, D. J. N. (2004). 'On Steering Wobble Oscillations of Motorcycles'. In: *Proceedings of the Institution of Mechanical Engineers, Part C: Journal of Mechanical Engineering Science* 218.12, pp. 1449–1456. DOI: 10.1243/0954406042690434. Available: <https://journals.sagepub.com/doi/10.1243/0954406042690434>.
- Sharp, R. S. and Watanabe, Y. (2013). 'Chatter Vibrations of High-Performance Motorcycles'. In: *Vehicle System Dynamics* 51.3, pp. 393–404. DOI: 10.1080/00423114.2012.727440. Available: <https://www.tandfonline.com/doi/10.1080/00423114.2012.727440>.
- Singh, D. and Goel, V. (1971). 'Stability of Rajdoot Scooter'. In: *1971 Automotive Engineering Congress and Exposition (11–15/01/1971)*. No. 710273. Detroit, USA: Society of Automotive Engineers, Inc. DOI: 10.4271/710273. Available: <https://www.sae.org/publications/technical-papers/content/710273>.
- Society of Automotive Engineers, Inc. (2022). *Vehicle Dynamics Terminology (SAE Standard J670)*. DOI: 10.4271/J670_202206. Available: https://www.sae.org/standards/content/j670_202206/.
- Somieski, G. (2001). 'An Eigenvalue Method for Calculation of Stability and Limit Cycles in Nonlinear Systems'. In: *Nonlinear Dynamics* 26.4, pp. 3–22. DOI: 10.1023/A:1017384211491. Available: <https://link.springer.com/article/10.1023/A:1017384211491>.
- Sorrentino, S. and Leonelli, L. (2017). 'A Study on the Stability of a Motorcycle Wheel–Swingarm Suspension With Chain Transmission'. In: *Vehicle System Dynamics* 55.11, pp. 1707–1730. DOI: 10.1080/00423114.2017.1319962. Available: <https://www.tandfonline.com/doi/10.1080/00423114.2017.1319962>.

- Splerings, P. T. J. (1981). 'The Effects of Lateral Front Fork Flexibility on the Vibrational Modes of Straight-Running Single-Track Vehicles'. In: *Vehicle System Dynamics* 10.1, pp. 21–35. DOI: 10.1080/00423118108968633. Available: <https://www.tandfonline.com/doi/10.1080/00423118108968633>.
- Taraborrelli, L., Favaron, V. and Doria, A. (2017). 'The Effect of Swingarm Stiffness on Motorcycle Stability: Experimental Measurements and Numerical Simulations'. In: *International Journal of Vehicle Systems Modelling and Testing* 12.3-4, pp. 240–261. DOI: 10.1504/IJVSMT.2017.089981. Available: <https://www.inderscienceonline.com/doi/10.1504/IJVSMT.2017.089981>.
- Tezuka, Y., Ishii, H. and Kiyota, S. (2001). 'Application of the Magic Formula Tire Model to Motorcycle Manueverability Analysis'. In: *JSAE Review* 22.3, pp. 305–310. DOI: 10.1016/S0389-4304(01)00113-8. Available: <https://www.sciencedirect.com/science/article/pii/S0389430401001138>.
- Tezuka, Y., Kokubu, S., Shiomi, Y. and Kiyota, S. (2004). 'Vibration Characteristics Analysis in Vehicle Body Vertical Plane of Motorcycle during Turning'. In: *Honda R&D Technical Review* 16.1, pp. 219–224. Available: <https://www.hondarandd.jp/point.php?pid=510&lang=en>.
- Timoshenko, S. and Young, D. H. (1948). *Advanced Dynamics*. New York, USA: McGraw-Hill. ISBN: 978-1258432294.
- Troger, H. and Zeman, K. (1984). 'A Nonlinear Analysis of the Generic Types of Loss of Stability of the Steady State Motion of a Tractor-Semitrailer'. In: *Vehicle System Dynamics* 13.4, pp. 161–172. DOI: 10.1080/00423118408968773. Available: <https://www.tandfonline.com/doi/10.1080/00423118408968773>.
- Troger, H. and Steindl, A. (2012). *Nonlinear Stability and Bifurcation Theory: An Introduction for Engineers and Applied Scientists*. Vienna, Austria: Springer. ISBN: 978-3-211-82292-0. Available: <https://link.springer.com/book/10.1007/978-3-7091-9168-2>.
- Weir, D. H. (1972). 'Motorcycle Handling Dynamics and Rider Control and the Effect of Design Configuration on Response and Performance' [Ph.D. Thesis]. Los Angeles, USA: University of California. Available: https://search.library.ucla.edu/permalink/01UCS_LAL/17p22dp/alma9935730773606533.
- Weir, D. H. and Zellner, J. W. (1978). 'Lateral-Directional Motorcycle Dynamics and Rider Control'. In: *1978 Automotive Engineering Congress and Exposition (01/02/1978)*. No. 780304. Society of Automotive Engineers, Inc. DOI: 10.4271/780304. Available: <https://www.sae.org/publications/technical-papers/content/780304>.
- Whipple, F. J. W. (1899). 'The Stability of the Motion of a Bicycle'. In: *Quarterly Journal of Pure and Applied Mathematics* 30.120, pp. 312–348.
- Wilson-Jones, R. A. (1951). 'Steering and Stability of Single-Track Vehicles'. In: *Proceedings of the Institution of Mechanical Engineers: Automobile Division* 5.1, pp. 191–213. DOI: 10.1243/PIME_AUTO_1951_000_023_02. Available: https://journals.sagepub.com/doi/10.1243/PIME_AUTO_1951_000_023_02.
- Yakubovich, V. A. and Starzhinskiĭ, V. M. (1975). *Linear Differential Equations With Periodic Coefficients: Part I and II*. Translated by D. Louvish. New York, USA: John Wiley & Sons. ISBN: 978-0-470-96953-3.
- Zellner, J. W. and Weir, D. H. (1979). 'Moped Directional Dynamics and Handling Qualities'. In: *1979 Automotive Engineering Congress and Exposition (01/02/1979)*. No. 790260. Society of Automotive Engineers, Inc. DOI: 10.4271/790260. Available: <https://www.sae.org/publications/technical-papers/content/790260>.

Appendix

A	Additional Model Development Material	91
A.1	Equations of Motion and Lagrange Method	91
A.2	Inertial Terms in the Equations of Motion	92
A.3	Dynamic Chain Length Proof	93
A.4	Non-Dimensional Variable Definitions	95

A Additional Model Development Material

A.1 Equations of Motion and Lagrange Method

To begin the derivation of the EOMs, first the kinematics of the system need to be derived. While the system contains a translating and rotating frame, it is simple enough to be completely described using a set of generalised coordinates, and the use of quasi-coordinates is not required. To begin, the constant linear and rotational velocity of point F are given by:

$$\mathbf{V}_f = \{V_{fx}, V_{fy}, 0\} \quad (\text{A.1})$$

$$\boldsymbol{\Omega}_f = \{0, 0, \Omega_{fz}\} \quad (\text{A.2})$$

and the relevant centre of mass location vectors are given by:

$$\mathbf{r}_{fr} = \begin{Bmatrix} -\eta_{fr} x_f \\ -\eta_{fr} h_f \sin(\phi(t)) \\ \eta_{fr} h_f \cos(\phi(t)) \end{Bmatrix} \quad (\text{A.3})$$

$$\mathbf{r}_{sa} = \begin{Bmatrix} -x_f - \eta_{sa} \ell_{sa} \cos(\alpha(t)) \\ -\sin(\phi(t)) (h_f + \eta_{sa} \ell_{sa} \sin(\alpha(t))) \\ \cos(\phi(t)) (h_f + \eta_{sa} \ell_{sa} \sin(\alpha(t))) \end{Bmatrix} \quad (\text{A.4})$$

$$\mathbf{r}_{wh} = \begin{Bmatrix} -x_f - \ell_{sa} \cos(\alpha(t)) \\ -\sin(\phi(t)) (h_f + \ell_{sa} \sin(\alpha(t))) \\ \cos(\phi(t)) (h_f + \ell_{sa} \sin(\alpha(t))) \end{Bmatrix} \quad (\text{A.5})$$

which can be used to find the system velocities using:

$$\mathbf{V}_i = \frac{d}{dt} \mathbf{r}_i + \boldsymbol{\Omega}_f \times \mathbf{r}_i + \mathbf{V}_f \quad (\text{A.6})$$

To find the rotation velocity vectors in the reference systems of each individual components, the rotation matrices for each relevant joint need to be defined. These are given by:

$$\mathbf{R}_z = \begin{bmatrix} \cos(\Omega_{fz} t) & -\sin(\Omega_{fz} t) & 0 \\ \sin(\Omega_{fz} t) & \cos(\Omega_{fz} t) & 0 \\ 0 & 0 & 1 \end{bmatrix} \quad (\text{A.7})$$

$$\mathbf{R}_\phi = \begin{bmatrix} 1 & 0 & 0 \\ 0 & \cos(\phi(t)) & -\sin(\phi(t)) \\ 0 & \sin(\phi(t)) & \cos(\phi(t)) \end{bmatrix} \quad (\text{A.8})$$

$$\mathbf{R}_\alpha = \begin{bmatrix} \cos(\alpha(t)) & 0 & \sin(\alpha(t)) \\ 0 & 1 & 0 \\ -\sin(\alpha(t)) & 0 & \cos(\alpha(t)) \end{bmatrix} \quad (\text{A.9})$$

Applying these rotation matrices, the individual rotational velocities for the components can be found. These are given in the reference frame of the component itself, to align with their inertia matrices. They are given by:

$$\boldsymbol{\omega}_{fr} = \mathbf{R}_\phi \cdot (\mathbf{R}_z \cdot \boldsymbol{\Omega}_f + \{\dot{\phi}(t), 0, 0\}) \quad (\text{A.10})$$

$$\boldsymbol{\omega}_{sa} = \mathbf{R}_\alpha \cdot \left(\mathbf{R}_\phi \cdot \left(\mathbf{R}_z \cdot \boldsymbol{\Omega}_f + \{\dot{\phi}(t), 0, 0\} \right) + \{0, \dot{\alpha}(t), 0\} \right) \quad (\text{A.11})$$

$$\boldsymbol{\omega}_{wh} = \mathbf{R}_\phi \cdot \left(\mathbf{R}_z \cdot \boldsymbol{\Omega}_f + \{\dot{\phi}(t), 0, 0\} \right) + \{0, -\dot{\theta}(t), 0\} \quad (\text{A.12})$$

This results in the position, velocity, orientation, and rotation rates of each component being defined. Using these, the kinetic and potential energy scalars are found to be:

$$T = \frac{1}{2} (m_{fr} \mathbf{V}_{fr}^2 + m_{sa} \mathbf{V}_{sa}^2 + m_{wh} \mathbf{V}_{wh}^2 + \boldsymbol{\omega}_{fr} \mathbf{J}_{fr} \boldsymbol{\omega}_{fr} + \boldsymbol{\omega}_{sa} \mathbf{J}_{sa} \boldsymbol{\omega}_{sa} + \boldsymbol{\omega}_{wh} \mathbf{J}_{wh} \boldsymbol{\omega}_{wh}) \quad (\text{A.13})$$

$$V = -g(m_{fr} z_{fr} + m_{sa} z_{sa} + m_{wh} z_{wh}) + \frac{1}{2} \left(k_f (\phi - \phi_{f0})^2 + k_s (\alpha - \alpha_{s0})^2 + k_c (\ell_c(\alpha, \theta) - \ell_{fc})^2 \right) \quad (\text{A.14})$$

where z_i is the third element of vector \mathbf{r}_i . The Lagrangian $L = T - V$ is then applied in the equation:

$$\frac{d}{dt} \frac{\partial L}{\partial \dot{q}_i} - \frac{\partial L}{\partial q_i} = Q_i \quad (\text{A.15})$$

to give the EOM for generalised coordinate i . Here Q_i are the generalised, non-conservative forces such as the dampers and tyre tangential forces acting on the system variable i . These are given by the principle of virtual work:

$$Q_i = \sum_{j=1}^n \mathbf{F}_j \cdot \frac{\partial \mathbf{r}_j}{\partial q_i} \quad (\text{A.16})$$

where \mathbf{F}_j are the non-conservative forces or moments, \mathbf{r}_j are the location vectors in which they act, and q_i are the system variables.

A.2 Inertial Terms in the Equations of Motion

The simplified inertia terms used in Equation (3.2)–(3.4) are given by:

$$J_\alpha = J_{say} + \ell_{sa}^2 (m_{sa} \eta_{sa}^2 + m_{wh}) \quad (\text{A.17})$$

$$J_\phi = J_{fix} + J_{whxz} + \cos^2(\alpha) J_{sax} + \sin^2(\alpha) J_{saz} + (\eta_{fr}^2 m_{fr} + m_{sa} + m_{wh}) h_f^2 + 2 \sin(\alpha) \ell_{sa} (\eta_{sa} m_{sa} + m_{wh}) h_f + \sin^2(\alpha) \ell_{sa}^2 (\eta_{sa}^2 m_{sa} + m_{wh}) \quad (\text{A.18})$$

$$M_{cent,\alpha} = \cos(\alpha) \left(\left(\sin(\alpha) (J_{saz} - J_{sax} + (\eta_{sa}^2 m_{sa} + m_{wh}) \ell_{sa}^2) + (\eta_{sa} m_{sa} + m_{wh}) h_f \ell_{sa} \right) \dot{\phi}^2 + \left(\sin(\alpha) \cos^2(\phi) (J_{saz} - J_{sax} + (\eta_{sa}^2 m_{sa} + m_{wh}) \ell_{sa}^2) - (\eta_{sa} m_{sa} + m_{wh}) \ell_{sa} (\sin^2(\phi) h_f + \tan(\alpha) x_f) \right) \Omega_{fz}^2 \right) \quad (\text{A.19})$$

$$M_{cor,\alpha} = \cos(\alpha) \ell_{sa} (\eta_{sa} m_{sa} + m_{wh}) \left(\sin(\phi) V_{fx} + \tan(\alpha) V_{fy} \right) \Omega_{fz} \quad (\text{A.20})$$

$$M_{gyro,\alpha} = \left(J_{say} - (\cos^2(\alpha) - \sin^2(\alpha)) (J_{saz} - J_{sax}) - 2 \sin(\alpha) \ell_{sa} (\eta_{sa} m_{sa} + m_{wh}) h_f - 2 \sin^2(\alpha) \ell_{sa}^2 (\eta_{sa}^2 m_{sa} + m_{wh}) \right) \cos(\phi) \Omega_{fz} \dot{\phi} \quad (\text{A.21})$$

$$M_{cent,\phi} = (J_{fry} - J_{frz} + J_{say} - \cos^2(\alpha) J_{saz} - \sin^2(\alpha) J_{sax} + J_{why} - J_{whxz} + (\eta_{fr}^2 m_{fr} + m_{sa} + m_{wh}) h_f^2 + 2 \sin(\alpha) \ell_{sa} (\eta_{sa} m_{sa} + m_{wh}) h_f + \sin^2(\alpha) \ell_{sa}^2 (\eta_{sa}^2 m_{sa} + m_{wh})) \cos(\phi) \sin(\phi) \Omega_{fz}^2 \quad (\text{A.22})$$

$$M_{cor,\phi} = ((\eta_{fr} m_{fr} + m_{sa} + m_{wh}) h_f + \sin(\alpha) \ell_{sa} (\eta_{sa} m_{sa} + m_{wh})) \cos(\phi) \Omega_{fz} V_{fx} \quad (\text{A.23})$$

$$M_{gyro,\phi} = J_{why} \cos(\phi) \Omega_{fz} \dot{\theta} - \left(J_{say} - (\cos^2(\alpha) - \sin^2(\alpha)) (J_{saz} - J_{sax}) - 2 \sin(\alpha) \ell_{sa} (\eta_{sa} m_{sa} + m_{wh}) h_f - 2 \sin^2(\alpha) \ell_{sa}^2 (\eta_{sa}^2 m_{sa} + m_{wh}) \right) \cos(\phi) \Omega_{fz} \dot{\alpha} - 2 \cos(\alpha) \left(\sin(\alpha) J_{saz} - \sin(\alpha) J_{sax} + \ell_{sa} (\eta_{sa} m_{sa} + m_{wh}) h_f + \sin(\alpha) \ell_{sa}^2 (\eta_{sa}^2 m_{sa} + m_{wh}) \right) \dot{\phi} \quad (\text{A.24})$$

A.3 Dynamic Chain Length Proof

This section gives the proof that Equation (3.24) meets the conservative force requirements given by Equation (3.12)–(3.13). Beginning with Equation (3.14):

$$\begin{aligned}\frac{\partial \ell_c(\theta, \alpha)}{\partial \alpha} &= \frac{\partial}{\partial \alpha} \left(\ell_{tc}(\alpha) - \delta(r_p - r_c)(\alpha + \psi(\alpha) - \psi(0)) - \delta(r_p \theta_p - r_c \theta) \right) \\ &= \frac{\partial \ell_{tc}(\alpha)}{\partial \alpha} - \delta(r_p - r_c) \left(1 + \frac{\partial \psi(\alpha)}{\partial \alpha} \right) \\ &= \frac{\partial \ell_{tc}(\alpha)}{\partial \alpha} - \delta(r_p - r_c) \left(1 + \frac{1}{\cos(\psi(\alpha))} \frac{\partial}{\partial \alpha} (\sin(\psi(\alpha))) \right)\end{aligned}$$

From here, the terms are converted into terms of ψ_1 and ψ_2 :

$$\begin{aligned}\frac{\partial \ell_c(\theta, \alpha)}{\partial \alpha} &= \frac{\partial \ell_{tc}(\alpha)}{\partial \alpha} + \sin(\psi_1) d(\alpha) \left(1 + \frac{1}{\cos(\psi(\alpha))} \frac{\partial}{\partial \alpha} (\sin(\psi_1) \cos(\psi_2) + \cos(\psi_1) \sin(\psi_2)) \right) \\ &= \frac{\partial \ell_{tc}(\alpha)}{\partial \alpha} + \sin(\psi_1) \left(d(\alpha) + \frac{d(\alpha)}{\cos(\psi(\alpha))} \left(\frac{\partial}{\partial \alpha} (\sin(\psi_1)) \cos(\psi_2) \right. \right. \\ &\quad \left. \left. + \sin(\psi_1) \frac{\partial}{\partial \alpha} (\cos(\psi_2)) + \frac{\partial}{\partial \alpha} (\cos(\psi_1)) \sin(\psi_2) + \cos(\psi_1) \frac{\partial}{\partial \alpha} (\sin(\psi_2)) \right) \right)\end{aligned}$$

Next, the derivatives of Equation (3.25)–(3.28) need to be determined:

$$\frac{\partial}{\partial \alpha} (\cos(\psi_1)) = \frac{1}{d(\alpha)^2} \left(d(\alpha) \frac{\partial \ell_{tc}(\alpha)}{\partial \alpha} - \ell_{tc}(\alpha) \frac{\partial d(\alpha)}{\partial \alpha} \right) = \frac{1}{d(\alpha)} \left(\frac{\partial \ell_{tc}(\alpha)}{\partial \alpha} - \cos(\psi_1) \frac{\partial d(\alpha)}{\partial \alpha} \right) \quad (\text{A.25})$$

$$\frac{\partial}{\partial \alpha} (\sin(\psi_1)) = \frac{\delta(r_p - r_c)}{d(\alpha)^2} \frac{\partial d(\alpha)}{\partial \alpha} = \frac{1}{d(\alpha)} \left(-\sin(\psi_1) \frac{\partial d(\alpha)}{\partial \alpha} \right) \quad (\text{A.26})$$

$$\begin{aligned}\frac{\partial}{\partial \alpha} (\cos(\psi_2)) &= \frac{1}{d(\alpha)^2} \left(\ell_p \sin(\beta_p - \alpha) d(\alpha) - (\ell_{sa} + \ell_p \cos(\beta_p - \alpha)) \frac{\partial d(\alpha)}{\partial \alpha} \right) \\ &= \frac{1}{d(\alpha)} \left(\sin(\psi_2) d(\alpha) - \cos(\psi_2) \frac{\partial d(\alpha)}{\partial \alpha} \right) \quad (\text{A.27})\end{aligned}$$

$$\begin{aligned}\frac{\partial}{\partial \alpha} (\sin(\psi_2)) &= \frac{1}{d(\alpha)^2} \left(-\ell_p \cos(\beta_p - \alpha) d(\alpha) - \ell_p \sin(\beta_p - \alpha) \frac{\partial d(\alpha)}{\partial \alpha} \right) \\ &= \frac{1}{d(\alpha)} \left(\ell_{sa} - \cos(\psi_2) d(\alpha) - \sin(\psi_2) \frac{\partial d(\alpha)}{\partial \alpha} \right) \quad (\text{A.28})\end{aligned}$$

Introducing these results into the proof, note that the $d(\alpha)$ cancels out:

$$\begin{aligned}\frac{\partial \ell_c(\theta, \alpha)}{\partial \alpha} &= \frac{\partial \ell_{tc}(\alpha)}{\partial \alpha} + \sin(\psi_1) \left(d(\alpha) + \frac{1}{\cos(\psi(\alpha))} \left(\left(-\sin(\psi_1) \frac{\partial d(\alpha)}{\partial \alpha} \right) \cos(\psi_2) \right. \right. \\ &\quad \left. \left. + \sin(\psi_1) \left(\sin(\psi_2) d(\alpha) - \cos(\psi_2) \frac{\partial d(\alpha)}{\partial \alpha} \right) + \left(\frac{\partial \ell_{tc}(\alpha)}{\partial \alpha} - \cos(\psi_1) \frac{\partial d(\alpha)}{\partial \alpha} \right) \sin(\psi_2) \right. \right. \\ &\quad \left. \left. + \cos(\psi_1) \left(\ell_{sa} - \cos(\psi_2) d(\alpha) - \sin(\psi_2) \frac{\partial d(\alpha)}{\partial \alpha} \right) \right) \right) \\ &= \frac{\partial \ell_{tc}(\alpha)}{\partial \alpha} + \sin(\psi_1) \left(d(\alpha) + \frac{1}{\cos(\psi(\alpha))} \left((\sin(\psi_1) \sin(\psi_2) - \cos(\psi_1) \cos(\psi_2)) d(\alpha) \right. \right. \\ &\quad \left. \left. - 2(\sin(\psi_1) \cos(\psi_2) + \cos(\psi_1) \sin(\psi_2)) \frac{\partial d(\alpha)}{\partial \alpha} + \cos(\psi_1) \ell_{sa} + \sin(\psi_2) \frac{\partial \ell_{tc}(\alpha)}{\partial \alpha} \right) \right)\end{aligned}$$

$$\begin{aligned}
&= \frac{\partial \ell_{tc}(\alpha)}{\partial \alpha} + \frac{\sin(\psi_1)}{\cos(\psi(\alpha))} \left(-2(\sin(\psi_1) \cos(\psi_2) + \cos(\psi_1) \sin(\psi_2)) \frac{\partial d(\alpha)}{\partial \alpha} \right. \\
&\quad \left. + \cos(\psi_1) \ell_{sa} + \sin(\psi_2) \frac{\partial \ell_{tc}(\alpha)}{\partial \alpha} \right)
\end{aligned}$$

where the $d(\alpha)$ terms cancel out again due to the use of Equation (3.30). The required derivatives are:

$$\frac{\partial d(\alpha)}{\partial \alpha} = \frac{\ell_{sa} \ell_p \sin(\beta_p - \alpha)}{d(\alpha)} = \sin(\psi_2) \ell_{sa} \quad (\text{A.29})$$

$$\frac{\partial \ell_{tc}(\alpha)}{\partial \alpha} = \frac{\ell_{sa} \ell_p \sin(\beta_p - \alpha)}{\ell_{tc}(\alpha)} = \frac{\sin(\psi_2)}{\cos(\psi_1)} \ell_{sa} \quad (\text{A.30})$$

Substituting these into the above gives:

$$\begin{aligned}
\frac{\partial \ell_c(\theta, \alpha)}{\partial \alpha} &= \ell_{sa} \left(\frac{\sin(\psi_2)}{\cos(\psi_1)} + \frac{\sin(\psi_1)}{\cos(\psi(\alpha))} \left(-2(\sin(\psi_1) \cos(\psi_2) + \cos(\psi_1) \sin(\psi_2)) \sin(\psi_2) \right. \right. \\
&\quad \left. \left. + \cos(\psi_1) + \sin(\psi_2) \frac{\sin(\psi_2)}{\cos(\psi_1)} \right) \right) \\
&= \ell_{sa} \left(\frac{\sin(\psi_2) (\cos(\psi_1) \cos(\psi_2) - \sin(\psi_1) \sin(\psi_2))}{\cos(\psi_1) \cos(\psi(\alpha))} + \frac{\sin(\psi_1) \sin(\psi_2)^2}{\cos(\psi_1) \cos(\psi(\alpha))} \right. \\
&\quad \left. + \frac{\sin(\psi_1)}{\cos(\psi(\alpha))} (\cos(\psi_1) - 2(\sin(\psi_1) \cos(\psi_2) + \cos(\psi_1) \sin(\psi_2)) \sin(\psi_2)) \right) \\
&= \ell_{sa} \left(\frac{\cos(\psi_2) \sin(\psi_2)}{\cos(\psi(\alpha))} \right. \\
&\quad \left. + \frac{\sin(\psi_1)}{\cos(\psi(\alpha))} (\cos(\psi_1) - 2(\sin(\psi_1) \cos(\psi_2) + \cos(\psi_1) \sin(\psi_2)) \sin(\psi_2)) \right) \\
&= \frac{\ell_{sa}}{\cos(\psi(\alpha))} \left(\cos(\psi_2) \sin(\psi_2) - \cos(\psi_2) \sin(\psi_2) \sin(\psi_1)^2 \right. \\
&\quad \left. + \cos(\psi_1) \sin(\psi_1) - \cos(\psi_1) \sin(\psi_1) \sin(\psi_2)^2 \right. \\
&\quad \left. - \sin(\psi_1)^2 \cos(\psi_2) \sin(\psi_2) - \cos(\psi_1) \sin(\psi_1) \sin(\psi_2)^2 \right) \\
&= \frac{\ell_{sa}}{\cos(\psi(\alpha))} \left(\cos(\psi_2) \sin(\psi_2) \cos(\psi_1)^2 + \cos(\psi_1) \sin(\psi_1) \cos(\psi_2)^2 \right. \\
&\quad \left. - \sin(\psi_1)^2 \cos(\psi_2) \sin(\psi_2) - \cos(\psi_1) \sin(\psi_1) \sin(\psi_2)^2 \right) \\
&= \frac{\ell_{sa}}{\cos(\psi(\alpha))} (\cos(\psi_1) \cos(\psi_2) - \sin(\psi_1) \sin(\psi_2)) \\
&\quad \cdot (\sin(\psi_1) \cos(\psi_2) + \cos(\psi_1) \sin(\psi_2)) \\
&= \frac{\ell_{sa}}{\cos(\psi(\alpha))} \cos(\psi_1 + \psi_2) \sin(\psi_1 + \psi_2) \\
&= \frac{\ell_{sa}}{\cos(\psi(\alpha))} \cos(\psi(\alpha)) \sin(\psi(\alpha)) \\
&= \ell_{sa} \sin(\psi(\alpha))
\end{aligned}$$

Next, the verification of Equation (3.15) is much easier:

$$\begin{aligned}
\frac{\partial \ell_c(\theta, \alpha)}{\partial \theta} &= \frac{\partial}{\partial \theta} (\ell_{tc}(\alpha) - \delta(r_p - r_c) (\alpha + \psi(\alpha) - \psi(0)) - \delta(r_p \theta_p - r_c \theta)) \\
&= \frac{\partial}{\partial \theta} (-\delta(r_p \theta_p - r_c \theta)) \\
&= \delta r_c
\end{aligned}$$

The passages above show that the dynamic chain length determined in Equation (3.24) is a valid representation that follows the geometric and conservative equations of the chain force.

A.4 Non-Dimensional Variable Definitions

Acceleration Vector

Mass Matrix

$$m_\alpha = \frac{J_\alpha}{\ell_\alpha^2} \quad (\text{A.31})$$

$$\mathcal{J}_\theta = \frac{J_{\text{why}}}{m_\alpha R_{\text{c0}} R_{\text{R0}}} \quad (\text{A.32})$$

$$\mathcal{J}_\phi = \frac{J_\phi}{m_\alpha \ell_\phi^2} \quad (\text{A.33})$$

$$\omega_n = \sqrt{\frac{k}{m_\alpha}} \quad (\text{A.34})$$

Velocity Vector

Damping Matrix

$$\zeta = \frac{c_s}{2\ell_\alpha^2 \sqrt{k m_\alpha}} \quad (\text{A.35})$$

$$\Psi_f = \frac{c_f \ell_\alpha^2}{c_s \ell_\phi^2} \quad (\text{A.36})$$

$$\Psi_\omega = c_\phi \frac{J_{\text{why}} \omega_0 \ell_\alpha^2}{c_s \ell_\phi^2} \quad (\text{A.37})$$

Gyroscopic Matrix

$$\mathcal{G} = \frac{R_{\text{R0}}}{J_{\text{why}} \ell_\alpha} \left(J_{\text{say}} - (c_\alpha^2 - s_\alpha^2)(J_{\text{saz}} - J_{\text{sax}}) - 2(\tau_\alpha(\eta_{\text{sa}} m_{\text{sa}} + m_{\text{wh}}) h_f \ell_\alpha + \tau_\alpha^2(\eta_{\text{sa}}^2 m_{\text{sa}} + m_{\text{wh}}) \ell_\alpha^2) \right) \quad (\text{A.38})$$

Tyre Slip Matrix

$$\nu_x = \frac{V_{\text{fx}}}{R_{\text{R0}} \omega_0} \quad \nu_y = \frac{V_{\text{fy}}}{R_{\text{R0}} \omega_0} \quad \nu_\psi = \frac{\Omega_{\text{fz}}}{R_{\text{R0}} \omega_0} \quad (\text{A.39})$$

$$\gamma_{\text{xx}} = \frac{C_{\sigma_{x,x}} \ell_\alpha^2}{c_s V_{\text{fx}}} \quad \gamma_{\text{xy}} = \frac{C_{\sigma_{y,x}} \ell_\alpha^2}{c_s V_{\text{fx}}} \quad \gamma_{\text{yx}} = \frac{C_{\sigma_{x,y}} \ell_\alpha^2}{c_s V_{\text{fx}}} \quad \gamma_{\text{yy}} = \frac{C_{\sigma_{y,y}} \ell_\alpha^2}{c_s V_{\text{fx}}} \quad (\text{A.40})$$

$$\Gamma_x = \gamma_{\text{xx}} \nu_x + \gamma_{\text{xy}} \nu_y + \left(\gamma_{\text{xx}} \tau_\phi \ell_\phi - \gamma_{\text{xy}} (x_f + \ell_\alpha) \right) \nu_\psi \quad (\text{A.41})$$

$$\Gamma_y = \gamma_{\text{yx}} \nu_x + \gamma_{\text{yy}} \nu_y + \left(\gamma_{\text{yx}} \tau_\phi \ell_\phi - \gamma_{\text{yy}} (x_f + \ell_\alpha) \right) \nu_\psi \quad (\text{A.42})$$

Displacement Vector

Stiffness Matrix

$$k = \frac{k_s}{\ell_\alpha^2} + \cos^2(\phi_0) k_z + \frac{\tau_\alpha c_\phi (\eta_{\text{sa}} m_{\text{sa}} + m_{\text{wh}})}{\ell_\alpha} g \quad (\text{A.43})$$

$$\Phi_z = \frac{k_z}{k} \quad \Phi_f = \frac{k_f}{k \ell_\phi^2} \quad (\text{A.44})$$

$$g_{\alpha\phi} = \frac{\eta_{sa}m_{sa} + m_{wh}}{k\ell_\phi} g \quad (\text{A.45})$$

$$g_\phi = \frac{c_\phi \left((\eta_{fr}m_{fr} + m_{sa} + m_{wh})h_f + \tau_\alpha(\eta_{sa}m_{sa} + m_{wh})\ell_\alpha \right)}{k\ell_\phi^2} g \quad (\text{A.46})$$

Gyroscopic Matrix

$$\Phi_{\text{gyro}} = s_\phi \frac{J_{\text{why}}\omega_0\Omega_{fz}}{k\ell_\phi^2} \quad (\text{A.47})$$

Centrifugal Matrix

$$\Phi_{\text{cent}} = \frac{\Omega_{fz}^2}{k\ell_\alpha\ell_\phi} \left(\eta_{sa}(m_{sa} + m_{wh})h_f\ell_\alpha + \tau_\alpha (J_{\text{saz}} - J_{\text{sax}} + (\eta_{sa}^2 m_{sa} + m_{wh})\ell_{sa}^2) \right) \quad (\text{A.48})$$

$$C_\alpha = \frac{(\eta_{sa}^2 m_{sa} + m_{wh})\ell_{sa}^2 + (\eta_{sa}m_{sa} + m_{wh})(\tau_\alpha s_\phi^2 h_f + x_f)\ell_\alpha + c_\phi^2 (c_\alpha^2 - s_\alpha^2)J_{\text{saz}} - J_{\text{sax}}}{(\eta_{sa}m_{sa} + m_{wh})h_f\ell_\alpha + \tau_\alpha (J_{\text{saz}} - J_{\text{sax}} + (\eta_{sa}^2 m_{sa} + m_{wh})\ell_{sa}^2)} \quad (\text{A.49})$$

$$C_\phi = \frac{\left(J_{\text{fry}} - J_{\text{fz}} + J_{\text{say}} - c_\alpha^2 J_{\text{saz}} - s_\alpha^2 J_{\text{sax}} + J_{\text{why}} - J_{\text{whxz}} + (\eta_{fr}^2 m_{fr} + m_{sa} + m_{wh})h_f^2 \right) + 2\tau_\alpha (m_{sa}\eta_{sa} + m_{wh})h_f\ell_\alpha + \tau_\alpha^2 (\eta_{sa}^2 m_{sa} + m_{wh})\ell_{sa}^2}{(\eta_{sa}m_{sa} + m_{wh})h_f\ell_\alpha + \tau_\alpha (J_{\text{saz}} - J_{\text{sax}} + (\eta_{sa}^2 m_{sa} + m_{wh})\ell_{sa}^2)} \quad (\text{A.50})$$

Coriolis Matrix

$$\Phi_{\text{Cori}} = \frac{(\eta_{sa}m_{sa} + m_{wh})V_{fx}\Omega_{fz}}{k\ell_\phi} \quad (\text{A.51})$$

$$\zeta = \frac{V_{fy}}{V_{fx}} \quad (\text{A.52})$$

$$C_\phi = \frac{(\eta_{fr}m_{fr} + m_{sa} + m_{wh})h_f + \tau_\alpha(\eta_{sa}m_{sa} + m_{wh})\ell_\alpha}{(\eta_{sa}m_{sa} + m_{wh})\ell_\phi} \quad (\text{A.53})$$

Chain Stiffness Matrix

$$\Phi_c = \frac{k_c r_c^2}{kR_{c0}R_{R0}} \quad (\text{A.54})$$

$$\delta = \begin{cases} -1 & \rightarrow \text{acceleration} \\ 1 & \rightarrow \text{braking} \end{cases} \quad (\text{A.55})$$

$$\sigma = \frac{\sin(\psi(\alpha_0))R_{c0}}{c_\alpha r_c} \quad (\text{A.56})$$

$$\sigma' = \left(\frac{\cos^2(\psi(\alpha_0))}{\sin^2(\psi(\alpha_0))\ell_{tc}(\alpha_0)} - \frac{\cos(\psi(\alpha_0))}{\sin^2(\psi(\alpha_0))\ell_{sa}} \right) \Delta\ell_c \quad (\text{A.57})$$

$$\Delta\ell_c \rightarrow \text{Equilibrium chain stretch} \quad (\text{A.58})$$

Tyre Slip Matrix

$$\lambda_{x1} = c_\phi C_{F_z,x} \Phi_z - c_\phi^2 \frac{\eta}{kR_{R0}} \chi_x - \frac{1}{k} (s_\phi C_{\sigma_x,x} + \tau_\alpha C_{\sigma_y,x}) \nu_\psi \quad (\text{A.59})$$

$$\lambda_{y1} = c_\phi C_{F_z,y} \Phi_z - c_\phi^2 \frac{\eta}{kR_{R0}} \chi_y - \frac{1}{k} (s_\phi C_{\sigma_x,y} + \tau_\alpha C_{\sigma_y,y}) \nu_\psi \quad (\text{A.60})$$

$$\lambda_{x2} = \tau_\phi C_{F_z,x} \Phi_z + \frac{1}{k\ell_\phi} \left(C_{\phi,x} - \tau_\phi \frac{\eta R_{c0}'^\phi}{R_{R0}} \chi_x \right) + \frac{C_{\sigma_x,x} \nu_\psi}{k} \quad (\text{A.61})$$

$$\lambda_{y2} = \tau_\phi C_{F_z, y} \Phi_z + \frac{1}{k l_\phi} \left(C_{\phi, y} - \tau_\phi \frac{\eta R_{c0}'^\phi}{R_{R0}} \chi_y \right) + \frac{C_{\sigma_{x,y}} \nu_\psi}{k} \quad (\text{A.62})$$

$$\chi_x = C_{\sigma_{x,x}} \nu_x + C_{\sigma_{y,x}} \nu_y + \left(C_{\sigma_{x,x}} \tau_\phi l_\phi - C_{\sigma_{y,x}} (x_f + l_\alpha) \right) \nu_\psi \quad (\text{A.63})$$

$$\chi_y = C_{\sigma_{x,y}} \nu_x + C_{\sigma_{y,y}} \nu_y + \left(C_{\sigma_{x,y}} \tau_\phi l_\phi - C_{\sigma_{y,y}} (x_f + l_\alpha) \right) \nu_\psi \quad (\text{A.64})$$

Tyre Stationary Matrix

$$f = \frac{F_{z0}}{k l_\alpha} \quad (\text{A.65})$$

$$R_{c0} = R_r - \rho_r + c_\phi^2 (z_f - l_\phi) \quad (\text{A.66})$$

$$R_{c0}'^\alpha = -c_\phi^2 l_\alpha \quad R_{c0}'^\phi = c_\phi (2 - \xi_z) l_\phi \quad (\text{A.67})$$

$$\mu_{x0} = \frac{F_{x0}}{F_{z0}} \quad \mu_{y0} = \frac{F_{y0}}{F_{z0}} \quad (\text{A.68})$$